The role of HIF signaling during *Staphylococcus aureus* osteomyelitis and biomaterial-based treatment strategies

By

Caleb Ford

Dissertation

Submitted to the Faculty of the

Graduate School of Vanderbilt University

in partial fulfillment of the requirements

for the degree of

DOCTOR OF PHILOSOPHY

in

Biomedical Engineering

May 14, 2021

Nashville, Tennessee

Approved:

James E. Cassat, M.D., Ph.D.
Craig L. Duvall, Ph.D.
Scott A. Guelcher, Ph.D.
Rachelle W. Johnson, Ph.D.
Carlos H. Serezani, Ph.D.

DEDICATION

To my supportive wife and the family that raised me

—

Ad maiorem Dei gloriam

ACKNOWLEDGEMENTS

The work described in this thesis would not have been possible without the professional and personal help from many people and core facilities. The core facilities and research centers at Vanderbilt made my experiments much more manageable and smooth. In particular, I would like to acknowledge Josh Johnson, Ph.D., at Vanderbilt University Medical Center's Vanderbilt Center for Bone Biology for his assistance with histology of infected femurs, Vanderbilt University Medical Center's Digital Histology Shared Resource (DHSR) core facility that assisted in the imaging of histological sections, the Vanderbilt University Institute of Imaging Sciences (VUIIS) and Jarrod True for assisting with *in vivo* and *ex vivo* IVIS imaging techniques, the Small Molecule NMR Facility Core at Vanderbilt University for assistance with NMR analyses, and the Vanderbilt University Medical Center Division of Animal Care (DAC) for assistance with animal care. Thank you to Sasidhar Uppuganti, Ph.D., for all of your help with microCT and Scanco analyses. Thank you to Fiona Harrison, Ph.D., and Meghan Joly, Ph.D., for help with investigating ascorbic acid in the context of osteomyelitis.

I am grateful for the privilege to have received funding to complete my training in the Medical Scientist Training Program (MSTP) and within the lab of Jim Cassat. This work was in part possible because of funding from the National Institute of Allergy and Infectious Diseases which provided funding for my F30 (F30AI138424) and Jim's R01 (R01AI132560) that funded the bulk of this research project along with Jim's Career Award for Medical Scientists from the Burroughs Wellcome Fund. I have also received support from the Vanderbilt MSTP through a T32 training grant (T32GM007347). The Vanderbilt MSTP has been an excellent setting for my training thus far. I look forward to continuing my progress as a medical student.

Thank you to the MSTP leadership team, all of the current members and the past members during my time here. In particular, thank you to Terry Dermody for admitting me to the program. I was grateful for my brief time to be mentored at Vanderbilt by you. Thank you to Melissa Krasnove for constant support for me and other members of the MSTP even after moving to a new position. Thank you to Chris Williams for being available for quick chats in the hall and our individual meetings. I was grateful to have been able to get to know you better during my time with the Student Advisory Committee. Thank you to the other members of the MSTP leadership team current and past: Bryn Sierra, Megan Williams, Lourdes Estrada, Jim Bills, Larry Swift, Danny Winder, Ambra Pozzi, and Sally York.

Thank you to Jim Cassat for welcoming me into your lab. It takes a lot of trust to give someone in their twenties a key to a room with expensive tools and priceless samples! I am grateful for your mentorship. The road to this degree has not always been as smooth as I had hoped. It was frequently very difficult. You were always there to keep me calm and reassured. You have a mind that seems to always be linking disparate concepts and planning new experiments. I loved hearing all of your experimental ideas. I am appreciative of the time you have given me and the grace you have given me when mistakes happen. I look forward to a continued mentorship in our futures.

I am thankful to have been a member of the Cassat lab with Aimee (Wilde) Potter, Ph.D., Niki Putnam, Ph.D., Tom Spoonmore, Ph.D., Andrew Hendrix (overlapped for a day on my rotation so I will count it), Jacob Curry, Laura Fulbright, Chris Peek, Jenna Petronglo, Casey Butrico, Teresa Torres, Virginia Cruz, Ian Hurford, Kara Eichelberger, Ph.D., and Brittney Gimza, Ph.D. You have all helped me get to this point. Thank you to Aimee and Niki for showing me the ropes in the lab as senior graduate students. Thank you to Tom for all of 2019

and 2020, in particular. We bonded those years… a lot. Many procedures and experiments later, I can call you a close friend. I am very thankful we got to hit Phoenix together, share our project, and explore a different city before COVID shutdown conferences until (date TBD). I am proud of our work together and our co-first authorship. I could not have done it without you. Thank you to Chris Peek for your experimental help, your friendship, and your constant ability to look past my missteps. I enjoyed our time together in lab, in Montreal, and on MSTP retreats as the Cassat duo. Thank you for your expertise with many experiments. I really appreciate it. Thank you to the dynamic duo of Jacob and Laura, two of the best lab assistants money can buy. I always looked forward to coming into lab knowing I would be working with you two! Thank you to Casey and Jenna for being the most organized members of the Cassat lab. Along with Virginia, you two have kept the lab running smoothly. You are both selfless people who are more helpful than either of you two realize because you are both too humble to acknowledge how amazing you two are. Thank you to Virginia for maintaining the lab during the difficulty that has been 2020 with COVID. So many backordered products and weird hours, and you were always available to help. Thank you to my fellow St. Louis University High (SLUH) alumnus, Ian Hurford. You have been a workhorse for me the last several months especially. You have been up to the challenge and always say yes when I add more to your plate. I enjoyed getting to know you better after you joined the lab fulltime and look forward to watching you progress in your future career. Thank you to the inaugural post-doctoral fellows of the Cassat lab, Kara and Brittney. You have both been such strong influences and help in the lab and have not even been here a year yet. I am so glad that we got to overlap and get to know each other. Best of luck to you both!

Thank you to members of the Duvall lab group for helping me with polymer synthesis. Specifically, thank you to Prarthana Patil and Mukesh Gupta. I am very happy I got to work with you, Prarthana. You taught me many of the principles of RAFT polymer synthesis and were very patient with me. Thank you to Mukesh for endless patience, self-sacrifice, and expertise on all things polymer chemistry.

Thank you to my prior research mentors who continue to be available for advice. In particular, thank you to Stavros (Steve) Thomopoulos for welcoming me into your lab at WashU. Thank you for the trust you placed in me to take on a new project as an undergraduate student. I learned a lot from my time with you. Thank you to Megan Killian who has been such a supportive mentor to me to this day. You treated me with respect and listened to my questions and suggestions even though you were a post-doc, and I was a lowly undergraduate. You gave me a lot of confidence and helped me develop as a scientist.

Thank you to my good friends in the Vanderbilt MSTP. When in a city with no family for the first time as an M1 student, I was extremely thankful for my friends in this program. Thank you especially to Jack Walker, Cam Bermudez, Joe Luchsinger, and Ben Reisman, with whom I have remained close even as graduate school took us all in different directions. I am thankful to have gotten to know all of you during my time in the MSTP. Our trips together, game nights, dinners, racquetball games, and explorations of Nashville together have been a true highlight of my time in the MSTP. My twenties would not be the same without each of you, and I am thankful for our friendship. You have all done such impressive work in graduate school, and I have learned and grown as a scientist in our conversations about our projects.

Thank you to my family for constant support. My parents, Denise and Dave Ford, have given me more than I can ever repay. I still do not think I can comprehend the love and support I

have received from you these past 29 years. Thank you to my dad for introducing me to science and teaching me how to be a loving husband. Thank you to my mom for immeasurable love and helping me to grow every day of my life. I am lucky to call you two "Mom and Dad." Thank you to my twin brother, Ben. I feel blessed to be a twin. You have heard me stress out over many challenges along the way to this dissertation. Thank you for always challenging me and being there for me. Thank you to my sister, Meghan, and her husband Kevin. You are two of the most selfless people that I know. I am thankful to have you in my life. Thank you to my younger sister, Kaitlin. You have always been there for me even when I am not deserving of it.

Thank you to my loving wife, Elizabeth. I am so lucky to have you in my life. You have brought me dinners in lab when experiments have run long. You have put up with hourly texts that say I will be leaving lab "in an hour." Thank you for following me to Nashville so I could train at Vanderbilt. Thank you for listening to me vent when things in lab do not go well and listening to me go on and on when things in lab are going well. You have been more supportive than I deserve. I could not have done this without you. I love you.

Thank you to my mentors during my thesis training and in my career moving forward. Thank you to Jon Schoenecker, M.D., Ph.D., for welcoming me into your clinic and operating room. I appreciate the career mentorship you have given me so far and know I will be seeking only more mentorship from you moving forward. Thank you to the members of my committee that are outside of my lab, Scott Guelcher, Ph.D., Craig Duvall, Ph.D., Rachelle Johnson, Ph.D., and Carlos Henrique Serezani, Ph.D. Each of you have provided tangible and actionable advice to improve my project. I appreciate the time you have each given me to improve my project, my knowledge base, and myself as a scientist. The work that follows is a testament to your support.

TABLE OF CONTENTS

Page

LIST OF TABLES

Table Page

LIST OF FIGURES

Figure Page

LIST OF ABBREVIATIONS

accessory gene regulator (*agr*)
adenovirus containing GFP (AdGFP)
adenovirus containing Cre and GFP (AdCre)
alendronate (Aln)
α-minimal essential media (α-MEM)
analysis of variance (ANOVA)
arginine catabolic mobile element (ACME)
aryl hydrocarbon receptor nuclear translocator (ARNT)
autoinducing peptide (AIP)
2,2'-azobis(isobutyronitrile) (AIBN)
bone surface (BS)
bone volume-per-total volume (BV/TV)
colony forming units (CFU)
CREB-binding protein (CBP)
dentin matrix acidic phosphoprotein 1 (DMP1)
Diffuse Luminescence Imaging Tomography (DLIT)
dimethylacrylamide (DMA)
dimethylformamide (DMF)
dimethyloxalylglycine (DMOG)
dimethyl sulfoxide (DMSO)
dynamic light scattering (DLS)
enhanced permeability and retention (EPR)
erythropoietin (EPO)
excitation/emission (Ex, Em)
extracellular matrix (ECM)
extravasation through leaky vasculature and subsequent inflammatory cell-mediated sequestration (ELVIS)
factor inhibiting HIF-1α (FIH-1)
fetal bovine serum (FBS)
Fluorescence Imaging Tomography (FLIT)
green fluorescent protein (GFP)
group A *Streptococcus* (GAS)
hypoxia-inducible factor (HIF)
hypoxia response element (HRE)
insulin-like growth factor-1 (IGF-1)
interleukin (IL)
In Vivo Imaging System (IVIS)
L-gulonolactone oxidase (GULO)
macro chain transfer agent (macroCTA)
macrophage colony-stimulating factor (M-CSF)
methicillin-resistant *Staphylococcus aureus* (MRSA)
microbial surface components recognizing adhesive matrix molecule (MSCRAMM)
microcomputed tomography (microCT)
nonsteroidal anti-inflammatory drug (NSAID)

not significant (ns)
number of osteoclasts (N.Oc)
optical density at 600 nm (OD_{600})
osteocalcin (Ocn)
osteoclast surface (Oc.S)
osteoprotegerin (OPG)
osterix (Osx)
oxygen-dependent domain (ODD)
pathogen-associated molecular pattern (PAMP)
pattern recognition receptor (PRR)
pentafluorophenyl acrylate (PFPA)
phenol-soluble modulin (PSM)
phosphate-buffered saline (PBS)
poly(benzoyloxypropyl methacrylamide) (pHPMA-Bz)
poly(ethylene glycol) (PEG)
polymerase chain reaction (PCR)
poly[(oligoethylene glycol)$_9$ methyl ether acrylate] (POEGA)
poly(propylene sulfide) (PPS)
poly(propylene sulfide)-*b*-poly(dimethylacrylamide)-*b*-poly(*N*-isopropylacrylamide) (PDN)
poly(propylene sulfide)-4-cyano-4-(ethylsulfanylthiocarbonyl)sulfanylpentanoic acid (PPS_{135}-ECT)
prolyl hydroxylase domain protein (PHD)
reactive oxygen species (ROS)
real-time polymerase chain reaction (RT-PCR)
receptor activator of NF-κB (RANK)
receptor activator of NF-κB ligand (RANKL)
reversible addition–fragmentation chain-transfer (RAFT)
Roswell Park Memorial Institute (RPMI)
runt-related transcription factor 2 (Runx2)
small colony variant (SCV)
staphylococcal binding protein (Sbi)
staphylococcal protein A (SpA)
standard error of the mean (*SEM*)
Sigma Factor B (sigB)
superfolder-green fluorescent protein (sfGFP)
tartrate-resistant acid phosphatase (TRAP)
tetramethylsilane (TMS)
threshold value for RT-PCR (C_T)
transforming growth factor-β (TGF-β)
tryptic soy agar (TSA)
tryptic soy broth (TSB)
tumor necrosis factor (TNF)
vascular endothelial growth factor (VEGF)
volume-per-volume (v/v)
von Hippel Lindau protein (VHL)
wildtype (WT)

CHAPTER I:
INTRODUCTION

Osteomyelitis is a destructive inflammatory state of bone most commonly caused by infection of the Gram-positive pathogen *Staphylococcus aureus*. *S. aureus* possesses virulence factors that allow *S. aureus* to bind to bone, evade host immune responses, and contribute to host tissue damage and cell death. In part because of these virulence factors, *S. aureus* osteomyelitis is difficult to treat and frequently requires long-term antibiotic therapy and surgical intervention. Since the introduction of antimicrobial therapy in the mid-20th century, osteomyelitis outcomes have remained largely unchanged. Despite effective antimicrobial therapy, chronic infection still occurs and is difficult to eradicate.

To better understand the disease mechanisms underlying bone infection, our lab developed a murine model of osteomyelitis. Using this model of osteomyelitis, our lab previously established that over the course of infection, tissue hypoxia occurs within the infectious niche. We further explored the impact of hypoxia on the response of *S. aureus* and found that hypoxia increased virulence factor production and contributed to poor outcomes. This led to an interest in the host response to hypoxia during osteomyelitis. Interestingly, the canonical response to hypoxia, hypoxia-inducible factor (HIF) signaling, is critical for bone repair as well as antibacterial responses to *S. aureus* infection in skin. In Chapter II (Background), I review the current body of knowledge regarding osteomyelitis pathogenesis, HIF signaling, and the role of HIF signaling in skeletal biology and the antibacterial immune response.

In addition to studies related to hypoxia, our lab previously discovered that an antivirulence drug (diflunisal) limits infection-mediated bone loss. Antivirulence drugs limit virulence factor production without impacting pathogen survival. Since our initial study used a

local delivery device that was at risk of bacterial seeding, we sought to develop an alternative delivery strategy and investigate the use of polymeric nanoparticles during osteomyelitis. Thus, Chapter II continues with a focus on antivirulence therapies and nanoparticle-based drug delivery strategies. The goal of Chapter II is to provide the necessary background information and rationale for the studies performed in Chapters III and IV. Chapter III focuses on original research investigating the role of skeletal cell HIF signaling during osteomyelitis, and Chapter IV investigates the impact of diflunisal-loaded nanoparticles during osteomyelitis.

The goal of these studies is to develop a systemic drug delivery system for treating osteomyelitis and to understand the role of HIF signaling in skeletal cells during osteomyelitis as a potential therapeutic target. Treatment of *S. aureus* osteomyelitis is difficult because of biofilm formation that limits drug efficacy, virulence mechanisms that evade immune eradication, and widespread antimicrobial resistance among clinical isolates of *S. aureus*. Improved drug delivery will likely help overcome challenges related to drug penetration into biofilm, and alternative delivery vehicles may expand the available set of therapeutics that could be delivered to infected bone. My data with PPS nanoparticles in our murine model of post-traumatic osteomyelitis is the first to demonstrate that systemically administered nanoparticles accumulate at the infectious focus of osteomyelitis *in vivo*. Given the prominent role of HIF signaling during bone development and repair as well as during immune responses, understanding HIF in skeletal cells during osteomyelitis will determine if HIF augmentation or inhibition will potentially improve treatment of bone infections. In this light, the Specific Aims of this study are as follows:

Specific Aim 1: Determine the role of osteoblast-lineage HIF signaling in bone remodeling and antibacterial immunity during *S. aureus* osteomyelitis.

Specific Aim 2: Develop a nanoparticle-based drug delivery platform for bone infection

Specific Aim 3: Deliver an efficacious therapeutic to improve antibacterial immunity and/or bone healing during osteomyelitis

The central hypothesis explored in Chapter III is that *HIF signaling augments skeletal cell immune responses to protect against bone loss during osteomyelitis*. This set of studies follows the goals of Specific Aim 1. To test this hypothesis, I generated mice with conditional deletion of genes of the HIF signaling pathway in cells of both the osteoblast lineage and the myeloid lineage. These data show that conditional deletion of *Vhl* in osteoblast-lineage cells increases trabecular bone volume and prevents infection-mediated trabecular bone loss. Furthermore, it is shown that manipulation of the HIF signaling pathway through conditional deletion of *Hif1a* in both cell lineages does not impact bacterial burdens during *S. aureus* osteomyelitis. By investigating the impact of *Vhl* deletion in myeloid-lineage cells, it was found that *Vhl* deletion in the myeloid lineage leads to increased trabecular bone loss during osteomyelitis.

With an interest in drug delivery methods that could preferentially deliver antivirulence drugs or HIF modulators, I investigated poly(propylene) sulfide (PPS)-based nanoparticles as a potential drug delivery strategy in Chapter IV. The experiments and data described in Chapter IV were designed to fulfill Specific Aims 2 and 3. In Chapter IV, the data demonstrate that PPS-based nanoparticles preferentially accumulate at the infected femur. Moreover, diflunisal-loaded PPS-based nanoparticles decrease cortical bone loss.

Chapters III and IV are based on original research data. The final chapter, Chapter V, discusses the key findings of the presented studies and the future directions. Following the chapters, a four-part appendix is included that details incomplete studies that were initiated as a part of this thesis project.

A portion of the following section (*CHAPTER II: BACKGROUND*) was originally published in *Frontiers in Microbiology.* (January 2021).

Ford, CA, Hurford, IM, Cassat, JE. 2021. Antivirulence Strategies for the Treatment of *Staphylococcus aureus* Infections: A Mini Review. *Front Microbiol*. 11:3568. doi.org/10.3389/fmicb.2020.632706

A portion of the following section (*CHAPTER II:*

BACKGROUND) was originally published in *Expert Review of Anti-infective Therapy.*

(September 2017).

Ford, CA, Cassat, JE. 2017. Advances in the local and targeted delivery of anti-infective agents for management of osteomyelitis. *Expert Rev Anti Infect Ther*. 15(9):851-860.

doi.org/10.1080/14787210.2017.1372192

https://www.tandfonline.com/doi/full/10.1080/14787210.2017.1372192

CHAPTER II:
BACKGROUND

Osteomyelitis

Osteomyelitis is a difficult-to-treat disease of bone that has been clinically recognized since at least the time of Ancient Egypt [1]. A devastating inflammatory state of bone, osteomyelitis is most commonly triggered by invasive infection and is characterized by pathologic changes in bone remodeling [2]. The term, "osteomyelitis," in this dissertation will refer to infectious osteomyelitis and does not necessarily refer to noninfectious causes of the disease. The incidence of osteomyelitis is increasing for all patterns of disease, most notably diabetic foot osteomyelitis due to the increased incidence of diabetes [3]. Three clinical patterns of osteomyelitis are recognized: 1) osteomyelitis occurring secondary to vascular insufficiency [e.g., diabetic foot infection], 2) osteomyelitis resulting from spread from a contiguous source [e.g., accidental trauma or surgical contamination], and 3) hematogenous osteomyelitis, which is more common among pediatric patients [2–4]. Each pattern of osteomyelitis has its own characteristic array of etiologic pathogens, but across all three patterns of disease, the Gram-positive *Staphylococcus aureus* is by far the most common causative agent [3,5,6]. Patients with osteomyelitis experience profound morbidity and mortality [3]. Osteomyelitis, particularly involving an orthopedic prosthetic, causes a significant economic burden beyond the physical hardships of invasive infection [7,8]. On average, diagnosis of *S. aureus* infection in a patient who has undergone orthopedic surgery increases costs by $56,000, increases length of stay by 14 days, and increases mortality rate by 8% [9]. Of particular clinical importance are strains of *S. aureus* bearing antimicrobial resistance, such as methicillin-resistant *S. aureus* (MRSA), which is responsible for approximately 30-46% of deaths related to antimicrobial-resistant pathogens in the United States [10,11].

Due to the difficultly of eradicating established infection in bone, treatment guidelines generally suggest long-term antibiotic therapy with or without surgery, though specific strategies vary depending on the location and pattern of disease [12–17]. In addition to widespread antimicrobial resistance, treatment of osteomyelitis is complicated by a number of microbial and host factors such as biofilm formation, molecular reprogramming that promotes bacterial tolerance to antibiotics, and poor antibiotic penetration into infected bone [18–20]. *S. aureus* is capable of forming biofilms on both the extracellular matrix of bone and foreign bodies such as orthopedic implants [15,21]. The formation of biofilms, frequently defined as aggregates of bacteria embedded in an extracellular polymeric matrix, leads to reduced antimicrobial susceptibility and prolonged infection [15,22,23]. Furthermore, *S. aureus* small colony variants (SCVs) and persisters are known to enhance the chronicity of infection through antibiotic tolerance [19,24–26]. Such bacterial populations are capable of dynamic reversion to the wildtype state and can exhibit enhanced virulence when growing in bacterial communities that share nutrients [27]. These pathogen-associated treatment challenges necessitate long-term antibiotic therapy with high penetration of the infectious foci. However, treatment of osteomyelitis is also challenged by host factors, such as the formation of sequestrum, defined as avascular and necrotic bone, which limits the penetration of antimicrobial agents into the infectious focus and serves as a nidus for relapsing infection [2]. Taken together, these microbial and host factors significantly challenge antimicrobial therapy, and therefore it is imperative to better understand the mechanisms of disease pathogenesis and develop improved treatments and drug delivery strategies. To better understand the pathogenesis of osteomyelitis, one must understand the basic principles of skeletal biology.

Skeletal biology

Osteomyelitis frequently impacts long bones such as the femur and tibia [3]. Long bones of the appendicular skeleton are complex tissues composed of a mineralized matrix housing a medullary canal [28]. Anatomically, the mineralized tissue of bone is composed of two morphologies: trabecular (cancellous) bone and cortical (lamellar) bone (**Figure 1**). Trabecular bone exists as spongy bone near the physis (growth plate) in the epiphysis and metaphysis while cortical bone forms a compact outer shell that is thickest near the diaphysis. Due to their distinct geometries, trabecular bone contains most bone surface area, promoting faster turnover, while cortical contains most of the mass of bone [29]. Functionally, bones provide a scaffold for locomotion, protect vital organs, regulate serum electrolytes and metabolic hormones, and house the hematopoietic stem cells of the bone marrow [30–33]. During *in utero* development and until closure of the growth plates, long bones develop through endochondral ossification [28]. Long bones are first constructed as avascular, hypoxic cartilaginous scaffolds [34]. With the recruitment and invasion of blood vessels, cartilage ossifies to form mineralized bone. Unique from the purely intramembranous ossification of flat bones of the axial skeleton, long bones maintain a reservoir of propagating avascular cartilage followed by a wave of ossification [34]. This area—the physis, known colloquially as the growth plate—continues the process of endochondral bone formation until late adolescence when the growth plate fully ossifies as the epiphyseal plate [35].

The cells at the physis are demonstrative of the breadth of mesenchymal cells within bone. At the physis, chondrocytes proliferate, elongating the bone along its long axis [28]. A subset of chondrocytes near the ossifying border begin to express osteogenic factors such as osterix (Osx, Sp7), a zinc-finger transcription factor, and subsequently ossify [28,36,37]. Newly

ossified matrix in the metaphysis is remodeled. While many hypertrophic chondrocytes will undergo apoptosis, a subset transdifferentiate into osteoblasts and participate in further bone remodeling [38,39]. Remodeling begins with the resorption of osteoclasts, myeloid-derived multinucleated cells that degrade the organic matrix of bone (mostly collagen) and the inorganic matrix of bone (hydroxyapatite, a calcium-phosphate crystal) through production of proteases and acids, respectively [40,41]. Anabolic actions of bone-forming osteoblasts follow the resorption of bone. Osteoblasts proliferate, produce an extracellular matrix (ECM) primarily composed of type 1 collagen and fibronectin, and mineralize the matrix by depositing hydroxyapatite [42]. As osteoblasts become embedded in the new matrix, osteoblasts terminally differentiate to become osteocytes, the most abundant cell in bone tissue [43].

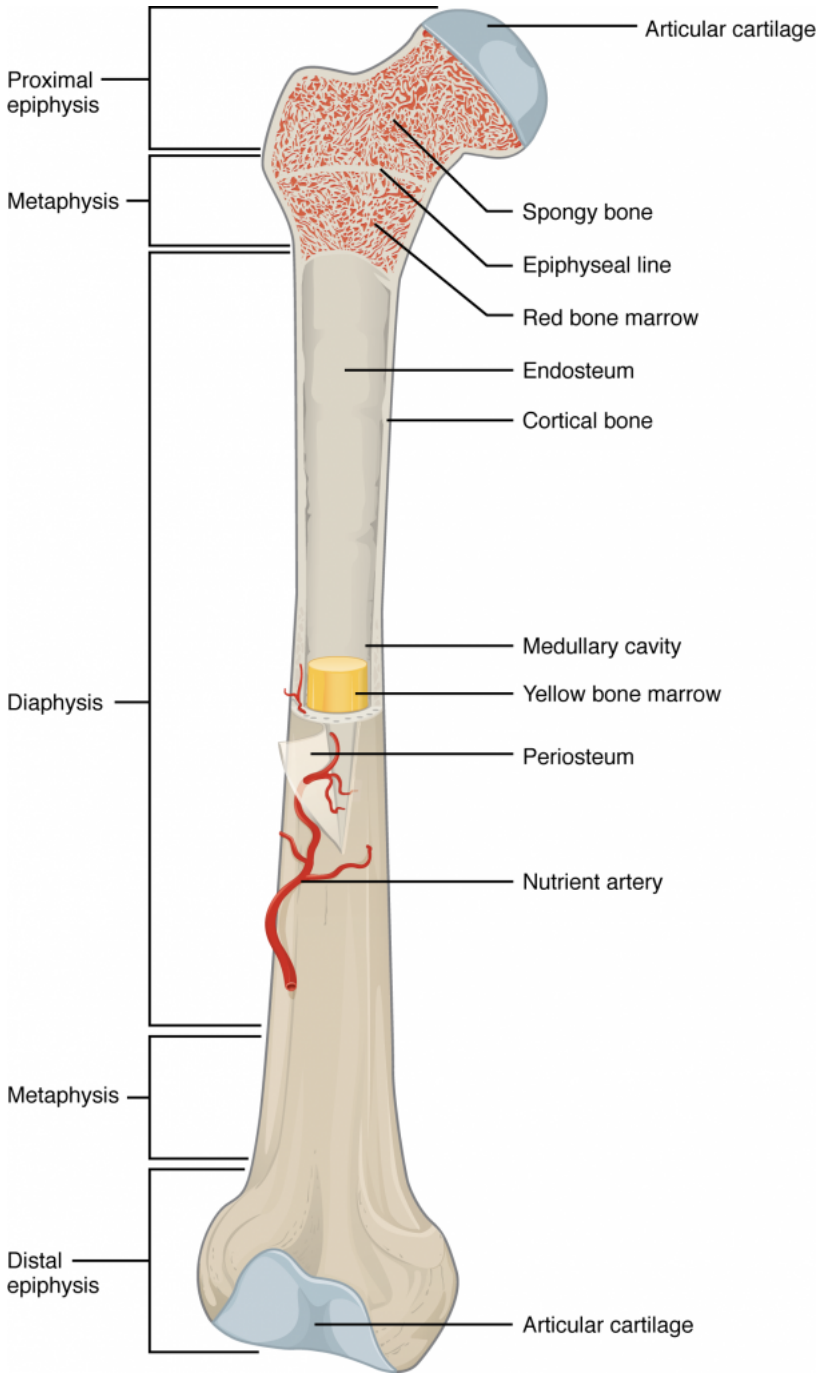

Figure 1: Anatomy of a long bone

The gross anatomical features of the humerus are shown. The epiphyseal plate represents the closed growth plate (physis). The trabecular (spongy) bone is present in the metaphysis and the epiphysis. The metaphysis and epiphysis are separated by the epiphyseal plate, which is the closed, mineralized remnant of the growth plate (physis). Between the proximal and distal

physes, the diaphysis exists. Within the diaphysis and between the trabecular bone spicules, bone marrow is composed of a mix of hematopoietic stem cells (represented in red) and adipose tissue (represented in yellow). The periosteum lines the outer surface of the bone while the endosteum lines the inner surface. The bone is capped at its articulating surfaces with articular cartilage. Image copied without modification from: (Oregon State University for open access use) https://open.oregonstate.education/aandp/chapter/6-3-bone-structure/

Bone resorption and apposition remain in balance throughout postnatal life and are intricately linked (**Figure 2**) [44]. Osteoblast-lineage cells produce the two canonical cytokines necessary for osteoclast differentiation, fusion, and function: macrophage colony-stimulating factor (M-CSF) and receptor activator of NF-κB ligand (RANKL)—a tumor necrosis factor (TNF) family cytokine [41]. M-CSF maintains cell viability and proliferation [45,46]. RANKL binds the RANK receptor on the cell membrane of osteoclast precursors [47]. RANK shares immense homology with osteoprotegerin (OPG) which lacks the membrane-embedding domains of RANK and therefore acts as a soluble decoy receptor that competitively inhibits RANKL [48]. Thus, the ratio of RANKL and OPG influences the local resorptive activities of osteoclasts [49,50]. Just as osteoblasts are coupled to osteoclasts through the production of RANKL and OPG, osteoclasts and osteoclast resorption stimulate bone formation [51]. Osteoclast resorption releases embedded osteogenic growth factors (e.g., transforming growth factor-β1 and insulin-like growth factor 1) from the ECM of bone and thus promotes proliferation and matrix production by osteoblasts [52,53]. Furthermore, RANK, present on released vesicles from maturing osteoclasts, was recently identified as an osteogenic protein that acts through reverse signaling on membrane-bound RANKL on osteoblast-lineage cells [54]. Through balanced bone resorption and formation by osteoclasts and osteoblasts, respectively, daily occurring microscopic fractures are repaired to maintain the structural integrity of bone and allow adaptation to new stress [44].

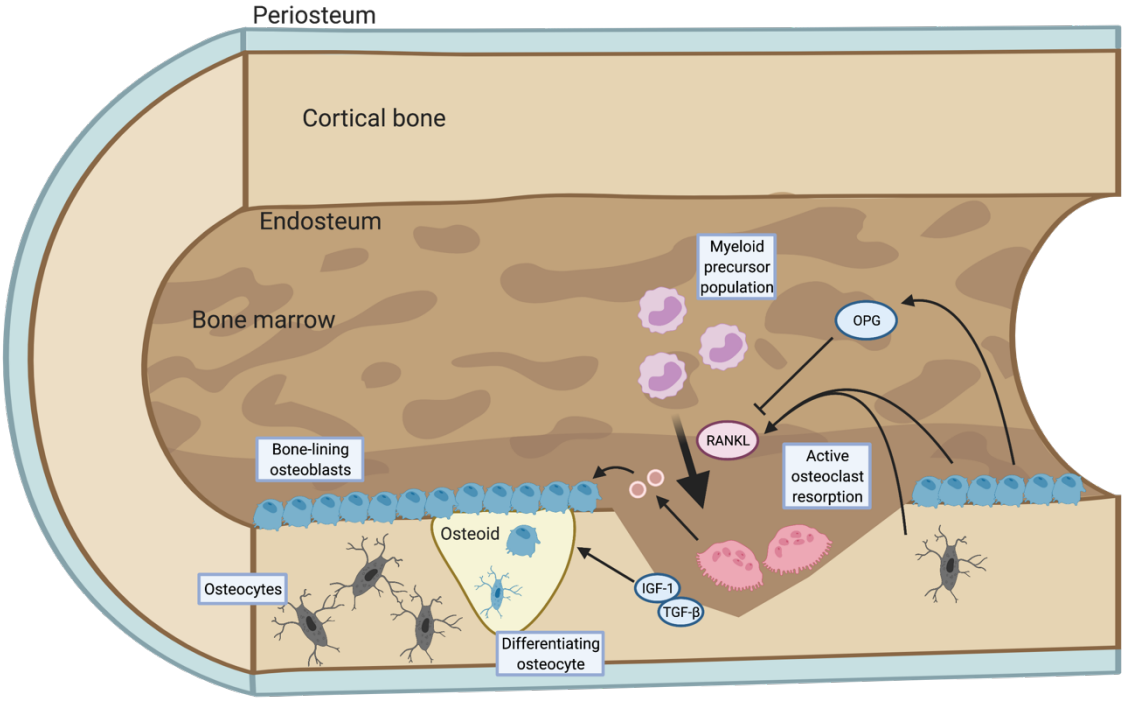

Figure 2: Coupling of bone formation and resorption

Blue bone-forming osteoblasts line the endosteal surface of the cortical bone in this cartoon. When fully embedded in the bone matrix, osteoblasts differentiate into osteocytes (depicted in grey). Purple myeloid precursor cells fuse and differentiate into multinucleated, bone-resorbing osteoclasts (shown in pink). Osteoclast differentiation is mediated in part by receptor activator of NF-κB ligand (RANKL) which binds RANK receptor on osteoclast precursor cells. RANKL is released from and maintained as a membrane-bound protein on osteoblast-lineage cells, coupling osteoblast-lineage cells to bone resorption. Osteoblast-lineage cells also secrete soluble osteoprotegerin (OPG), which acts as a decoy receptor for RANKL, competitively inhibiting RANKL and thus osteoclast activity. Osteoclasts resorb bone through the release of acids and proteases. In degrading the bone matrix, embedded growth factors such as insulin-like growth

factor-1 (IGF-1) and transforming growth factor-β (TGF-β) are released which contribute to anabolic actions of osteoblast-lineage cells to replace resorbed bone with new osteoid that is then mineralized to form mature bone. In addition, maturing osteoclasts release vesicles, depicted as circular, pink micelles. The released vesicles contain membrane-embedded RANK, which binds membrane-bound RANKL on osteoblasts and promotes bone formation through reverse signaling. Image created with BioRender.com.

Several transcription factors are required for the formation of bone [42]. These transcription factors include the canonical osteogenic factor Runx2 (runt-related transcription factor 2), which activates Osx (gene: *Sp7*) to commit osteochondroprogenitor cells to the osteoprogenitor lineage [37,55,56]. *Sp7*-expressing cells in the postnatal skeleton include stromal cells in the bone marrow, preosteoblasts, osteoblasts, osteocytes, and even hypertrophic chondrocytes [57]. Osx activity is required to form bone, and mice with a germline deletion of *Sp7* do not produce bone matrix [37]. This population of cells can, thus, be targeted by *OsxCre* when employing Cre-lox mouse breeding strategies to generate conditional knockout mice in the osteoblast lineage [58]. *OsxCre* has been shown previously to target these osteoblast-lineage cells (bone marrow stromal cells, preosteoblasts, osteoblasts, and osteocytes) with limited off target effects [57]. Osteoblasts at later stages of development may be targeted with alternative promoters driving Cre recombinase expression. *OcnCre* (osteocalcin [Ocn] promoter) targets mature osteoblasts, and *Dmp1Cre* (dentin matrix acidic phosphoprotein 1 [DMP1] promoter) targets differentiated osteocytes [58]. For example, *OcnCre*, targeting mature osteoblasts, was used to conditionally delete genes of the hypoxia-inducible factor (HIF) pathway in foundational studies demonstrating the coupling of osteogenesis with angiogenesis [59]. Since this seminal study, HIF signaling has been further understood to play key roles in skeletal development and healing. In the context of osteomyelitis, HIF signaling is intriguing because this signaling pathway is intricately linked with both bone biology and the immune response [60,61]. It is, thus, conceivable that HIF signaling may offer an attractive therapeutic target during osteomyelitis.

HIF signaling

HIF signaling (**Figure 3**) is a canonical response to hypoxic stress conserved across all metazoan species [62]. When investigating the mechanisms behind hypoxic regulation of

erythropoietin (EPO) production, a transcription factor was identified, now termed HIF-1α [63,64]. HIF-1α heterodimerizes to HIF-1β (also known as the aryl hydrocarbon receptor nuclear translocator [ARNT]) and regulates transcription in a complex with CREB-binding protein (CBP) or p300, a homologous protein [64–66]. The HIF transcriptional complex activates genes with a conserved hypoxia response element (HRE) locus upstream of the target gene [67]. Though initially studied in the context of EPO production, HIF-1α protein was identified in non-EPO-producing cells, suggesting broad activities [68]. HIF signaling has now been recognized to directly regulate more than 1,000 genes, most notably glycolytic genes and angiogenic genes [62]. In this way, HIF-1α permits cells to better withstand hypoxic stress metabolically while promoting reoxygenation through angiogenesis. In addition to HIF-1α, HIF-2α (also known as EPAS-1; gene: *Epas1*) has been identified, which also heterodimerizes with HIF-1β, and regulates a partially overlapping set of genes [69]. HIF-1α may represent immediate responses to hypoxic stress while HIF-2α may represent more chronic responses to hypoxic stress though the exact interplay between both genes remains to be fully understood [70]. HIF-3α exists as multiple splice alternatives including a truncated protein (IPAS) that acts as a negative-feedback inhibitor of HIF-1α, though the full set of functions of HIF-3α are less well understood [71,72]. HIF-1α and HIF-2α activity is largely regulated by post-translational modifications that are dependent in part upon hypoxic stress [71].

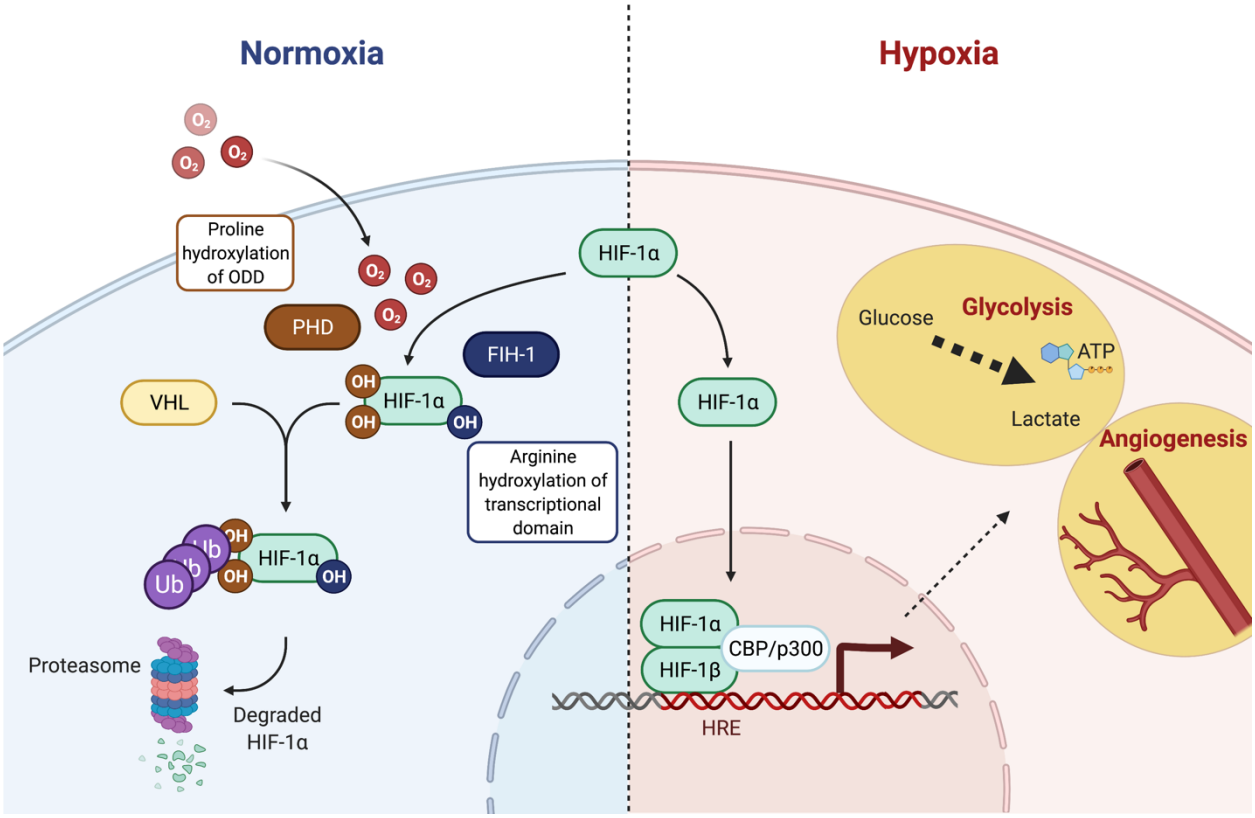

Figure 3: Regulation of HIF signaling

Hypoxia-inducible factor-1α (HIF-1α) heterodimerizes with HIF-1β in hypoxic environments (right) and acts as a transcription factor with the coactivator CREB binding protein (CBP) or homolog p300. The transcriptional regulators modulate transcription of genes marked with a conserved hypoxia response element (HRE). While thousands of genes are regulated, primary pathways include glycolysis and angiogenesis. In normoxic environments (left), HIF-1α is post-translationally modified to inhibit its activity and degrade the protein itself. Prolyl hydroxylase domain proteins (PHDs) hydroxylate two proline residues of the oxygen-dependent domain of HIF-1α. Upon hydroxylation, von Hippel Lindau protein (VHL) polyubiquinates HIF-1α, targeting HIF-1α for proteasomal degradation. In addition to inhibition through PHDs and VHL, factor inhibiting HIF-1α (FIH-1) hydroxylates an arginine residue in the transcriptional domain of HIF-1α inhibiting binding with coactivator CBP/p300. Image created with BioRender.com.

HIF-1α transcription is regulated through cell growth pathways (e.g., mTOR signaling) as well as immune response pathways, notably NF-κB signaling [73,74]. Following translation, HIF-1α experiences a short half-life, as short as 5-15 minutes in well-oxygenated environments [64]. In hypoxic environments, HIF-1α is stabilized in the cytoplasm, allowing heterodimerization with HIF-1β and association with co-activators, CBP/p300 [71]. Prolyl hydroxylase domain proteins (PHDs) hydroxylate two proline residues of the oxygen-dependent domain (ODD) of HIF-1α [75–77]. At least three HIF PHDs exist (PHD-1, PHD-2, and PHD-3) with varying activities [71]. PHD-2 is the most influential individual isoform that regulates HIF-1α activity [78]. Upon hydroxylating proline residues of HIF-1α, von Hippel Lindau protein (VHL), an E3 ligase, is recruited and polyubiquinates HIF-1α [79,80]. Polyubiquinated HIF-1α is rapidly degraded in the proteasome, preventing activation in inappropriate (oxygenated) environments [64,79,81]. To stabilize HIF-1α, oxygen levels must fall to less than approximately 5%, and concentrations of HIF-1α increase exponentially at oxygen tensions less than 5% [82,83]. Hypoxia inhibits PHD activity because oxygen is a necessary co-substrate in the hydroxylation reaction; additional cofactors and co-substrates include ascorbic acid (Vitamin C), iron (II), and α-ketoglutarate [71,77,84]. In addition to PHD hydroxylation, HIF-1α transcriptional activity is further inhibited in oxygenated environments through hydroxylation of an asparagine residue by factor inhibiting HIF-1α (FIH-1), which inhibits the interaction of HIF-1α with its binding partner CBP/p300 [85].

Clinically, HIF modulation has been sought through pharmacologic inhibition of PHDs that act as competitive inhibitors of α-ketoglutarate binding (e.g., dimethyloxalylglycine [DMOG], FG-4592 [Roxadustat]) [77,86]. Roxadustat, for example, has reached clinical trials for treatment of anemia by activating HIF signaling to endogenously increase EPO levels and

induce red blood cell production [86,87]. Since the initial discovery of HIF-1α as the transcription factor responsible for this very process (EPO production), HIF signaling has been recognized for its diverse influence on many physiologic and pathologic functions with potential therapeutic implications [62]. Notably in the context of osteomyelitis, HIF signaling is understood to influence bone repair and immune responses [59,60,88].

Role of HIF during skeletal development and healing

Wang and colleagues first identified a direct link between HIF signaling and bone development that has led to many notable discoveries connecting bone biology and HIF signaling (**Table 1**). Deletion of *Vhl* in osteoblasts through conditional knockout mice using the Cre-lox system ($Vhl^{fl/fl}$, *OcnCre*) increases trabecular bone volume in the metaphysis as well as cortical thickness in the mid-diaphysis. Furthermore, conditional knockout of *Hif1a* ($Hif1a^{fl/fl}$, *OcnCre*) slightly reduces cortical bone thickness. Finally, a double conditional knockout of *Vhl* and *Hif1a* ($Vhl^{fl/fl}$, $Hif1a^{fl/fl}$, *OcnCre*) causes an intermediate phenotype of increased bone volume compared to controls but less compared to the bones of the mice with a single conditional knockout of *Vhl* [59]. Since this seminal study, the role of HIF-1α signaling in osteoblasts has been shown to enhance osteoblast bone formation in part through vascular endothelial growth factor (VEGF) signaling, which induces angiogenesis and alters osteoblast activity in an intracellular, autocrine fashion [89,90].

Table 1: Key findings in studies exploring the role of HIF signaling in skeletal cells

In order of publication year and first-author name, key findings of studies exploring hypoxia-inducible factor (HIF) signaling in skeletal cells are shown with details including cell type targeted, animal model used, and brief details of the methods of HIF manipulation.

Cell type targeted	Animal model	Method	Key finding(s)	Reference
Osteoblasts	Mouse, bone development & homeostasis	*OcnCre*-mediated deletion of *Vhl*, *Hif1a*, *Vhl/Hif1a*	HIF augmentation in osteoblasts through *Vhl* deletion increases trabecular bone formation and is partially HIF-1α dependent. Osteoclast abundance is unchanged.	[59]
Osteoblasts + Untargeted pharmacologic	Mouse, distraction osteogenesis	*OcnCre*-mediated deletion of *Vhl*, *Hif1a*; Pharmacologic: deferoxamine	HIF augmentation in osteoblasts through *Vhl* deletion increases bone regeneration following injury while *Hif1a* deletion inhibits bone formation. PHD inhibition increases bone formation.	[88]
Osteoblasts	Mouse, bone development & homeostasis	*OcnCre*-mediated deletion of *Hif1a and Epas1*	Loss of both HIFα isoforms decreases trabecular bone volume in 6-week-old mice. Bone loss is greater with loss of HIF-1α activity than loss of HIF-2α activity. Osteoclast abundance is unchanged.	[91]
Osteoclasts	Mouse, sex hormone-depleted osteoporosis	*CtskCre*-mediated deletion of *Hif1a* in ovariectomized mice and orchiectomized mice	Osteoclast-specific HIF-1α is required for bone loss following loss of sex hormones.	[92,93]
Untargeted pharmacologic	Mouse, post-menopausal osteoporosis	Ovariectomized mice; Pharmacologic DMOG	HIF augmentation through DMOG administration limits bone loss in ovariectomized mice without altering osteoclast numbers from controls.	[94]
Osteoblasts	Mouse, bone development & homeostasis	*OsxCre*-mediated expression of O_2-stabilized HIF-1α with and without deletion of *Vegfa*	HIF-1α augmentation in osteoblasts increases trabecular bone volume through induction of glycolysis and not just VEGF-impacts. Osteoclast abundance is reduced with HIF-1α stabilization in osteoblasts.	[95]
Osteoblasts	Mouse, bone development & homeostasis	*OsxCre*-mediated combinatorial deletion of PHD1/2/3; *OsxCre*-mediated combinatorial deletion of *Hif1a* and *Epas1*	HIF augmentation in osteoblasts through PHD deletion increases trabecular bone volume with PHD1/2, PHD2/3, or PHD1/2/3 are deleted. HIF augmentation increases OPG production and limits osteoclast abundance.	[96]
Osteoblasts	Mouse, bone formation	*OsxCre*-mediated deletion *Vegfa* and/or *Flk1*	Osteoblast-derived VEGF is necessary for proper bone repair and is only partially recovered by	[89]

	following pinhole defect		exogenous VEGF. VEGFR2 (*Flk1*) activation inhibits bone formation.	
Osteoblast-lineage cells	Mouse, bone injury repair following stress fracture, pinhole defect, or transcortical femur fracture	*UBCCre*-, *OsxCre*-, or *Dmp1Cre*-mediated deletion *Vegfa*; all tamoxifen-inducible Cre models	VEGF in osteoblast-lineage cells at different differentiation states impacts bone healing variably depending on bone injury model. Regarding OsxCre, *Vegfa* deletion in *OsxCre* model impacts bone repair in transcortical fracture and stress fracture but not in pinhole defect model.	[97]
Osteoblasts & Osteoclasts	Mouse, bone formation and post-menopausal osteoporosis	*Col1a1Cre* (osteoblasts) and *CtskCre* (osteoclasts) deletion of *Epas1*	HIF-2α negatively impacts bone volume in skeletal cells. HIF-2α increases RANKL production in preosteoblasts, contributing to bone loss in 4-month-old mice. HIF-2α increases TRAF6 signaling in osteoclasts contributing to osteoclast formation and bone loss.	[98]

In addition to the anabolic effects of HIF-induced VEGF, HIF-1α increases bone formation independent of VEGF through the induction of glycolysis in osteoblasts [95]. In osteoblasts (expressing *OsxCre*) with conditional knock-in of oxygen-stabilized HIF-1α, cancellous bone formation is increased and is unchanged by simultaneous conditional knockout of *Vegfa*. On the contrary, inhibition of glycolysis limits enhanced bone formation, establishing that HIF-1α-induced glycolysis in osteoblasts increases bone formation independent of VEGF [95]. Interestingly, while Wang and colleagues did not observe alterations in osteoclast number per bone surface in osteoblasts with conditional deletion of *Vhl* (*OcnCre, Vhl*$^{fl/fl}$ mice), Regan and colleagues observed reduced osteoclast numbers per bone surface in *OsxCre* mice conditionally expressing oxygen-stabilized HIF-1α [59,95]. These data highlight the complexity of HIF signaling and suggest that conditional deletion of *Vhl* is not equivalent to constitutive HIF-1α activity, though other differences such as the age of mice may partially explain such differences.

HIF signaling has also been studied as a therapeutic pathway in the context of bone repair. To study the impact of HIF signaling augmentation as a therapeutic, Wan and colleagues modeled distraction osteogenesis in a mouse with conditional deletion of *Hif1a* or *Vhl* in osteoblasts using *OcnCre*. Conditional knockout of *Vhl* improved new bone formation while knockout of *Hif1a* inhibited new bone formation [88]. Furthermore, to pharmacologically alter HIF signaling, deferoxamine—which inhibits PHD hydroxylation through iron chelation—was administered *in vivo* and increased new bone formation and angiogenesis similar to conditional deletion of *Vhl* [88]. Since this study, pharmacologic inhibition of HIF-1α degradation has been shown to increase fracture callus formation, inhibit bone loss in ovariectomized mice and rats, and improve bone formation in osteogenic bone grafts [94,99–102].

Manipulation of HIF signaling in osteoblasts also impacts osteoblast regulation of osteoclast formation through alteration of the RANKL-OPG signaling axis. While ablation of VHL activity may be achieved through the deletion of one gene, multiple isoforms of PHD proteins exist, and therefore, HIF-1α augmentation through conditional deletion of PHD proteins requires combinatorial deletions [96]. Wu and colleagues established that, in osteoblasts, PHD2 is the dominant isoform for regulation of HIF signaling, and HIF augmentation may be achieved through combinatorial deletion of PHD1 and PHD2 or of PHD2 and PHD3 [96]. Deletion of only two isoforms of PHD proteins creates a phenotype that is less severe than the high bone formation of *Vhl* deletion or conditional deletion of all three isoforms of PHD proteins [96]. HIF stabilization through deletion of the genes encoding PHD proteins increases trabecular bone volume as observed with deletion of *Vhl* [96]. Furthermore, HIF signaling was also found to increase OPG and limit osteoclast abundance in trabecular bone while deletion of *Hif1a* and *Epas1* in osteoblasts limited OPG and increased osteoclast abundance [96].

While many studies have demonstrated the pro-osteogenic qualities of HIF signaling, HIF signaling has also been shown to reduce bone formation or enhance bone resorption. PHD inhibition with Roxadustat limits osteoclast formation in mono-culture and in co-culture with osteoblasts, mirroring the findings of Wu and colleagues with PHD deletion in osteoblasts *in vivo* [96,103]. However, PHD inhibition was found to also increase osteoclast activity and promote greater resorption in mature, differentiated osteoclasts [103]. Furthermore, one study has identified *Tnfsf11* (the gene encoding RANKL) as having an HRE regulated directly by HIF-2α [98]. *Epas1* (HIF-2α) over-expression increases RANKL production in preosteoblasts *in vitro*, and conditional deletion of *Epas1* in osteoblasts (*Col1a1Cre, Epas1*$^{fl/fl}$) decreases osteoclast abundance and increases bone mass in 4-month old mice [98]. Furthermore, in the

same model, osteoclast-specific deletion of *Epas1* decreases osteoclast abundance through TRAF6 regulation [98]. Curiously, these data are in opposition to a prior publication by Shomento and colleagues. Shomento and colleagues compared *OcnCre*-mediated deletion of *Hif1a* and *Epas1* and performed descriptive microcomputed tomography (microCT) and bone histomorphometry in 6-weeks-old mice [91]. *OcnCre*-mediated deletion of both HIFα isoforms decreased bone volume in trabecular bone and did not alter osteoclast numbers although the decreased bone volume was greater with loss of *Hif1a* [91]. Differences between these studies may be attributed in part to the differences in age of the mice as well as the alternative promoters regulating expression of the Cre recombinase.

In summary, osteogenesis requires HIF signaling to facilitate angiogenesis and glycolytic metabolism [59,95]. HIF-1α and HIF-2α have overlapping and diverging gene targets that may have positive and negative impacts on bone volume, and these differences may be dependent upon skeletal age and the specific cells targeted [59,71,91,98]. Despite a lack of unified data demonstrating the specific impacts of HIF-1α and HIF-2α, HIF augmentation in osteoblasts cells through pharmacologic manipulation has consistently been shown to enhance bone repair following injury [88,99,101,102]. HIF augmentation has been proposed as a promising technique to speed fracture repair and treat complications such as non-union [104]. The impact of HIF signaling on bone infection, another common complication of fracture, is unknown, but both antibacterial and HIF augmenting strategies are being considered for use in novel bone grafts [105]. Recently, Copper (II) was used in bone grafts and implants to enhance angiogenesis via HIF signaling induction and to limit bacterial infection [106–109]. Copper (II) inhibits PHD hydroxylation of HIF-1α by competitively inhibiting iron (II). Copper is also inherently antimicrobial against *S. aureus* [110]. These studies provide proof of principle that HIF

augmentation and infection control are possible in the same bone grafts and demonstrate the recognized interest in development of dual-purpose grafts.

Pathogenesis of osteomyelitis

Contamination at time of fracture or surgical trauma is one of several mechanisms that initiate bacterial osteomyelitis. *S. aureus* is the most commonly identified etiology of osteomyelitis in part because it possesses unique qualities that allow bacterial colonization and infection of the skeletal environment [2,3]. Microbial surface components recognizing adhesive matrix molecules (MSCRAMMs) of *S. aureus* bind to the ECM of bone [111]. Notable components of the bone ECM bound by *S. aureus* MSCRAMMs are bone sialoprotein, collagen, and fibronectin, which are bound by bone sialoprotein binding protein, collagen adhesin, and fibronectin binding proteins A/B, respectively [112–115]. After binding to bone, *S. aureus* adapts its metabolism to the unique metabolic environment of bone [116,117].

Pathogen-associated molecular patterns (PAMPs) of *S. aureus* such as peptidoglycan and lipoteichoic acids bind pattern recognition receptors (PRRs) of host cells including skeletal cells [111]. PRR binding activates NF-κB signaling and cytokine release as part of the innate immune response. Professional phagocytes such as neutrophils and macrophages are recruited to the infectious focus. Neutrophils and macrophages release antimicrobial peptides and kill *S. aureus* through production of reactive oxygen species (ROS) in the phagolysosomes. Neutrophils and macrophages form abscesses around *S. aureus* microcolonies.

To resist killing by innate immune cells, *S. aureus* produces an array of virulence factors that undermine the immune response [20]. *S. aureus* possesses a large set of cytolytic toxins including pore-forming toxins and phenol-soluble modulins (PSMs). These cytolytic toxins lyse host cells, notably host myeloid cells, by binding to cell-specific receptors and through cell-

indiscriminate mechanisms [118,119]. Myeloid cells include the professional immune cells, macrophages and neutrophils, as well as the specialized, tissue-resident osteoclasts. In fact, pro-inflammatory immune crosstalk contributes to osteoclast-mediated bone loss during osteomyelitis [120,121]. Bacterial cytolytic factors also contribute to bone destruction by lysing osteoblasts and other skeletal cells [122,123]. Additionally, *S. aureus* produces staphyloxanthin (a carotenoid antioxidant) and catalase (an enzyme) which both inhibit the toxicity of ROS attack from phagocytes [124–126]. To further evade killing by professional immune cells, *S. aureus* has been shown to be internalized in non-professional immune cells such as osteoclasts and osteoblasts—sheltering the bacteria from attack [111,127]. Moreover, bone matrix itself provides a surface for biofilm formation for *S. aureus*. Biofilms consist of a mix of nucleic acids, carbohydrates, and proteins that form an extracellular matrix surrounding *S. aureus* bacteria. In addition to limiting immune cells from accessing bacteria, biofilms limit the penetration of antimicrobials and provide nutrient gradients that contribute to formation of persister cells—cells that demonstrate increased antibiotic tolerance [18].

Following initiation of the innate immune response, the adaptive immune response is activated. B-cells are responsible for the production of antibodies, which often contribute to antibacterial immune responses [128]. However, *S. aureus* displays two immunoglobulin-binding proteins on its surface: staphylococcal binding protein (Sbi) and staphylococcal protein A (SpA), which both bind antibodies produced by B-cells, inhibiting their activity [129–133]. SpA binds the Fc domain of up to five different IgG antibodies, preventing opsonizing recognition by the Fc receptor on phagocytes [133–135]. Moreover, SpA binds the Fab of VH3 class B-cell receptors, skewing the immune response to poorly effective SpA clones, and, acting as a superantigen, SpA promotes the clonal expansion and collapse of off-target antibodies [136–139]. Recently, SpA

has been implicated in preventing a robust mucosal immune response, thereby enabling persistent colonization of nares of individuals [140]. Thus, *S. aureus* produces virulence factors that limit the innate and adaptive immune responses, promoting chronic infection. Clearance of osteomyelitis relies upon an effective immune response in conjunction with adequate antimicrobial therapy.

Role of HIF during immune responses

HIF signaling is an essential element of a robust immune response in myeloid cells [141,142]. Hypoxia and HIF signaling activation are general hallmarks of infection due to oxygen consumption in the production of ROS, the increased metabolism of immune cells, and the decreased vascular supply following tissue necrosis [143,144]. Hypoxia is also triggered during osteomyelitis, where there is a drop in the oxygen content of the infected bone marrow [117]. *S. aureus* adapts to hypoxia and the metabolic milieu of infected bone by changing its virulence factor production and metabolism [116,117]. The prototypical transcription factor of the proinflammatory response, NF-κB, activates HIF-1α transcription, and accumulation of HIF-1α during infection is dependent upon NF-κB activity [73,145]. Production of ROS during infection not only consumes oxygen, but also contributes to HIF-1α stabilization [143,146]. Inflammatory cytokines (TNF-α and interleukin [IL]-1) also contribute to increasing *Hif1a* transcripts and stabilizing HIF-1α post-translationally [147–150].

Upon activation, HIF-1α modulates the immune response. Inflammatory immune responses require HIF-1α to facilitate a shift to a glycolytic metabolism [141]. HIF-1α inhibits apoptosis of neutrophils, prolonging cell survival in the infectious niche [151,152]. Additionally, HIF-1α increases production of inflammatory cytokines and production of antimicrobial peptides [153]. Trained immunity, the process by which macrophages show increased inflammatory

responses following previous exposure to PAMPs, is dependent upon HIF-1α, as well [142,154]. Beyond professional immune cells, HIF-1α has been shown to regulate antimicrobial peptides and increase IL-1β production in keratinocytes during skin infection [155,156]. At times, HIF augmentation during infection may lead to extreme inflammatory responses that may be detrimental. For instance, following Gram-positive or Gram-negative endotoxin exposure, HIF-1α mediates robust cytokine responses, fostering a highly inflammatory immune response that contributes to sepsis-induced mortality [157,158]. HIF signaling is interconnected with inflammatory responses, and both immune signals and hypoxic signals exhibit modulating crosstalk [60,159]. HIF signaling has not been studied in the context of osteomyelitis, and it is unclear if modulation of HIF signaling may facilitate bacterial clearance or potentially exacerbate bone loss due to a heightened pro-inflammatory response that promotes osteoclast bone resorption. Pharmacologic targeting of HIF signaling during infection has been proposed as a therapeutic strategy [143,160]. A better understanding of the role of HIF signaling during osteomyelitis will elucidate whether pharmacologic targeting of HIF during osteomyelitis would be beneficial.

Advancements in drug delivery and alternative treatment strategies

In addition to the host immune response, the second pillar of bacterial clearance during osteomyelitis is antimicrobial therapy. Before the introduction of antibiotics, treatment regimens for osteomyelitis emphasized surgical debridement of any infected tissue with limited methods to further prevent infection recurrence [161]. Curative treatments often eluded physicians until the introduction of penicillin and subsequent antibiotics [1]. Despite advances in infection treatment, osteomyelitis is often recalcitrant, progressing from acute to chronic disease. *S. aureus* biofilm formation, toxin production, and immune evasion strategies limit host antibacterial immune

responses and effective antimicrobial therapy [20,138]. Therefore, *S. aureus* osteomyelitis often necessitates long-term antibiotics [2,162]. However, widespread antimicrobial resistance has highlighted the need to develop additional treatments [163].

S. aureus is the leading cause of nosocomial infections among antibiotic-resistant organisms, making staphylococcal infections a major target for investigation of antivirulence therapies [164,165]. Antivirulence therapies are defined as those that do not inhibit bacterial growth *in vitro* but limit the production or function of virulence factors that promote infection or incite host damage *in vivo*. Antivirulence strategies aim to mitigate host tissue damage as host immune responses or conventional antimicrobials eradicate infection. The number of published studies on antivirulence techniques has increased dramatically over the last decade [164,166].

The primary regulatory pathway studied as an antivirulence target in *S. aureus* has been the accessory gene regulator (*agr*) system. The proteins of the *agr* operon enable *S. aureus* quorum sensing and regulate many virulence factors, including pore-forming toxins and PSMs [167]. PSMs are a class of cytotoxic alpha-helical peptides and are one of the few toxins to be directly regulated by the system's response regulator, AgrA [168,169]. Given its broad impact on virulence factor production, targeting quorum sensing in multiple bacterial species and the *agr* system in *S. aureus* is a major target for study as an antivirulence treatment [170,171].

The *agr* quorum sensing system requires production and sensing of autoinducing peptide (AIP). Factors that inhibit *agr* can inhibit any step in AIP production, sensing, and subsequent transcriptional activation of the *agr* P2 and P3 promoters, as well as the promoter for PSMs [170,172]. For example, ambuic acid and solonamide B inhibit AIP production and sensing, respectively, while savirin inhibits downstream transcriptional activity of AgrA [173–175]. *S. aureus* contains four distinct AIP peptide sequences that exist in 3 cross-inhibition groups: I/IV,

II, and III [176,177]. I and IV differ by one amino acid and cross-activate [176]. Otherwise, the presence of alternative AIP sequences from any other *agr* group competitively inhibits AIP autorecognition [177]. This phenomenon has been observed for AIP peptides from many other staphylococcal species, which produce AIP molecules that cross-inhibit *S. aureus agr* signaling [178–181].

Treatment with AIP analogues has been investigated as an antivirulence mechanism using rational design and high-throughput screening mechanisms [182]. Changing native amino acid residues or the thiolactone ring of AIP can increase or decrease *agr* signaling [180,183,184]. Substitution of the AIP-III thiolactone ring with a lactam was demonstrated to inhibit AIP binding for all four *agr* types of *S. aureus* in the nanomolar range *in vitro* but has not yet been tested *in vivo* [185]. High-throughput screening also elucidated natural compounds that competitively inhibit AIP binding to its receptor kinase, AgrC. One of the first discovered natural inhibitors of *agr* signaling was solonamide B, a cyclodepsipeptide from *Photobacterium halotolerans* [173]. Solonamide B and its derivatives inhibit binding of AIP to AgrC, and through this mechanism, solonamide B mitigates toxin-mediated cytolysis of phagocytes and δ-toxin-mediated atopic dermatitis in mice [186–188]. Since the discovery of solonamide B, other compounds that inhibit AIP binding to AgrC have been discovered. For example, *agr*-inhibiting lipoproteins from *Bacillus subtilis* promote decolonization in mice, possibly through *agr*-regulated adhesins. Furthermore, colonization with probiotic *Bacillus* species is inversely related to *S. aureus* colonization in the gastrointestinal tract and nares in humans, corroborating the findings in mice [189].

Inhibitors of *agr* also target signaling downstream of the receptor kinase (AgrC) and response regulator (AgrA). Savirin is a well-characterized antivirulence compound that targets

AgrA by interfering with its transcriptional regulation [175]. In an air-pouch infection model, mice treated with savirin exhibit reduced dermatonecrosis. While most tested *agr* inhibitors are administered at the time of bacterial inoculation, savirin was tested in a delayed treatment model and still showed efficacy, though the effect size was reduced compared to immediate treatment [175]. An important future direction is therefore to evaluate the efficacy of antivirulence compounds in delayed treatment models, which perhaps more accurately reflect the clinical scenario in humans. In addition to novel small molecules, existing drugs have been identified that target AgrA and are amenable to drug repurposing. For example, diflunisal is an FDA-approved nonsteroidal anti-inflammatory drug (NSAID) predicted to inhibit phosphorylation of AgrA by AgrC [190,191]. Diflunisal is a derivative of salicylic acid, which also has antivirulence properties through effects on Sigma Factor B (SigB) activity [192]. We previously tested local delivery of diflunisal in a murine model of osteomyelitis and showed that diflunisal mitigates infection-mediated bone loss without impacting *S. aureus* burden in the infected femur [123]. *In vitro* diflunisal limits cytotoxicity of *S. aureus* supernatants when tested on several different skeletal cell types without impacting *S. aureus* growth [123].

Despite this therapeutic potential, targeting of *agr* quorum sensing is controversial in part because of its role in regulating biofilm dispersal [193,194]. Inactivation of *agr* in *S. aureus* promotes biofilm formation *in vitro* and impairs biofilm dispersal during osteomyelitis [195,196]. Biofilms are often associated with chronic infections, and *agr*-deficient mutants have emerged during the course of biofilm-associated infections [197–200]. Given that biofilms contribute to evasion of immune responses and antimicrobial therapy, *agr* inhibition may impair bacterial clearance at the expense of decreasing virulence factor production.

To better understand the impact of diflunisal therapy on antimicrobial recalcitrance, we previously delivered diflunisal through a local delivery device while simultaneously administering systemic vancomycin [201]. We found that diflunisal does not alter vancomycin efficacy *in vitro* or *in vivo* [201]. When examining infection-mediated bone loss, we found that both diflunisal and vancomycin inhibit cortical bone loss, and the result is not synergistically additive [201]. Though 10 mg/kg vancomycin decreased bacterial burdens in the femur, the local delivery device was also colonized by bacteria, and vancomycin therapy did not impact bacterial burdens on the foreign body [201]. These findings led to interest in developing an alternative delivery strategy that did not require a foreign body to be placed at the infected site. One alternative drug delivery strategy is polymeric nanoparticles.

Nanoparticles as drug delivery vehicles during infection

Nanoparticles refers to a class of solid (e.g., gold) or membrane-encapsulated (e.g., polymeric micelles) particles that have a diameter in the sub-micron range [202]. Nanoparticles have been investigated clinically since the 1980s, and now several polymeric nanoparticles are approved in the United States for delivery of chemotherapeutics and vaccines [202–204]. Advancements in polymer chemistry have facilitated production of a broad set of synthetic polymers capable of forming micelles or bilayer membranes that can encapsulate drug cargo for improved solubility, drug targeting, or sustained release [203]. As an anti-infective therapy, nanoparticles have previously been employed for treatment of osteomyelitis [205–208].

Nanoparticles have been used *in vitro* and *in vivo* in the context of bone infection [209–213]. *In vivo* studies have included delivery of nanoparticle-sized heavy metals such as silver that have inherent antimicrobial properties [207]. Furthermore, synthetic nanoparticles have been used to deliver antibiotics systemically to treat and diagnose bone infection [205,206]. Recently,

nanoparticles were shown to efficaciously deliver curcumin to sites of bone infection to decrease inflammation [208]. However, prior studies have not been designed to determine the nanoparticle accumulation patterns in the context of osteomyelitis. Nanoparticles are theorized to accumulate at sites of solid organ cancers through passive and active means [214]. Passive accumulation is theorized to occur through a set of phenomena known as the enhanced permeability and retention (EPR) effect [215–217]. Cancer often exhibits angiogenesis with leaky vasculature but does not increase lymphatic drainage which theoretically increases delivery without facilitating removal [217]. It is unknown if such accumulation would occur in the context of bone infection. Infected sites exhibit increased vascular permeability which may increase nanoparticle delivery [218]. It is theorized that inflamed sites may retain nanoparticles as well through the extravasation through leaky vasculature and subsequent inflammatory cell-mediated sequestration (ELVIS) effect [219,220]. Within the framework of the ELVIS effect, activated phagocytes at inflamed tissues phagocytose nanoparticles and act as functional drug depots at the inflamed site [219,220].

One aspect of nanoparticles as drug carriers is the potential for preferential drug release in response to therapeutic demand through careful selection of synthetic polymer chemistry. Poly(propylene sulfide) (PPS)-based nanoparticles are one type of polymer capable of such drug delivery [221–227]. PPS is hydrophobic in physiologic environments [221]. PPS-based polymers can be synthesized with a hydrophobic monomer such as dimethylacrylamide (DMA) or poly(ethylene glycol) (PEG) as a diblock copolymer. Thus, the polymer consists of a hydrophobic (PPS) tail attached to a hydrophilic tail (e.g., DMA or PEG). When emulsified with oil and an excess of water, such amphiphilic molecules spontaneously form micellar nanoparticles with hydrophobic cores and hydrophilic coronas [222]. When a hydrophobic drug

(such as diflunisal) is added to the emulsifying mixture, the drug is encapsulated in the core of the nanoparticle. Unique from other hydrophobic chains, the sulfur atom of the PPS core is liable to ROS attack to form sulfoxide and sulfone groups that result in increased hydrophilicity [221].

PPS-based nanoparticles have been explored previously in the context of bone disease. Vanderburgh and colleagues showed that PPS-based nanoparticles deliver the hydrophobic Gli2 inhibitor GANT-58 to metastatic breast cancer in bone [226]. In a follow-up study, PPS-DMA polymers were modified by grafting the bisphosphonate alendronate to the corona of the nanoparticle [227]. Bisphosphonates have been used previously to improve drug targeting to bone [228]. PPS-based nanoparticles that had alendronate grafted showed increased accumulation in bone and increased drug efficacy [227]. Because of the modularity of nanoparticles as drug delivery vehicles, the drug cargo may theoretically be substituted to deliver other hydrophobic compounds (such as diflunisal) to bone.

Conclusions

To summarize this wide breadth of material, osteomyelitis is an often difficult-to-eradicate infection of bone [2]. The most commonly identified pathogen responsible for osteomyelitis is *S. aureus* [3]. Bone is a dynamic organ that is under constant, coupled remodeling to maintain its structural integrity [229]. The canonical cell signaling pathway that responds to hypoxic stress is HIF signaling, which is essential for proper bone development [59,71]. HIF-1α and HIF-2a both impact HIF signaling in bone with similar and distinct phenotypes [91,98]. Pharmacologically induced HIF signaling has been demonstrated to improve bone repair within sterile injury models [88]. HIF also impacts innate immune responses, which are critical for control of *S. aureus* infection [60,155,156]. Though its impact during

osteomyelitis is unknown, HIF signaling may represent a therapeutic target to improve skeletal health during infection and/or control bacterial burden [160].

In addition to the immune response, antimicrobial therapy has been critical for treatment of osteomyelitis, and widespread antimicrobial resistance warrants development of alternative treatment strategies [2,165]. One alternative treatment strategy proposed is the inhibition of pathogen virulence factors [164]. Antivirulence strategies limit pathogen virulence to decrease injury to the host without directly impacting pathogen viability. The *agr* pathway is a commonly targeted system as a master regulator of *S. aureus* virulence pathways [230]. One *agr*-targeting drug that has been studied during osteomyelitis is diflunisal [191]. Diflunisal limits cortical bone destruction and does not impact antimicrobial dual therapy [123,201]. Prior studies have used local delivery devices to deliver diflunisal but have been colonized by *S. aureus* [201]. Nanoparticles offer the potential to increase targeted drug delivery without the presence of a foreign body that may serve as a nidus for biofilm development. A promising polymeric nanoparticle formulation uses PPS in its core to create ROS-responsive drug release [222]. Thus, PPS-based nanoparticles may be capable of delivering diflunisal and other immunomodulatory compounds during osteomyelitis.

CHAPTER III: THE ROLE OF HIF SIGNALING IN SKELETAL CELLS DURING OSTEOMYELITIS

Introduction

Osteomyelitis is a highly morbid disease of bone that is most commonly triggered by infection by *Staphylococcus aureus*, a Gram-positive opportunistic pathogen that colonizes about one in three individuals [2,3,231]. Osteomyelitis is difficult to treat because of its ability to evade antibacterial immune responses and its resistance and tolerance to antimicrobial therapy [20,228]. Infection of bone frequently results in chronic infection and concomitant bone destruction [2]. Therefore, curative treatment of osteomyelitis requires bacterial clearance and repair of pathologic bone loss.

Intriguingly, hypoxia-inducible factor (HIF) signaling has been identified as a critical cell signaling pathway in the response to *S. aureus* skin infection and in facilitating bone repair [88,155]. HIF signaling is activated in response to hypoxia, a hallmark of many infectious niches, including infected bone [117,143,232]. While we have recently demonstrated that *S. aureus* modulates its virulence in response to tissue hypoxia, the impact of host hypoxic responses during *S. aureus* osteomyelitis is unknown [117]. In normoxia, HIF-α activity is inhibited by the hydroxylation of proline residues within the oxygen-dependent domain of the HIF-α subunit, which is fulfilled by prolyl hydroxylase domain (PHD) proteins [75–77]. Following hydroxylation, von Hippel Lindau protein (VHL) polyubiquinates HIF-α, targeting it for rapid proteasomal degradation [64,79,81]. Canonically, the HIF-α subunit is stabilized in hypoxic environments through inhibition of PHD hydroxylation [71,233]. Stabilized HIF-α heterodimerizes with HIF-1β (aryl hydrocarbon receptor nuclear translocator [ARNT]) and binds with coactivators CREB-binding protein (CBP)/p300 [64–66]. The active HIF transcriptional

complex regulates a wide range of genes containing hypoxia response elements (HREs), principally genes of metabolic and angiogenic pathways [71].

The two most well studied HIF-α subunits are HIF-1α and HIF-2α (EPAS-1). HIF-1α is activated first in response to hypoxia and was the first to be identified [234]. Genetic or pharmacologic augmentation of HIF signaling has been shown to enhance bone formation in response to sterile injury [88,99,101,102]. Activation of HIF signaling in osteoblasts is thought to improve bone formation in part by shifting the metabolism of osteoblasts toward glycolysis and increasing the production of vascular endothelial growth factor (VEGF) [89,90,95]. HIF-1α is also essential for myeloid inflammatory responses [141]. HIF-1α prolongs myeloid cell longevity in the infectious niche; increases antimicrobial peptide production, cytokine production and reactive oxygen species production; and shifts the cell metabolism to a glycolytic state that supports the energetic demands of myeloid cells [60,141,151]. Moreover, HIF signaling has been shown to enhance antibacterial responses in non-professional immune cells such as keratinocytes during *S. aureus* infection [155]. It is possible that HIF signaling may have a similar function in bone cells.

As a critical signaling pathway during bone repair and antibacterial immune responses, HIF signaling may represent a tractable pharmacologic target for adjunctive osteomyelitis therapy. In this study, we investigated the impact of HIF signaling in skeletal cells of the osteoblast- and myeloid-lineages. To accomplish this, we used two different Cre recombinase models to conditionally delete *Vhl* or *Hif1a* to model states of high and low HIF signaling, respectively. Using these genetic models, we studied the impact on both bacterial clearance and pathologic changes to bone architecture in a mouse model of *S. aureus* osteomyelitis.

Materials and methods

Bacterial strains

The erythromycin-sensitized strain of USA300 LAC *S. aureus* (AH1263) was used for *in vivo* infections and is the parent strain of the toxin deficient strain used *in vitro* [235]. The toxin-deficient strain used *in vitro* was a double knockout mutant generated by knocking out *spa* in LAC Δ*psmα1-4*::*erm* (Δ*psm*)—a mutant which has been characterized and used previously [121,122]. To generate a double knockout of *psmα1–4* and *spa*, Δ*spa*::Tc^r was transduced into Δ*psm* from Newman Δ*spa*::Tc^r (DU5873) with the bacteriophage phi-85 as previously described [117,236]. The double knockout strain (herein referred to as Δ*psm*/Δ*spa*) limits cell death in *in vitro* assays and limits potential interference of staphylococcal protein A in downstream, antibody-based assays. Bacteria were grown on tryptic soy agar (TSA) or in a shaking incubator at 37°C in tryptic soy broth (TSB). Tetracycline (2 μg/mL) was added for growth of DU5873. Erythromycin (10 μg/mL) was added for growth of the Δ*psm* and Δ*psm*/Δ*spa*. Bacteria (Δ*psm*/Δ*spa*) were grown in RPMI with 10 g/L casamino acids for growth prior to concentration of bacterial supernatants as done previously [117]. To prepare the bacterial inoculum for *in vivo* infection, bacteria were grown in TSB overnight at 37°C on an orbital shaker. Then, the overnight bacterial culture was sub-cultured in TSB at a 1:100 dilution for 3 h before centrifuging to pellet the cells and resuspending in phosphate-buffered saline (PBS) as described previously [237].

Mouse strains

OsxCre (Jackson Labs #006361), *Vhl*$^{fl/fl}$ (Jackson Labs #012933), and *Hif1a*$^{fl/fl}$ (Jackson Labs #007561) mice were purchased from Jackson Labs [238–240]. *LysMCre*$^{+/+}$ (Jackson Labs #004781) mice were obtained from Dr. Carlos Serezani [241]. Cre mice and mice containing

floxed alleles were crossed in combination to generate conditional knockout mice: *Vhl*$^{fl/fl}$, *OsxCre*+; *Hif1a*$^{fl/f}$, *OsxCre*+; *Vhl*$^{fl/fl}$, *LysMCre*$^{+/-}$; and *Hif1a*$^{fl/f}$, *LysMCre*$^{+/-}$. Thus, the *LysMCre* conditional knockout mice contained one wildtype *Lyz2* allele and one nonfunctional *Lyz2* allele due to the insertion of *cre* into the transgenic copy of *Lyz2*. The *OsxCre* mice were maintained with only one copy of the bacterial artificial chromosome with the Cre-containing allele. Cre-negative littermate controls consisted of mice with corresponding homozygous or heterozygous floxed alleles, as shown in the figure legends, and no copy of *cre*. In some studies, age-matched, Cre-positive controls were used, as noted in figure legends, that were either *OsxCre*+ or *LysMCre*$^{+/-}$ (heterozygous). Mice bred in the *OsxCre*-containing colonies were maintained on 2 mg/mL doxycycline water to suppress Cre activity. In experimental studies, mice in the *OsxCre*-containing colonies had doxycycline withdrawn at postnatal age 4 weeks except when noted otherwise. Mice used in experiments were generated by crossing homozygous floxed mice to heterozygous floxed mice containing one copy of the Cre transgene (*OsxCre*+ or *LysMCre*$^{+/-}$). The progeny used in experiments were ear-punched and genotyped with Transnetyx, Inc., using RT-PCR.

Murine model of osteomyelitis

All experiments involving animals were reviewed and approved by the Institutional Animal Care and Use Committee at Vanderbilt University Medical Center on the animal protocols M12059 and M1800055. All experiments were performed according to NIH guidelines, the Animal Welfare Act, and US federal law. Osteomyelitis was induced in 7- to 8-week-old mice as described previously [122]. Anesthesia was maintained with isoflurane (1-5%). Post-operative analgesia was provided pre-operatively and every 8–12 hours for 48 hours post-infection (buprenorphine 0.5–0.1 mg/kg) or pre-operatively as a slow-release formula

(buprenorphine-SR 1 mg/kg) as described previously [121,242]. Briefly, the anterolateral surface of the femur was exposed, and a hole was bored through the cortical bone near the mid-diaphysis to access the medullary space. After accessing the medullary space, 10^6 colony forming units (CFU) of *S. aureus* were directly inoculated in 2 μL PBS. In a subset of experiments, 10^5 CFU were inoculated as noted. For the first 72 h post-infection, mice were monitored and weighed daily. Mice were weighed and monitored at twice weekly intervals at a minimum following 72 h post-infection. The infection continued for up to 14 days. In consultation with the veterinary staff, mice that experienced greater than 20% weight loss were euthanized as a humane endpoint. These mice were excluded from studies. Mice were euthanized by CO_2 asphyxiation with cervical dislocation as secondary confirmation.

Quantification of bacterial burdens

At post-infection Days 3, 5, or 14, mice were euthanized, and bacterial burdens were analyzed as done previously [121]. The femurs were dissected using sterile technique and homogenized in 500 μL CelLytic Buffer MT Cell Lysis Reagent (MilliporeSigma) using a BulletBlender and NAVY lysis tubes (Next Advance, Inc.). The homogenates were serially diluted in PBS and plated for CFU enumeration on TSA plates.

Analysis of bone architecture by microcomputed tomography

Microcomputed tomography (microCT) was used to measure changes in cortical and trabecular bone as done previously [121,122]. Following euthanasia at post-infection Day 14, dissected femurs were scanned using a microCT 50 (Scanco Medical) and analyzed using microCT Tomography V6.3–4 software (Scanco USA, Inc.). Scans were completed with 10 μm voxel size at 70 kV, 200 μA, and an integration time of 350 ms in a 10.24 mm view, resulting in 1088 slices of the femur that included the diaphysis and the distal metaphysis.

Cortical bone destruction was measured by drawing contours around the endosteal and periosteal surfaces for 818 slices surrounding the cortical defect as done previously [121]. In *Vhl*$^{fl/fl}$, *OsxCre+* mice and their Cre-negative littermate controls, cortical bone loss was measured by drawing contours along the periosteal surface for 409 slices surrounding the cortical defect in the infected femur and 409 slides surrounding the corresponding mid-diaphysis in the contralateral femurs. For *Vhl*$^{fl/fl}$, *OsxCre+* mice and their Cre-negative littermate controls, cortical bone loss is presented as the normalized cortical bone loss. The normalized cortical bone loss was calculated by dividing the quantified cortical bone loss per total contoured volume in the infected femur by the same calculated value in the contralateral femur of the given animal. This alternative approach was used to limit artifact from the trabecularization of cortical bone in the *Vhl*$^{fl/fl}$, *OsxCre+* mice as has been noted previously [243]. Normalization with the calculated bone loss in the contralateral limb also accounts for artifacts from increased vascularity in the cortical bone of *Vhl*$^{fl/fl}$, *OsxCre+* mice that may be falsely measured as infection-mediated bone loss. Trabecular bone volume-per-total volume (BV/TV) was measured as done previously [121]. Briefly, trabecular bone (excluding cortical bone) in the distal metaphysis of the femur was analyzed across 101 slices 300 μm (30 slices) from the growth plate to measure BV/TV.

Bone histomorphometry

Following microCT scanning and analysis, femurs were analyzed for osteoclast abundance in the distal metaphyseal trabecular bone using histomorphometry, as done previously [121]. Femurs were decalcified in 20% EDTA for 3 days, embedded in paraffin, and sectioned on a Leica RM2255 microtome at a thickness of 4 μm. Sections were stained for tartrate-resistant acid phosphatase (TRAP) with hematoxylin counterstain. TRAP-stained slides were imaged with a Leica SCN400 Slide Scanner in brightfield at 20X and loaded into Bioquant software

(Bioquant Image Analysis Corporation). Bioquant software was used to measure osteoclast number, osteoclast surface, and bone surface in the trabeculae of the distal metaphysis of the femur proximal to the growth plate on the TRAP-stained slides. According to ASBMR standards [244], osteoclast number, osteoclast surface, and bone surface were measured to calculate osteoclast number per bone surface (N.Oc/BS) and osteoclast surface per bone surface (Oc.S/BS).

Concentration of bacterial supernatants

Bacterial supernatants for Δ*psm*/Δ*spa* were prepared as done previously [117]. In brief, supernatants from overnight cultures of bacteria growth in RPMI supplemented with 10 g/L casamino acids were centrifuged in Amicon® Ultra 3 kDa molecular weight cutoff filter tubes to concentrate 45 mL to approximately 1.5 mL. Filter-sterilized, concentrated supernatants were aliquoted and stored at -80°C until being thawed for use in *in vitro* experiments.

Primary osteoblast isolation

Primary calvarial osteoblasts were obtained from neonatal $Vhl^{fl/fl}$ as described previously [245]. Briefly, calvariae were dissected from 24- to 48-h-old mice and digested five times in dispase (MilliporeSigma) and type II collagenase (MilliporeSigma). Digest fractions 2-5 were pooled and plated on tissue-culture treated 10-cm dishes (Corning) in α-minimal essential media (α-MEM; Gibco #A1049001; Thermo Fisher Scientific) containing 10% fetal bovine serum (FBS; Bio-Techne) and 1x penicillin/streptomycin (Thermo Fisher Scientific). At near confluency, the cells were passaged in 0.25% trypsin with 2.21 mM EDTA (Corning) to 24-well plates for experiments and maintained in α-MEM with 10% FBS and 1x penicillin/streptomycin.

Adenovirus infection and bacterial stimulation

Primary calvarial osteoblasts were treated with adenovirus (Vector Biolabs) containing green fluorescent protein (GFP) or adenovirus containing Cre recombinase and GFP (AdGFP or AdCre, respectively) at a multiplicity of infection of 100. 3 days following infection with adenovirus, the media was removed and replaced with fresh media containing 5% (v/v) bacterial supernatants from Δ*psm*/Δ*spa S. aureus*. Δ*psm*/Δ*spa S. aureus* was used to limit rapid toxin-mediated cell death and potential confounding of staphylococcal protein A in downstream antibody-based assays. The vehicle control for bacterial supernatants was RPMI media (Corning) containing 10 g/L casamino acids (MilliporeSigma). 6 h following bacterial supernatant exposure, cells were washed in PBS and lysed in RLT buffer (Qiagen) containing 1% (v/v) β-mercaptoethanol (MilliporeSigma).

RT-PCR

RNA was isolated from primary osteoblasts using the RNeasy Mini Kit (Qiagen) according to manufacturer's instructions with on-column treatment with RNase-Free DNase (Qiagen). Following isolation, cDNA was synthesized using qScript™ cDNA SuperMix (QuantaBio) according to manufacturer's instructions. RT-PCR was conducted on a thermocycler using diluted cDNA, with primers as shown (

Table 2), and iQ SYBR Green Supermix (Bio-Rad) for up to 40 cycles with a melting temperature of 55°C. Fold change in gene expression was determined by normalizing the threshold values (C_T) by the vehicle (RPMI)-AdGFP condition according to the $2^{-\Delta\Delta CT}$ method as described previously [246].

Table 2: Primer sequences used for RT-PCR

For each gene (protein in parentheses) tested by RT-PCR, the forward and reverse primer sequences are shown along with the Harvard PrimerBank ID for each primer pair. PrimerBank (available at: https://pga.mgh.harvard.edu/primerbank/index.html) was used as the reference for each primer set.

Gene		Sequences	PrimerBank ID
Actb (β-actin)	Forward	5'-GGCTGTATTCCCCTCCATCG-3'	6671509a1
	Reverse	5'-CCAGTTGGTAACAATGCCATGT-3'	
Tnfsf11 (RANKL)	Forward	5'-CAGCATCGCTCTGTTCCTGTA-3'	6755833a1
	Reverse	5'-CTGCGTTTTCATGGAGTCTCA-3'	
Tnfrsf11b (OPG)	Forward	5'-ACCCAGAAACTGGTCATCAGC-3'	31543882a1
	Reverse	5'-CTGCAATACACACACTCATCACT-3'	
Vhl (VHL)	Forward	5'-ACATCGTCAGGTCACTCTATGA-3'	118130344c3
	Reverse	5'-CTCTTGGCTCAGTCGCTGTAT-3'	
Sp7 (Osx)	Forward	5'-ATGGCGTCCTCTCTGCTTG-3'	18485518a1
	Reverse	5'-TGAAAGGTCAGCGTATGGCTT-3'	

Statistical analysis

Differences in post-infection weights, trabecular bone microCT analysis, histomorphometry measurement of osteoclasts *in vivo*, and RT-PCR following AdCre treatment were assessed by two-way analysis of variance (ANOVA) with multiple comparisons as shown. Differences in trabecular bone microCT analysis in Figure 9C were assessed by two-tailed, paired *t*-test. Differences in bacterial burdens were generally assessed by two-tailed, unpaired Student's *t*-test. Bacterial burdens in Figure 14C were compared by one-way ANOVA. Bacterial burdens in Figure 6 were compared by two-way ANOVA with multiple comparisons. Differences in cortical bone loss were assessed by two-tailed, unpaired Student's *t*-test. A p value of 0.05 was considered significant for all analyses. All statistical analyses were performed with GraphPad Prism.

Results

Conditional knockout of *Vhl* or *Hif1a* in osteoblast-lineage cells does not alter bacterial burdens at post-infection Day 14

Osteoblast-lineage conditional deletion of *Vhl* or *Hif1a* was achieved through Cre-lox breeding employing *OsxCre* and $Vhl^{fl/fl}$ or $Hif1a^{fl/fl}$, respectively. Bacterial burdens recovered from infected femurs of female conditional knockout mice at Day 14 post-infection did not differ from those of littermate controls that lack the *OsxCre* transgene (**Figure 4A,B**). Over the course of infection, the relative weight loss did not significantly differ between $Hif1a^{fl/fl}$, *OsxCre*+ mice and controls (**Figure 4C**). For $Vhl^{fl/fl}$, *OsxCre*+ mice, the relative weight loss significantly differed at early time points (**Figure 4D**), though the differences were small. To account for potential sex-dependent differences, parallel data were obtained for male mice, and no significant differences were observed for Day 14 post-infection bacterial burdens or post-infection weights

(**Figure 5**). Importantly, in the data obtained in male *Vhl*$^{fl/fl}$, *OsxCre*+ mice and controls, the weights did not differ from Cre-negative littermate controls at early time points.

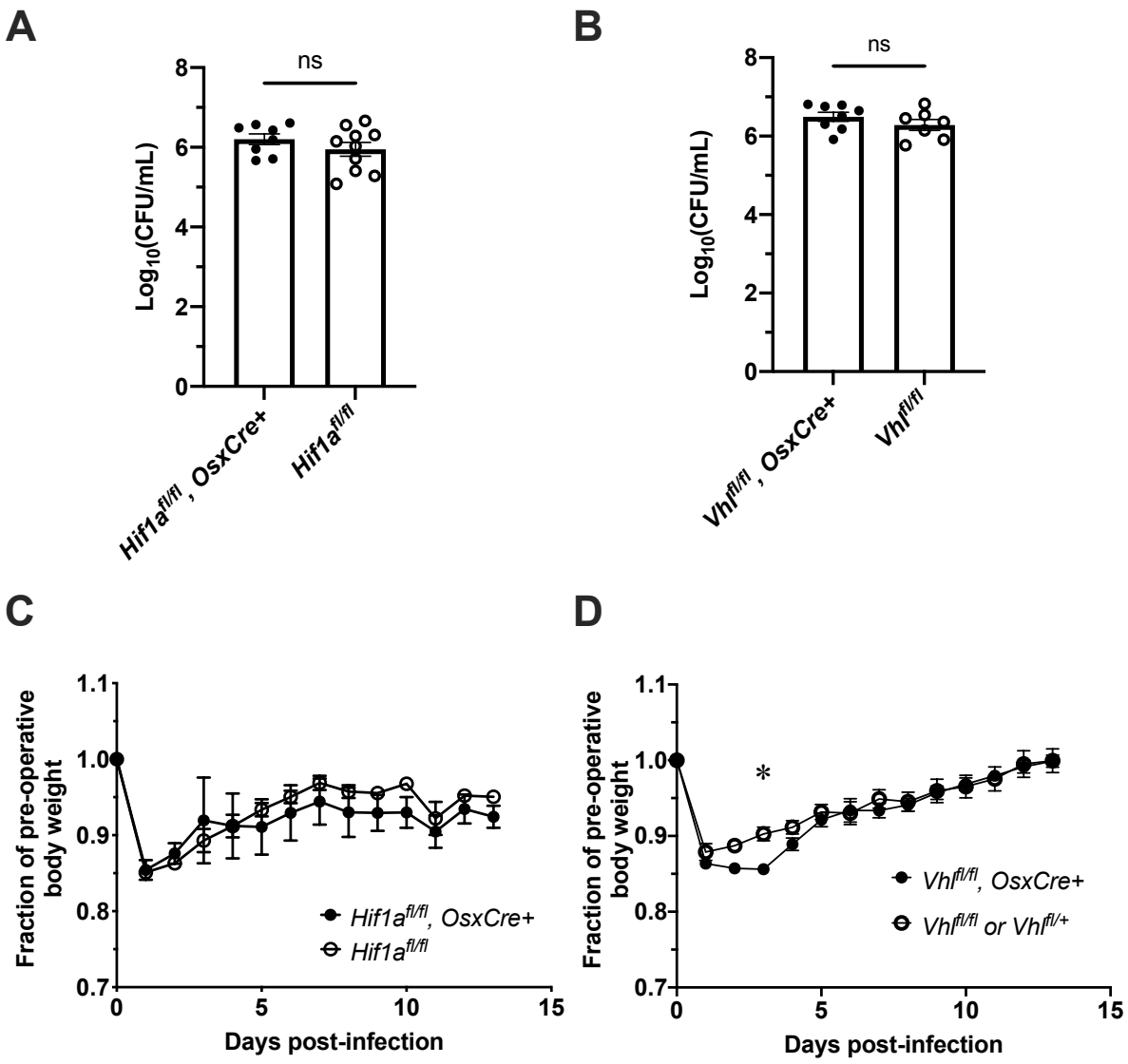

Figure 4: Conditional knockout of *Hif1a* or *Vhl* in the osteoblast lineage in female mice does not impact bacterial burdens at post-infection Day 14

Bacterial burdens in infected femurs of female mice containing conditional knockouts of *Hif1a* (**A**) and *Vhl* (**B**) were measured at post-infection Day 14 (n=7-10 as shown). The bacterial burdens were compared to those of Cre-negative littermate controls that were homozygous for the respective floxed alleles. ns denotes not significant ($p > 0.05$) as determined by unpaired, two-tailed Student's *t*-tests. The relative weights of the corresponding infected animals analyzed in (**A**) and (**B**) are shown in (**C**) and (**D**), respectively. The weights were measured daily and

normalized to the pre-operative, uninfected animal weights before comparison by two-way ANOVA. (**C**) The weights of mice with conditional knockout of *Hif1a* were not found to significantly differ from those of littermate controls. (**D**) The weights of mice with conditional knockout of *Vhl* were found to significantly differ from those of littermate controls at post-infection Day 3. Error bars represent mean ± *SEM*. *$p < 0.05$ as determined by two-way analysis of variance (ANOVA) with multiple comparisons. CFU=colony forming units.

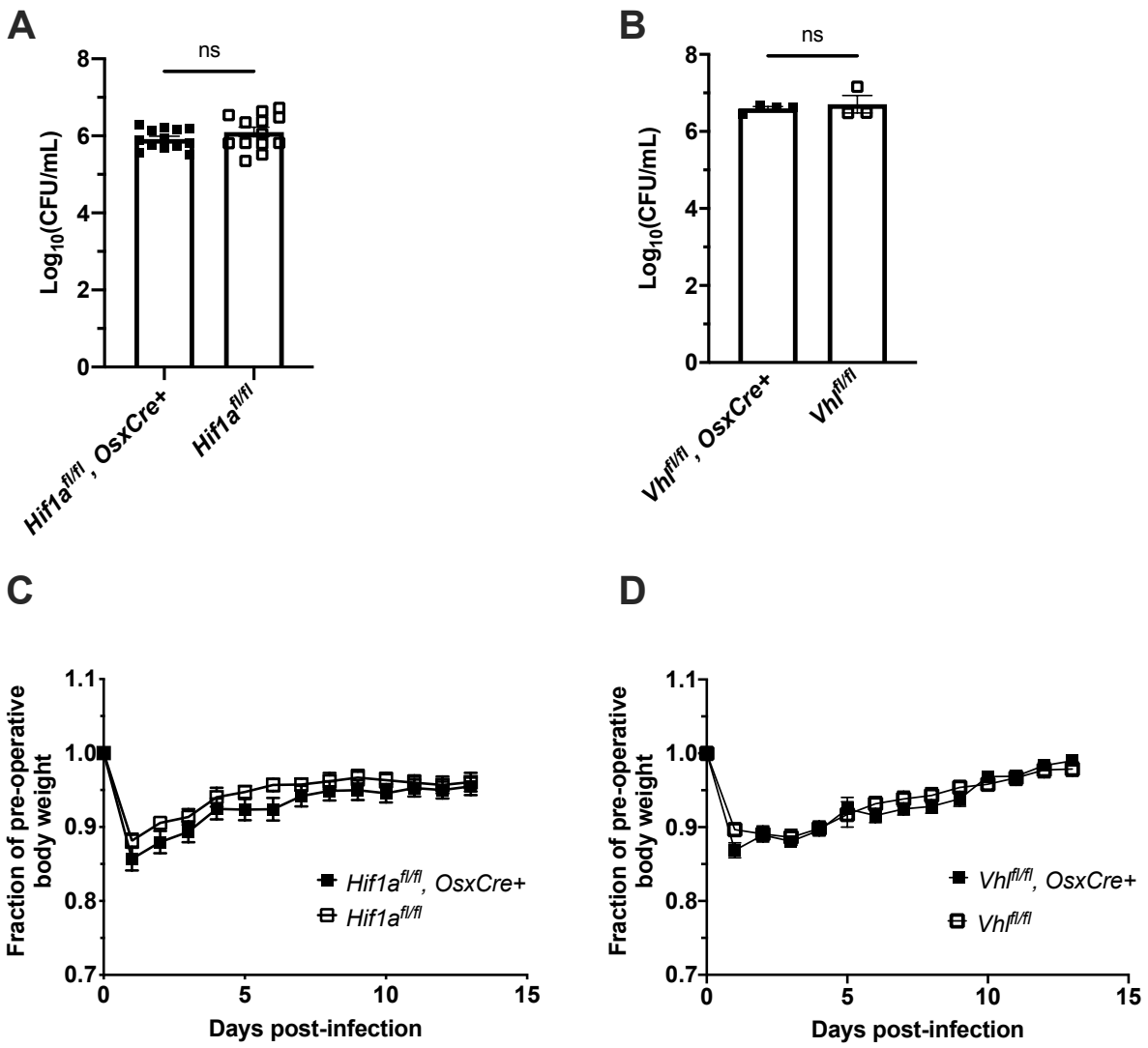

Figure 5: Conditional knockout of *Hif1a* or *Vhl* in the osteoblast lineage in male mice does not impact bacterial burdens at post-infection Day 14

Bacterial burdens in infected femurs of male mice containing conditional knockouts of *Hif1a* (**A**, *n*=13) and *Vhl* (**B**, *n*=3-4) were measured at post-infection Day 14. The colony forming units (CFU) were compared to those of Cre-negative littermate controls that were homozygous for the respective floxed alleles. ns denotes not significant ($p > 0.05$) as determined by unpaired, two-tailed Student's *t*-tests. The weights of the corresponding infected animals analyzed in (**A**) are shown in (**C**) (*n*=13). The weights shown in (**D**) represent those of animals analyzed for changes

in bone architecture, as well as those analyzed for bacterial burdens in (**B**) (n=9-10). The weights were measured daily and normalized to the pre-operative, uninfected animal weights before comparison by two-way analysis of variance (ANOVA). The relative weights of mice with conditional knockout of *Hif1a* (**C**) and *Vhl* (**D**) were not significantly different from those of littermate controls. Error bars represent mean ± *SEM*. CFU=colony forming units.

Conditional knockout of *Vhl* in osteoblast-lineage cells does not alter bacterial burdens at early time points

Because the weights statistically differed at early time points in *Vhl*$^{fl/fl}$, *OsxCre+* mice, bacterial burdens were investigated to determine if transient differences in antibacterial responses were present. Post-infection days 3 and 5 were selected because these times represented critical times for control of bacterial burdens in prior studies in our laboratory [121]. At both days 3 and 5 post-infection, the bacterial burdens in *Vhl*$^{fl/fl}$, *OsxCre+* mice did not differ from controls (**Figure 6**), suggesting that no substantial differences exist for bacterial burden control in these mice. Combined, the data from bacterial burdens and post-infection weights suggest that conditional knockout of *Hif1a* or *Vhl* in osteoblast-lineage cells does not substantially impact antibacterial responses during *S. aureus* osteomyelitis in this mouse model.

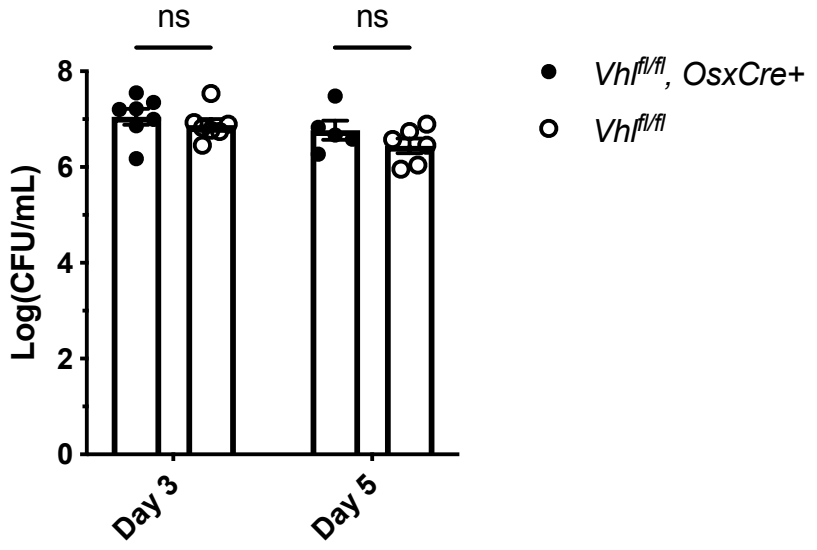

Figure 6: Bacterial burdens at early infection time points in *Vhl*$^{fl/fl}$, *OsxCre*+ mice do not differ from those of controls

The bacterial burdens of osteoblast-lineage *Vhl* conditional knockout mice were measured at post-infection Day 3 and Day 5. The bacterial burdens of conditional knockout mice were compared to those of homozygous floxed littermate controls (n=5-7 female mice as shown). Error bars represent mean ± *SEM*, and ns denotes not significant ($p > 0.05$) as determined by two-way analysis of variance (ANOVA). CFU=colony forming units.

The *OsxCre* model employs a unique transgene which enables suppression of Cre-mediated conditional deletion of floxed alleles through a Tet-off system [238]. With this transgene, doxycycline in the water suppresses Cre recombinase expression and activity to delay conditional gene deletion. Prior studies have demonstrated that constitutively active deletion of *Vhl* in osteoblasts causes profound changes in bone architecture [59,243]. To limit baseline differences in bone architecture, doxycycline was administered to delay onset of Cre-mediated gene deletion. Initial studies were modeled after previously published investigations of the role of intracellular VEGF in osteoblasts that employed the same *OsxCre* transgene to regulate Cre-mediated conditional gene deletion [89]. Based on the previous work, Cre activity was suppressed with continuous doxycycline exposure during *in utero* and early postnatal development until postnatal age 4 weeks, when doxycycline was withdrawn. Following 3-4 weeks of doxycycline washout and Cre activation, the infection took place at postnatal age 7 to 8 weeks of age. However, given the absence of differences in bacterial burdens, we investigated bacterial burdens in mice with an extended washout of doxycycline. To accomplish this, doxycycline was withdrawn at postnatal age 1 week and infections still took place at postnatal age 7-8 weeks. Similar to findings with withdrawal of doxycycline at postnatal age 4 weeks, no differences in bacterial burdens were observed in infected femurs of mice with withdrawal of doxycycline at postnatal age 1 week (**Figure 7A,C,E**). Similarly, no differences were observed in post-infection weights over the course of the infection (**Figure 7B,D,F**).

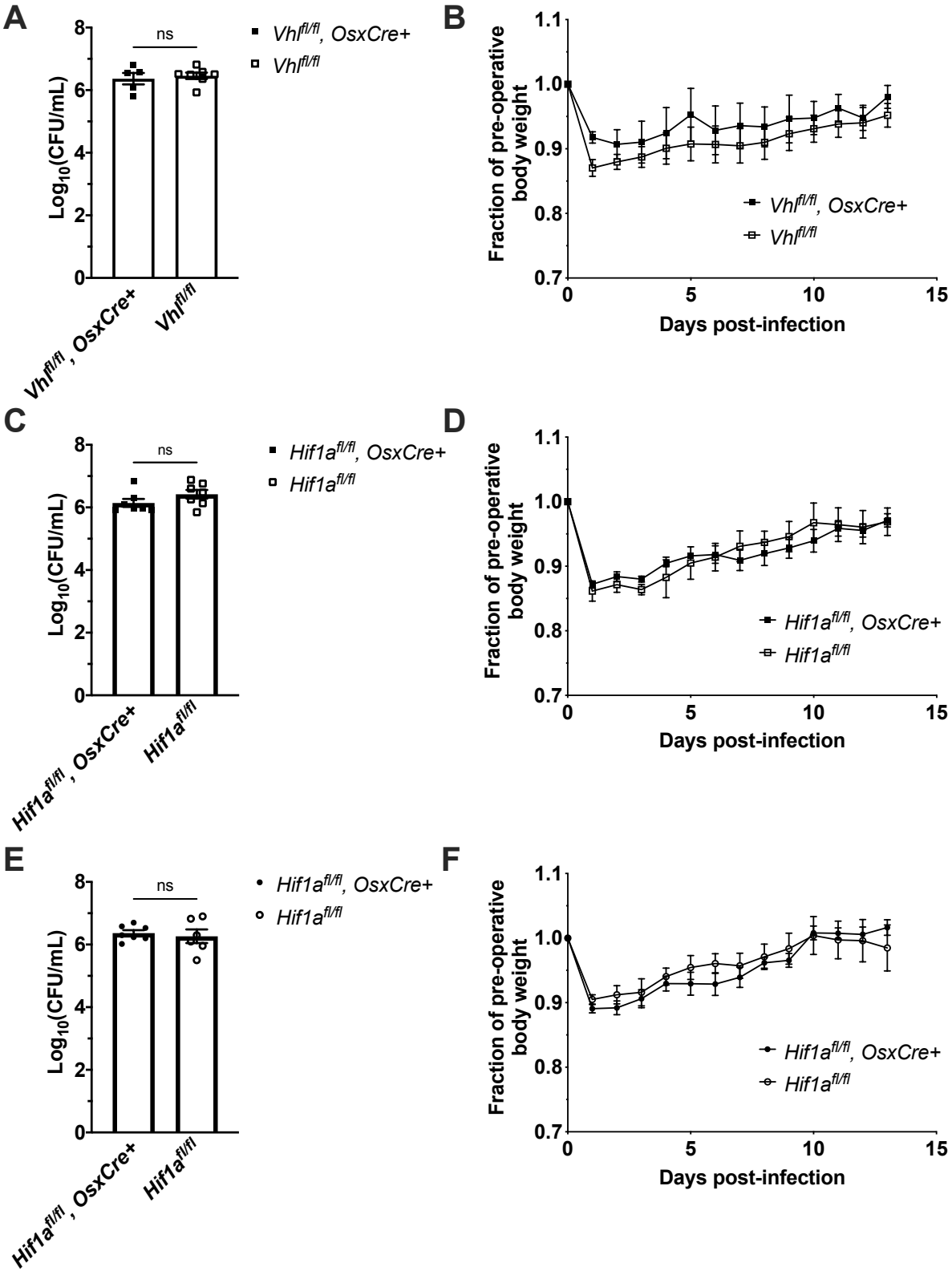
A
ns
Log10(CFU/mL)
Vhlfl/fl, OsxCre+
Vhlfl/fl
B
Fraction of pre-operative body weight
Days post-infection
C
Hif1afl/fl, OsxCre+
Hif1afl/fl
D
E
F

Figure 7: Bacterial burdens in mice with osteoblast-lineage conditional knockouts of *Hif1a* or *Vhl* do not differ from controls with extended doxycycline withdrawal

Following withdrawal of doxycycline at postnatal age 1 week, bacterial burdens of male $Vhl^{fl/fl}$, *OsxCre*+ mice and $Vhl^{fl/fl}$ controls (**A**, n=5-7), male $Hif1a^{fl/fl}$, *OsxCre*+ mice and $Hif1a^{fl/fl}$ controls (**C**, n=7), and female $Hif1a^{fl/fl}$, *OsxCre*+ mice and $Hif1a^{fl/fl}$ controls (**E**, n=6,7) were measured in infected femurs at post-infection Day 14. Error bars represent mean ± *SEM*, and ns denotes not significant ($p > 0.05$) as determined by unpaired, two-tailed Student's *t*-tests with comparison to burdens of Cre-negative littermate controls. For each experiment in (**A)**, (**C)**, and (**E)**, corresponding post-infection weights were recorded as a fraction of the uninfected, pre-operative weight (**B**, male $Vhl^{fl/fl}$, *OsxCre*+ mice and $Vhl^{fl/fl}$ controls; **D**, male $Hif1a^{fl/fl}$, *OsxCre*+ mice and $Hif1a^{fl/fl}$ controls; and **F**, female $Hif1a^{fl/fl}$, *OsxCre*+ mice and $Hif1a^{fl/fl}$ controls). For each assessment of changes weights over the course of the 14-day infection, no significant differences were observed between the conditional knockout animals and the corresponding control group as determined by two-way analysis of variance (ANOVA). Error bars represent mean ± *SEM*. CFU=colony forming units.

Osteoblast-lineage knockout of *Vhl* limits trabecular bone loss during *S. aureus* osteomyelitis

After confirming that the bacterial burdens of osteoblast-lineage conditional knockout mice did not differ from those of controls, we tested the impact of osteoblast-lineage deletion of *Hif1a* on changes to bone architecture incurred during infection. To do this, we performed microCT on infected femurs and the corresponding uninfected, contralateral femurs. In previous studies in our lab, we have observed changes in trabecular bone volume between the infected and contralateral femurs in response to *S. aureus* osteomyelitis [121]. The distal metaphyseal trabecular bone was analyzed to determine the bone volume-per-total volume (BV/TV). *OsxCre*-mediated deletion is repressible in this Cre model by administration of doxycycline in a Tet-OFF system. Animals with doxycycline withdrawal at postnatal age 4 weeks were used to limit the changes in bone at baseline because animals with doxycycline withdrawal at postnatal age 1 week demonstrate greater baseline differences in trabecular bone (**Figure 8**). In $Hif1a^{fl/fl}$, *OsxCre*+ mice, the trabecular BV/TV did not differ from those of genotypic controls. Consistent with prior studies, the infection-induced decline in BV/TV was present in both the $Hif1a^{fl/fl}$, *OsxCre*+ mice as well as the Cre-negative littermate controls (**Figure 9A**). While the BV/TV was not different between $Hif1a^{fl/fl}$, *OsxCre*+ mice and Cre-negative littermate controls, the trabecular BV/TV was markedly increased in $Vhl^{fl/fl}$, *OsxCre*+ mice compared to Cre-negative littermate controls (**Figure 9B**). The dramatic increase in trabecular BV/TV has been reported previously and supports the appropriate activity of the Cre-lox model [59,243]. Furthermore, when measuring changes in BV/TV in response to infection, no difference in trabecular bone loss was observed relative to the contralateral limb in $Vhl^{fl/fl}$, *OsxCre*+ mice (**Figure 9B**). As previously observed, the Cre-negative littermate control group demonstrated significant loss of

BV/TV during the course of infection between the infected and contralateral femurs (**Figure 9C**). These data suggest that loss of osteoblast-lineage *Hif1a* does not impact *S. aureus*-mediated changes in trabecular BV/TV during infection, but loss of osteoblast-lineage *Vhl* limits infection-mediated decreases in trabecular BV/TV during *S. aureus* osteomyelitis.

In addition to analyzing changes in trabecular bone, cortical bone loss was also measured by microCT. Despite observing genotype-specific changes in trabecular bone loss, no differences in cortical bone loss were observed for mice with osteoblast-lineage conditional knockout of *Hif1a* or *Vhl* (**Figure 10**). Prior studies have identified that cortical bone is trabecularized (with gaps in the cortical shell) along the diaphysis in $Vhl^{fl/fl}$, *OsxCre*+ mice, most prominently near the metaphyses. Therefore, methods for cortical bone analysis were altered for this genotype to limit falsely elevated measurement of cortical bone lysis that may be mixed with trabecularized cortical bone. Thus, the area of analysis for cortical bone lysis was confined to a central region of the diaphysis that further excluded the metaphyseal area where trabecularized cortical bone is most prevalent. Additionally, the cortical bone analysis was completed on the equivalent region of the contralateral femur. The value of the measured bone "lysis" on the contralateral limb was then used to normalize the measured lysis in the infected limb. This modification was used for both the $Vhl^{fl/fl}$, *OsxCre*+ and the $Vhl^{fl/fl}$ littermate control mice. For the standard analysis in the $Hif1a^{fl/fl}$, *OsxCre*+ and for modified analysis in the $Vhl^{fl/fl}$, *OsxCre*+ mice, cortical lysis was not found to significantly differ between the conditional knockout mice and their Cre-negative littermate controls, respectively (**Figure 10A,B**).

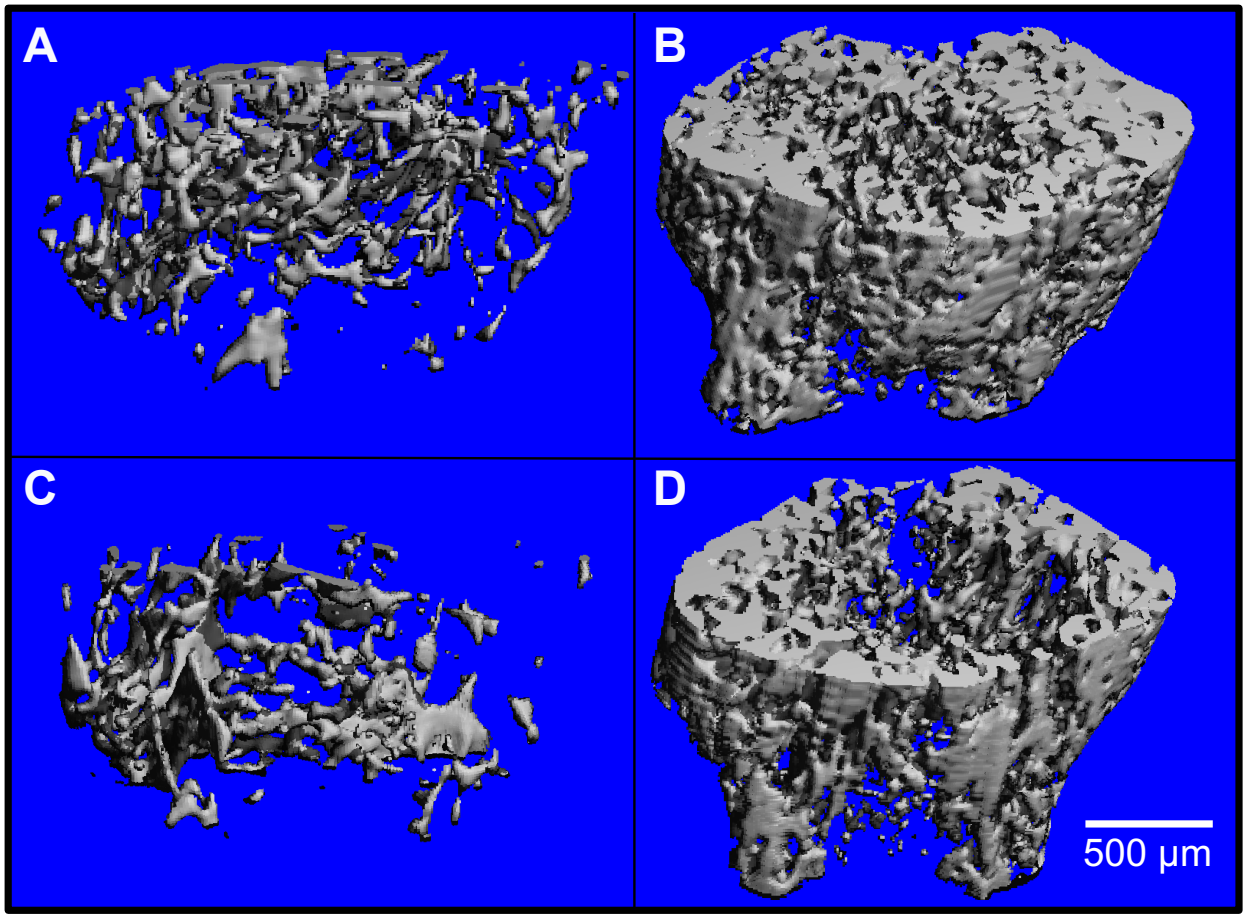

Figure 8: The duration of doxycycline withdrawal impacts trabecular bone volume in *Vhl*$^{fl/fl}$, *OsxCre*+ mice

MicroCT reconstructions of trabecular bone from the distal metaphysis of the right femur of a *Vhl*$^{fl/fl}$ control (**A**) is shown in relation to that of its corresponding *Vhl*$^{fl/fl}$, *OsxCre*+ littermate (**B**). The animals in (**A**) and (**B**) were both maintained on doxycycline until postnatal age 1 week, at which time doxycycline was no longer administered to allow for activation of the Cre recombinase. (**C**) and (**D**) represent equivalent regions of the trabecular bone of femurs from *Vhl*$^{fl/fl}$ and *Vhl*$^{fl/fl}$, *OsxCre*+ littermates for which doxycycline was withdrawn at postnatal age 4 weeks. All femurs analyzed are the right (contralateral) femur of mice at post-infection Day 14.

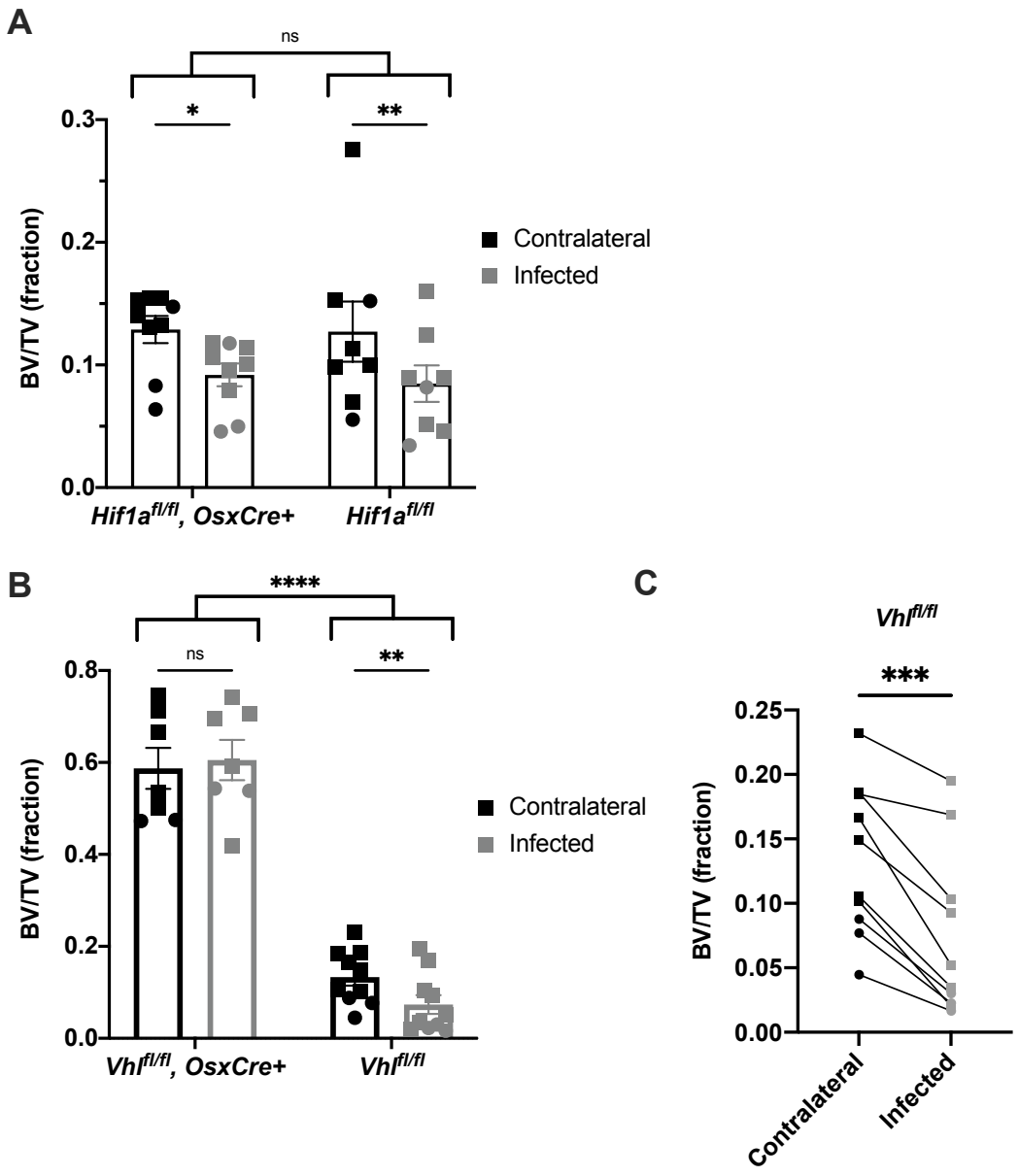

Figure 9: *Vhl*$^{fl/fl}$, *OsxCre*+ mice do not exhibit declines in trabecular bone volume during osteomyelitis

(**A**) Trabecular bone volume-per-total volume (BV/TV) in *Hif1a*$^{fl/fl}$, *OsxCre*+ mice and *Hif1a*$^{fl/fl}$ littermate control mice (n=8-9) was measured in the distal metaphysis of infected and contralateral femurs using microCT. Squares represent males, and circles represent females. *$p < 0.05$, **$p < 0.01$ as determined by two-way analysis of variance (ANOVA) with multiple comparisons. ns denotes that the genotypes (two bracketed groups) are not significantly different

($p > 0.05$) as determined by two-way ANOVA. (**B**) BV/TV was measured in the infected and contralateral distal metaphyses of femurs in *Vhl*$^{fl/fl}$, *OsxCre*+ mice and *Vhl*$^{fl/fl}$ littermate control mice (n=7-10). Squares represent males, and circles represent females. **$p < 0.01$ and ns denotes not significant ($p > 0.05$) as determined by two-way analysis of variance (ANOVA). Comparison of bracketed genotypes refers to two-way ANOVA comparison of genotypes, denoted with ****$p < 0.0001$. Error bars represent mean ± *SEM*. (**C**) The data from *Vhl*$^{fl/fl}$ littermate control mice (n=10) analyzed in (**B**) are shown in an enlarged graph for clarity with lines denoting paired contralateral and infected femurs. ***$p < 0.001$, as determined by paired, two-tailed Student's *t*-test. Error bars represent mean ± *SEM*.

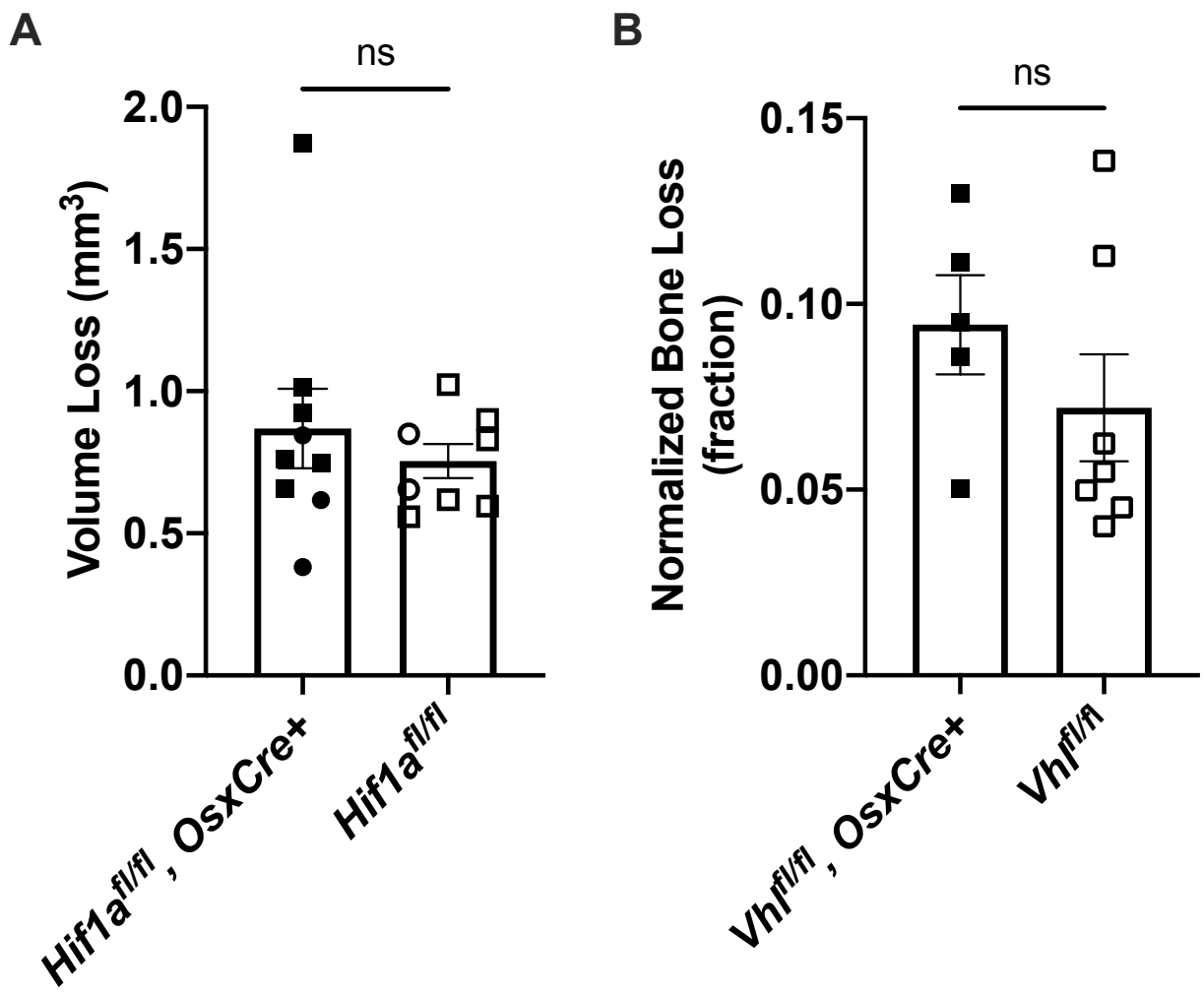

Figure 10: Osteoblast-lineage *Hif1a* or *Vhl* conditional knockout does not alter cortical bone loss compared to littermate controls

(**A**) Volume of cortical bone loss in the infected femur in *n*=8 *Hif1a*$^{fl/fl}$, *OsxCre*+ or *Hif1a*$^{fl/fl}$ littermate control mice was determined using microCT at post-infection Day 14. Squares represent males, and circles represent females. (**B**) Cortical bone loss at post-infection Day 14 in the infected femurs of *n*=5-7 male *Vhl*$^{fl/fl}$, *OsxCre*+ or *Vhl*$^{fl/fl}$ littermate control mice was determined using microCT and is expressed as a normalized ratio relative to equivalent analysis performed on the contralateral (uninjured, uninfected) femur. ns denotes not significant

($p > 0.05$) as determined by unpaired, two-tailed Student's *t*-test. Error bars represent mean ± *SEM*.

Recognizing that injury itself may contribute to trabecular bone loss, we investigated changes in trabecular BV/TV following sterile injury (mock infection). Animals were subjected to the same procedure used to induce osteomyelitis; however, sterile PBS was injected into the medullary space instead of *S. aureus*. Following mock infection, no changes were observed in the trabecular BV/TV between the injured and contralateral femurs of $Vhl^{fl/fl}$, *OsxCre*+ mice (**Figure 11**). No changes were also observed between the injured and contralateral femurs of Cre-negative littermate control mice (**Figure 11**). These data suggest that trabecular bone loss occurs to a greater extent in infected femurs compared to mock-infected femurs. Moreover, the observed difference between the genotypes (i.e., the Cre-negative mice show a decline in BV/TV in the infected femur versus the contralateral unlike the $Vhl^{fl/fl}$, *OsxCre*+ mice) is dependent upon infection.

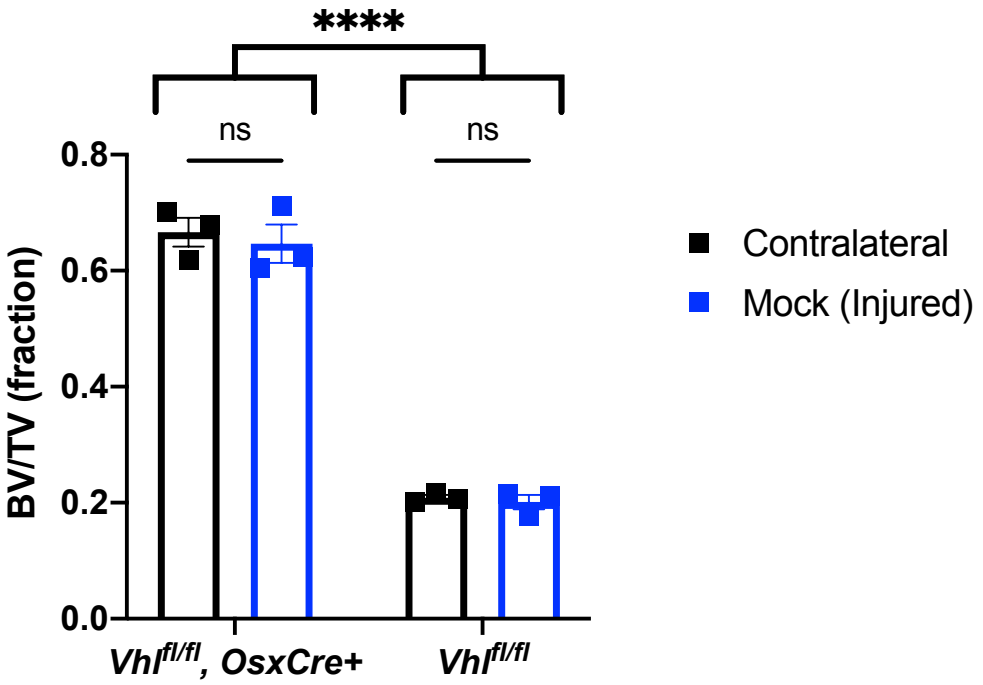

Figure 11: Trabecular bone loss does not occur in *Vhl*$^{fl/fl}$, *OsxCre*+ mice or Cre-negative littermate controls following sterile mock infection

Trabecular bone volume-per-total volume (BV/TV) was assessed in the distal metaphysis of left femurs of *Vhl*$^{fl/fl}$, *OsxCre*+ and *Vhl*$^{fl/fl}$ littermates (n=3) following sterile mock infection (injury only) and compared to the BV/TV of the trabecular bone in the contralateral femur. ****$p < 0.0001$ (comparison of bracketed genotypes) and ns denotes not significant ($p > 0$ .05) as determined by two-way analysis of variance (ANOVA). Error bars represent mean ± *SEM*.

Conditional knockout of *Vhl* in osteoblast-lineage cells limits infection-induced increases in osteoclasts *in vivo*

Previous studies in our lab showed that trabecular bone loss during *S. aureus* osteomyelitis is associated with an increase in osteoclasts in trabecular bone [121]. To better understand the processes that prevent decreases in BV/TV in $Vhl^{fl/fl}$, *OsxCre*+ mice, we performed bone histomorphometry on bone sections from infected mice. $Vhl^{fl/fl}$, *OsxCre*+ mice demonstrated a decreased number of osteoclasts and osteoclast surface relative to bone surface compared to age-matched *OsxCre*+ mice lacking the *Vhl* floxed alleles (**Figure 12A,B**). These data show that loss of *Vhl* in the osteoblast lineage limits osteoclast formation in trabecular bone during *S. aureus* osteomyelitis *in vivo*.

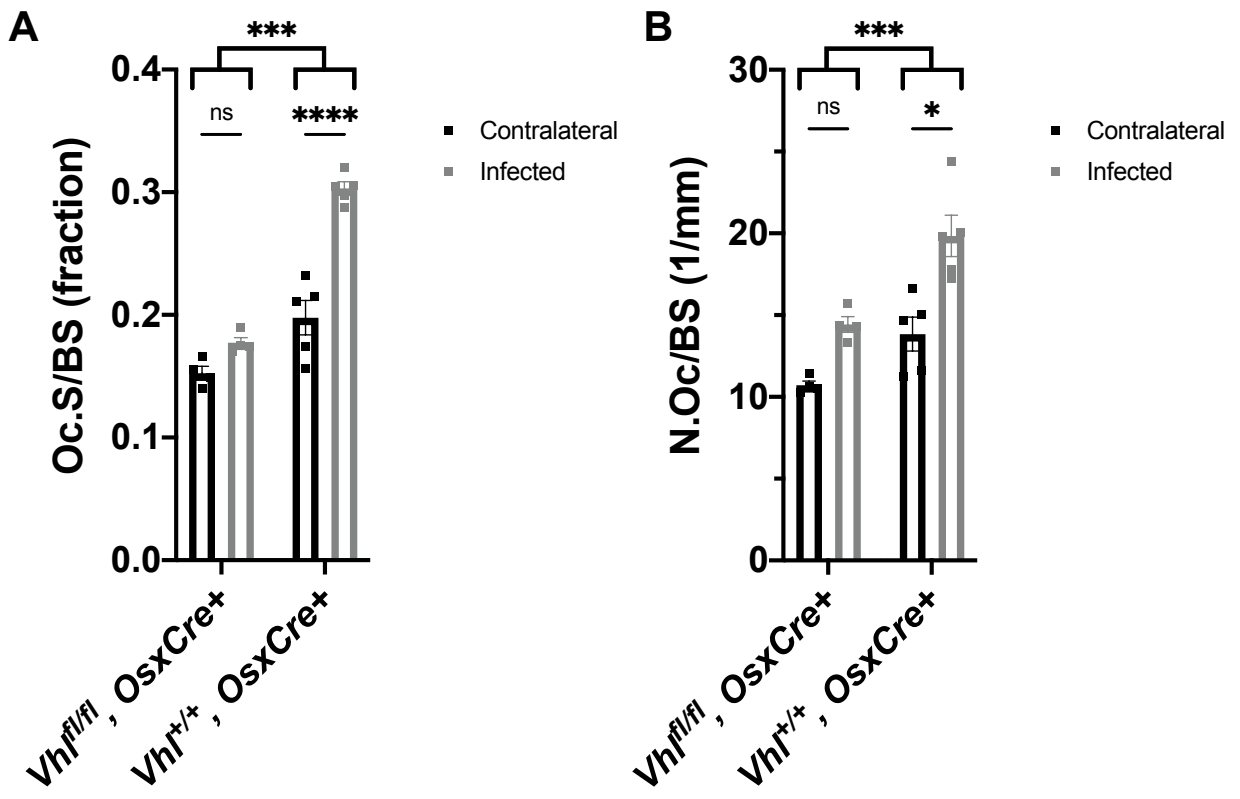

Figure 12: Fewer osteoclasts are present in trabecular bone of *Vhl$^{fl/fl}$*, *OsxCre*+ mice during osteomyelitis compared to age-matched *OsxCre*+ controls

(**A**) Osteoclast surface per bone surface (Oc.S/BS) is expressed as a fraction from bone histomorphometry performed on trabecular bone in the distal metaphysis of infected and contralateral femurs for *Vhl$^{fl/fl}$, OsxCre*+ mice (n=4) and *Vhl$^{+/+}$, OsxCre*+ mice (age-matched, n=4). ***$p < 0.001$, ****$p < 0.0001$, and ns denotes not significant ($p > 0.05$) as determined by two-way analysis of variance (ANOVA) with multiple comparisons. (**B**) Equivalent analysis of sections analyzed in (**A**) were performed to measure the number of osteoclasts per bone surface (N.Oc/BS). *$p < 0.05$, ***$p < 0.001$, and ns denotes not significant ($p > 0.05$) as determined by two-way analysis of variance (ANOVA) with multiple comparisons. Straight lines refer to comparison between contralateral and infected femurs in each genotype; comparison between

bracketed groups refers to two-way ANOVA comparison of genotypes. Error bars represent mean ± *SEM*.

Vhl deletion blunts *S. aureus*-mediated induction of *Tnfsf11* (RANKL) transcription relative to that of *Tnfrsf11b* (OPG)

One of the primary ways that osteoblast-lineage cells (the cells targeted by *OsxCre*) impact osteoclast abundance is through RANKL and OPG signaling [41]. During *S. aureus* osteomyelitis, osteoblastic RANKL is increased, which facilitates bone loss [120]. We previously found that *S. aureus* supernatants are potently cytotoxic to osteoblasts, and this cytotoxicity is dependent upon phenol-soluble modulins (PSMs) [122]. To understand if the RANKL-OPG signaling axis impacts differences in observed osteoclast numbers during *S. aureus* osteomyelitis, *in vitro* studies were performed in which osteoblasts were treated with toxin-deficient bacterial supernatants that lack PSMs. Bacterial stimulation with toxin-deficient bacterial supernatants limits concomitant cell death that may confound interpretations [122]. As published previously, adenovirus containing green fluorescent protein (AdGFP) or containing Cre recombinase with GFP (AdCre) was used to transfect $Vhl^{fl/fl}$ osteoblasts *in vitro* [243]. The transfection with AdCre causes deletion of the floxed *Vhl* exon resulting in knockout. Following transfection with AdGFP or AdCre, osteoblasts were stimulated with toxin-deficient bacterial supernatants. Because the ratio of RANKL-to-OPG is known to impact osteoclast formation, real-time polymerase chain reaction (RT-PCR) was used to assess changes in *Tnfsf11* (RANKL) transcription relative to *Tnfrsf11b* (OPG) transcription. When analyzed as the normalized ratio between RANKL and OPG gene transcription, the differences reach statistical significance, suggesting that knockout of *Vhl* blunts the induction of RANKL gene transcription relative to that of OPG (**Figure 13A**). To further validate the *in vitro* experiments, transcription of *Vhl* was analyzed between the samples and confirmed that Cre-mediated deletion significantly reduced *Vhl* transcription (**Figure 13B**). Moreover, *Sp7* (Osx) transcription was measured to confirm that

the cells assayed match the cells targeted in the *Vhl*$^{fl/fl}$, *OsxCre*+ mouse. *Sp7* transcription was transcribed in all conditions and did not differ between groups (**Figure 13C**).

These data demonstrate that osteoblast-lineage conditional knockout of *Hif1a* is dispensable for control of bacterial burdens and pathologic changes to bone architecture. Similarly, conditional knockout of *Vhl* in the osteoblast lineage does not alter bacterial burdens. Despite this, *Vhl*$^{fl/fl}$, *OsxCre*+ mice exhibit reduced trabecular bone loss during infection compared to Cre-negative littermate control mice. *In vivo* bone histomorphometry revealed that osteoclast abundance following infection is reduced in *Vhl*$^{fl/fl}$, *OsxCre*+ mice, and *in vitro* data indicate that *Vhl* deletion in osteoblasts diminishes *S. aureus*-mediated increases in the transcription of *Tnfsf11* (RANKL) relative to *Tnfsf11b* (OPG).

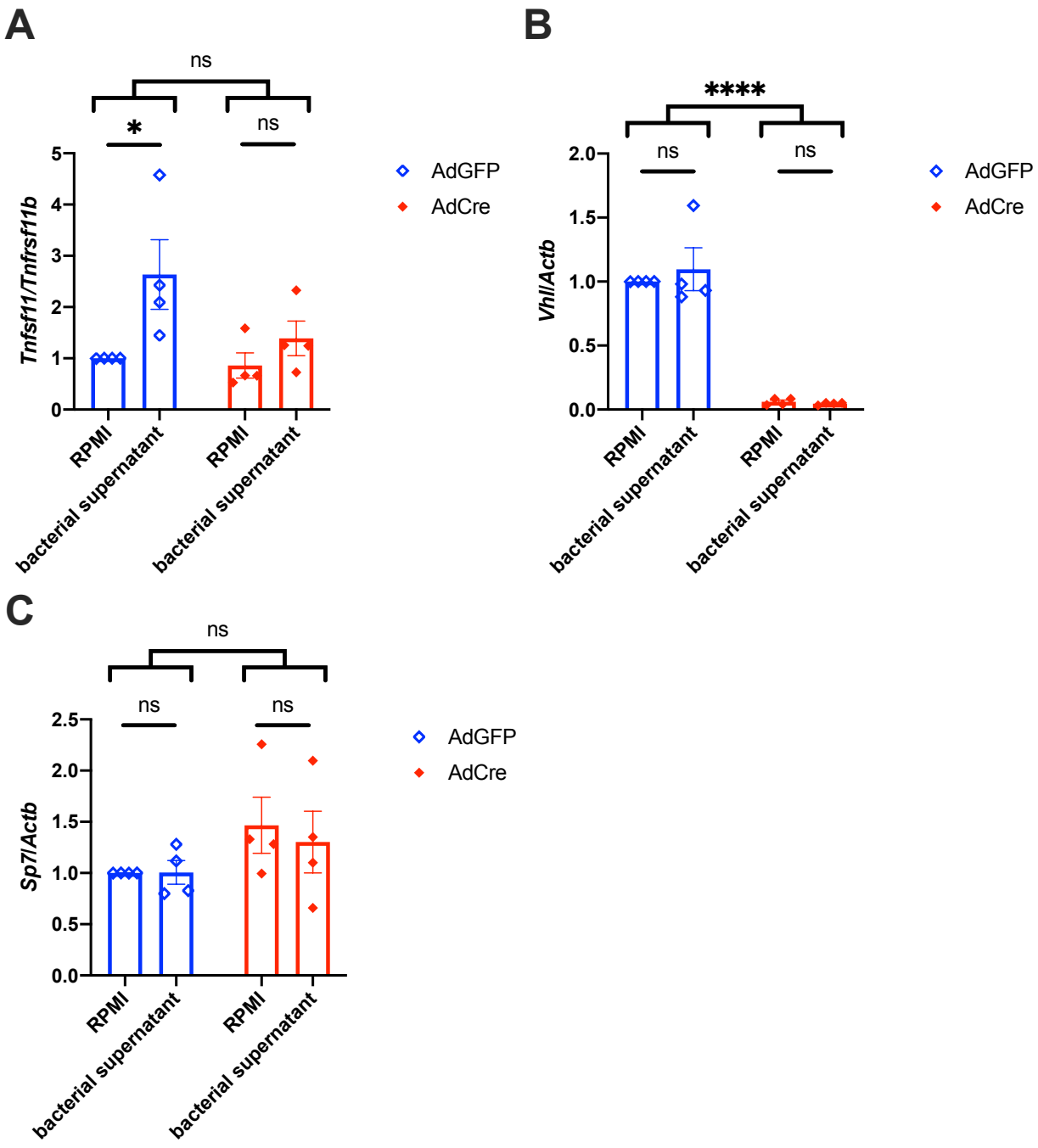

Figure 13: Deletion of *Vhl* in osteoblasts blunts the *S. aureus*-induced increase in transcription of *Tnfsf11* relative to *Tnfrsf11b*

(**A**) Fold change in *Tnfsf11* (RANKL) is shown relative to *Tnfrsf11* (OPG) using the $2^{-\Delta\Delta CT}$ method and normalized to the RPMI-AdGFP condition. RPMI is the vehicle control for toxin-

deficient (Δ*psm*/Δ*spa* USA300 *S. aureus*) bacterial supernatant. Fold changes in transcription of *Vhl* (**B**) and *Sp7* (Osx) (**C**) relative to the control gene *Actb* are shown as determined by the $2^{-\Delta\Delta CT}$ method and normalized to the RPMI-AdGFP condition. *$p < 0.05$, ****$p < 0.0001$, and ns denotes not significant ($p > 0.05$) as determined by two-way analysis of variance (ANOVA) of the log-transform of the fold changes in gene expression. Straight lines refer to comparison between RPMI and bacterial supernatant in each adenovirus-treated group; comparison between bracketed groups refers to two-way ANOVA comparison between AdGFP- and AdCre-treated cells. Error bars represent mean ± *SEM*. n=4 independent replicates, each with 3 technical replicates of cells. AdGFP=adenovirus containing GFP, and AdCre=adenovirus containing Cre recombinase and GFP.

Conditional knockout of *Vhl* or *Hif1a* in myeloid cells does not alter bacterial burdens during osteomyelitis

With an interest in better understanding the impact of HIF signaling in skeletal cells in response to *S. aureus* osteomyelitis, we next focused on the myeloid lineage which gives rise to bone-resorbing osteoclasts and important innate immune cells such as neutrophils and macrophages. To test the impact of myeloid cell HIF signaling on antibacterial responses and maintenance of bone architecture during *S. aureus* osteomyelitis, a second set of conditional knockout mice were generated. Using *LysMCre* and the corresponding floxed $Hif1a^{fl/fl}$ and $Vhl^{fl/fl}$ alleles, myeloid-lineage conditional knockouts of *Hif1a* ($Hif1a^{fl/fl}$, $LysMCre^{+/-}$) and *Vhl* ($Vhl^{fl/fl}$, $LysMCre^{+/-}$) were generated and subjected to *S. aureus* osteomyelitis. Unlike the *OsxCre* model, this *LysMCre* model does not use doxycycline as there is no inherent repressor or inducer. Therefore, the Cre recombinase is active throughout *in utero* and postnatal development.

First, bacterial burdens in both groups were assessed to understand the impact of myeloid HIF-1α and VHL on antibacterial responses. As observed with conditional knockout in the osteoblast lineage, bacterial burdens at post-infection day 14 did not differ between control mice versus those with conditional knockout of *Hif1a* or *Vhl* in the myeloid lineage (**Figure 14**). These data further support that myeloid-lineage conditional knockout of *Hif1a* or *Vhl* does not impact bacterial burdens at Day 14 post-infection.

Prior studies have shown that *Vhl* inactivation improves myeloid cell longevity and bacterial phagocytosis [152]. Therefore, we further explored bacterial burdens at earlier time points when phagocytes are interacting with *S. aureus* at the time of abscesses formation. Bacterial burdens at an early time point, Day 5 post-infection, were measured to determine if transient changes occurred early during infection. As at Day 14 post-infection, bacterial burdens

were not found to differ between *Vhl*$^{fl/fl}$, *LysMCre*$^{+/-}$ mice and those of their Cre-negative littermate controls at Day 5 post-infection (**Figure 15**). However, it should be noted that the mean difference in log(CFU/mL) of 0.4 yielded a *p*-value of 0.0512 with *n*=4-5, meaning that we may have been underpowered to detect a significant difference. In a second experiment, a reduced bacterial inoculum (10^5 CFU) was delivered with the hypothesis that a standard inoculum of 10^6 CFU may overwhelm antibacterial responses. In this second experiment, again bacterial burdens between *Vhl*$^{fl/fl}$, *LysMCre*$^{+/-}$ mice and Cre-negative littermate control mice did not differ, indicating that *Vhl* conditional knockout in the myeloid lineage does not significantly alter bacterial clearance during *S. aureus* osteomyelitis in this infection model (**Figure 16**). Overall, the studies suggest that no differences in bacterial burdens occur that substantially alter the clearance of *S. aureus* by post-infection Day 14.

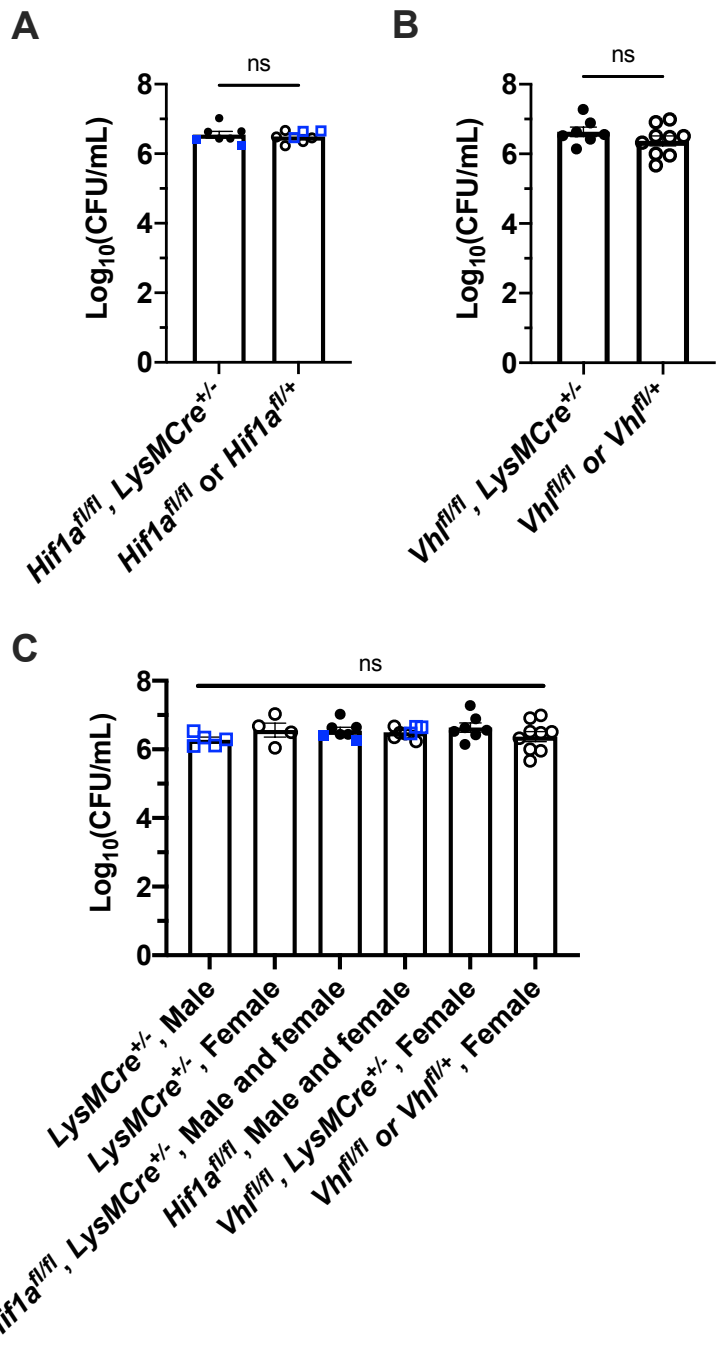

Figure 14: Myeloid-lineage conditional knockout of *Hif1a* or *Vhl* does not alter bacterial burdens at Day 14 post-infection

(**A**) Day 14 post-infection bacterial burdens from infected femurs of *Hif1a*$^{fl/fl}$, *LysMCre*$^{+/-}$ mice are shown with bacterial burdens from Cre-negative controls, which are comprised of both *Hif1a*$^{fl/f}$ and *Hif1a*$^{fl/+}$ littermates. Mice (*n*=7-8) are female except for those marked with blue

squares, which represent data from male mice. Error bars represent mean ± *SEM*, and ns denotes not significant ($p > 0.05$) as determined by unpaired, two-tailed Student's *t*-tests. (**B**) Day 14 post-infection bacterial burdens from infected femurs of female $Vhl^{fl/fl}$, $LysMCre^{+/-}$ mice are shown with those of female Cre-negative controls comprised of both $Vhl^{fl/f}$ and $Vhl^{fl/+}$ littermates (n=7-9). Error bars represent mean ± *SEM*, and ns denotes not significant ($p > 0.05$) as determined by unpaired, two-tailed Student's *t*-tests. (**C**) Day 14 post-infection bacterial burdens from infected femurs of male and female (as labeled) age-matched $LysMCre^{+/-}$ mice (n=4) that do not contain floxed alleles are shown along with the data displayed in (**A**) and (**B**) for comparison between all groups. Error bars represent mean ± *SEM*, and ns denotes not significant ($p > 0.05$) as determined by 1-way analysis of variance (ANOVA). CFU=colony forming units.

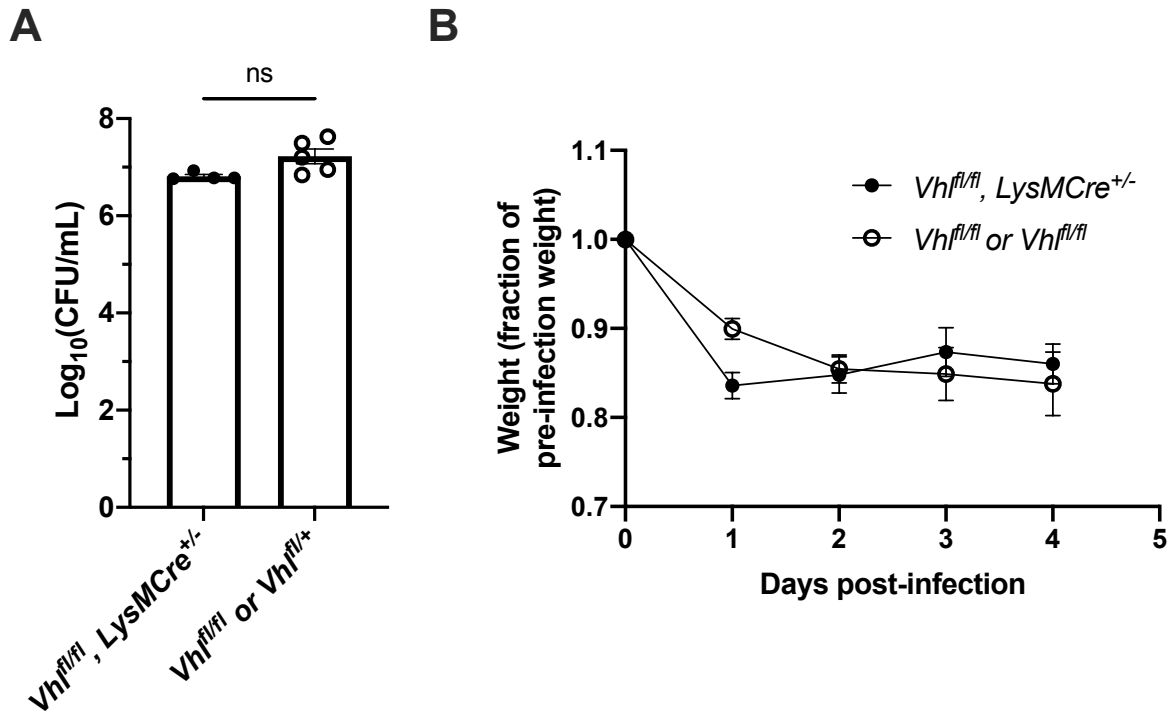

Figure 15: Myeloid-lineage conditional knockout of *Vhl* does not substantially alter bacterial burdens at Day 5 post-infection

(**A**) Bacterial burdens were determined in the infected femurs of $Vhl^{fl/fl}$, $LysMCre^{+/-}$ mice and Cre-negative littermate controls ($Vhl^{fl/fl}$ or $Vhl^{fl/+}$) at Day 5 post-infection (n=4-5). Error bars represent mean ± *SEM*, and ns denotes difference did not meet the $p<0.05$ standard for significance (p=0.0512) as determined by unpaired, two-tailed Welch's *t*-test. CFU=colony forming units. (**B**) The relative post-infection weights corresponding to the experiment shown in (**A**) are shown relative to the pre-infection starting weight. Relative post-infection weights do not differ between genotypes as compared by two-way analysis of variance (ANOVA). Error bars represent mean ± *SEM*.

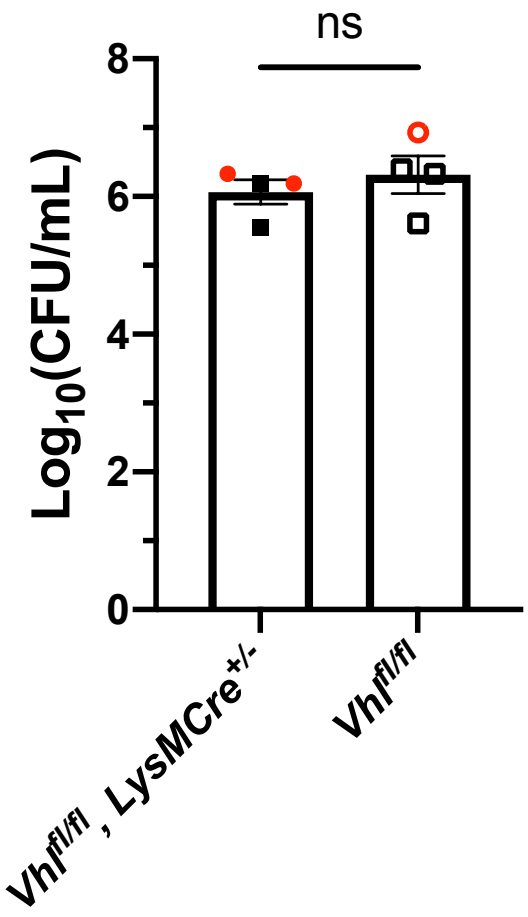

Figure 16: Bacterial burdens in femurs infected with a lower inoculum do not differ following conditional deletion of *Vhl* in the myeloid lineage

Bacterial burdens were determined in the infected femurs of $Vhl^{fl/fl}$, $LysMCre^{+/-}$ myeloid-lineage conditional knockout mice and Cre-negative littermate controls ($Vhl^{fl/fl}$) at Day 14 post-infection following infection with a lower initial inoculum of 10^5 CFU. Error bars represent mean ± *SEM*, and ns denotes difference did meet the $p < 0.05$ standard for significance (p=0.4663) as determined by unpaired, two-tailed Student's *t*-tests. CFU=colony forming units.

Conditional knockout of *Vhl* in myeloid cells enhances bone loss during *S. aureus* osteomyelitis

After confirming that bacterial burdens do not significantly differ during *S. aureus* osteomyelitis following genetic ablation of *Hif1a* or *Vhl* in the myeloid lineage, we next tested the impacts of such genetic knockouts on pathologic changes to bone architecture. Active HIF signaling in myeloid-lineage cells increases proinflammatory cytokines that are known to alter osteoclastogenic bone resorption [60,120]. Thus, we investigated the impact of myeloid-lineage conditional knockouts of *Hif1a* or *Vhl* on pathologic changes to bone architecture using microCT following 14 days of infection. Initial studies have been conducted in male mice. In $Vhl^{fl/fl}$, $LysMCre^{+/-}$ mice, the average BV/TV in the trabecular bone was decreased compared to the trabecular BV/TV in Cre-negative littermate control mice as assessed by two-way ANOVA comparing the two genotypes at post-infection Day 14 (**Figure 17A**). As published previously in wildtype mice [121], the trabecular BV/TV in infected femurs was significantly lower than that in contralateral limbs. By two-way ANOVA with multiple comparisons, we observed this difference between the infected and contralateral limbs was present in both $Vhl^{fl/fl}$, $LysMCre^{+/-}$ and Cre-negative littermate control mice. There was no evidence of an interaction between the genotype and the laterality of the limb by two-way ANOVA (**Figure 17A**). In $Hif1a^{fl/fl}$, $LysMCre^{+/-}$ mice, BV/TV in trabecular bone did not differ between the $Hif1a^{fl/fl}$, $LysMCre^{+/-}$ mice and the Cre-negative littermate controls by genotype but again showed significant declines in BV/TV in the infected femurs of both genotypes (**Figure 17B**). For $Hif1a^{fl/fl}$, $LysMCre^{+/-}$ mice, female mice have also been assessed and showed similar results to males (**Figure 18**). Therefore, we can conclude that conditional knockout of *Hif1a* does not impact trabecular bone changes. On

the contrary, *Vhl*$^{fl/fl}$, *LysMCre*$^{+/-}$ mice have lower trabecular BV/TV compared to that of Cre-negative littermate controls following *S. aureus* osteomyelitis.

The differences in trabecular BV/TV between *Vhl*$^{fl/fl}$, *LysMCre*$^{+/-}$ mice and Cre-negative littermate control mice at post-infection Day 14 are unlikely caused by baseline differences as mice subjected to mock infection showed no differences between genotypes as post-injury Day 14. To better understand why differences in trabecular BV/TV exist between *Vhl*$^{fl/fl}$, *LysMCre*$^{+/-}$ mice and Cre-negative littermate control mice following infection, animals were injured in a mock infection model for 14 days and analyzed for changes in BV/TV as done in infected animals. In the mock-infected (injured) mice, the differences in BV/TV between genotypes were not present (p=0.8725) (**Figure 19**). Thus, differences between the genotypes are dependent upon the inoculation of *S. aureus* at time of injury. The injury itself in mock-infected animals caused a significant difference in trabecular BV/TV compared to the contralateral limbs as assessed by two-way ANOVA (p=0.0309); however, no difference was observed within individual genotypes upon multiple comparisons, suggesting that injury itself causes a mild decrease in trabecular BV/TV (**Figure 19**). Though studies were not powered to directly compare *S. aureus*-infected and mock-infected trabecular BV/TV directly, the BV/TV in contralateral femurs of infected mice were lower than BV/TV in contralateral femurs in mock-infected femurs for *Vhl*$^{fl/fl}$, *LysMCre*$^{+/-}$ mice and their Cre-negative littermate control mice as well as *Vhl*$^{fl/fl}$, *OsxCre*+ mice and their Cre-negative littermate control mice.

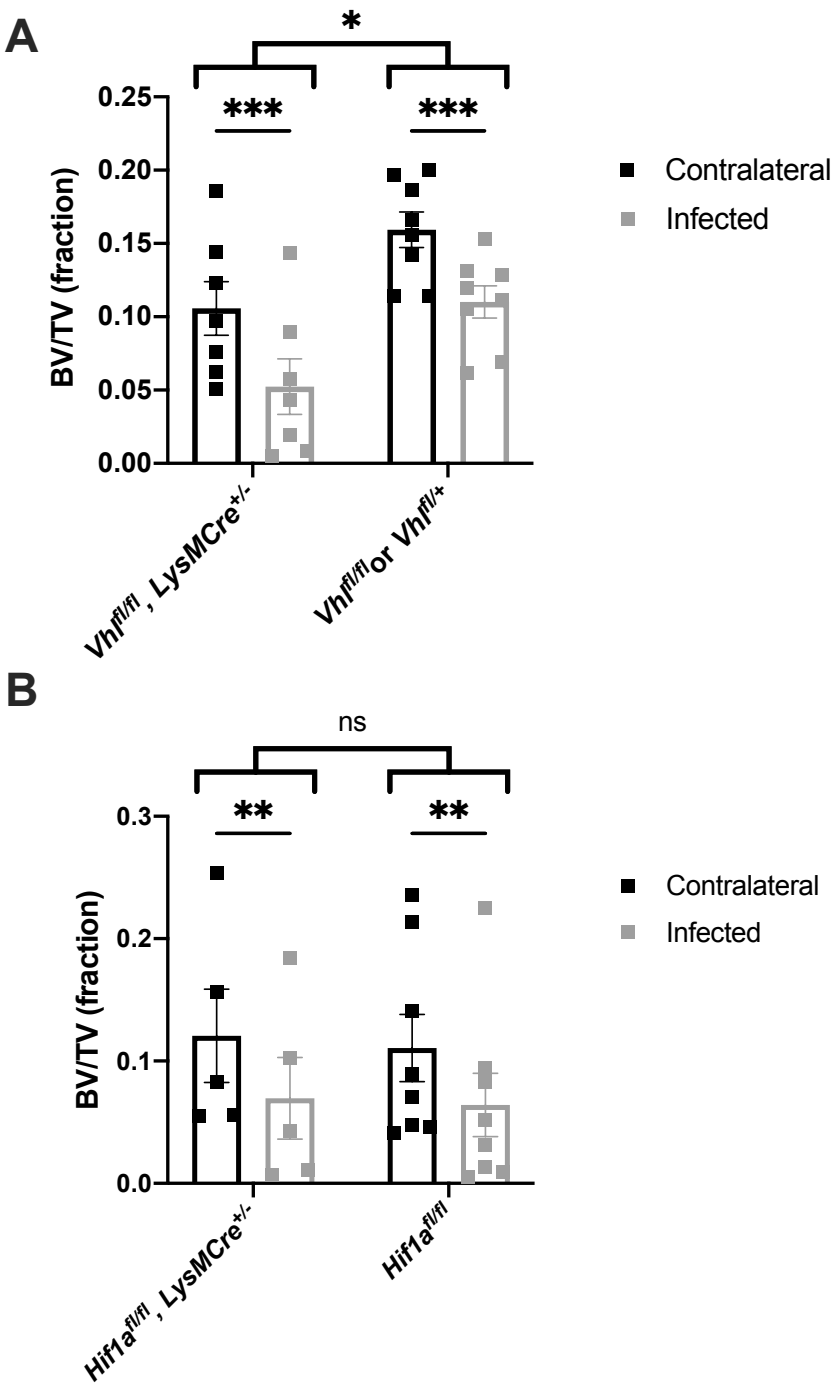

Figure 17: Conditional knockout of *Vhl* in myeloid cells decreases trabecular bone volume during *S. aureus* osteomyeltis

(**A**) Trabecular bone volume-per-total volume (BV/TV) in $Vhl^{fl/fl}$, $LysMCre^{+/-}$ mice and Cre-negative littermate $Vhl^{fl/fl}$ or $Vhl^{fl/+}$ control mice (n=7-8, male) at post-infection Day 14 was

measured in the distal metaphysis of infected and contralateral femurs. The differences between the groups were compared by two-way analysis of variance (ANOVA), which revealed that the genotypes (two bracketed groups) significantly differ with p=0.0169 (denoted as *, $p < 0.05$). ***$p < 0.001$, as determined by two-way ANOVA with multiple comparisons of the infected and contralateral limbs for each genotype individually. (**B**) Trabecular BV/TV in *Hif1a*$^{fl/fl}$, *LysMCre*$^{+/-}$ mice and littermate *Hif1a*$^{fl/fl}$ control mice (n=5-8, male) at post-infection Day 14 was measured in the distal metaphysis of infected and contralateral femurs. The genotypes (two bracketed groups) did not significantly differ (ns, p=0.8607) as compared by two-way analysis of variance (ANOVA). **$p < 0.01$, as determined by two-way ANOVA with multiple comparisons of the infected and contralateral limbs for each genotype individually. Error bars represent mean ± *SEM*.

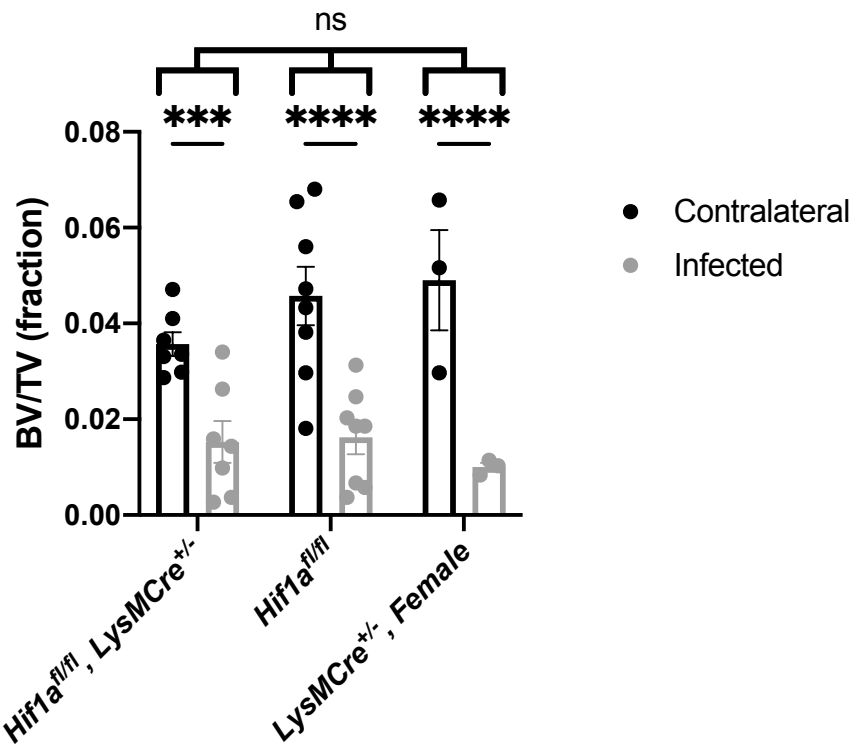

Figure 18: Trabecular bone changes in female *Hif1a*$^{fl/fl}$, *LysMCre*$^{+/-}$ mice do not differ from that of Cre-negative littermate controls

The bone volume-per-total volume (BV/TV) in *Hif1a*$^{fl/fl}$, *LysMCre*$^{+/-}$ and littermate *Hif1a*$^{fl/fl}$ control mice (n=3-8, female) at post-infection Day 14 was measured in the trabecular bone of the distal metaphysis of infected and contralateral femurs. Infection significantly reduced BV/TV compared to contralateral femurs in all genotypes ($p < 0.0001$), and genotypes (3 bracketed groups) did not significantly differ from one another (p=0.6229) as compared by two-way analysis of variance (ANOVA) with multiple comparisons. ***$p < 0.001$, ****$p < 0.0001$, and ns denotes not significant ($p > 0.05$) as determined by two-way ANOVA with multiple comparisons. Error bars represent mean ± *SEM*.

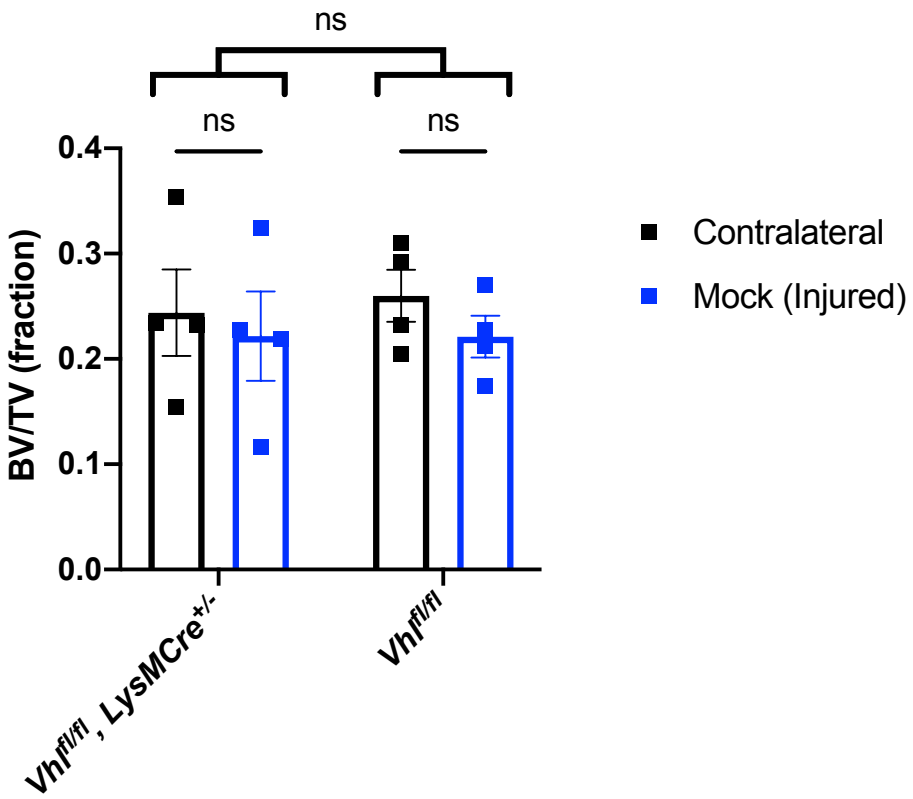

Figure 19: Mock infection in myeloid-lineage *Vhl* conditional knockout mice does not cause genotype-specific differences in trabecular bone

The bone volume-per-total volume (BV/TV) in $Vhl^{fl/fl}$, $LysMCre^{+/-}$ mice and littermate $Vhl^{fl/fl}$ control mice (n=4, male) at post-injury Day 14 was measured in the trabecular bone of the distal metaphysis of injured and contralateral femurs. Injury significantly reduced BV/TV compared to contralateral femurs ($p < 0.0309$, not depicted), but injury did not significantly reduce trabecular BV/TV within individual genotypes as compared by two-way analysis of variance (ANOVA) with multiple comparisons. The genotypes (bracketed groups) did not significantly differ (p=0.8725) as compared by two-way ANOVA. ns denotes difference did not meet the $p < 0.05$ standard for significance as determined by two-way ANOVA with multiple comparisons. Error bars represent mean ± *SEM*.

In addition to analyzing infection-mediated bone loss in trabecular bone, cortical bone loss was also analyzed in mice with conditional deletion of *Hif1a* and *Vhl* in the myeloid lineage. Similar to data obtained in the trabecular bone, the average volume of cortical bone loss was lower in $Vhl^{fl/fl}$, $LysMCre^{+/-}$ mice compared to cortical bone loss in Cre-negative littermate controls; however, this difference was not significantly different (**Figure 20A**). Notably, the mean difference in cortical bone loss of 0.3 mm^3 (25% higher in $Vhl^{fl/fl}$, $LysMCre^{+/-}$ mice) yielded a *p*-value of 0.1085 with *n*=5-8, meaning that we may have been underpowered to detect a significant difference. Consistent with other outcomes analyzed with conditional knockout of *Hif1a*, conditional knockout in the myeloid lineage does not alter cortical bone loss during *S. aureus* osteomyelitis (**Figure 20B**). Thus, *Hif1a* conditional knockout in the myeloid lineage does not impact bacterial burdens or pathologic changes in bone architecture; however, trabecular BV/TV in $Vhl^{fl/fl}$, $LysMCre^{+/-}$ mice is significantly lower at post-infection Day 14 compared to trabecular bone of Cre-negative littermate control mice.

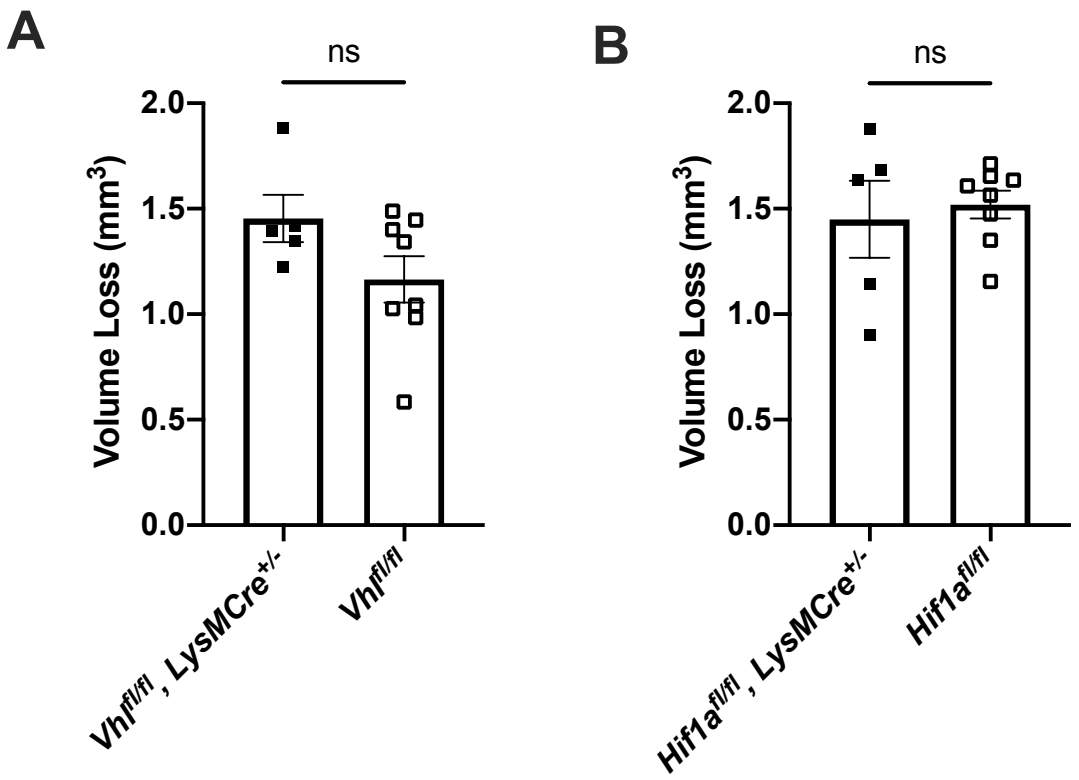

Figure 20: Conditional knockout of *Vhl* or *Hif1a* in the myeloid lineage does not significantly impact cortical bone loss during osteomyelitis

(**A**) The volume of cortical bone loss in male $Vhl^{fl/fl}$, $LysMCre^{+/-}$ mice and littermate controls at post-infection Day 14 was assessed by microcomputed tomography (n=5-8). The difference in cortical bone loss was compared by unpaired, two-tailed Student's t-test and did not meet the $p<0.05$ standard for significance (ns) with p=0.1085. Error bars represent mean ± *SEM*. (**B**) The volume of cortical bone loss in male $Hif1a^{fl/fl}$, $LysMCre^{+/-}$ mice and littermate controls at post-infection Day 14 was assessed by microcomputed tomography (n=5-8). The difference in cortical bone loss was compared by unpaired, two-tailed Student's t-test and did not meet the $p<0.05$ standard for significance (ns) with p=0.6775. Error bars represent mean ± *SEM*.

Discussion

Osteomyelitis is a complex disease that involves many different cell signaling pathways to regulate bone architecture and immune responses. HIF signaling is critical during bone development and augmentation of HIF signaling is known to improve bone regeneration following injury [59,88]. Furthermore, HIF signaling is intricately linked to innate immune responses and has been proposed as a therapeutic target during infection [60]. While studied in the context of other infection models [155], the role of HIF signaling during osteomyelitis is unknown despite the interest in HIF signaling modulation in both bone repair and infection treatment, independently. Two different Cre recombinase mouse strains, *OsxCre* and *LysMCre*, were used to target osteoblast- and myeloid-lineage cells, respectively, to determine the cell-specific contributions of HIF signaling during osteomyelitis [57,238,241]. Paired in combination with both Cre models, $Hif1a^{fl/fl}$ and $Vhl^{fl/fl}$ alleles were crossed to generate mice with conditional knockout of *Hif1a* or *Vhl* in either the osteoblast or myeloid lineages. These two Cre models target the lineages that give rise to the canonical cell types present in bone: osteoblasts/osteocytes (osteoblast lineage) and osteoclasts (myeloid lineage). In addition to targeting osteoclasts, *LysMCre* targets innate immune cells such as granulocytes and macrophages, cells in which HIF signaling has been shown to be essential for inflammatory responses [141].

Conditional knockout of *Hif1a* in both the osteoblast and myeloid lineages did not appear to impact bacterial burdens or infection-associated changes in bone architecture, suggesting that *Hif1a* does not contribute to pathogenesis during *S. aureus* osteomyelitis. It is possible that HIF-1α may play an important role in bacterial clearance in other models of osteomyelitis or that differences may exist at time points not investigated in this study. However, it has also been

suggested that, despite distinct gene targets between HIF-1α and HIF-2α, the overlap of large sets of genes may allow HIF-2α to compensate for much of HIF-1α influences [59,71]. To confirm such a theory, it will be important to test a double knockout of *Hif1a* and *Epas1* or a knockout of the joint heterodimer *Arnt* to better understand the impact of loss of HIF signaling during osteomyelitis and not just HIF-1α. Direct measurement of HIF-2α by immunohistochemistry in mice lacking *Hif1a* may provide insight into such compensation, as well.

MicroCT analysis of trabecular and cortical bone revealed no differences in bone changes during *S. aureus* infection following conditional knockout of *Hif1a* in both cell lineages tested. Prior bone phenotypes following osteoblast-lineage knockout of *Hif1a* have frequently revealed relatively subtle phenotypes, which may not have been readily detected in these studies given the potentially overwhelming influence of infection in our model. The role of HIF target, VEGF, is dependent upon skeletal injury model [97]. Similarly, it is possible that alternative infection models that employ a prosthetic and/or transcortical fracture of the femur may reveal differences not observed following a pinhole defect, in which only a small hole is drilled through the cortical bone. However, given the data regarding bacterial burdens and microCT findings, no evidence from these data exists to indicate that HIF-1α is essential during *S. aureus* osteomyelitis.

Conditional knockout of *Vhl* in osteoblast versus myeloid lineages cause different phenotypes in the trabecular bone following infection. Conditional knockout of *Vhl* in the osteoblast lineage caused a profound increase in trabecular BV/TV as observed previously [59,243]. Unlike Cre-negative control mice, $Vhl^{fl/fl}$, *OsxCre+* mice did not demonstrate a decline in BV/TV in infected bone suggesting that deletion of *Vhl* in osteoblast-lineage cells alters bone formation or bone destruction during infection. Investigation of osteoclasts *in vivo* showed that,

compared to trabecular bone of age-matched control mice, surface-normalized osteoclast numbers and resorbing surface did not increase in the infected femur of *Vhl*$^{fl/fl}$, *OsxCre*+ mice following infection. Testing osteoclast abundance in littermate control mice will be an important next step to confirm this phenotype. It will be important to perform studies to understand how *Vhl* deletion in osteoblast-lineage cells alters *S. aureus*-induced osteoclast formation. *In vitro* data indicate that deletion of *Vhl* in osteoblasts decreases transcription of the gene for RANKL relative to that for OPG, indicating that *Vhl* deletion in osteoblasts may regulate osteoclast formation through impacts on the RANKL-to-OPG ratio. Such an impact may explain observed differences in osteoclast abundance *in vivo*. Functional *in vitro* studies that test osteoclast formation in co-culture with osteoblasts lacking *Vhl* will help to establish if *Vhl* deletion in osteoblasts impacts osteoclastogenesis. Direct measurements of RANKL and OPG from *in vivo* bone samples may further validate if such a mechanism occurs *in vivo* during infection. While alternative mechanisms may also impact osteoclast formation *in vivo*, these data suggest *Vhl* deletion in osteoblasts limits infection-mediated RANKL production and downstream loss of trabecular bone. It will be important to directly test this hypothesis in future studies. The mechanism by which *Vhl* deletion alters the RANKL-to-OPG ratio is unknown. Prior studies investigating HIF-1α have not directly linked HIF signaling to RANKL production [96]. Investigation of HIF-2α in osteoblasts-lineage cells has suggested that HIF-2α activation increases RANKL production and osteoclast formation [98]. However, this phenotype was not observed in another study, which instead found that HIF-2α increases OPG production and limits osteoclast formation [96]. The findings of our study are consistent with a prior investigation which found that *Vhl* knockout inhibited osteoclast formation in co-culture and decreased RANKL gene expression [247]. Conditional deletion of *Vhl* in osteoblasts has also been shown

to inhibit osteoclasts through increased OPG and through a microRNA-IL-33-Notch1 signaling axis, which may be an alternative mechanism [248]. Beyond HIF signaling, VHL interacts with several other proteins that may impact the response of osteoblasts to *S. aureus* stimulation independent of HIF signaling [249]. To better understand if HIF signaling mediates the observations in $Vhl^{fl/fl}$, *OsxCre+* double knockout mice lacking *Vhl* along with *Hif1a*, *Epas1*, or *Arnt* could be tested.

While $Vhl^{fl/fl}$, *OsxCre+* mice display protection from declines of trabecular BV/TV during osteomyelitis, $Vhl^{fl/fl}$, $LysMCre^{+/-}$ mice exhibit BV/TV values lower than that of Cre-negative control mice, indicative of increased bone loss. Interestingly, the contralateral femurs show a similar decline in trabecular BV/TV relative to that of littermate control mice, indicating that the increase in trabecular bone loss may be global in the mouse during infection. Multiple studies have shown that increased cytokines, such as osteoclastogenic TNF-α and IL-1β, and increased hematopoiesis (which both occur during osteomyelitis) are associated with increased trabecular bone loss [121,250–252]. Given that prior studies associate increased HIF signaling in myeloid lineage cells with increased pro-inflammatory cytokine production [60], it is possible that more robust cytokine responses at early time points or throughout the infection course could enhance trabecular bone loss. It will be important to perform cytokine analyses and bone histomorphometry on *S. aureus*-infected and mock-infected femurs from $Vhl^{fl/fl}$, $LysMCre^{+/-}$ mice and their genotype controls to determine if cytokines contribute to bone loss and if osteoclast formation is associated with increased bone loss, respectively.

While these data lay the framework for understanding the impact of HIF signaling on antibacterial responses and bone remodeling during *S. aureus* osteomyelitis, multiple questions remain unanswered that must be investigated through future studies. $Vhl^{fl/fl}$, $LysMCre^{+/-}$ mice

may exhibit enhanced bacterial clearance at early time points and increased cortical bone loss during infection, but the current data sets are underpowered and must be tested further. Based on this initial study, a sample size of n=7 is required to test for differences in bacterial burdens in $Vhl^{fl/fl}$, $LysMCre^{+/-}$ mice at Day 5 post-infection for adequate power (β=0.8) with a type I error of 0.05 (α=0.05), and a sample size of n=16 is required to test for differences in cortical bone destruction in $Vhl^{fl/fl}$, $LysMCre^{+/-}$ mice at Day 14 post-infection for β=0.8 and α=0.05. It may be advantageous to test early time points in mice infected with a lower inoculum (10^5 CFU), as well.

Though not tested statistically, the average trabecular BV/TV in the contralateral femurs of mock-infected animals was higher than the BV/TV in contralateral femurs of *S. aureus*-infected femurs for all genotypes tested ($Vhl^{fl/fl}$, $LysMCre^{+/-}$ mice and their Cre-negative littermate controls as well as $Vhl^{fl/fl}$, *OsxCre*+ mice and their Cre-negative littermate controls). These experiments were not designed to make such comparisons statistically. However, the consistency of these data suggests that a systemic response to infection such as granulopoiesis or increased circulation of inflammatory cytokines alters trabecular bone architecture. Supporting the hypothesis that systemic inflammatory responses during *S. aureus* osteomyelitis cause trabecular bone loss, multiple diseases that trigger systemic inflammation have been associated with bone loss [253–255]. Future studies should directly test if trabecular bone loss occurs in non-infected bones of mice infected with *S. aureus* (or other pathogens) in the bone or non-osseous sites.

Genetic studies were conducted with an interest in understanding the basic biology and potential for therapeutic intervention. Thus, future studies should investigate pharmacologic targeting of the HIF signaling pathway. Pharmacologic studies would allow investigation of cell

agnostic manipulation of HIF signaling to understand overall cell signaling influences. Furthermore, baseline differences in *Vhl*$^{fl/fl}$, *OsxCre*+ mice may substantially impact trabecular bone biology outside of cell signaling itself. Pharmacologic intervention would permit investigation of augmented HIF signaling without extreme differences in bone architecture prior to infection. The potential to target VHL [256] or HIF PHDs [257] will also improve understanding of HIF-independent VHL functions versus HIF-dependent functions of VHL. Pharmacologic targeting of HIF during osteomyelitis could also offer attractive therapeutic solutions such as dual-purpose copper (II) treatment which inhibits HIF PHDs and is inherently antibacterial [106,109].

There are multiple limitations to the studies performed. While most experiments were performed in male and female mice, not all studies were powered to necessarily draw sex-specific conclusions, though generally the data do not support a dramatic difference between the sexes. Expanding the number of animals to confirm whether sex-specific phenotypes exist may be important. Not all studies have included age-matched, Cre-positive controls, which may more appropriately control for Cre-mediated effects independent of deletion of floxed alleles. These studies explored a single model of osteomyelitis, and alternative models may reveal different findings. Additionally, only discrete time points were selected up to 14 days and transient phenotypes may have been missed as well as phenotypes dependent upon chronic infection exceeding the 14-day experiment. The mechanisms by which *Vhl* deletion in osteoblast and myeloid cells alters trabecular bone loss has not been established. Despite using *Vhl* deletion with the aim to model augmented HIF signaling, HIF-independent mechanisms remain possible and have not been explored. Despite these limitations, these studies demonstrate that skeletal cell *Hif1a* does not contribute to control of bacterial burdens and pathologic changes in bone

architecture during osteomyelitis. Furthermore, *Vhl* has been shown to impact trabecular BV/TV in response to infection in distinct ways in a cell-type specific manner. These studies support further investigation of HIF signaling during osteomyelitis as a means to regulate skeletal architecture.

A portion of the following section (*CHAPTER IV:*

DIFLUNISAL-LOADED PPS NANOPARTICLES DECREASE BONE DESTRUCTION DURING *S. AUREUS* OSTEOMYELITIS) was originally published in the *Journal of Orthopaedic Research.* (January 2021).

Ford, CA, Spoonmore, TJ, Gupta, MK, Duvall, CL, Guelcher, SA, Cassat, JE. 2021. Diflunisal-loaded poly(propylene sulfide) nanoparticles decrease *S. aureus*-mediated bone destruction during osteomyelitis. *J Orthop Res*. 39(2):426-437.

doi.org/10.1002/jor.24948

CHAPTER IV: DIFLUNISAL-LOADED POLY(PROPYLENE SULFIDE) (PPS) NANOPARTICLES DECREASE BONE DESTRUCTION DURING *S. AUREUS* OSTEOMYELITIS

Introduction

Osteomyelitis, or inflammation of bone, is commonly caused by bacterial infection. This disease afflicts an estimated 1 in 4000 people annually and is projected to impact up to 30% of orthopedic procedures [3,258]. Due in part to the widespread emergence of antimicrobial resistance, treatment of osteomyelitis can be extremely difficult [164,259]. Efforts to cure osteomyelitis often involve invasive debridement procedures and long-term antibiotic therapy that together result in substantial strain on the patient and healthcare system [2,162,258,260]. *Staphylococcus aureus*, a Gram-positive bacterium, is the most common etiologic agent of osteomyelitis [3]. *S. aureus* possesses an arsenal of virulence factors that lyse host cells, including skeletal cells, thereby contributing to osteomyelitis-induced bone loss [122]. Thus, effective therapies are necessary to ameliorate concomitant morbidities, such as bone loss, that may increase the risk of fracture or treatment failure.

Antivirulence therapies inhibit bacterial virulence pathways without directly impacting bacterial viability and are actively being investigated as adjunctive treatment strategies for infection [164]. We have recently demonstrated the antivirulence potential of diflunisal, a nonsteroidal anti-inflammatory drug, to decrease *S. aureus*-induced bone destruction in a murine osteomyelitis model [123]. Diflunisal inhibits the quorum-sensing *agr* pathway of *S. aureus*, limiting production of numerous virulence factors, including cytolytic toxins [191]. In previous studies, local delivery of diflunisal from resorbable poly(ester urethane) foams significantly reduced bone resorption [123,201]. While local delivery presents the advantage of achieving high drug concentrations near target sites, the avascular delivery depot can function as a nidus

for bacterial colonization [201,261,262]. Thus, effective delivery of diflunisal and other antivirulence compounds requires an alternative method to avoid exacerbation of infection.

While parenteral therapy potentially circumvents the challenges of local delivery devices, diflunisal is hydrophobic and therefore has low aqueous solubility. Encapsulation of compounds within nanoparticles has enabled effective systemic delivery of hydrophobic drugs and demonstrated distribution to target sites [212,226,263–265]. Our group has previously shown that poly(propylene sulfide) (PPS) nanoparticles provide a reactive oxygen species (ROS)-responsive carrier for delivery of the Gli2 inhibitor, GANT58, to sites of bone cancer metastases [226]. The PPS nanoparticles distributed preferentially to tumor-bearing limbs compared to contralateral limbs, presumably due to increased vascular permeability at tumor sites that allows for nanoparticle extravasation and decreased lymphatic drainage. These phenomena allow for nanoparticle retention and are known as the enhanced permeability and retention (EPR) effect [215]. Furthermore, PPS-based biomaterials break down in the presence of high levels of ROS, providing a potential mechanism for targeted drug release at inflamed sites [221–223]. However, few studies have investigated systemically (e.g., intravenously) delivered nanoparticles in the context of osteomyelitis [205–208].

The objectives of this study were to understand the biodistribution of PPS nanoparticles during osteomyelitis and evaluate the efficacy of diflunisal-loaded nanoparticles in limiting *S. aureus*-induced bone loss. We hypothesized that PPS nanoparticles would accumulate at infectious foci during osteomyelitis and that diflunisal-loaded PPS nanoparticles would limit *S. aureus*-mediated cortical bone destruction. To test these hypotheses, we evaluated PPS nanoparticle delivery in a murine model of osteomyelitis and investigated the efficacy of diflunisal-loaded PPS nanoparticles both *in vitro* and *in vivo*.

Materials and methods

Cell lines, bacterial strains, and reagents

The murine preosteoblast MC3T3-E1 subclone 4 cell line was obtained from the American Type Culture Collection. The cells were propagated in a humidified 37°C incubator with 5% CO_2 and maintained in α-MEM (Gibco #A1049001; Thermo Fisher Scientific) supplemented with 10% fetal bovine serum (Bio-Techne) and 1X penicillin–streptomycin (Thermo Fisher Scientific). An erythromycin-sensitive derivative of the methicillin-resistant *S. aureus* (MRSA) USA300-lineage strain LAC (AH1263) was used for all experiments, as it represents the most commonly isolated clonal complex causing musculoskeletal infection in the United States [235,266]. For bacterial growth, unless otherwise noted, 5-mL cultures were grown in tryptic soy broth at 37°C, shaking at 180 rpm. Diflunisal, dimethylformamide (DMF), dioxane, *N*,*N*-dimethylacrylamide (DMA), propylene sulfide, dimethyl sulfoxide (DMSO), 2,2'-azobis(isobutyronitrile) (AIBN), Nile red, and hydrogen peroxide (H_2O_2) were purchased from MilliporeSigma. Cy7-amine was purchased from Lumiprobe. DMA was purified by distillation under reduced pressure before polymerization. PPS (10 kDa), poly(propylene sulfide)-4-cyano-4-(ethylsulfanylthiocarbonyl)sulfanylpentanoic acid (PPS_{135}-ECT), and poly(benzoyloxypropyl methacrylamide) (pHPMA-Bz) were synthesized as described previously [227].

Synthesis and characterization of the polymer

The diblock copolymer consists of PPS (135 repeat units) and DMA (149 repeat units). All copolymer solutions were synthesized with 1 repeat unit of pentafluorophenyl acrylate (PFPA) for which Cy7-amine was substituted to provide a fluorescent marker for in vivo tracking. Synthesis of PPS_{135}-*b*-p($Cy7_1$-*ran*-DMA_{149}) was conducted as previously published[18] with modifications as follows. Reversible addition–fragmentation chain-transfer

(RAFT) polymerization of the second block (i.e., the DMA block with single repeat unit of PFPA) of PPS_{135}-*b*-p($PFPA_1$-*ran*-DMA_{149}) was performed with a 5-to-1 molar ratio of PPS_{135}-ECT (macro chain transfer agent, macroCTA) to initiator (AIBN). The polymerization was conducted in a 10-mL, round-bottom reaction vessel containing 0.02687 mmol (268.7 mg) macroCTA, 4.02 mmol (415 μL) DMA, 0.0067 mmol (1.1 μL) PFPA, 0.0054 mmol (88.3 μL of 10-mg/mL AIBN dioxane) AIBN, and 4 mL of 1:1::DMF:dioxane solvent. The reaction vessel was purged with nitrogen, and the resulting solution was stirred at 65°C for 24 h, after which time the reaction was quenched at −80°C. To graft Cy7-amine, 0.5 mL of thawed polymer solution was removed and replaced with 0.5 mL of DMSO containing 0.00672 mmol (4.8 mg) of Cy7-amine for 24 h, stirring at room temperature. The resulting solution was dialyzed against methanol and deionized water for 24 h each before lyophilization. A ^{1}H NMR spectrum of polymer was collected in $CDCl_3$ with a Brüker 400 MHz spectrometer as before [224].

Fabrication and characterization of nanoparticles

Following synthesis of the polymer, micellar nanoparticles were fabricated using an oil-in-water emulsion technique. Nanoparticles were fabricated using two techniques: bulk solvent evaporation for small batches to optimize drug loading parameters and a microfluidics approach to scale up nanoparticle production for animal experiments. For diflunisal loading experiments, batches of nanoparticle solutions were fabricated using a bulk solvent evaporation procedure performed previously [226]. Briefly, PPS_{135}-*b*-p($Cy7_1$-*ran*-DMA_{149}) (10.0 mg) was co-dissolved with diflunisal (1.0 mg) in chloroform (0.1 mL) and added dropwise to a vial containing vigorously stirring phosphate-buffered saline (PBS). In addition, pHPMA-Bz was added to a subset of batches at a ratio of 1:1 pHPMA-Bz:diflunisal by mass to determine the influence of facilitated π–π stacking on diflunisal encapsulation as shown before [267]. The chloroform-PBS

biphasic solution was left stirring overnight to allow chloroform evaporation and micelle formation. The resulting micelle solution was passed through a 0.45-μm syringe filter. Diflunisal loading was quantified by the aqueous concentration calculated from the measurement of diflunisal fluorescence (Ex. 310 nm, Em. 420 nm) with reference to a standard curve using a microplate reader (Tecan Infinite 500; Tecan Group Ltd.). To characterize ROS-mediated release of loaded agents, Nile red release from nanoparticles was measured as previously reported at the stated H_2O_2 concentrations [222,225,226].

After determining optimal parameters for drug loading, nanoparticles were fabricated in large batches by microfluidics processes as described previously for animal studies [268]. Briefly, PPS_{135}-*b*-p($Cy7_1$-*ran*-DMA_{149}) (60.0 mg) was co-dissolved with pHPMA-Bz (6.0 mg) and/or diflunisal (6.0 mg) in methanol (0.6 mL) and mixed with sterile PBS using a benchtop NanoAssemblr (Precision Nanosystems, Inc.). All formulations were prepared with a 10:1::aqueous:organic flow rate ratio and 4 mL/min total flow rate. Methanol was removed using a rotovap heated to 40°C for 30 min. Resulting solutions were passed through 0.45-μm syringe filters. All nanoparticles contained Cy7-grafted polymer for imaging purposes. Dif-NPs refers to nanoparticles loaded with diflunisal and pHPMA-Bz. Blank-NPs refers to blank nanoparticles containing pHPMA-Bz only and serves as the vehicle control for Dif-NPs. Empty-NPs refers to empty nanoparticles and are used to visualize biodistribution of the nanoparticle. Dynamic light scattering (DLS) was used to measure the hydrodynamic diameter of synthesized nanoparticles in PBS using a Malvern Zetasizer Nano-ZS (Malvern Instruments Ltd.) equipped with a 4 mW He–Ne laser operating at $\lambda = 632.8$ nm.

Biodistribution of PPS nanoparticles

Empty-NPs were delivered to 7–8-week-old female FVB/NJ mice ($n = 4$ mice) by tail vein injection. Mice were imaged at 1 h (under 1%–5% isoflurane anesthesia) and 24 h (immediately post-euthanasia) following nanoparticle-injection using an IVIS Spectrum imaging system (PerkinElmer). Cy7 detection (Excitation: 675 nm, Emission: 780 nm) was used to characterize nanoparticle distribution in whole-body images with a 5-s fluorescent exposure on high intensity and small binning with an f/stop value of 8. Images were analyzed using ROI analysis with Living Image Software.

Synthesis, fabrication, and biodistribution of alendronate-tagged nanoparticles

Synthesis and fabrication of empty alendronate-containing PPS nanoparticles (Empty-AlnNPs) was performed as for Empty-NPs, except as follows. At time of synthesis of the second block (predominantly DMA), the monomer input feed was altered such that DMA was reduced and replaced by additional PFPA. As a result, PFPA consisted of 10% of the monomer feed and DMA consisted of 90% of the polymer feed. As performed with non-alendronate-containing polymer (polymer for Empty-NPs, Blank-NPs, and Dif-NPs), Cy7 amine was incubated to graft approximately 1 repeat unit to the polymer backbone as described above. Following Cy7 grafting, alendronate (Aln) was grafted to replace the remaining PFPA as described by the Cy7 grafting process above. Aln was chosen because it is a bisphosphonate with calcium binding potential that has been used previously to enhance delivery to bone and because it has a primary amine that permits grafting to PFPA repeat units of the polymer. The polymer product (PPS_{135}-*b*-p($Cy7_1$-*ran*-Aln_{14}-*ran*-DMA_{135})) was dialyzed and fabricated into nanoparticles by bulk solvent evaporation as described above. As done previously, infected mice were injected at 24 hours post-infection and analyzed by IVIS for biodistribution in the infected and contralateral femurs at 2, 8, and 24 hours post-injection.

Alendronate bone-binding assay

Bilateral femurs from two healthy mice (C57BL/6J) were harvested using sterile technique. The epiphyses were cut off with scissors, and the bone marrow was flushed by centrifugation at 12,000g in a microcentrifuge tube. The diaphysis of each bone was then cut at the midpoint to generate a total of 4 halves. The bone pieces were then placed in wells of a 96-well plate and submersed in 190 μL PBS. To the solution, 10 μL of Empty-NPs or Empty-AlnNPs (both prepared by bulk-solvent evaporation) were added. The plate was shaken overnight at room temperature. The following day, the bone pieces were washed three times in fresh PBS before imaging on IVIS for Cy7 signal intensity as described.

Preparation of concentrated supernatants

One colony of *S. aureus* from a tryptic soy agar plate was used to inoculate a 15-mL sample of Roswell Park Memorial Institute (RPMI; Corning) supplemented with 10 g/L casamino acids (MilliporeSigma) in a 50-mL conical tube. Samples were supplemented with either 15 μL DMSO, 10 μg/mL diflunisal (solubilized in 15-μL DMSO), Blank-NPs, or Dif-NPs (at a final concentration of 10-μg/mL diflunisal). Samples were prepared in triplicate. Bacteria were grown for 15 h at 37°C and 180 rpm. The triplicate cultures of each group were combined into a single culture of approximately 45-mL volume and concentrated in Amicon Ultra 3-kDa nominal molecular weight columns as done previously [123,201]. Resulting samples were filter-sterilized and frozen at −80°C.

To measure the effect of diflunisal and nanoparticles on bacterial growth, 15-mL cultures were supplemented with DMSO, 10μg/mL diflunisal, PBS, or Blank-NPs. The bacterial cultures were subsequently grown in 200-μL volumes in round-bottom, tissue culture-treated 96-well plates for 15 h at 37°C. The optical density at 600 nm (OD_{600}) was recorded each hour to monitor

bacterial growth using a BioTek Synergy HT microplate reader (BioTek Instruments, Inc.). The initial OD_{600} reading was subtracted from each well to serve as a baseline.

MC3T3 cytotoxicity assay

MC3T3 cytotoxicity was analyzed as reported previously [123,201]. Cells were intoxicated 12–24 h after initial seeding in 96-well plates with either prepared supernatants or vehicle (RPMI containing casamino acids) at 20% vol/vol for 22 h. Cell viability was determined using CellTiter 96® AQueous One Solution (Promega) according to manufacturer's instructions. The percent viability following treatment was expressed as a percentage of the absorbance of the vehicle-treated wells.

Murine model of osteomyelitis

This study was approved by the Institutional Animal Care and Use Committee of Vanderbilt University Medical Center and conducted in compliance with Animal Welfare Regulations and the principles of the Guide for the Care and Use of Laboratory Animals. All procedures were performed in an ABSL-2 facility. Following 1 week of acclimation, osteomyelitis was induced in 7–8-week-old female C57BL/6J, FVB/NJ, or BALB/cJ mice (Jackson Laboratory) as previously described with the difference that buprenorphine (analgesic) was administered as a long-acting dose (Buprenorphine-SR; ZooPharm) [122]. An inoculum of 10^6 colony-forming units in 2 μL PBS was delivered into femurs. Mice that experienced more than 20% weight loss following infection (humane endpoint determined a priori in consultation with veterinary staff) were euthanized and excluded from analyses. Dif-NPs and Blank-NPs ($n = 12$) were injected via tail vein daily at a volume of 100 μL starting approximately 1 h post-infection. $N = 12$ was based on power calculations from the initial pilot study ($n = 5$) analyzing cortical bone loss between these groups and is the primary comparison of the study. These

treatments were performed in an unblinded manner and using a random group assignment by cage. The Dif-NP group received the nanoparticle treatment immediately before the Blank-NP group. A PBS injection was used as a control ($n = 5$) for comparison. Mice were euthanized at multiple time points up to 14 days post-infection and imaged by IVIS as above. The infected femur, contralateral femur, liver, kidneys, and spleen were then removed and imaged ex vivo by IVIS. To account for intrinsic autofluorescence of tissues, the fluorescence intensity of all ex vivo organs was normalized to the fluorescence intensity of the respective organs harvested from a PBS-injected control mouse at each time point. Following IVIS imaging, infected femurs were then analyzed by microCT as described previously [122]. Briefly, axial images of each femur were captured with 5.0-μm voxels at 70 kV, 200 μA, 2000 projections per rotation, and an integration time of 350 ms in a 10.24 mm field-of-view. Each imaging scan comprised 1635 slices (8.125 mm), centered on the mid-diaphysis near the inoculation site. Volume of interest was limited to the original cortical bone, and any destruction was selected by drawing contours on the endosteal and periosteal surfaces. A subset ($n = 5$) of Blank-NP and Dif-NP femurs were decalcified, paraffin-embedded, and stained by a modified hematoxylin and eosin stain as reported previously [121].

To understand the effect of systemically delivering a nanoparticle-free diflunisal formulation, mice were treated with a saturated solution of free diflunisal in PBS ($n = 16$) and compared to mice receiving Dif-NP injections in studies adding additional mice ($n = 9$) to the Dif-NP treatment group. Within these studies an additional PBS control ($n = 4$) served as a baseline. Across three experimental trials analyzing cortical bone destruction, group sizes were as follows: PBS ($n = 9$), Blank-NP ($n = 12$), Dif-NP ($n = 21$), and free-drug diflunisal ($n = 16$). The free-drug diflunisal solution was prepared by mixing twice the maximum aqueous solubility

of diflunisal (maximum solubility: 14.5 μg/mL) in PBS, heating in a 37°C water bath for 30 min, and vortexing for 30 min. The solution was passed through a 0.45-μm syringe filter before treatment. In a separate experiment to further determine the impact of Dif-NPs on bacterial burdens in vivo, an additional group of mice ($n = 5$) were treated and euthanized at Day 7, and bacterial burdens were assessed as conducted previously [121].

To determine the impact of Dif-NPs during vancomycin treatment, a combinatorial study was completed with 10 mg/kg of vancomycin delivered subcutaneously at twelve-hour intervals starting at the time of infection as done previously [201]. Normal saline served as the vehicle control. In combination, Blank-NPs and Dif-NPs were delivered daily by tail vein injection. Thus, groups consisted of normal saline with Blank-NPs (n=5), normal saline with Dif-NPs (n=5), 10 mg/kg vancomycin with Blank-NPs (n=5), and 10 mg/kg vancomycin with Dif-NPs (n=5) in a study with 20 total animals. At Day 14 post-infection, the infected femurs of the mice were harvested and analyzed for cortical bone destruction as stated previously.

In total, 94 animals were used to complete these studies.

Statistical evaluation

Differences in diflunisal encapsulation, Nile red release, supernatant-mediated cytotoxicity, and OD_{600} growth curves were assessed by two-way analysis of variance (ANOVA). Differences in nanoparticle biodistribution and Cy7 signal in alendronate binding assays were assessed by paired Student's t-test. Differences in fluorescence intensity of organs were assessed by one-way ANOVA or two-way ANOVA as stated. Differences in cortical bone destruction and bacterial burdens were compared using a one-way ANOVA. A p value of 0.05 was considered significant for all analyses. All statistical analyses were performed with GraphPad Prism.

Results

PPS diblock copolymer nanoparticle synthesis and cargo release

To generate the building blocks necessary for fluorescent nanoparticle synthesis, PPS-*b*-p(Cy7$_1$-*ran*-DMA$_{149}$) polymer (**Figure 21A**) was synthesized by RAFT polymerization. Polymer structure was confirmed by ^{1}H NMR (**Figure 22**). An oil-in-water emulsion formed the micellar nanoparticles in which the hydrophilic DMA blocks compose the hydrophilic corona and the hydrophobic PPS blocks compose the ROS-responsive core which releases loaded drug upon destabilization (**Figure 21B**).

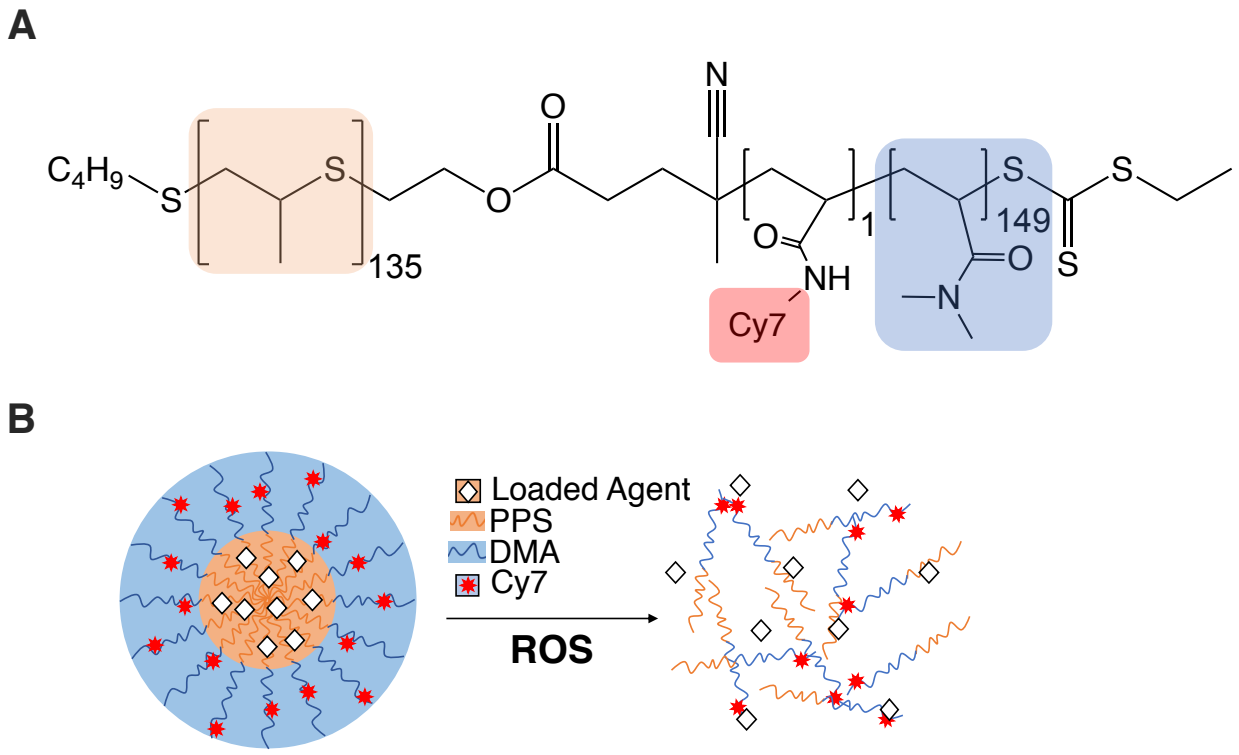

Figure 21: PPS$_{135}$-*b*-p(Cy7$_1$-*ran*-DMA$_{149}$) forms reactive oxygen species (ROS)-responsive nanoparticles

(**A**) PPS$_{135}$-*b*-p(Cy7$_1$-*ran*-DMA$_{149}$) structure contains repeat units of propylene sulfide (orange), Cy7 (red), and *N*,*N*-dimethylacrylamide (DMA; blue). (**B**) Schematic of micellar poly(propylene sulfide) (PPS) nanoparticles encapsulating a loaded agent. Upon oxidation by ROS, PPS nanoparticles become unstable due to PPS conversion from hydrophobic to hydrophilic, releasing the loaded agent.

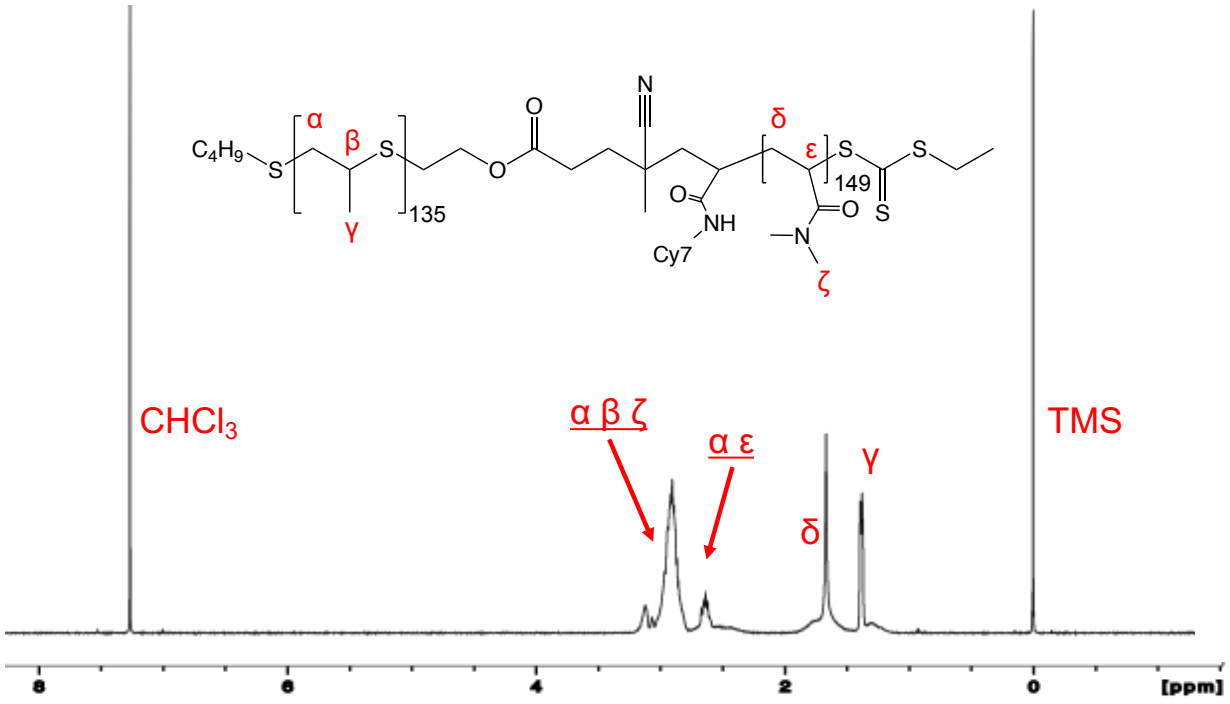

Figure 22: ^{1}H NMR spectral analysis of PPS$_{135}$-*b*-p(Cy7$_{1}$-*ran*-DMA$_{149}$) in CDCl$_3$

Hydrogen peaks of monomer repeats shown with corresponding labels α through ζ. Tetramethylsilane (TMS) reference and $CHCl_3$ contaminant also labeled at expected chemical shifts.

Formation of diflunisal-loaded PPS nanoparticles for drug delivery

To determine the optimal process for encapsulation of diflunisal within PPS nanoparticles (Dif-NPs), the quantity of loaded drug and encapsulation efficiency of two different drug-to-polymer ratios were characterized. The addition of pHPMA-Bz as an excipient was also tested to determine the benefits of facilitated π–π stacking on diflunisal encapsulation. Increasing the drug-to-polymer ratio from 1:10 to 1:4 was found to improve drug loading (**Figure 23A**); however, the encapsulation efficiency was substantially greater for the 1:10 formulation (**Figure 23B**). Use of pHPMA-Bz approximately doubled diflunisal loading in a 1:10 formulation compared to PPS nanoparticles without pHPMA-Bz (**Figure 23A**), resulting in the formulation with the highest weight percentage of diflunisal. Thus, the optimal Dif-NP formulation was determined to be a drug-to-polymer ratio of 1:10 with addition of pHPMA-Bz in a 1:1 mass ratio with diflunisal. To examine the influence of diflunisal loading on nanoparticle size, Dif-NPs and Blank-NPs were evaluated by DLS to determine the average hydrodynamic diameter (**Figure 23C**). The observed diameters for Blank-NPs and Dif-NPs were 65.4 ± 0.4 and 65.4 ± 0.4 nm, respectively, showing no change upon drug loading. Similarly, the polydispersity indices for Blank-NPs and Dif-NPs were 0.138 ± 0.004 and 0.163 ± 0.009, respectively, demonstrating a comparable dispersity of nanoparticle size within each formulation. Therefore, a 1:10 drug-to-polymer ratio co-encapsulated with pHPMA-Bz was chosen as the optimal formulation for diflunisal loading in PPS nanoparticles. Finally, to confirm ROS potentiates drug release from PPS nanoparticles, Nile red-loaded nanoparticles were treated with H_2O_2 and loss of fluorescence was measured as a sign of drug release (**Figure 23D**).

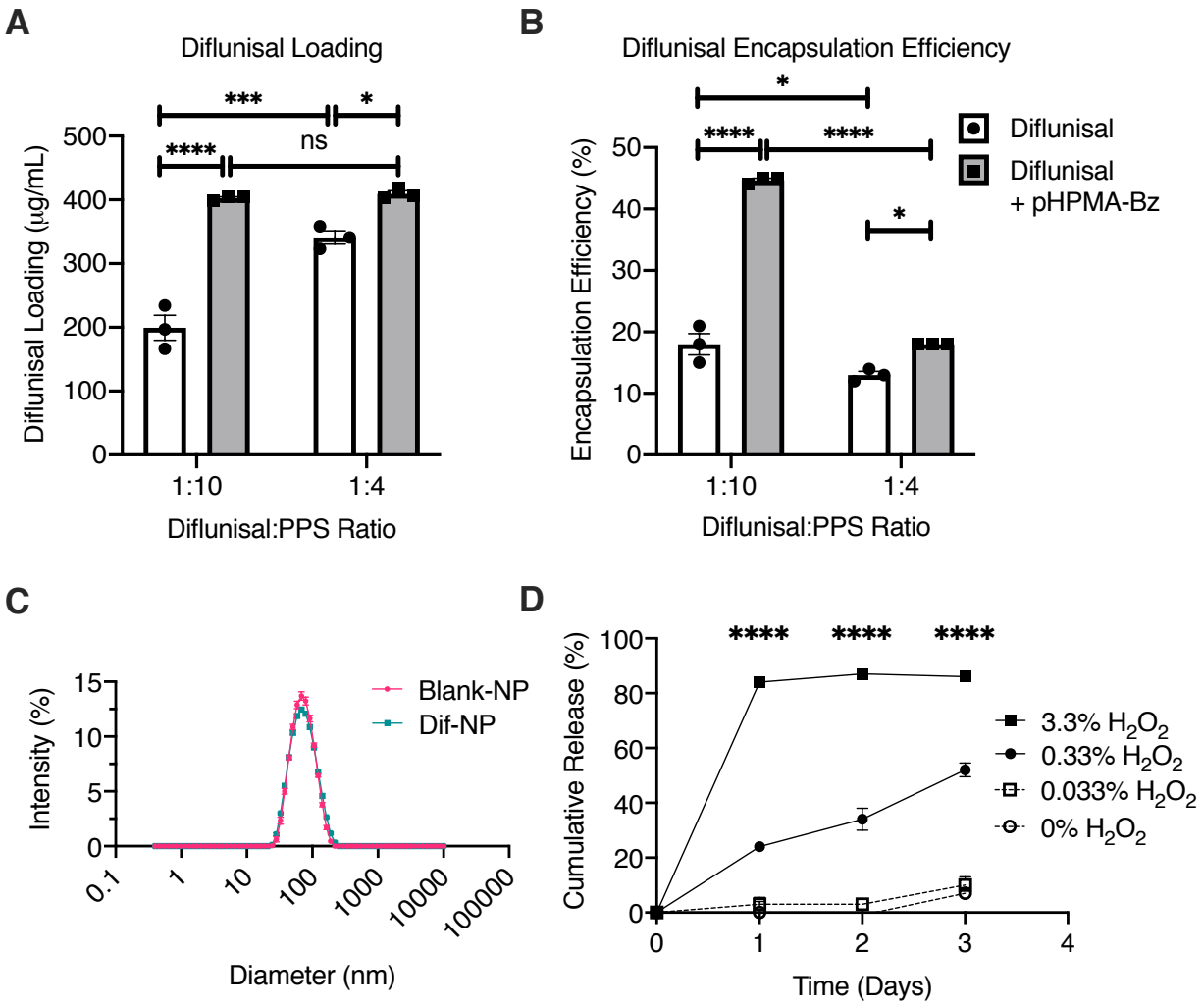

Figure 23: PPS nanoparticles effectively load diflunisal with no effect on nanoparticle size

Diflunisal encapsulation by bulk solvent evaporation was quantified by (**A**) loading and (**B**) encapsulation efficiency. For both drug-to-polymer ratios, the excipient pHPMA-Bz was tested (gray bars). $N = 3$. Error bars represent mean ± *SEM*. *$p < .05$, ***$p < .001$, ****$p < .0001$, and ns denotes no significance ($p > .05$) as determined by two-way analysis of variance (ANOVA). (**C**) Nanoparticle hydrodynamic diameter was analyzed by dynamic light scattering for Blank-NPs and Dif-NPs. (**D**) Cumulative release measured as the loss of fluorescence of Nile red (a dye that is fluorescent in hydrophobic environments such as the PPS core) from PPS nanoparticles exposed to various concentrations of the reactive oxygen species H_2O_2. Error bars represent

mean ± *SEM*. ****$p < .0001$ between the individual 0.33% and 3.3% H_2O_2 groups and all other groups at the given time point as determined by two-way ANOVA

Systemically administered nanoparticles accumulate at infected femurs

Having identified an optimal nanoparticle formulation, we sought to determine the systemic biodistribution of PPS nanoparticles to infectious sites in vivo. To first understand the biodistribution in healthy animals, uninfected FVB/NJ mice were injected with Empty-NPs via the lateral tail vein and imaged in the IVIS system at 1 and 24 h post-injection for Cy7 fluorescence. As expected, un-injected animals showed autofluorescence in the gastrointestinal tract from regular chow [269]. Measurements of Cy7 fluorescence demonstrated that Empty-NPs distributed systemically throughout the mouse within 1 h post-injection, consistent with intravenous administration (**Figure 24A**). The Cy7 signal persisted after 24 h at a decreased intensity, suggesting that nanoparticles were still present at lower concentrations (**Figure 24A**). Next, FVB/NJ mice were subjected to osteomyelitis and injected with Empty-NPs 24 h post-infection to assess the biodistribution of nanoparticles following infection. Previous experiments in our group have predominantly used C57BL/6J mice to model osteomyelitis; however, we sought a nonpigmented mouse for imaging and confirmed that bacterial burdens on post-infection Day 7 did not differ between C57BL/6J, BALB/cJ, and FVB/NJ mice (**Figure 25**). Organs were dissected and immediately assessed by IVIS to determine Cy7 fluorescent signal intensity at 2, 8, and 24 h post-injection. The infected femurs showed accumulation compared to the contralateral femurs over 24 h (**Figure 24B**). Nanoparticle accumulation was also compared to three highly vascularized organs (livers, kidneys, and spleens) up to 24 h post-injection (**Figure 24C-F**). At all tested time points, the well-vascularized organs displayed consistently high Cy7 signal intensity. These data establish that a single administration of Empty-NPs yields greater accumulation at the infected femur relative to the contralateral femur 24 h post-injection.

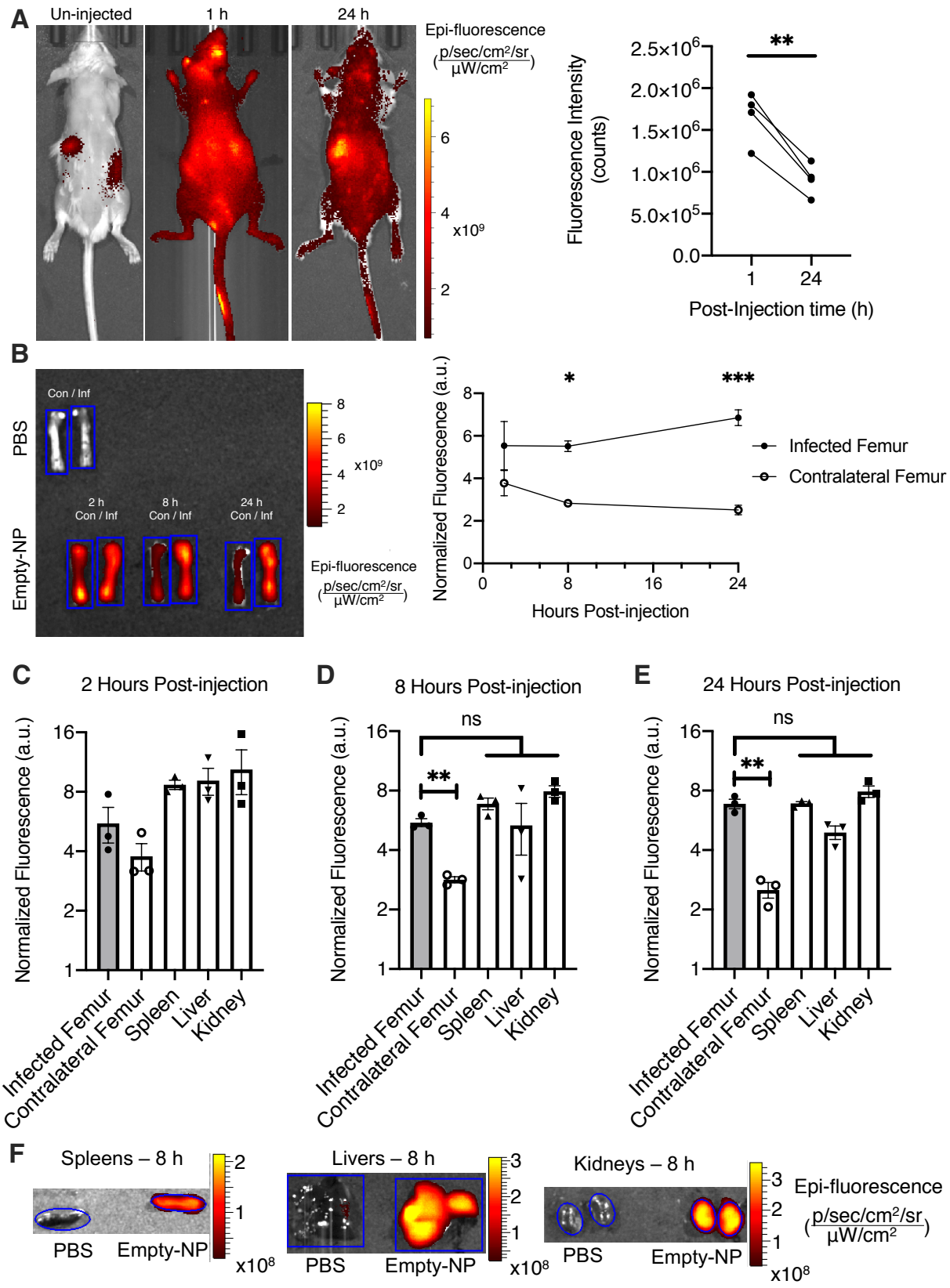
A
Un-injected
1 h
24 h
Epi-fluorescence
(p/sec/cm²/sr / µW/cm²)
x10⁹
Fluorescence Intensity (counts)
Post-Injection time (h)
B
PBS
Empty-NP
Con / Inf
2 h Con / Inf
8 h Con / Inf
24 h Con / Inf
Normalized Fluorescence (a.u.)
Hours Post-injection
Infected Femur
Contralateral Femur
C
2 Hours Post-injection
D
8 Hours Post-injection
E
24 Hours Post-injection
ns
Infected Femur
Contralateral Femur
Spleen
Liver
Kidney
F
Spleens – 8 h
Livers – 8 h
Kidneys – 8 h
PBS
Empty-NP

Figure 24: PPS nanoparticles accumulate at infected femurs

(**A**) Whole-body IVIS images of Cy7 in uninfected mice at 1 and 24 h following injection with Empty-NPs 1- and 24 h post-injection. ROI analysis of the entire animal was quantified at 1- and 24 h post-injection ($n = 4$). $^{**}p < .01$ as determined by paired Student's *t*-test. (**B**) A representative image with corresponding numerical analysis of Cy7 fluorescent signal in infected (Inf) and contralateral (Con) femurs following injection of Empty-NPs in infected mice at 2-, 8-, and 24 h post-injection. Blue outlines represent ROIs used for numerical analyses. A set of femurs from a phosphate-buffered saline (PBS)-injected animal is shown as the nonfluorescent control to which the fluorescence intensity was normalized. $N = 3$ mice per group. Error bars represent mean ± *SEM*. $^{*}p < .05$ as determined by two-way analysis of variance (ANOVA). At 2 h (**C**), 8 h (**D**), and 24 h (**E**), organs (spleen, liver, and kidneys) were dissected and similarly analyzed to determine difference from fluorescent intensity of the femurs and organs of the same mice in (**B**). As before, $n = 3$ mice per group. Error bars represent mean ± *SEM*. $^{**}p < .01$ as determined by one-way ANOVA. (**F**) A representative image at 8 h post-injection is shown for each organ from an Empty-NP-injected mouse relative to that of the PBS-injected control mouse to demonstrate the ROIs used for the analyses

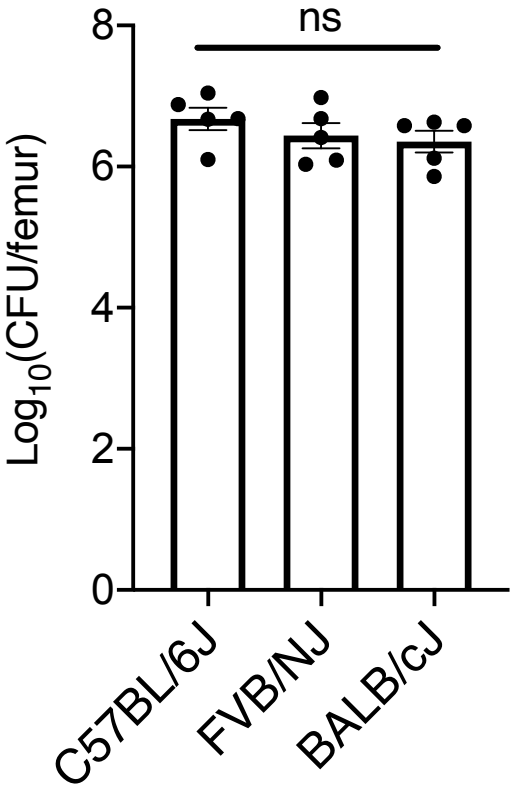

Figure 25: Bacterial burdens of *S. aureus* in different mouse strains are similar

Quantification of bacterial burden by CFU enumeration 7 days post-infection in C57Bl/6J, FVB/NJ, and BALB/cJ mice. N=5 mice per group. Error bars represent mean ± SEM. ns denotes no significance (p>0.05) as determined by 1-way ANOVA.

Dif-NPs limit *S. aureus* cytotoxicity

To determine the antivirulence efficacy of Dif-NPs, we utilized a previously published *in vitro* method to assess the influence of Dif-NPs on staphylococcal cytotoxicity towards a preosteoblast cell line [123]. MC3T3 cells were exposed to concentrated *S. aureus* supernatants prepared from bacterial cultures treated with Blank-NPs, Dif-NPs, or diflunisal as a free drug. Diflunisal, delivered either as free drug or encapsulated within PPS nanoparticles, significantly inhibited the cytotoxicity of *S. aureus* supernatants (**Figure 26A**). To determine the effects of diflunisal and PPS nanoparticles on bacterial growth, optical density of *S. aureus* cultures grown in the presence of 10-μg/mL diflunisal or Blank-NPs was assessed over a 15 h time period. Bacterial growth was also assessed in the presence of DMSO and PBS as vehicle controls for free-drug diflunisal and Blank-NPs, respectively. We did not observe a significant difference in OD_{600} between any of the groups (**Figure 26B**), suggesting that neither component of Dif-NPs (diflunisal or Blank-NPs) hinders bacterial growth. Thus, diflunisal released from Dif-NPs inhibits *S. aureus* cytotoxicity, and neither component of Dif-NPs affects bacterial growth.

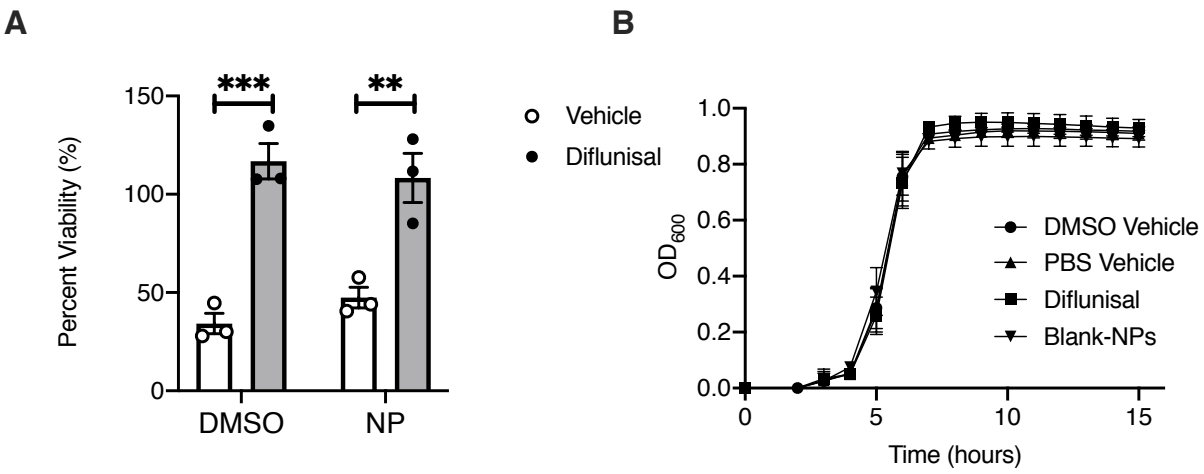

Figure 26: Dif-NPs inhibit *S. aureus* cytotoxicity toward MC3T3s

(**A**) MC3T3 murine preosteoblast cells were intoxicated with 20% (vol/vol) of concentrated supernatant from *S. aureus* grown in the presence of vehicle control (dimethyl sulfoxide [DMSO]), nanoparticle vehicle control (Blank-NP), diflunisal (10 μg/mL in DMSO), or diflunisal-loaded nanoparticles (10 μg/mL encapsulated in poly(propylene sulfide) nanoparticles). MC3T3 viability is depicted as a percentage relative to mock intoxication with sterile Roswell Park Memorial Institute. $N = 3$ independent replicates. Error bars represent mean ± *SEM*. $^{**}p < .01$ and $^{***}p < .001$ as determined by two-way analysis of variance. (**B**) Optical density of *S. aureus* grown in presence of vehicle controls (phosphate-buffered saline [PBS] and DMSO), diflunisal (10 μg/mL in DMSO), or Blank-NPs. $N = 3$ independent replicates. Error bars represent mean ± *SEM*

Dif-NPs decrease *S. aureus*-induced cortical bone loss during osteomyelitis

Given the observations that Dif-NPs inhibit the cytotoxicity of *S. aureus in vitro* and that nanoparticles accumulate at infectious foci, we sought to investigate the therapeutic capability of Dif-NPs. First, to characterize the distribution of diflunisal-loaded nanoparticles, femurs and organs of mice injected daily with Dif-NPs or Blank-NPs for 14 days were assessed by fluorescent imaging. On Day 14 post-infection, mice treated with either Dif-NPs or Blank-NPs were both found to have significant increases in fluorescence intensity in the infected limb compared to the contralateral limb (**Figure 27A,B**). When assessed ex vivo post-dissection, infected femurs at Day 14 post-infection showed significantly greater signal intensity compared to the intensities of all other tested organs (**Figure 27C,D**). Thus, Dif-NPs and Blank-NPs accumulated at the infected femur following 14 days of daily injections.

To determine the ability of Dif-NPs to decrease *S. aureus*-induced bone loss during osteomyelitis, infected mice were treated with daily injections of Dif-NPs or Blank-NPs starting 1 h post-infection. Infected femurs were isolated at Day 14 and analyzed by microCT to quantify bone loss. Femoral reconstructions upon which calculations were made are shown in **Figure 28**. Mice treated with Dif-NPs demonstrated significantly less cortical bone destruction compared to mice treated with Blank-NPs at Day 14 (**Figure 29A**). Thus, diflunisal-loaded PPS nanoparticles decrease *S. aureus*-induced bone loss in infected femurs. To compare the efficacy of delivering free-drug (unencapsulated) compared to nanoparticle-encapsulated diflunisal, infected mice were injected daily with free-drug diflunisal in PBS or Dif-NPs. Mice treated with Dif-NPs demonstrated significantly lower bone destruction than mice treated with free-drug 14 days post-infection (**Figure 29A**). Notably, cortical bone loss in PBS-injected mice did not differ from that

of Blank-NP-injected mice or free-drug diflunisal-injected mice (**Figure 29A**). Thus, nanoparticle encapsulation resulted in enhanced efficacy of systemically delivered diflunisal, likely as a function of overcoming the limited aqueous solubility of free-drug diflunisal.

To assess the effect of Dif-NPs on bacterial burden, a separate cohort of mice were injected with PBS, Dif-NPs, or Blank-NPs daily for 7 days post-infection. No differences in bacterial enumeration were measured between the groups (**Figure 29B**), and histological sections revealed evidence of abscesses in all mice treated with either Blank-NPs or Dif-NPs (**Figure 29C**, **Figure 30**), suggesting that Dif-NPs had no effect on bacterial burdens. Thus, diflunisal-loaded PPS nanoparticles decrease *S. aureus*-induced bone loss in infected femurs during osteomyelitis without significantly influencing bacterial burdens. Taken together, these data support findings that PPS nanoparticles efficaciously deliver diflunisal to infectious foci to decrease bone destruction during osteomyelitis.

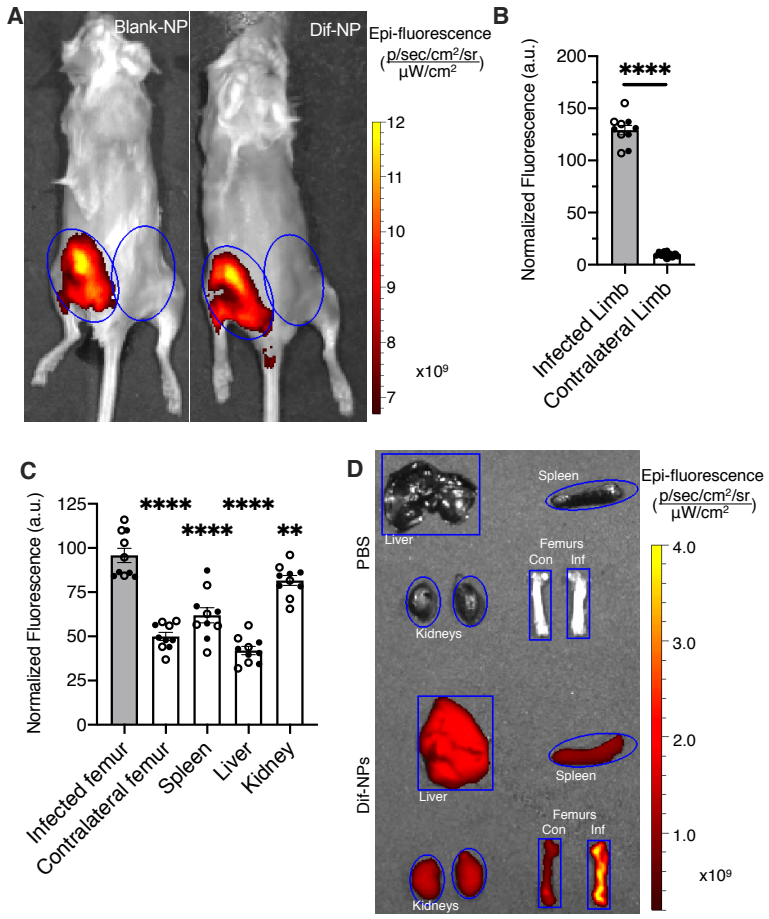

Figure 27: PPS nanoparticles accumulate at the infected femur during osteomyelitis

(**A**) Representative IVIS images of mice 14 days post-infection following daily tail vein injections of either Dif-NPs ($n = 5$) or Blank-NPs ($n = 5$). Blue circles denote ROIs for quantitative analyses. (**B**) Fluorescence of infected and contralateral limbs in both groups of mice were assessed using ROI analysis of the limbs. Filled circles represent mice treated with Blank-NPs, and open circles represent mice treated with Dif-NPs. Fluorescence intensity was normalized to the intensity of the corresponding ROI of phosphate-buffered saline (PBS)-injected animals. Error bars represent mean ± *SEM*. ****$p < .0001$ as determined by Student's *t*-test. (**C**) Quantification of dissected organs ex vivo 14 days post-infection following daily tail vein injections of Dif-NPs or Blank-NPs (same groups of mice as in A). Filled circles represent organs of mice treated with Blank-NPs, and open circles represent organs of mice treated with

Dif-NPs. Error bars represent mean ± *SEM*. $^{**}p < .01$ and $^{****}p < .0001$ as determined by one-way analysis of variance (ANOVA). (**D**) A representative image of the analyzed dissected organs of (**C**) is shown: livers, spleens, kidneys, infected (Inf) femurs, and contralateral (Con) femurs. Organs of a PBS-injected mouse and a Dif-NP-injected mouse are shown with ROIs. The organs of the PBS-injected animal do not show fluorescence intensity above the image threshold.

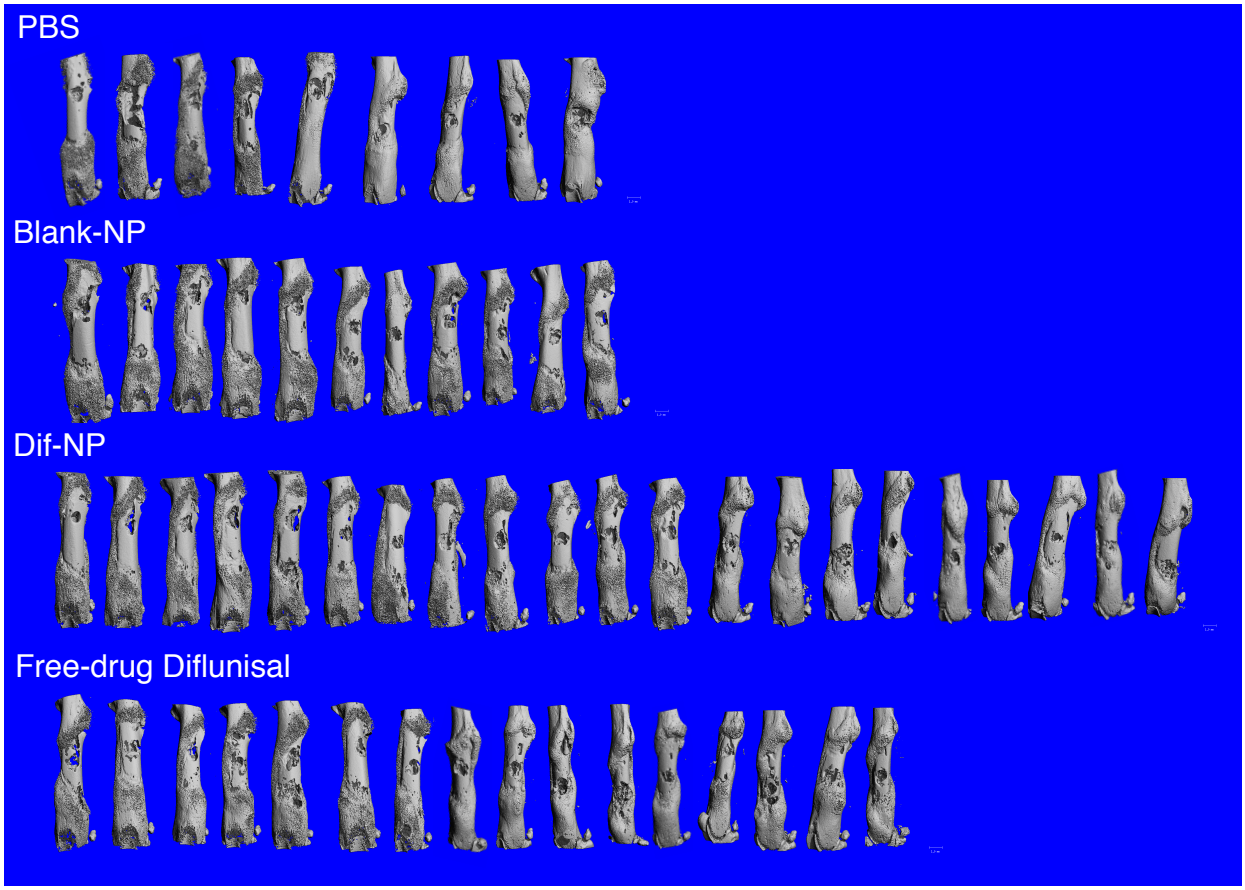

Figure 28: MicroCT three-dimensional reconstructions of infected femurs following diflunisal nanoparticle treatment during osteomyelitis

MicroCT reconstructions of femurs subjected to either PBS, Blank-NPs, Dif-NPs, or free-drug diflunisal via tail vein injection. N=9, 11, 21, or 16 mice per group as shown. One mouse in the Blank-NP group experienced >20% weight loss and was euthanized.

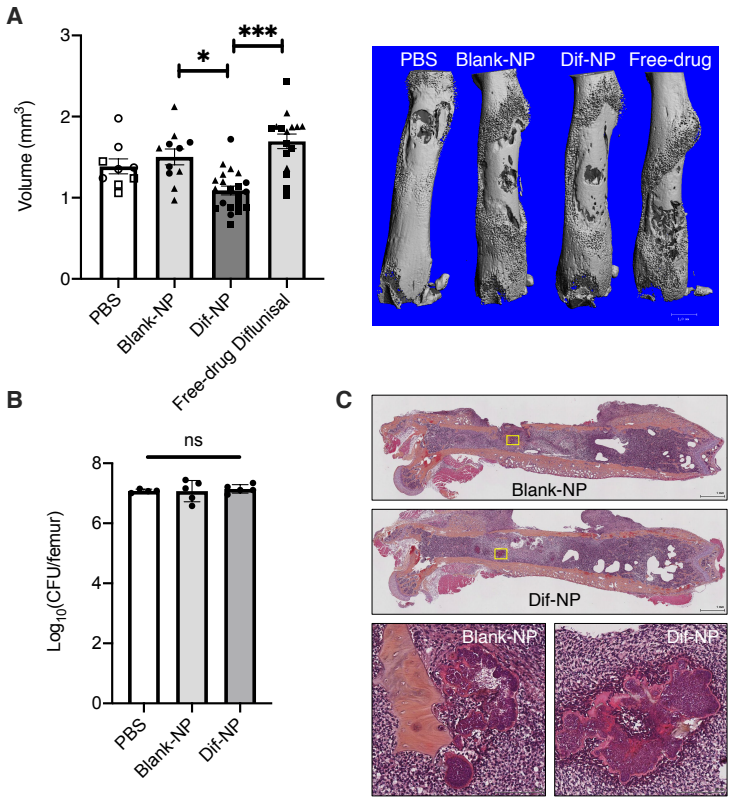

Figure 29: Dif-NPs decrease *S. aureus*-induced bone destruction during osteomyelitis

(**A**) Quantification of cortical bone destruction 14 days post-infection with *S. aureus* and following daily treatment with PBS, Blank-NPs, Dif-NPs, or free-drug diflunisal via tail vein injection. $N = 9–21$ mice per group. One mouse in the Blank-NPs group experienced more than 20% weight loss and was euthanized. Different symbols (circles, triangles, and squares) represent three independent trials that included the groups as indicated by the corresponding symbols. Effect size (Hedges' g) between Blank-NP and Dif-NP groups = −1.500 (95% confidence interval: −0.684, −2.317). The median femur from each group is shown in a three-dimensional reconstruction to the right of the graph. Error bars represent mean ± *SEM*. $^{**}p < .01$ and $^{****}p < .0001$ as determined by one-way ANOVA. (**B**) Quantification of bacterial burden by colony-forming units enumeration 7 days post-infection following daily treatment with PBS, Blank-NPs, or Dif-NPs. $N = 5$ mice per group. One mouse in the PBS group was euthanized

following an adverse response to anesthesia. Error bars represent mean ± *SEM*. ns denotes no significance as determined by one-way ANOVA. (**C**) Representative histology images of femurs harvested from mice treated with Blank-NPs or Dif-NPs and stained with a modified hematoxylin and eosin stain. Scale bars are as shown in the lower right corner of images.

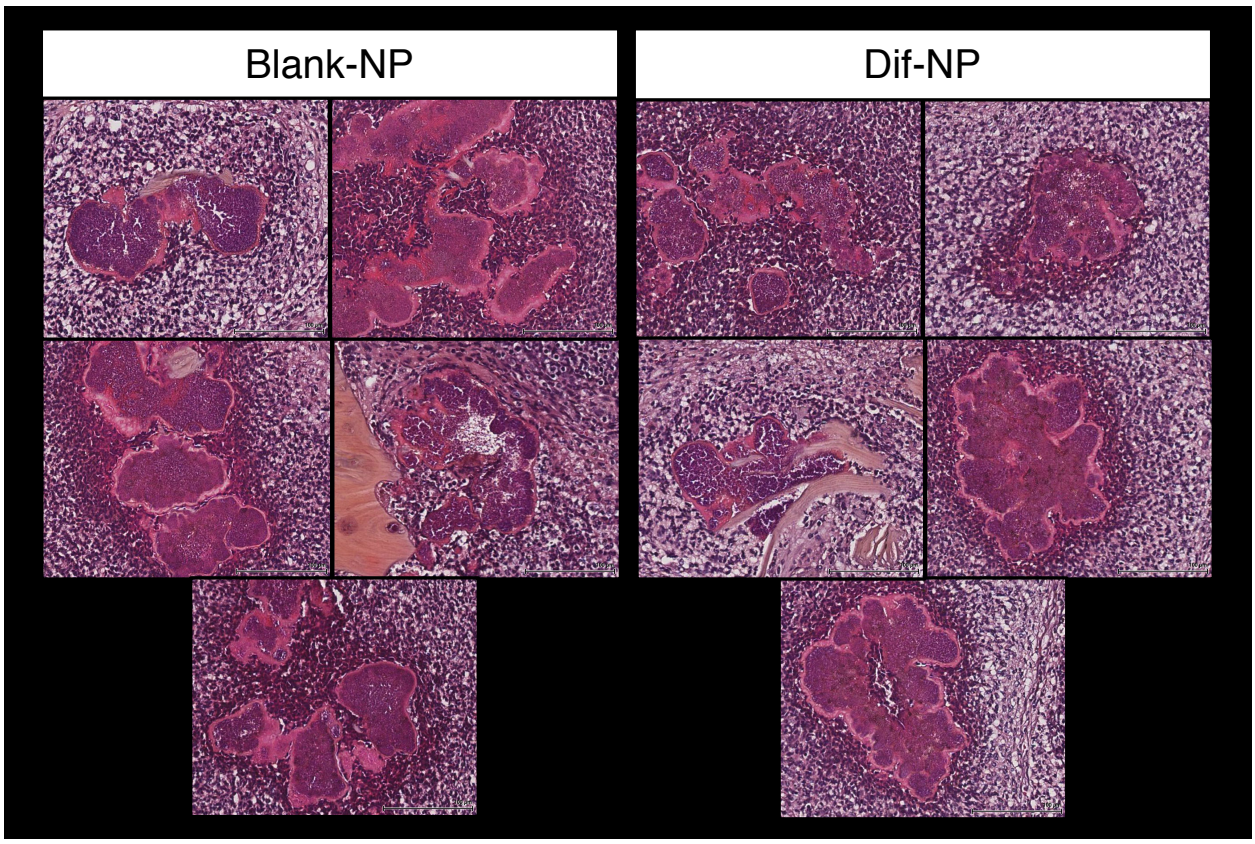

Figure 30: Qualitative images of bacterial abscess formation following diflunisal nanoparticle treatment of osteomyelitis

Representative histology images of *S. aureus* microcolonies within abscesses of infected femurs harvested from mice treated with Blank-NPs or Dif-NPs and stained with a modified hematoxylin and eosin stain. Each image corresponds to a *S. aureus* microcolony of a unique femur as abscesses were present in all ten sectioned femurs, five femurs per group. Scale bars at bottom right of each image represent 100 μm.

Addition of Aln to PPS nanoparticles improves adherence to cortical bone *ex vivo* and early delivery *in vivo*

For use as micellar nanoparticles, synthetic polymers offer tunable properties as the monomers used during synthesis may be adjusted to alter desired qualities of the nanoparticle. Therefore, we sought to investigate the effect of a targeting moiety in the polymer composition on the accumulation of PPS nanoparticles at the infectious site. Prior studies have investigated the influence of bisphosphonates (such as Aln) in PPS nanoparticles to promote delivery to diseased bone in the setting of bone metastasis [227]. To determine if Aln covalently linked to the nanoparticle corona would enhance nanoparticle delivery to infected bones, Empty-AlnNPs, containing 10% Aln monomer in the hydrophilic, coronal block, were fabricated. Empty-AlnNPs were first tested in an *ex vivo* assay to determine if Aln improved binding to bone. Cortical bone pieces (comprising half of the diaphysis) were flushed of bone marrow and incubated overnight in 96-well plates with Empty-AlnNPs or Empty-NPs (no Aln) with PBS, shaking at room temperature. The next day, the cortical bone pieces were washed 3 times in fresh PBS and imaged for Cy7 signal on IVIS. The bones that incubated with Empty-AlnNPs showed significantly higher Cy7 signal intensity, indicating greater adherence to the cortical bone pieces (**Figure 31**). The fluorescence intensity of Empty-AlnNPs or Empty-NPs in PBS was compared and found to not significantly differ (data not shown).

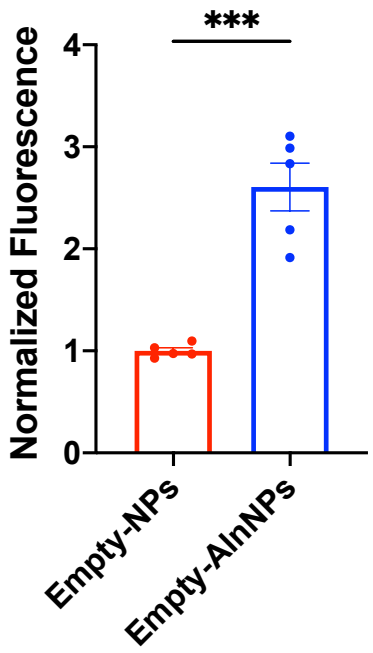

Figure 31: Aln-conjugation increases Cy7 signal intensity in an *ex vivo* bone-binding assay

Normalized Cy7 fluorescent signal intensity from cortical bone treated overnight with Empty-NPs and Empty-AlnNPs (n=5). Error bars represent mean ± *SEM*. ***$p < 0.001$ as determined by unpaired, two-tailed Student's *t*-test.

After finding that Empty-AlnNPs displayed greater Cy7 signal intensity in a bone-binding assay, Empty-AlnNPs were compared to Empty-NPs in our *in vivo* osteomyelitis model. In parallel to studies described previously (**Figure 24B**), Empty-AlnNPs were injected into mice 24 h post-infection and femurs were dissected and measured for Cy7 signal intensity via IVIS at 2, 8, and 24 h post-injection. At early time points, Empty-AlnNPs exhibit increased Cy7 signal intensity relative to that of Empty-NP-injected femurs (**Figure 32A-C**). However, by 24 h post-injection, the signal intensity from infected femurs in Empty-AlnNP-injected mice and Empty-NP-injected mice no longer differ (**Figure 32D**). Furthermore, at 8 h and 24 h post-injection, both Empty-AlnNPs and Empty-NPs show significantly greater accumulation in the infected femurs relative to the contralateral femurs (**Figure 32C,D**). These data indicate that the inclusion of a bone-targeting moiety such as Aln in the PPS nanoparticle corona may expedite delivery to infected bone compared to Empty-NPs.

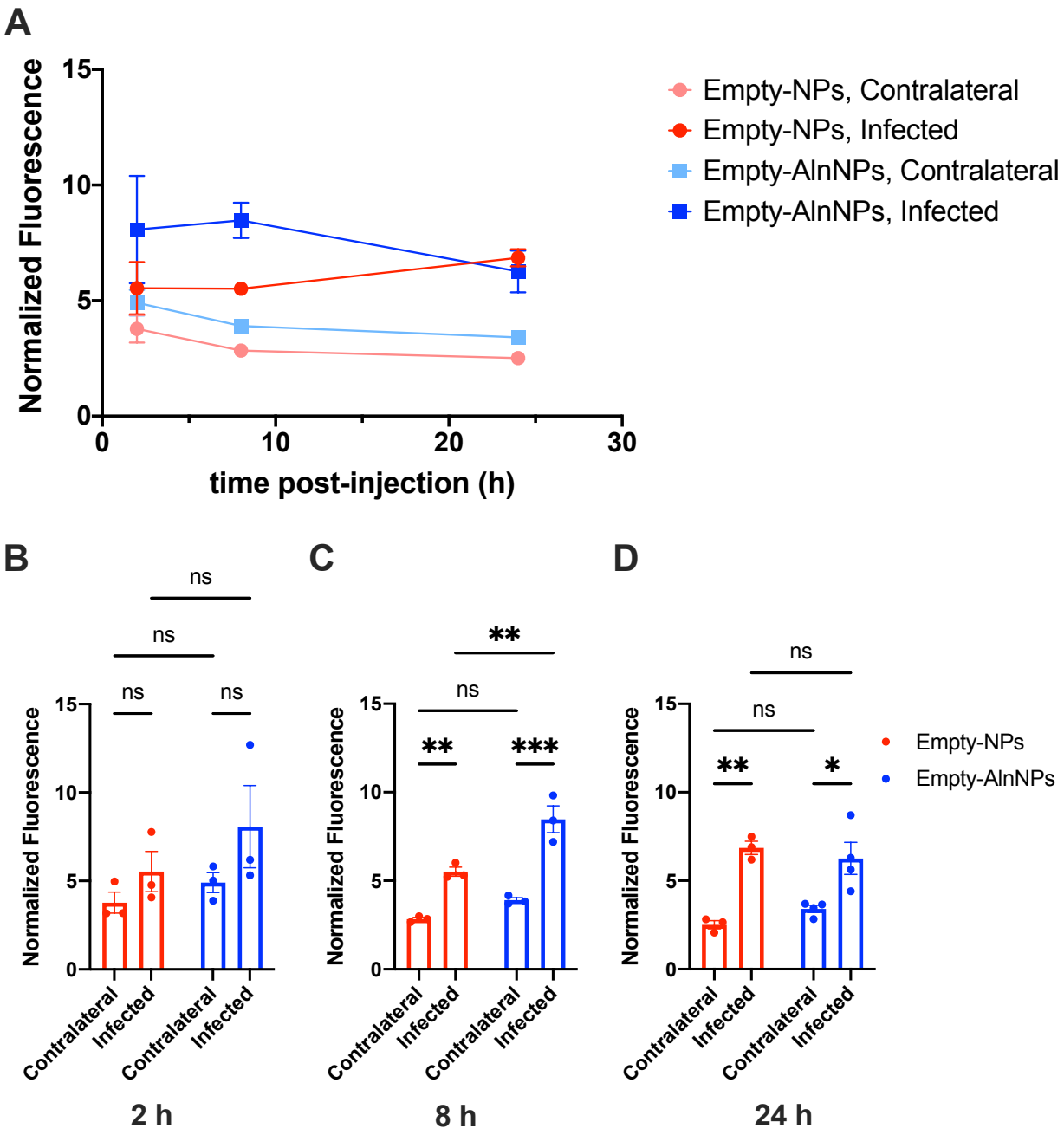

Figure 32: Empty-AlnNPs show increased early nanoparticle accumulation at the infected femur compared to Empty-NPs

(**A**) Mice (*n*=3-4) were injected with Empty-NP (previously graphed in **Figure 24**) or Empty-AlnNP at 24 h post-infection, and the dissected femurs were analyzed for Cy7 fluorescent signal intensity at 2 h, 8 h, and 24 h post-injection. Normalized to a signal intensity from femur of PBS-

injected control mouse, the Cy7 signal intensity from infected and contralateral femurs of Empty-NP- and Empty-AlnNP-injected mice is shown at 2, 8, and 24 h post-injection. The data represented in (**A**) at 2 h (**B**), at 8 h (**C**), and at 24 h (**D**) post-injection is graphed and compared by two-way analysis of variance (ANOVA). Error bars represent mean ± *SEM*. *$p < 0.05$, **$p < 0.01$, ***$p < 0.001$ and ns denotes not significant as determined by two-way ANOVA.

Vancomycin therapy significantly decreases cortical bone loss, and co-administration of Dif-NP does not further decrease cortical bone loss

In addition to modifying the polymer chemistry, changing the overall treatment regimen by incorporating standard-of-care antibiotics is important to understand the influence of antivirulence compounds on antibiotic efficacy. Previously, we demonstrated that vancomycin significantly decreased cortical bone destruction and that dual delivery of diflunisal in a local delivery device did not further reduce cortical bone loss during *S. aureus* osteomyelitis [201]. To test for potential synergism of a sub-therapeutic dose of vancomycin with Dif-NPs, a combinatorial experiment was conducted in which daily Dif-NP (or Blank-NPs as vehicle) and twice daily 10 mg/kg vancomycin (normal saline as vehicle) was delivered to mice for 14 days before analyzing cortical bone destruction in the infected femurs. Vancomycin was found to significantly decrease cortical bone destruction relative to that of normal saline-treated groups (**Figure 33**). In this small pilot study (n=5), Dif-NPs+normal saline-treated mice showed a lower but not significantly lower cortical bone destruction than Blank-NPs+normal saline-treated mice (**Figure 33**). Dif-NPs did not further decrease cortical bone destruction in mice treated with 10 mg/kg vancomycin relative to the Blank-NPs+vancomycin-treated group (**Figure 33**). These data in conjunction with prior data demonstrate that Dif-NPs show a mild decrease in cortical bone destruction but do not decrease cortical bone destruction beyond that achieved by monotherapy of vancomycin, the standard-of-care treatment for MRSA.

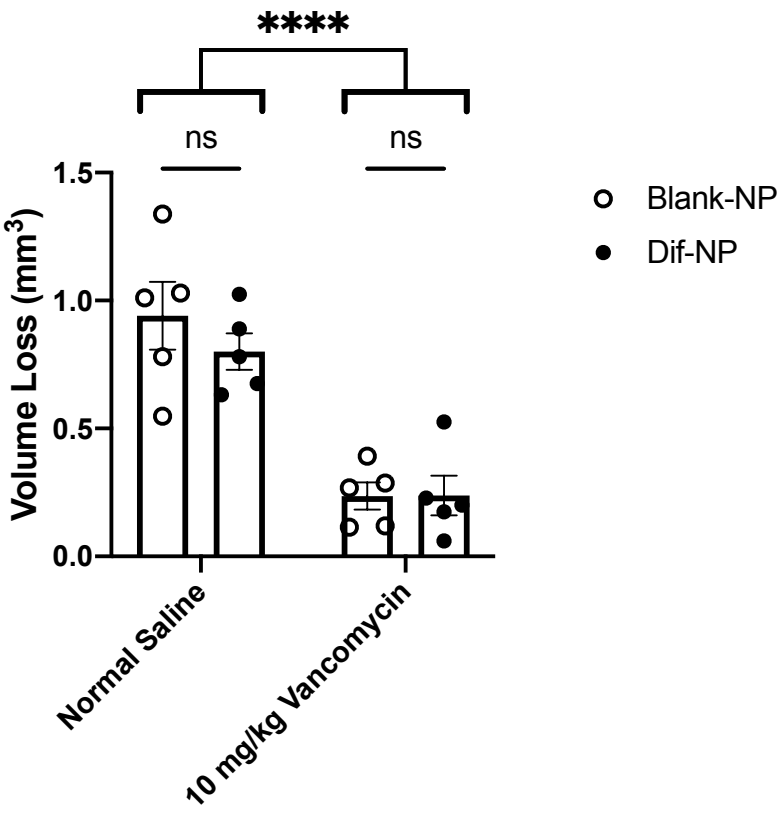

Figure 33: Dif-NPs fail to improve decreases in cortical bone destruction following vancomycin treatment

Cortical bone destruction was measured in infected femurs of mice treated with combinatorial therapy with Blank-NP or Dif-NP and normal saline or 10 mg/kg vancomycin at post-infection Day 14. Error bars represent mean ± *SEM*. ****$p < 0.0001$ and ns denotes not significant as determined by two-way analysis of variance (ANOVA).

Discussion

Delivery of hydrophobic drugs such as diflunisal is limited by low aqueous solubility, which can lead to unfavorable pharmacokinetic profiles and poor biodistribution when delivered parenterally [270,271]. Local delivery systems have been designed to overcome solubility limitations; however, foreign devices are known to be a nidus for bacterial colonization and biofilm formation [201,261,262]. While some compounds (including diflunisal) can achieve systemic delivery through oral delivery, oral administration is not feasible in all clinical settings (e.g., moribund or perioperative patients), and alternative parenteral options may be advantageous. For such compounds without parenteral compatibility, nanoparticle delivery systems offer a parenteral delivery vehicle for pharmaceuticals to target sites. Although nanoparticle accumulation has not been extensively studied in the context of osteomyelitis, effective treatment of bone infection with systemically administered nanoparticles has been reported [205–208]. Delivery of antimicrobial compounds using locally administered nanoparticles has also been investigated both *in vitro* [212,213] and *in vivo* [209–211], but systemic delivery of nanoparticles capable of carrying hydrophobic drugs is under-investigated in osteomyelitis. Delivery of diflunisal using nanoparticles may provide effective therapy and limit potential complications associated with avascular local delivery devices.

In this study, we evaluated the efficacy of PPS nanoparticles to deliver diflunisal, which we previously demonstrated inhibits *S. aureus*-induced cortical bone destruction when delivered locally from resorbable poly(ester urethane) scaffolds [123,201]. We hypothesized that diflunisal-loaded PPS nanoparticles would accumulate at infectious foci during osteomyelitis and inhibit *S. aureus*-mediated bone destruction. Reconciling this hypothesis in a model of invasive *S. aureus* disease is crucial given the known limitations of avascular drug depots. Our

results indicate that PPS nanoparticles accumulate at infected femurs in a murine model of posttraumatic osteomyelitis. Moreover, we discovered that diflunisal-loaded PPS nanoparticles effectively mitigated osteomyelitis-induced bone destruction. Importantly, we also determined that bacterial burdens were unaffected by nanoparticle presence compared with mice treated with PBS alone. Therefore, PPS nanoparticles provide efficacious treatment of diflunisal without exacerbating the infection. Given that PPS nanoparticles accumulate at the site of infection, investigation into other drug cargoes such as novel antivirulence compounds or antimicrobials should be performed. When studying diflunisal-loaded nanoparticles relative to standard-of-care vancomycin, vancomycin alone decreased cortical bone destruction to a greater extent than diflunisal-loaded nanoparticles, and co-administration of diflunisal-loaded nanoparticles did not further prevent cortical bone loss. These data indicate that effective antimicrobial control is more effective at limiting disease pathology such as cortical bone loss during *S. aureus* osteomyelitis than antivirulence treatment via diflunisal administration. Concern about emerging antimicrobial resistance still warrants investigation into alternative therapies such as diflunisal or other antivirulence compounds [230]. Given the observed increases in nanoparticle accumulation, the data from the vancomycin co-administration experiment may also suggest that future investigations should employ more well-established drugs such as hydrophobic antimicrobials in the near-term. Future investigations should explore the efficacy of delayed treatment and the optimal timing between administrations of diflunisal-loaded PPS nanoparticles.

Compared to free-drug administration via intravenous or oral delivery routes, synthetic nanoparticles offer the potential to accumulate and release loaded compounds at target sites [212,226,263–265]. As described by the EPR effect, both tumors and inflammation result in enhanced vascular permeability allowing for extravasation of nanoparticles [216]. Our results

suggest that PPS nanoparticles accumulate at the infectious foci; however, the exact mechanisms that drive nanoparticle retention during posttraumatic osteomyelitis must be investigated further. One possible mechanism may include phagocytic cell uptake as described in the "ELVIS" effect (extravasation via leaky vasculature followed by inflammatory cell sequestration) [219,220]. Nevertheless, modifications to the nanoparticle chemistry have shown enhanced retention at target sites and allow for further improvement of nanoparticle accumulation in bone in other disease models [227]. Our data suggest that Aln conjugation improves nanoparticle accumulation at time points early time points (8 h post-injection) but not at later time points (24 h). Further studies should test whether such a difference in time to delivery alters efficacy of bioactive cargo such as diflunisal. Testing nanoparticle abundances at times beyond 24 h post-injection could reveal if Aln-conjugated nanoparticles and non-Aln-conjugated nanoparticles demonstrate different delivery or retention dynamics at the infected femur at later time points post-injection. Such a finding may suggest that a hybrid therapy may be advantageous in which a tailored mixture of PPS nanoparticles and Aln-conjugated PPS nanoparticles are delivered to maximize sustained nanoparticle accumulation at the infected femur.

Considering that sites of inflammation and infection are known to produce ROS and that release of compounds from PPS nanoparticles is responsive to ROS concentration, it is likely that ROS levels at infected sites contribute to drug cargo release within bone [272]. However, more extensive in vivo analyses must be performed to conclude that ROS-mediated degradation is the primary mechanism of drug release at the infectious site.

Limitations of this study include the use of only one bacterial strain and a single infection model. Due to the different virulence and metabolic profiles of various bacterial pathogens, future studies should explore the use of alternative bacterial species to understand PPS

nanoparticle delivery to different infectious foci. *S. aureus* was chosen to model infection in bone due to its high association with bone infection, but PPS nanoparticles delivered to infections in other infected organs have yet to be studied. Similarly, a focus on treatment times greater than 14 days should be investigated to understand the extent to which longer treatments may impact therapeutic outcomes. In the future, experiments should test the ability of PPS nanoparticles to decrease deleterious side effects of toxic agents that would otherwise limit systemic delivery of the drug. Nevertheless, this study suggests PPS nanoparticles efficaciously deliver drug to infectious foci and promotes investigation of nanoparticles as small molecule carriers for osteomyelitis therapy.

CHAPTER V: CONCLUSIONS AND FUTURE DIRECTIONS

Summary of experimental findings: HIF signaling during osteomyelitis

Despite first being described millennia ago, osteomyelitis continues to cause substantial morbidity and frequently results in chronic infection despite modern antibiotic treatments [1,2]. Difficulty in the treatment of osteomyelitis is in part because of the unique features of the most common pathogenic etiology, *Staphylococcus aureus* [3]. The work of this thesis was designed to better understand the basic biology at the host-pathogen interface during *S. aureus* osteomyelitis and to explore alternative treatment strategies. Discovery of the hypoxia-inducible factor (HIF) signaling pathway was recently recognized with a Nobel Prize because of the broad impacts that HIF signaling has in physiology and pathophysiology [273]. Of note, HIF signaling has demonstrated crosstalk with immune response pathways and has been studied in the context of several infections [60]. The work outlined in Chapter III of this thesis has begun to investigate the role of components of the HIF signaling pathway during *S. aureus* osteomyelitis. Specifically, the objective of experiments described in Chapter III was to determine the role of skeletal cell HIF signaling in bone remodeling and antibacterial immunity during *S. aureus* osteomyelitis.

I investigated HIF signaling in osteoblast-lineage and myeloid-lineage cells through lineage-specific genetic knockout of *Hif1a* and *Vhl* to model states of low and high HIF-1α signaling, respectively. The osteoblast lineage includes bone marrow stromal cells, osteoblasts, and osteocytes, which are responsible for forming the extracellular matrix of bone [28]. The myeloid lineage includes osteoclasts, which are responsible for bone resorption [41]. Additionally, the myeloid lineage includes immune cells like neutrophils and macrophages, which are derived from the hematopoietic niche in the bone marrow and are important for

controlling *S. aureus* infection [274]. By using two different Cre systems to target osteoblast-lineage and myeloid-lineage cells and two different floxed genes for conditional deletion, studies of Chapter III tested (1) the role of osteoblast-lineage *Hif1a*, (2) the role of osteoblast-lineage *Vhl*, (3) the role of myeloid-lineage *Hif1a*, and (4) the role of myeloid-lineage *Vhl*, on antibacterial immune responses and pathologic bone remodeling during *S. aureus* osteomyelitis. The following text discusses the key findings in each of these conditional knockout models during *S. aureus* osteomyelitis.

The role of osteoblast-lineage *Hif1a* during *S. aureus* osteomyelitis

Analyzing bacterial burdens and bone architecture changes in $Hif1a^{fl/fl}$, *OsxCre*+ mice revealed that HIF-1α in osteoblast-lineage (*Sp7*-expressing cells) is largely dispensable in our model of osteomyelitis. Despite published data supporting the essentiality of HIF-1α in inflammatory responses of other cells types including myeloid-lineage cells and keratinocytes, conditional deletion of HIF-1α in osteoblast-lineage cells did not impact bacterial burdens at post-infection Day 14 [141,155]. Prior studies have shown that conditional deletion of HIF-1α in osteoblast-lineage cells (*OcnCre*) causes a mild decrease in bone volume [59]. No difference in cortical bone architecture was detected following infection. This may be because the Cre recombinase was repressed until postnatal age 4 weeks, because the subtle phenotype was overshadowed by the dominant effects of the infection and injury, or because the two experiments used different Cre recombinase models. The lack of impact of *Hif1a* deletion under the action of the *OsxCre* may also be related to the method of injury. Prior studies testing the role of VEGF-A in *Sp7*-positive (Osx-expressing) cells have shown that loss of VEGF-A (a HIF target) in this population was impactful in sterile transcortical femur fracture but not in sterile pinhole defects like that used in our model of osteomyelitis [97]. It may also be possible that

HIF-2α (EPAS-1) compensates for HIF-1α in osteoblast-lineage cells as suggested in prior studies exploring *Hif1a* deletion in osteoblast-lineage cells [59]. While *Hif1a*$^{fl/fl}$, *OsxCre*+ mice may demonstrate a phenotype in other osteomyelitis models that include transcortical injury or an metallic implant, the data presented in Chapter III suggest that HIF-1α in osteoblast-lineage cells does not contribute to the measured outcomes during *S. aureus* post-traumatic osteomyelitis.

The role of osteoblast-lineage *Vhl* during *S. aureus* osteomyelitis

Similar to findings in *Hif1a*$^{fl/fl}$, *OsxCre*+ mice, *Vhl*$^{fl/fl}$, *OsxCre*+ mice did not display differences in bacterial burdens at post-infection Day 14. Because of differences in trabecular bone, early time points of infection were also explored to test if transient differences in bacterial burdens occurred. However, at post-infection Day 3 and Day 5, no significant differences in bacterial burdens were present. Therefore, *Vhl* deletion in osteoblast-lineage cells does not significantly impact bacterial clearance during osteomyelitis.

Prior studies have demonstrated that *Vhl* deletion in osteoblast-lineage cells dramatically increases trabecular bone volume [59,243]. The data in Chapter III support this finding. Furthermore, data are presented that demonstrate that trabecular bone in *Vhl*$^{fl/fl}$, *OsxCre*+ mice is protected from infection-mediated declines in bone volume-per-total volume (BV/TV) compared to that of controls. Moreover, histomorphometry data suggest that the lack of decline in trabecular BV/TV may be related to differences in osteoclast abundance following infection. These data suggest that one mechanism by which trabecular bone is protected from bone loss is through inhibition of infection-mediated osteoclast activation; however, alternative mechanisms may be at play such as increased bone formation that compensates for concomitant bone loss. Additionally, the mechanism by which *Vhl* deletion in osteoblast-lineage cells prevents

osteoclast formation is not determined. One possible way that condition deletion in osteoblast-lineage cells impacts osteoclast formation is through regulation of receptor activator of NF-κB ligand (RANKL) and osteoprotegerin (OPG). Chapter III presents data from an *in vitro* study that shows that Cre-mediated deletion of *Vhl* in calvarial osteoblasts from $Vhl^{fl/fl}$ mice limits *S. aureus*-mediated induction of *Tnfsf11* (RANKL) transcription relative to that of *Tnfrsf11b* (OPG). However, this change has not yet been shown to be directly impactful in osteoclast formation *in vitro* (co-culture assays) or *in vivo* (direct measurement of RANKL and OPG from infected bone). The data represent a plausible theory by which *Vhl* deletion limits *S. aureus*-mediated production of RANKL relative to OPG, which limits osteoclast-mediated resorption of trabecular bone. It will be important to explore causal links to validate such a mechanism.

The role of myeloid-lineage *Hif1a* during *S. aureus* osteomyelitis

Relative to control mice, $Hif1a^{fl/fl}$, $LysMCre^{+/-}$ mice exhibited no differences in bacterial burdens or changes in pathologic bone remodeling. This result was surprising because prior studies have demonstrated the essentiality of HIF-1α for myeloid inflammatory responses in different models [141,153]. Specifically, HIF-1α has been shown to be essential for myeloid cell recruitment and infiltration to inflamed skin following application of tetradecanoylphorbol acetate, a Protein Kinase C activator (and thereby NF-κB) [141]. Moreover, loss of *Hif1a* in the myeloid lineage allows higher bacterial burdens during cutaneous infection by group A *Streptococcus* (GAS) skin [153]. However, prior publications have noted myeloid-lineage deletion of *Hif1a* to be dispensable during other inflammatory diseases, such as in endotoxin-induced uveitis [275]. It is clear that within different models of infection and inflammation, the impact of myeloid HIF-1α has differed. Additionally, each Cre-lox model expresses *cre* at different levels, and not all genes are equally excised. For the *LysMCre* model, a mouse model

used in experiments of Chapter III, *cre* has been inserted in the *Lyz2* gene in chromosome 10 of the mouse [241]. Therefore, experiments using the *LysMCre* mouse model can breed the mice such that conditional knockout mice are homozygous for the *LysMCre* allele or heterozygous. In the experiments of Chapter III, mice heterozygous for *LysMCre* (*LysMCre*$^{+/-}$) were used, which preserves a functional copy of *Lyz2* in the mouse. While it is possible that *Hif1a*$^{fl/fl}$, *LysMCre*$^{+/-}$ mice do not experience a complete deletion of *Hif1a*, mice heterozygous for the *LysMCre* allele have demonstrated successful deletion of floxed alleles in prior studies [276]. In the initial characterization of the *LysMCre* mouse model, *LysMCre* mice crossed to *Polb*$^{fl/fl}$ mice (*Polb*$^{fl/+}$, *LysMCre*$^{+/-}$) demonstrated deletion efficiencies of the floxed *Polb* allele ranged from 75-99% among macrophage and neutrophil populations [241]. Future studies should test the level of *Hif1a* deletion achieved within the *Hif1a*$^{fl/fl}$, *LysMCre*$^{+/-}$ mice. In sum, the data from Chapter III suggest that HIF-1α activity in osteoblast- and myeloid-lineage cells (*OsxCre*+ or *LysMCre*$^{+/-}$) is not essential for host responses in our model of *S. aureus* osteomyelitis.

The role of myeloid-lineage *Vhl* during *S. aureus* osteomyelitis

As in studies of the osteoblast lineage, myeloid-lineage conditional deletion of *Vhl* appeared to be more phenotypically impactful than deletion of *Hif1a*. Chapter III demonstrates that *Vhl*$^{fl/fl}$, *LysMCre*$^{+/-}$ mice may have a mild decrease in bacterial burdens at early time points. However, this study is currently underpowered. If this phenotype is substantiated, it may indicate a more robust immune response early in the infection in *Vhl*$^{fl/fl}$, *LysMCre*$^{+/-}$ mice. It is plausible that a more robust immune response may also contribute to osteomyelitis pathology by increasing bone loss. Prior studies have linked cytokines involved in the immune response to *S. aureus* infection with bone loss during *S. aureus* osteomyelitis *in vivo* [121]. Indicative that such a phenomenon may be present, *Vhl*$^{fl/fl}$, *LysMCre*$^{+/-}$ mice demonstrate reduced trabecular BV/TV

compared to that of Cre-negative littermate control mice. The decrease in BV/TV appears to be infection specific as genotype-dependent differences were not present in trabecular bone of mock-infected (sterile) animals. Though underpowered, the average volume of cortical bone loss in $Vhl^{fl/fl}$, $LysMCre^{+/-}$ mice was also greater than that Cre-negative littermate control mice. It will be important to validate these results with further studies and to investigate the underlying mechanism behind this increased bone loss during infection. *Vhl* deletion may increase HIF-mediated cytokines, alter metabolism, or even act through HIF-independent mechanisms. Furthermore, *LysMCre* targets osteoclasts, a myeloid cell, and it is possible that osteoclast intrinsic changes from *Vhl* deletion drive changes in bone architecture.

By characterizing bacterial and skeletal outcomes in four different Cre-lox mice, the studies outlined in Chapter III have investigated role of HIF signaling in skeletal cells during osteomyelitis. A summary of the results is outlined (**Table 3**).

Table 3: Summary of experimental findings from Chapter III

For each conditional knockout mouse generated in experiments of Chapter III, the impact on bacterial burdens, cortical bone destruction, and trabecular bone is shown relative to that of control mice. BV/TV=bone volume-per-total volume.

Cell lineage targeted	Gene deleted	Bacterial burdens	Cortical bone destruction	Trabecular bone
Osteoblast (*OsxCre)*	*Hif1a*	No impact	No impact	No impact
	Vhl	No impact	No impact	Protection from infection-mediated decline in BV/TV; decreased osteoclast abundance
Myeloid (*LysMCre)*	*Hif1a*	No impact	No impact	No impact
	Vhl	May decrease early burdens*	May increase cortical bone loss*	Decreased BV/TV
*underpowered, requires further study for confirmation				

Future directions: Investigating HIF signaling in the context of *S. aureus* osteomyelitis

The work outlined in this thesis has expanded the understanding of how components of the HIF signaling pathway impact host responses during osteomyelitis. However, many questions remain unanswered or incompletely understood. There are multiple future directions for this project. Several future directions outlined in the following paragraphs aim to clarify and confirm results of Chapter III.

Determine the percentage of excision of floxed alleles in conditional knockout mice

To assuredly conclude that the conditional knockout mice differ as expected from the Cre-negative littermate control mice, measurement of Cre-mediated gene knockout is necessary. To confirm excision of the floxed alleles in the *OsxCre+* mice, I propose to isolate long bone osteoblasts from the cortical bone of femurs and tibias of the conditional knockout mice. The long bone osteoblasts can be differentiated in α-minimal essential media (α-MEM) containing 10% fetal bovine serum (FBS) and 1x penicillin/streptomycin in addition to 50 μg/mL ascorbic acid. After one week in culture, the cells can be alkaline phosphatase stained to confirm the cells exhibit osteogenic differentiation. In the *LysMCre*$^{+/-}$ mice, cells can be isolated and differentiated by plating whole bone marrow in the presence of M-CSF for 5 days to drive bone marrow macrophage proliferation and longevity. Then, RNA from the differentiated cells (osteoblast and bone marrow macrophage) can be isolated, and RT-PCR can be conducted to measure transcript levels of *Hif1a* and *Vhl* in the respective mice for comparison to Cre-negative controls. RT-PCR using a primer set in which at least one primer is within the floxed allele can be used to indicate successful gene deletion. Relative declines in RNA abundance will be indicative of excision. Theoretically, genomic DNA may be used as a template as well using the same or similar primers.

Investigate osteoclast formation in *Vhl$^{fl/fl}$*, *OsxCre*+ mice

One of the most exciting phenotypes identified was the lack of trabecular bone loss in the *Vhl$^{fl/fl}$*, *OsxCre*+ mice relative to the control mice in conjunction with histomorphometry data showing lower trabecular osteoclasts in *Vhl$^{fl/fl}$*, *OsxCre*+ mice following infection. This histomorphometry data has been done in comparison to age-matched controls. It will be necessary to confirm this phenotype with littermate, Cre-negative control mice. An *in vitro* assay can also be performed to corroborate the *in vivo* data using a functional assay. One *in vitro* assay that will help confirm that osteoclast formation is altered in *Vhl$^{fl/fl}$*, *OsxCre*+ mice is a whole bone marrow culture containing osteoclast precursors and osteoblast-lineage stromal cells. Whole bone marrow culture using cells from *Vhl$^{fl/fl}$*, *OsxCre*+ mice or Cre-negative littermate control mice can be used to test the hypothesis that deletion of *Vhl* in the osteoblast-lineage limits osteoclast production. In a pilot study conducted with whole bone marrow from *Vhl$^{fl/fl}$*, *OsxCre*+ mice (n=3) and *Vhl$^{fl/+}$* (Cre-negative) mice (n=2), $5x10^5$ cells were plated in each well with 5 wells per mouse per condition. The assay had two treatment conditions: 5% (v/v) RPMI with 10 g/L casamino acids or 5% (v/v) Δ*psm* supernatant. All the wells received 10 nM 24,25-dihydroxyvitamin D_3. The cells were fed new media every other day for 14 days by replacing half of the media with fresh media. At day 14, the wells were stained for tartrate-resistant acid phosphatase (TRAP), a marker of osteoclasts. The results of this pilot study indicate that *Vhl$^{fl/fl}$*, *OsxCre*+ whole bone marrow culture may in fact have a blunted increase in *S. aureus*-mediated osteoclastogenesis (**Figure 34**). The data represent a small n, and the data show high variability. It will be important to repeat this study to better understand if *Vhl* deletion in the osteoblast lineage limits osteoclast formation in a functional assay. A robust *in vitro* assay will allow careful study of HIF signaling cascade. *Vhl$^{fl/fl}$*, *OsxCre*+ whole bone marrow cultures can be

tested with different inhibitors of HIF-1α or HIF-2α to test which isoforms of HIF-α are potentially responsible for the observed phenotypes with deletion of *Vhl*. Finally, differences in bone mineral apposition rate should be measured in $Vhl^{fl/fl}$, *OsxCre*+ mice and their littermate controls to understand if bone formation differs and contributes to the observed phenotype in trabecular bone of $Vhl^{fl/fl}$, *OsxCre*+ mice as it is possible that increased bone formation occurs which offsets bone destruction.

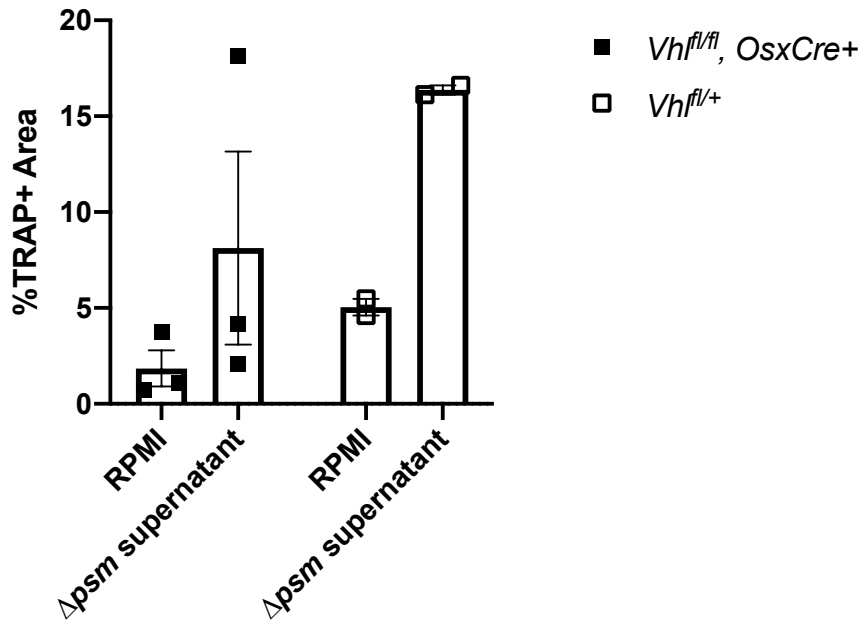

Figure 34: Osteoclast formation in whole bone marrow culture from *Vhl*$^{fl/fl}$, *OsxCre*+ mice and controls

Whole bone marrow was flushed from long bones (femur, tibia, and humerus) of *Vhl*$^{fl/fl}$, *OsxCre*+ mice and *Vhl*$^{fl/+}$ (Cre-negative) littermate controls. $5x10^5$ cells were seeded per well in 96-well plates. Media containing 10 nM 24,25-dihydroxyvitamin D_3 and 5% (v/v) RPMI with casamino acids (10 g/L) or concentrated bacterial supernatants from Δ*psm S. aureus* was changed every other day for 14 days before staining for tartrate-resistant acid phosphatase (TRAP), a marker of osteoclasts. The percentage TRAP-positive area (%TRAP+ area) of each well was measured by imaging the wells on a Biotek Cytation at 20x and via a color thresholding macro on ImageJ. *N*=2-3 mice, as shown, each with 5 well replicates per condition. Error bars represent mean ± *SEM*.

Determine the mechanism by which conditional deletion of *Vhl* in osteoblasts limits transcription of *Tnfsf11* relative to *Tnfrsf11b*

The purpose of the whole bone marrow culture is to better understand if *Vhl* deletion in osteoblast-lineage cells limits *S. aureus*-mediated osteoclast formation. This hypothesis is based on *in vitro* data using an adenovirus to deliver Cre to $Vhl^{fl/fl}$ calvarial osteoblasts. This experiment, outlined in Chapter III, demonstrated the *Vhl* deletion in the osteoblast lineage limits *Tnfsf11* (receptor activator of NF-κB ligand, RANKL) transcription relative to that of *Tnfrsf11b* (osteoprotegerin, OPG). The underlying hypothesis is that *Vhl* deletion impacts osteoblasts through augmentation of HIF signaling. However, it is possible that HIF-independent mechanisms cause the observed phenotype. To test the hypothesis that this phenotype in osteoblast-lineage cells lacking *Vhl* is dependent upon HIF-1α, a double conditional knockout of *Vhl* and *Hif1a* may be important and necessary to see if double knockout rescues the induction of *Tnfsf11* transcription relative to *Tnfrsf11b* transcription. Such a finding would suggest that this phenotype is mediated through von Hippel Lindau protein (VHL) regulation of HIF-1α. An additional method to test the hypothesis that HIF signaling is responsible for the blunting of *S. aureus*-mediated induction of *Tnfsf11* transcription relative to *Tnfrsf11b* transcription is to use pharmacologic approaches to model states of high HIF signaling. If the phenotype is consistent across genetic and pharmacologic models of HIF augmentation, then this will support the hypothesis that VHL acts through HIF and not an independent mechanism. Dimethyloxalylglycine (DMOG) inhibits prolyl hydroxylation of HIF-1α upstream of VHL polyubiquination and proteasomal degradation. DMOG is a commonly used drug to model hypoxia *in vitro*. Using RT-PCR primers outlined in Chapter III, a pilot study was conducted with one replicate containing n=3-4 technical replicates (wells of a 24-well plate). DMOG

treatment of wildtype calvarial osteoblasts was found to blunt the induction of *Tnfsf11* transcription and prevent a rise in the RANKL/OPG ratio at the transcriptional level in response to stimulation with toxin-deficient bacterial supernatant (**Figure 35**). It will be important to repeat this experiment to validate this finding. Additional studies should use alternative pharmacologic agents that augment HIF to confirm that this finding is intrinsic to HIF and not off-target effects.

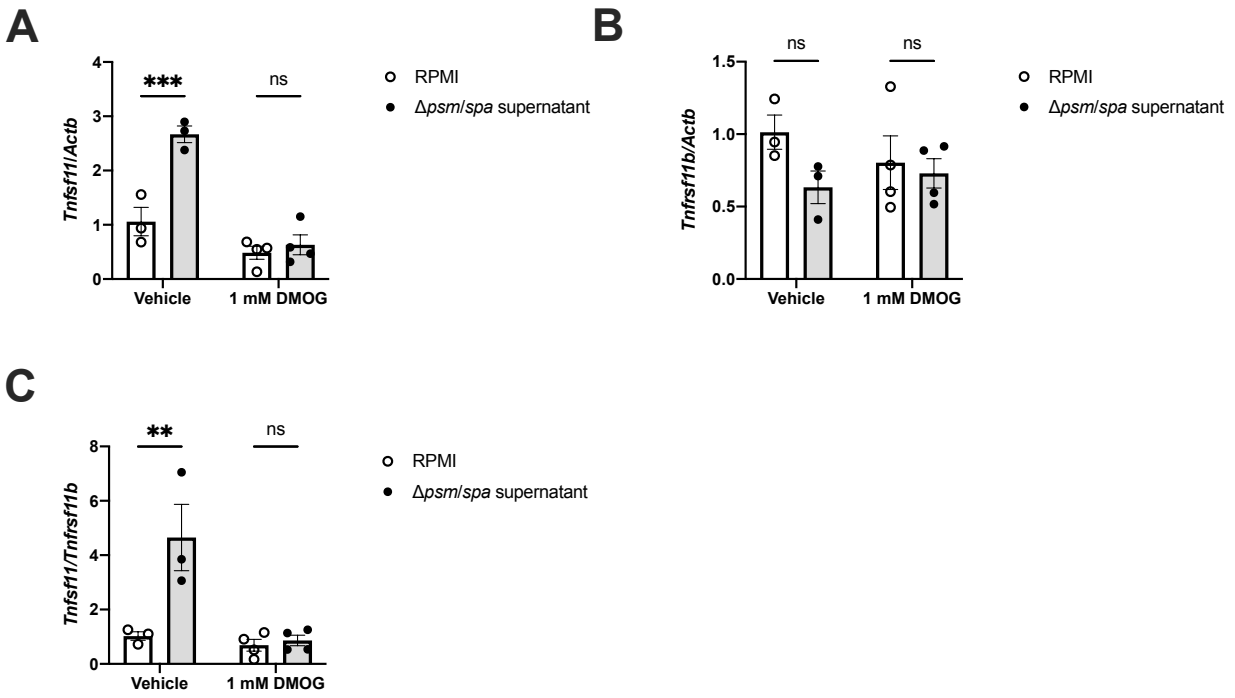

Figure 35: Treatment with DMOG limits *S. aureus*-mediated transcription of *Tnfsf11* (RANKL) in a pilot study

(**A**) Pretreatment (24 h) with 1 mM DMOG or PBS (vehicle) defines two experimental groups in a pilot study (n=3-4 technical replicates [wells of a 24-well plate] as shown). Fold change in transcription of *Tnfs11* (RANKL) relative to *Actb* (β-actin) is shown normalized to the PBS-RPMI group. (**B**) In the same study, fold change in transcription of *Tnfrs11b* (OPG) relative to *Actb* (β-actin) is shown normalized to the PBS-RPMI group. (**C**) Fold change in transcription of *Tnfs11* (RANKL) relative to *Tnfrs11b* (OPG) is shown normalized to the PBS-RPMI group. Fold change was calculated by the $2^{-\Delta\Delta CT}$ method. $^{**}p<0.01$, $^{***}p<0.001$, and ns denotes not significant as determined by two-way analysis of variance (ANOVA) with multiple comparisons. Error bars represent mean ± *SEM*.

Test pharmacologic manipulation of HIF *in vivo*

In addition to studying pharmacologic augmentation of HIF *in vitro*, pharmacologic augmentation of HIF should be tested *in vivo* to determine if alternative methods of HIF augmentation cause similar phenotypes to those observed with genetic knockout of *Vhl*. DMOG has been used previously to test HIF signaling in bone following sterile fracture or ovariectomy [94,101]. In similar studies, DMOG treatment can be tested *in vivo* during *S. aureus* osteomyelitis. In a pilot study, mice were injected subcutaneously over the infected femur with 20 μL of 500 μM DMOG dissolved in PBS (or PBS vehicle) every other day starting on the day of infection for a total of five doses. This dosing schedule has been used previously in a femur fracture model in mice [101]. Following 14 days of infection, mice were euthanized, and the femurs were removed using sterile technique. The femurs were processed for bacterial burdens and for cortical bone loss as described previously [242]. Bacterial burdens were assessed in both male and female mice, and cortical bone loss was assessed in female mice (n=4 mice/group/study). In both males and females, bacterial burdens were found to not significantly differ (**Figure 36A**,**B**). The infected femurs from female mice were analyzed by microcomputed tomography (microCT). The microCT analysis did not reveal any differences in cortical bone destruction between the groups following DMOG treatment with the given dosing schedule (**Figure 36C**). It is possible that DMOG administration did not substantially alter HIF signaling. DMOG may have been inadequately dosed to increase HIF signaling during infection or may not have reached the target at sufficient levels. In order to conclude that HIF augmentation did not alter outcomes in this study, further analysis of HIF-1α accumulation following DMOG treatment must be conducted because it is possible that the dose was not high enough in this model. More potent HIF modulators have recently been developed that may impact HIF

signaling to a greater extent and thereby elucidate impacts of pharmacologic modulation of HIF during osteomyelitis [257]. Finally, future studies should investigate infection-induced changes in trabecular bone as trabecular bone changes were the most striking within the genetic studies of *Vhl* conditional knockout of Chapter III.

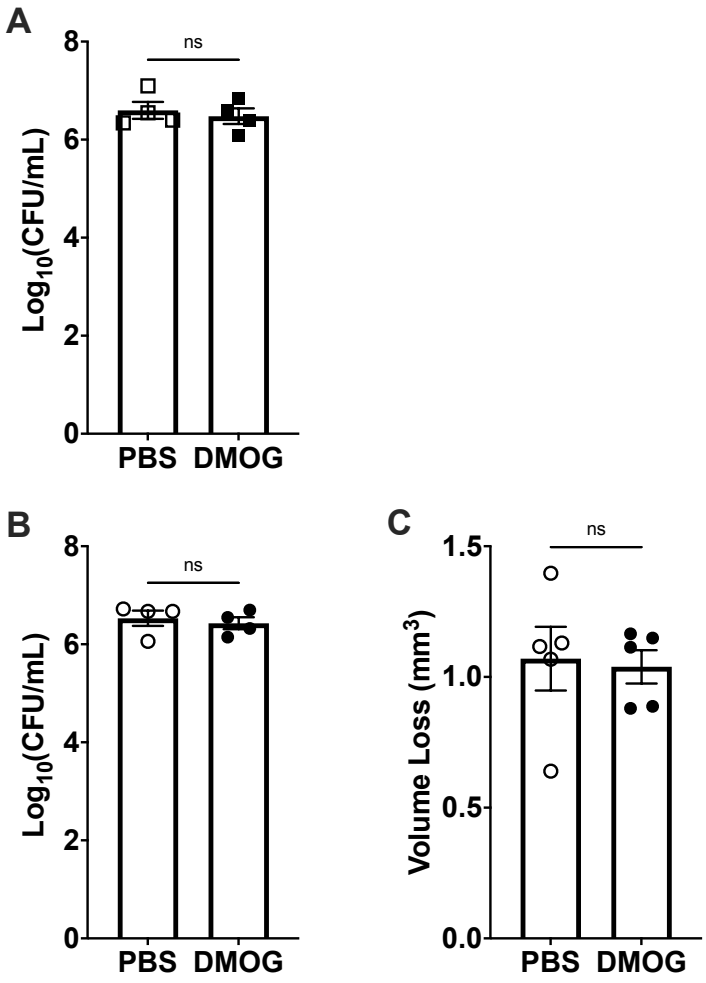

Figure 36: DMOG treatment does not alter bacterial burdens or cortical bone loss during *S. aureus* osteomyelitis

Mice were injected subcutaneously over the infected femur with 20 µL of 500 µM DMOG dissolved in PBS (or PBS vehicle) every other day starting on the day of infection for a total of five doses. (**A**) At post-infection Day 14, infected femurs from PBS- and DMOG-injected mice (*n*=4 male C57Bl6/J mice) were measured for colony forming units (CFU)/mL following homogenization in CelLytic Buffer with serially dilution and counting of CFU. The bacterial burdens do not significantly differ (ns) as determined by unpaired, two-tailed Student's *t*-test. (**B**) Similarly to males in (**A**), bacterial burdens were enumerated in infected femurs from PBS- and

DMOG-injected female mice (*n*=4 female C57Bl6/J mice). The bacterial burdens do not significantly differ (ns) as determined by unpaired, two-tailed Student's *t*-test. (**C**) Cortical bone loss was quantified in the infected femurs of PBS- and DMOG-injected mice (*n*=4 female C57Bl6/J mice) at post-infection Day 14. Cortical bone loss does not significantly differ (ns) as determined by unpaired, two-tailed Student's *t*-test. Error bars represent mean ± *SEM*.

Test alternative Cre-lox models and mouse models of osteomyelitis

It is possible that phenotypes in *Hif1a*$^{fl/fl}$, *OsxCre*+ mice and *Hif1a*$^{fl/fl}$, *LysMCre*$^{+/-}$ mice are masked by compensation from HIF-2α. To better determine if HIF signaling at large is dispensable during osteomyelitis, double knockout with *Hif1a*$^{fl/fl}$ and *Epas1*$^{fl/fl}$ mice may reveal phenotypes previously not observed with individual knockout. Alternatively, knockout of the gene for the common HIF subunit, HIF-1β (also known as the aryl hydrocarbon receptor nuclear translocator [ARNT]) may offer a single knockout method to achieve the same result as both HIF-1α and HIF-2α heterodimerize with HIF-1β to regulate transcription.

Particularly when assessing knockout of genes in the osteoblast lineage in which baseline phenotypes are noted with *Vhl* knockout, alternative Cre models may be advantageous. Inducible Cre models in which Cre is activated days prior to infection may help reveal the influence of cell signaling pathways divorced from baseline architectural changes. An inducible *OsxCre* and other osteoblast-lineage-targeting Cre models have been used to investigate the role of HIF target genes in sterile fracture healing [97]. In a study by Buettmann and colleagues, the authors demonstrate that fracture model greatly impacts the observed role of VEGF-A, a HIF-target [97]. It is also possible that changing the infection model by allowing transcortical femur fracture (as opposed to a pinhole defect) or by incorporating a metallic orthopedic implant will alter the role of HIF signaling during infection. The presence of metallic implants substantially changes the infectious niche in bone. With an implant, bacterial inoculation as low as 10^2 CFU reliably cause stable infection, compared to the standard doses used in our model of osteomyelitis, 10^5-10^6 CFU [121,277]. A comparison of outcomes between infection models may reveal the role of cell signaling pathways previously thought to be necessary or dispensable.

Understand the mechanism by which *Vhl* deletion in the myeloid lineage alters outcomes during osteomyelitis

In addition to increasing the sample sizes for several studies investigating the role of VHL in myeloid-lineage cells during osteomyelitis, it is important to further understand the mechanism by which deletion of *Vhl* in myeloid-lineage cells decreases trabecular BV/TV in infected $Vhl^{fl/fl}$, $LysMCre^{+/-}$ mice compared to the BV/TV of Cre-negative littermate controls. *Vhl* deletion has been shown to increase HIF signaling and thereby increase pro-inflammatory cytokine production in myeloid cells [60]. We have previously shown that IL-1 cytokine signaling contributes to bone loss during *S. aureus* osteomyelitis [121]. In future studies, cytokines should be measured at early and late time points from *in vivo* femur samples in $Vhl^{fl/fl}$, $LysMCre^{+/-}$ mice and compared to levels in control mice. If cytokines are found to be different between the groups, future studies should investigate specific blockade of cytokines to reveal which factors cause changes in trabecular bone. Additionally, bone histomorphometry should be performed on infected and contralateral femurs from $Vhl^{fl/fl}$, $LysMCre^{+/-}$ mice to determine if, in fact, changes in osteoclast abundance are present relative to that of control mice during infection. If such changes are observed, whole bone marrow culture *in vitro* may help determine specific mechanisms as described for $Vhl^{fl/fl}$, *OsxCre*+ mice.

While investigating trabecular bone changes in $Vhl^{fl/fl}$, $LysMCre^{+/-}$ mice, mock infection was used to compare trabecular BV/TV in injured and contralateral femurs of $Vhl^{fl/fl}$, $LysMCre^{+/-}$ mice and Cre-negative littermate controls. It was observed that the average trabecular BV/TV in contralateral limbs was higher in the respective mock-infected femurs of both $Vhl^{fl/fl}$, $LysMCre^{+/-}$ mice and Cre-negative littermate control mice. This finding was not tested statistically as it was not a comparison that was initially considered, and the initial data were not powered for this

additional comparison. However, the difference in the average BV/TV measurements is suggestive that systemic factors (circulating cytokines or infection-associated hematopoiesis) may contribute to declines in trabecular BV/TV. The hypothesis that *S. aureus* osteomyelitis causes global declines in trabecular bone can be tested by comparing trabecular BV/TV of wildtype littermate mice randomly assigned to *S. aureus* infection or mock infection with subsequent comparison at post-infection/post-injury Day 14. By comparing the injured/infected and contralateral trabecular BV/TV, it may be determined if global changes occur due to *S. aureus* infection. If such a change is found, *S. aureus* infection in other tissue types could be incorporated as a variable to determine if the location (osseous or otherwise) of infection impacts changes in trabecular BV/TV or not.

Investigation of incidental findings

Though the experiments in Chapter III were designed to investigate phenotypes related to *S. aureus* osteomyelitis, several incidental findings were observed that warrant future investigation. $Vhl^{fl/fl}$, $LysMCre^{+/-}$ mice were observed to bleed from the nares following CO_2 asphyxiation unlike Cre-negative littermate control mice (**Figure 37**). This phenotype was reproducible and present in every mouse of this genotype that was euthanized in this study regardless of sex, active infection, or age (data not shown). With the help of the Bastarache group at Vanderbilt University Medical Center, the lungs from $Vhl^{fl/fl}$, $LysMCre^{+/-}$ mice were examined for histology and demonstrated diffuse alveolar hemorrhage, unlike the lungs of Cre-negative littermate control mice (data not shown). Alveolar hemorrhage has been observed previously secondary to CO_2 asphyxiation and varies by mouse strain [278]. One mechanism theorized to contribute to acute lung injury is production of reactive oxygen species (ROS) during acute hypoxia [279]. HIF signaling has been described to contribute to ROS production in

myeloid cells [60]. Therefore, it may be possible that pro-inflammatory-primed myeloid cells in *Vhl*$^{fl/fl}$, *LysMCre*$^{+/-}$ mice cause a more profound hemorrhage. The lungs of mice with conditional deletion of *Vhl* in macrophages have been studied previously. Previous studies have shown that *Vhl* deletion in alveolar macrophages impacts cell differentiation and metabolism [280,281]. However, increased alveolar hemorrhage upon euthanasia was not described in these studies despite a focus on lungs. This may be due to the method of euthanasia, as isoflurane and pentobarbital overdose cause substantially less alveolar hemorrhage and edema upon histology in wildtype mice compared to CO_2 asphyxiation [282,283]. This phenotype of hemorrhage is robust and dramatic. Given the prominent role myeloid cells have during infection, future studies should also investigate the role of *Vhl* in myeloid-lineage cells during infectious pneumonia. Elucidating the underlying mechanism behind CO_2 asphyxiation-induced hemorrhage in this mouse may have broad ramifications for understanding lung homeostasis in wildtype mice and even human patients suffering from acute lung injury.

Figure 37: *Vhl*$^{fl/fl}$, *LysMCre*$^{+/-}$ mice exhibit nasal and pulmonary hemorrhage upon CO_2 asphyxiation

(**A**) Cre-negative littermates (*Vhl*$^{fl/fl}$ *or Vhl*$^{fl/+}$) are shown post-mortem from CO_2 asphyxiation (3 minutes with CO_2 flowing at 5 L/min with a Euthanex SMARTBOX system per Vanderbilt University Medical Center guidelines). *N*=4 female mice. At right, a representative lung shown from a male *Vhl*$^{fl/fl}$ mouse is shown following dissection after CO_2 asphyxiation. (**B**) *Vhl*$^{fl/fl}$, *LysMCre*$^{+/-}$ mice (littermates of [**A**]) are shown post-mortem from CO_2 asphyxiation. *N*=4 female mice. At right, a representative lung shown from a male *Vhl*$^{fl/fl}$, *LysMCre*$^{+/-}$ mouse is shown following dissection after CO_2 asphyxiation. The representative lung shown (**B**) is from littermate of that shown in (**A**). All mice shown were euthanized on post-infection Day 14 in our murine model of *S. aureus* osteomyelitis.

An additional incidental finding from studies of Chapter III was the profound decrease in lymphocytes in peripheral blood when analyzing complete blood counts of *Vhl*$^{fl/fl}$, *OsxCre+* mice (**Figure 38**). This phenotype has been observed previously in published studies with knockout of *Vhl* in the osteoblast-lineage cells, and prior studies have shown that B-cells decline but not T-cells [284]. However, the mechanism is unclear how *Vhl* deletion in the osteoblast-lineage (including stromal cells of the bone marrow) alters B-cell production in the bone marrow. It was previously established that stromal cells in the bone marrow regulate the B-cell hematopoietic niche [285]. Recent studies have shown that stromal cells in the bone marrow regulate lymphocytes upon mechanical stimulation, by the release of exosomes, and through production of cytokines [286–288]. It is possible that the differences in bone architecture alter mechanical sensing in the bone marrow or the predominance of stromal cell subpopulations. It is also possible that perturbation of B-cell development in *Vhl*$^{fl/fl}$, *OsxCre+* mice is by another mechanism such as sclerostin. It has been suggested that *Vhl* deletion in osteoblasts decreases sclerostin which thereby alters B-cell development [289]. However, the phenotype is greater in *Vhl* knockout than in mice lacking sclerostin suggesting that alternative mechanisms are contributing. Future studies should investigate the mechanisms by which *Vhl* deletion in osteoblasts impacts lymphocyte development.

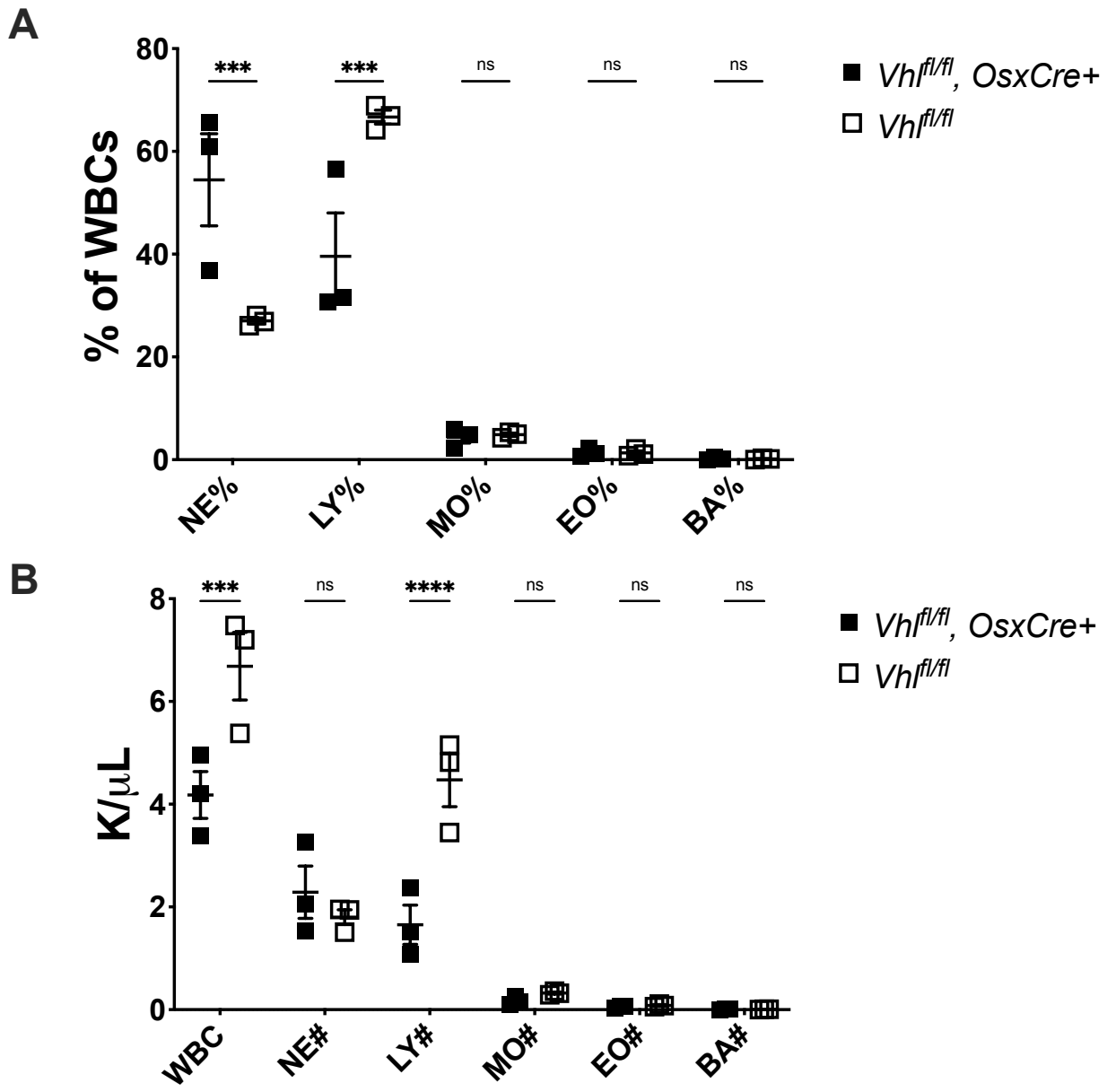

Figure 38: *Vhl*$^{fl/fl}$*, OsxCre+* mice have reduced lymphocytes in the peripheral blood

(**A**) The percentage of total white blood cells (WBC) is shown for neutrophils (NE), lymphocytes (LY), monocytes (MO), eosinophils (EO), and basophils (BA) from the blood of *Vhl*$^{fl/fl}$, *OsxCre+* mice and littermate *Vhl*$^{fl/fl}$ mice (*n*=3 males) following euthanasia at post-infection Day 3 in our murine model of *S. aureus* osteomyelitis. Of note, these mice had doxycycline withdrawn from the drinking water at postnatal age 1 week unlike most experiments presented in

Chapter III. ***p<0.001 and ns denotes not significant as determined by two-way analysis of variance (ANOVA) with multiple comparisons. (**B**) The same data presented of (**A**) is shown as absolute numbers in thousand cells per μL (K/μL) for the corresponding cell populations and the total count for WBC. ***p<0.001, ****p<0.0001, and ns denotes not significant as determined by two-way ANOVA with multiple comparisons. Error bars represent mean ± *SEM*.

Summary of experimental findings: Development of a poly(propylene sulfide) (PPS)-based nanoparticle delivery system for treatment during osteomyelitis

In addition to exploring the basic biology of HIF signaling during osteomyelitis, a major objective of this dissertation work was to explore alternative treatment delivery mechanisms for osteomyelitis. *S. aureus*, the most common cause of osteomyelitis, has demonstrated dynamic flexibility to weather antimicrobial attack through direct resistance and mechanisms of antimicrobial tolerance [20]. It is critical that novel therapeutics be developed to maintain superiority in the antimicrobial-antimicrobial resistance arms race between treatments and pathogens [230]. Many therapeutics in developmental pipelines exhibit poor aqueous solubility, which prevents parenteral delivery without the aid of a carrier such as nanoparticles [270,271]. In Chapter IV, poly(propylene sulfide) (PPS)-based nanoparticles were investigated for delivery of diflunisal, an antivirulence compound with poor aqueous solubility. The aims of Chapter IV were to (1) develop a nanoparticle-based drug delivery platform for bone infection and (2) deliver an efficacious therapeutic to improve antibacterial immunity and/or bone healing during osteomyelitis. In Chapter IV, it is shown that diflunisal-loaded PPS nanoparticles accumulate in infected femurs and limit cortical bone loss during *S. aureus* osteomyelitis [242].

A nanoparticle-based drug delivery platform for bone infection

Data from experiments performed in Chapter IV demonstrated that PPS nanoparticles that are approximately 65 nm in diameter accumulate at infected femurs preferentially compared to the uninfected, contralateral femur. To our knowledge, these are the first studies to demonstrate that a synthetic polymeric nanoparticle itself accumulates at infected bone. One advantage of developing a nanoparticle carrier for the treatment of infections is the intrinsic modularity. The pharmacologic carrier may be substituted for any drug with similar chemistry—

in this case hydrophobic—that is compatible with the hydrophobic PPS core of the nanoparticle. We demonstrate that PPS nanoparticles accumulate preferentially in the first 24 h after injection and that repeated, daily injection during the 14-day study results in significantly greater accumulation relative to any other organ tested, including well-vascularized organs such as the kidney, liver, and spleen. The studies outlined in Chapter IV also begin to test the influence of alendronate (Aln) conjugation to the nanoparticle corona. Aln is a bisphosphonate that has been used previously to enhance drug delivery of PPS nanoparticles to bone [227]. We show that Aln-conjugation may improve delivery kinetics by accelerating accumulation. Overall, these studies demonstrate that nanoparticles accumulate at infected femurs during *S. aureus* osteomyelitis and are a viable drug-delivery treatment strategy.

Diflunisal-loaded PPS nanoparticles limit cortical bone loss during osteomyelitis

After confirming that nanoparticles accumulate, we went on to show that loading diflunisal, an antivirulence compound, decreases cortical bone destruction without impacting bacterial burdens. We have previously shown that diflunisal decreases toxin-mediated cell death and limits cortical bone destruction when released from a local device [123]. We confirmed that diflunisal limits cortical bone destruction during *S. aureus* osteomyelitis *in vivo* following an alternative drug delivery strategy.

In Chapter IV, we went on to investigate the delivery of diflunisal-loaded PPS nanoparticles with vancomycin, an antibiotic used to treat methicillin-resistant *S. aureus* (MRSA) infections. We showed that vancomycin limits cortical bone destruction, and co-administration of diflunisal-loaded nanoparticles does not further limit cortical bone destruction beyond that of vancomycin alone. Continuing to explore antivirulence treatments in the context

of standard-of-care treatments is important to properly define the potential translational impact of such therapeutics.

Future directions: Investigating poly(propylene sulfide) (PPS)-based nanomaterials for treatment of invasive infection

The future directions for the experiments described in Chapter IV can be divided into those focused on modifying the polymer carrier, the drug cargo, and the infection model.

Modification of the polymer carrier

One of the advantages of synthetic polymeric nanoparticles is that the desired properties (e.g., tissue targeting, circulation time) can be tuned by adjusting the monomers used to synthesize the polymers. In the studies outlined in Chapter IV, PPS nanoparticles were synthesized with a dimethylacrylamide (DMA) corona. DMA is not thought to be inherently targeted to bone. For this reason, alendronate was considered as a grafted agent to improve targeting to bone in Chapter IV. Study of how alendronate alters nanoparticle tracking during osteomyelitis should be continued. However, the use of multiple monomers may further improve drug delivery compared to DMA for untargeted nanoparticles. It would be important to test such compounds as poly(ethylene glycol) (PEG) or polymers with similar chemistries (i.e., poly[(oligoethylene glycol)$_9$ methyl ether acrylate], POEGA). PEG and its derivative, POEGA, are thought to prolong circulation times because of high hydrophilicity [226]. It is important to consider the best polymer for both bone-targeted and untargeted nanoparticles. Future studies could compare the drug delivery between these chemistries during osteomyelitis.

Though Chapter IV investigated the use of nanoparticles to avoid a local delivery device, it may be beneficial to use a demand-responsive, hydrogel device. Recently a PPS-based polymer was designed that can encapsulate hydrophobic drugs in the PPS core as nanoparticles.

These nanoparticles behave as a viscous liquid in solution but reversible crosslinking above physiologic body temperature (37°C) forms a hydrogel [224]. In addition, hydrophilic compounds can be delivered using this hydrogel by avoiding initial nanoparticle fabrication and relying upon hydrogel crosslinking to maintain the drug delivery depot. Such a drug delivery system can also be delivered percutaneously by injection.

To understand if a PPS-based hydrogel drug delivery system can deliver drug to the infected femur during osteomyelitis, I collaborated with Mukesh Gupta, Ph.D., (Duvall lab group, Vanderbilt University) to deliver a HIF-modulating drug within such a polymeric vehicle. The hydrogel polymer, poly(propylene sulfide)-*b*-poly(dimethylacrylamide)-*b*-poly(*N*-isopropylacrylamide)—abbreviated PDN, was used to encapsulate FG-4592 (Roxadustat), a next-generation inhibitor of HIF-1α hydroxylation to stabilize HIF-1α and augment HIF signaling [103,224]. FG-4592 was encapsulated by dissolving PDN polymer and FG-4592 in a 1:1 methanol-tetrahydrofuran solution and adding the resulting solution to water dropwise. PDN nanoparticles with encapsulated FG-4592 were measured by dynamic light scattering to determine nanoparticle size (**Figure 39A**). Encapsulated FG-4592 and free FG-4592 were delivered to cultured primary calvarial osteoblasts from ODD-Luc mice. ODD-Luc mice constitutively express a luciferase that is post-translationally modified similarly to the oxygen-dependent domain (ODD) of HIF-1α [290]. Thus, luminescence can be measured to determine drug activity. It was confirmed that, like free FG-4592, PDN nanoparticles loaded with FG-4592 caused increased luminescence in a dose-responsive manner (**Figure 39B,C**). Of note, excessively high doses of FG-4592 appear to be toxic and decrease luminescence in the assay (**Figure 39B,C**). FG-4592-loaded PDN hydrogels (~30 mg FG-4592 per kg mouse) were subsequently delivered to ODD-Luc mice at the conclusion of surgery (i.e., the beginning of the

S. aureus infection). At post-infection Day 3, the mice were injected with luciferin (3 mg/mouse, 200 μL of 15 mg/mL luciferin via intraperitoneal injection) and imaged via IVIS Spectrum for luminescence. Mice receiving the FG-4592-loaded PDN hydrogel displayed higher luminescent signal at the infected limb compared to that of empty PDN hydrogel-treated animals (p=0.0551, **Figure 39D**). At post-infection Day 7, mice were euthanized, and bacterial burdens were enumerated from the infected femurs. No difference in bacterial burdens was detected in the infected femurs of mice injected with FG-4592-loaded PDN hydrogel or empty PDN hydrogel (**Figure 39E**). These data indicate that the PDN hydrogel successfully delivered FG-4592 to the infected femur of ODD-Luc mice. However, it is unclear if FG-4592 was active at times after post-infection Day 3. It is possible that the drug was exhausted shortly thereafter. We can conclude that delivery of FG-4592 at 30 mg/kg in a PDN hydrogel does not impact bacterial burdens at post-infection Day 7. It will be important in future studies to determine the kinetics of drug release to test if HIF augmentation requires a second administration of FG-4592 via PDN hydrogels. Furthermore, the primary phenotypes observed with conditional deletion of *Vhl* (HIF augmentation like FG-4592 treatment) in skeletal cells were in trabecular bone. Trabecular BV/TV was not assessed in this trial. Future studies should investigate if HIF augmentation via FG-4592 impacts bone remodeling during *S. aureus* osteomyelitis.

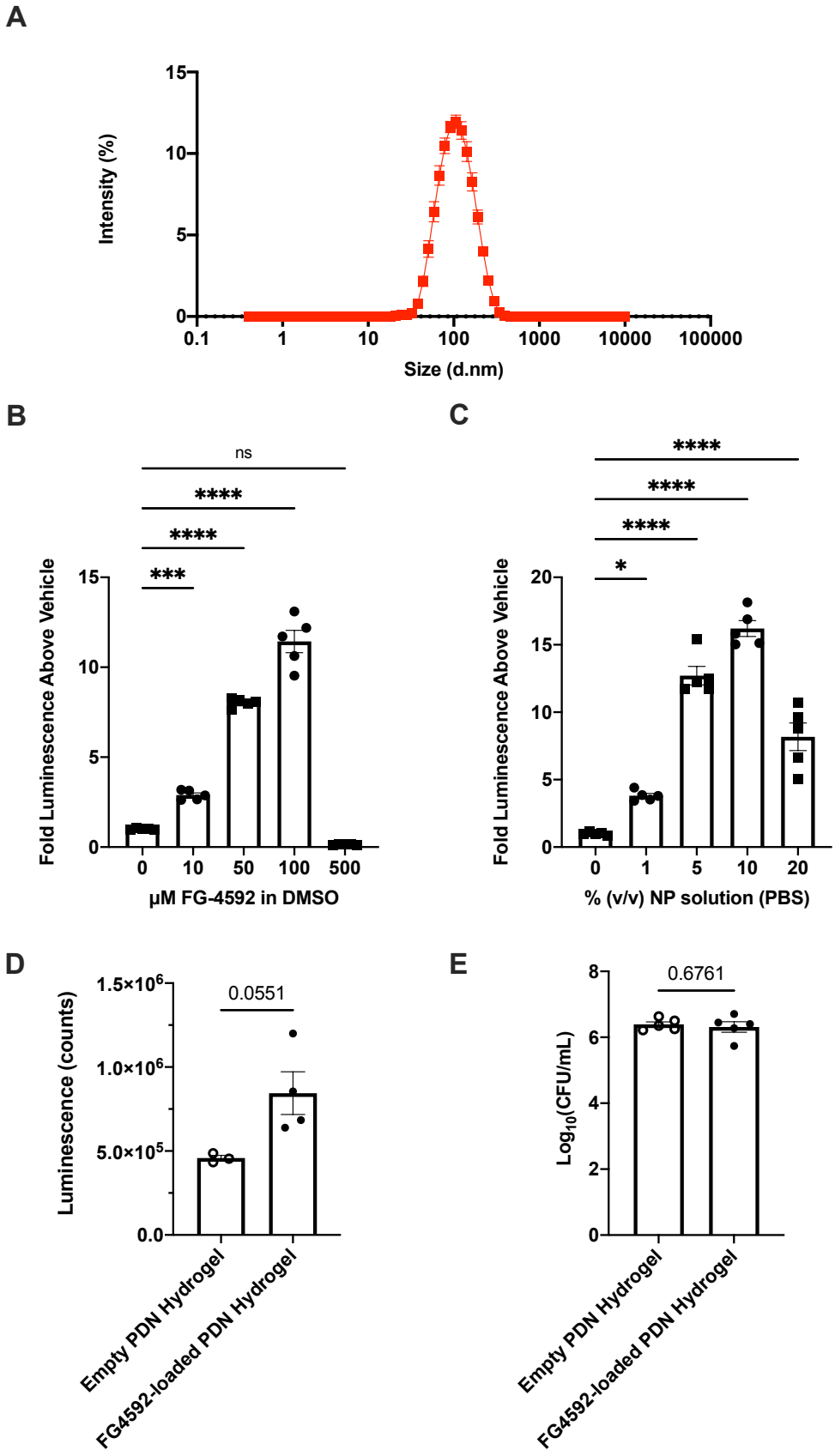
A
Intensity (%)
Size (d.nm)
B
Fold Luminescence Above Vehicle
μM FG-4592 in DMSO
ns
****
****
***
C
Fold Luminescence Above Vehicle
% (v/v) NP solution (PBS)
****
****
****
*
D
Luminescence (counts)
0.0551
Empty PDN Hydrogel
FG4592-loaded PDN Hydrogel
E
Log10(CFU/mL)
0.6761
Empty PDN Hydrogel
FG4592-loaded PDN Hydrogel

Figure 39: Delivery of FG-4592 in a hydrogel-forming PPS-based nanoparticle

(**A**) Dynamic light scattering was used to measure the hydrodynamic diameter of FG-4592-loaded poly(propylene sulfide)-*b*-poly(dimethylacrylamide)-*b*-poly(*N*-isopropylacrylamide) (PDN) nanoparticles. (**B**) Primary calvarial osteoblasts from ODD-Luc mice were treated with FG-4592 delivered in dimethyl sulfoxide (DMSO) vehicle at the doses shown. The "0" condition received DMSO vehicle only. The fold luminescence above the vehicle-only treatment is displayed. Luminescence was read on a Biotek plate reader after treatment with SteadyGlo (Promega). *N*=5 wells from a single biologic replicate. (**C**) Primary calvarial osteoblasts from ODD-Luc mice were treated with FG-4592-loaded PDN nanoparticles at the concentrations shown. Concentrations are displayed in percent volume-per-volume (v/v). The "0" condition received PBS vehicle only. The fold luminescence above the vehicle-only treatment is displayed. *N*=5 wells from a single biologic replicate. For (**B**) and (**C**), **p*<0.05, ****p*<0.001, *****p*<0.0001, and ns denotes not significant as determined by one-way analysis of variance (ANOVA) with multiple comparisons relative to the vehicle control group. (**D**) ODD-Luc mice infected with 10^6 colony forming units (CFU) *S. aureus* had 30 mg/kg FG-4592 administered via PDN hydrogel at time of surgery. Mice were anesthetized with isoflurane on post-infection Day 3. Approximately 15 minutes after intraperitoneal injection of 3 mg luciferin, mice were imaged to detect luminescence from the infected left hindlimb of the animals. *N*=5; 2 mice in empty group did not display any luminescence likely due to poor injection of luciferin and were excluded. Raw luminescent counts are shown. *p*-value is as shown as determined by Welch's *t*-test. (**E**) At post-infection Day 7, bacterial burdens (shown as colony forming units [CFU] per mL) were enumerated from infected femurs of the same mice analyzed in (**D**). *N*=5. *p*-value is as shown as determined by unpaired, two-tailed Student's *t*-test. Error bars represent mean ± *SEM*.

Alternative drug cargo for biomaterial-based treatment of *S. aureus* osteomyelitis

HIF modulators are an important drug class to study as cargo in PPS nanoparticles given the data presented in Chapter III that demonstrate that *Vhl* deletion in osteoblasts limits osteoclast abundance in infected trabecular bone and that *Vhl* deletion in myeloid-lineage cells may impact early bacterial burdens. Even if HIF modulators are not demonstrated to be superior therapies to antimicrobials, PPS nanoparticles or other biomaterial-based treatment strategies (e.g., PDN hydrogels) offer important tools for testing basic biologic questions. By providing preferential or local delivery, biomaterial-based treatments help deliver drugs to the intended target. Genetic approaches like those outlined in Chapter III have the potential consequence of triggering baseline differences in bone architecture that may impact outcomes unrelated to cell signaling during infection. Effective and efficient pharmacologic approaches avoid baseline differences because the drugs are not delivered until the time of infection. Thus, PPS nanoparticles and related biomaterials should be used as tools to administer difficult-to-deliver drugs to test hypotheses, regardless of translational potential as a therapeutic in itself.

An obvious drug class to consider as cargo in PPS nanoparticles is antimicrobials, the standard-of-care for treatment of osteomyelitis. Some antibiotics like fusidic acid are relatively hydrophobic, a characteristic amenable to encapsulation in PPS nanoparticles. It will be important to test antimicrobials as cargo in nanoparticles as these offer the swiftest path to clinical translation. For any drug cargo used, it will be important to test drug delivery directly at the site of infection to determine percentage of drug delivered that reaches the target site.

Use of diflunisal-loaded nanoparticles for treatment of other infections

Exploration of diflunisal for the treatment of *S. aureus* infection should not be limited to osteomyelitis. While diflunisal has been shown to limit cortical bone destruction in osteomyelitis

secondary to inhibition of virulence pathways, these same virulence pathways directly contribute to disease mortality in other infection models such as systemic infection and pneumonia. Diflunisal-loaded PPS nanoparticles were shown to accumulate at the infected femur. Although surgical trauma likely also contributes to nanoparticle accumulation at the infected femur, it is likely that infection itself contributes to this accumulation. The hypothesis that PPS nanoparticles accumulate at infected sites in other organs should be tested. During systemic infection via intravenous inoculation of *S. aureus*, the kidneys are frequently infected. Testing if nanoparticle accumulation in the kidneys increases following *S. aureus* infection of the organ would test this hypothesis. In this same model, the hypothesis that diflunisal-loaded nanoparticles limit disease mortality during *S. aureus* systemic infection may also be tested. Because of the strong preclinical work demonstrating that diflunisal limits toxin production in *S. aureus*, further research is necessary to understand the impacts of such treatment strategies in other infection models.

APPENDIX

The appendix consists of data that did not pertain directly to key studies in the thesis proposal and that are less well-established. Four parts comprise the appendix. The titles of the appendix subsections are as follows:

A: Impact of ascorbic acid on osteomyelitis

B: Post-operative systemic infection with *S. aureus*

C: Development of a fluorescent-luminescent double reporter strain of *S. aureus*

D: Interference of staphylococcal protein A in a multiplexed cytokine analysis technique

A: Impact of ascorbic acid on osteomyelitis

Introduction

Osteomyelitis, inflammation of bone, is most commonly caused by infection from the Gram-positive bacterium *Staphylococcus aureus* [2,3]. High rates of antimicrobial resistance have fostered interest in alternative therapies and improved drug delivery strategies [10,228]. Ascorbic acid (Vitamin C) is an essential vitamin for humans as the gene, *Gulo*, necessary for synthesis, is nonfunctional [291,292]. In 1932, ascorbic acid was identified as the critical Vitamin C found in citrus fruits that when absent causes scurvy [293,294]. Ascorbic acid is an antioxidant that has been implicated in multiple diseases and physiologic functions [295]. In bone, ascorbic acid is critical for collagen synthesis by serving as a cofactor for collagen prolyl hydroxylation [296–298]. Many of the hallmark phenotypes observed in scurvy are secondary to deficient collagen synthesis [297]. Interestingly, ascorbic acid is also a cofactor for the related hydroxylation of proline residues on HIF-1α, a transcription factor that is critical for proper bone formation and healing [59,77,299].

In addition to its critical role in collagen synthesis and as an antioxidant, ascorbic acid also impacts immune responses [300,301]. Ascorbic acid has been studied in the context of multiple infection models; however, ascorbic acid has not been extensively studied in the context of osteomyelitis [300]. It has been observed that ascorbic acid excretion decreases over the course of infection in human patients with osteomyelitis and oxidation of ascorbic acid is increased in patients with osteomyelitis suggesting that transient increases in ascorbic acid demand may occur in humans with osteomyelitis [302,303].

Ascorbic acid is a relatively cheap supplement that could be rapidly employed in the treatment of *S. aureus* osteomyelitis if evidence suggests its importance *in vivo*. These studies

test the hypotheses that (I) ascorbic acid supplementation improves control of bacterial burdens during osteomyelitis *in vivo* and (II) ascorbic acid deficiency alters bacterial clearance and maintenance of bone architecture during *S. aureus* osteomyelitis.

Results

To determine if ascorbic acid supplementation impacts antibacterial responses and bone healing during *S. aureus* osteomyelitis, mice were treated with 2 g/kg of ascorbic acid by intraperitoneal injection daily during the course of infection. Normal saline, the diluent, served as the vehicle control. 7-week-old, female C57Bl/6J mice were infected using a previously validated mouse model of *S. aureus* osteomyelitis by directly inoculating 10^6 colony forming units (CFU) of AH1263, a USA300-lineage strain of methicillin-resistant *S. aureus* (MRSA) [122,235]. After 14 days of infection, infected femurs were dissected using sterile technique, homogenized, and serially diluted to measure bacterial burdens as done previously [242]. Bacterial burdens and post-infection weight loss did not differ between the ascorbic acid supplementation group and the vehicle control showing that ascorbic acid supplementation does not impact bacterial clearance at post-infection Day 14 (**Figure 40**).

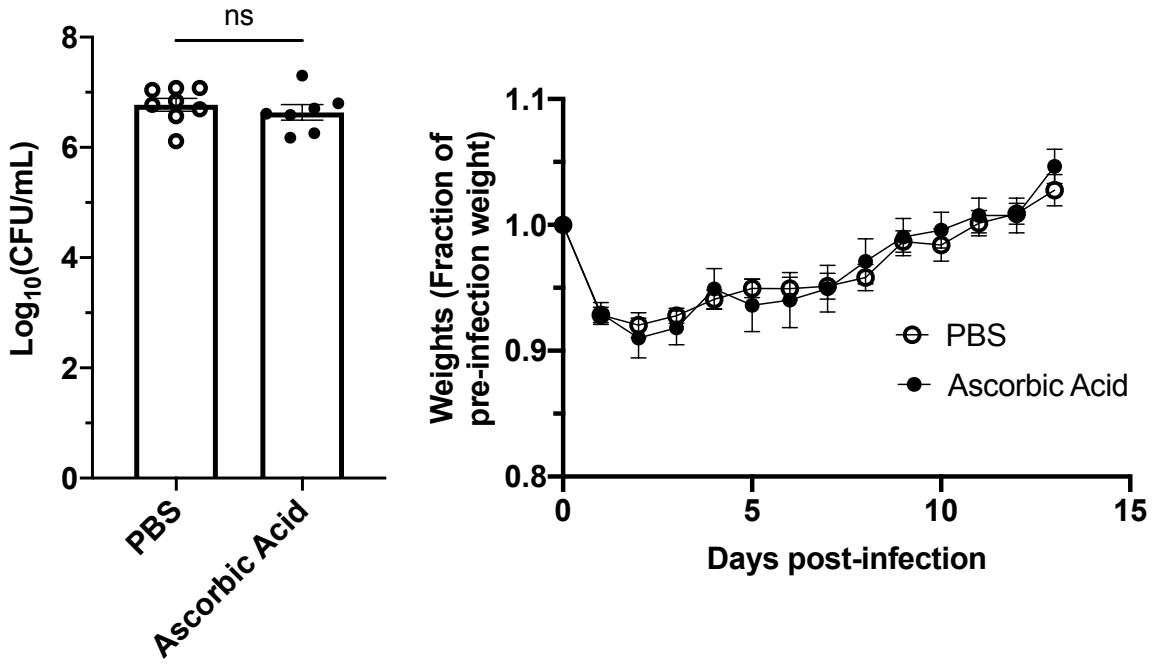

Figure 40: Ascorbic acid supplementation does not alter bacterial burdens or infection-mediated weight loss

At left, the bacterial burdens in infected femurs at post-infection Day 14 are shown for C57Bl/6J mice treated with PBS (vehicle) or 2 g/kg ascorbic acid daily by intraperitoneal injection. At right, the corresponding animal weights are graphed over the course of the infection normalized to the pre-infection starting weights. The bacterial burdens are not significantly different (ns) as determined by unpaired, two-tailed Student's *t*-test. The post-infection weights are not significantly different as determined by mixed effects analysis. *N*=7-8 mice. Error bars represent mean ± *SEM*.

In addition to testing if ascorbic acid supplementation impacts outcomes during osteomyelitis, we also tested if ascorbic acid deficiency alters pathologic changes to bone architecture during osteomyelitis. Unlike humans, mice, like most mammals, produce ascorbic acid *de novo* because of the presence of a functional *Gulo* gene which codes for L-gulonolactone oxidase (GULO) [304,305]. GULO is necessary for the final step of *de novo* ascorbic acid synthesis [291,292,306]. Thus, ascorbic acid deficiency in mice requires not only dietary limitation but also genetic ablation of the functional *Gulo* gene [307]. *Gulo*$^{-/-}$ mice were kindly provided by Fiona Harrison, Ph.D., (Vanderbilt University Medical Center). At 3 weeks of age, half of the *Gulo*$^{-/-}$ mice were switched from standard water containing 1 g/L ascorbic acid (denoted as high ascorbic acid) to 0.03 g/L ascorbic acid (denoted as low ascorbic acid). The mice were fed the standard rodent diet LabDiet 5L0D[1], which does not contain ascorbic acid. The low ascorbic acid mice were maintained on low ascorbic acid water for 4 weeks before being subjected to osteomyelitis using our murine osteomyelitis model [122]. The bacterial strain used was the same used in ascorbic acid supplementation experiments; however, the strain was modified to include a green fluorescent protein fluorophore and the *luxBADCE* operon to permit bacterial burden measurement using an In Vivo Imaging System (IVIS). For reference to strain development, please see Appendix C: Development of a fluorescent-luminescent double reporter strain of *S. aureus*. 4 weeks on low ascorbic acid water has been used previously to induce low ascorbic acid levels in *Gulo*$^{-/-}$ mice without detrimental impacts on overall animal health [308].

After 14 days of infection, the mice were euthanized. The post-infection weights did not significantly differ, suggesting that neither group experienced greater morbidity during the

[1] LabDiet. 5L0D - PicoLab Laboratory Rodent Diet. Available at: https://www.labdiet.com/cs/groups/lolweb/documents/web_content/ndjf/ndy1/~edisp/36142_465407.pdf (Accessed: 13 February 2021)

course of infection for females and males (**Figure 41A**,**B**). The infected femurs and contralateral femurs of infected mice were dissected using sterile technique. To gain an initial understanding of bacterial burdens in the mice, the femurs were imaged by IVIS for luminescence on autoexposure. The quantification of luminescent intensity did not differ between the high ascorbic acid and low ascorbic acid groups for females and males (**Figure 41C**,**D**). *In vitro* data (see Appendix C: Development of a fluorescent-luminescent double reporter strain of *S. aureus*) suggest that bacterial burdens correlate with luminescent signal, suggesting that the bones did not have dramatically different bacterial burdens. This assumption must be confirmed directly in future studies.

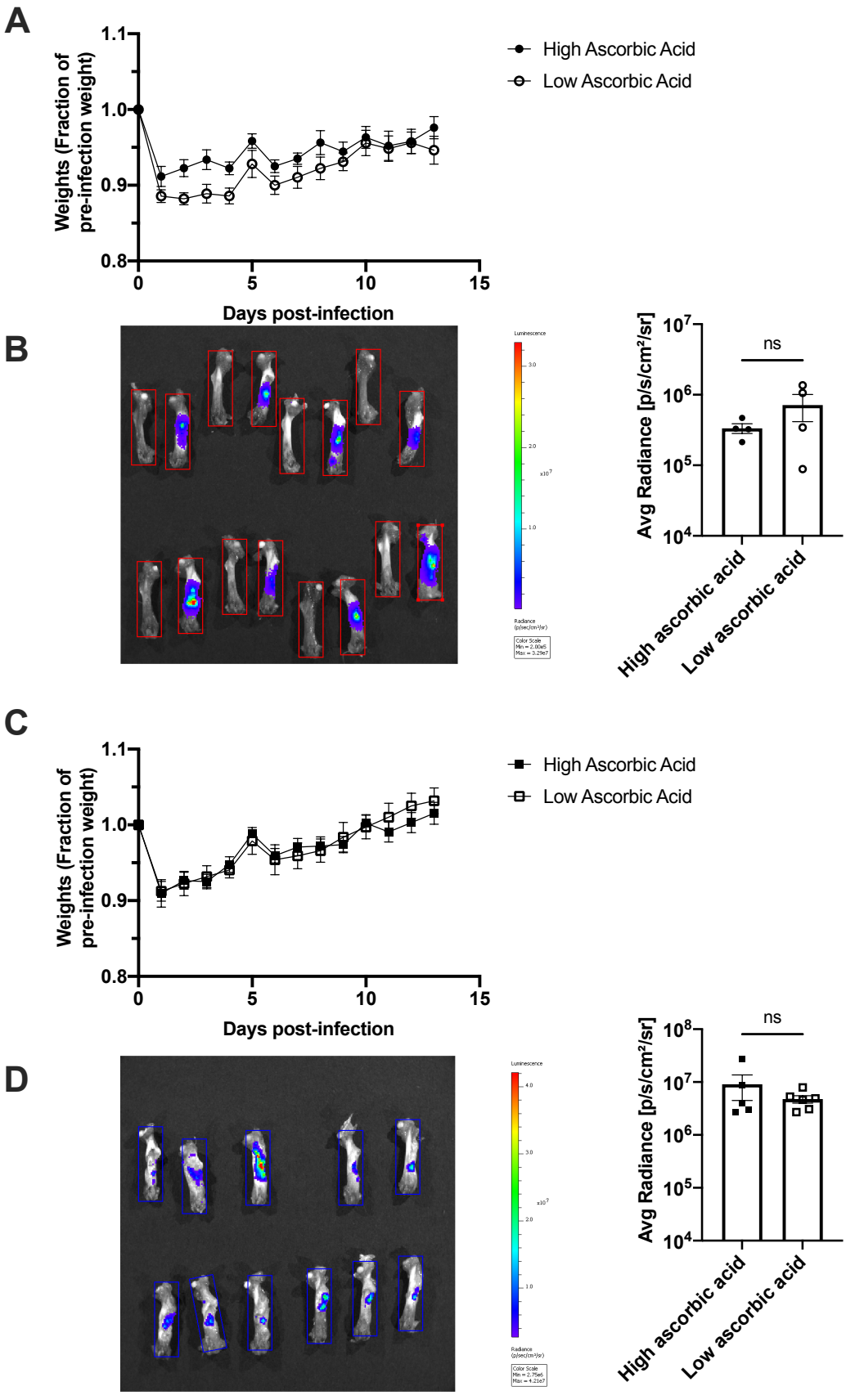
A
Weights (Fraction of pre-infection weight)
1.1
1.0
0.9
0.8
0
5
10
15
Days post-infection
High Ascorbic Acid
Low Ascorbic Acid
B
Luminescence
Radiance (p/sec/cm²/sr)
Color Scale
Min = 2.00e5
Max = 3.29e7
Avg Radiance [p/s/cm²/sr]
ns
High ascorbic acid
Low ascorbic acid
C
Weights (Fraction of pre-infection weight)
Days post-infection
High Ascorbic Acid
Low Ascorbic Acid
D
Luminescence
Radiance (p/sec/cm²/sr)
Color Scale
Min = 2.75e6
Max = 4.21e7
Avg Radiance [p/s/cm²/sr]
ns
High ascorbic acid
Low ascorbic acid

Figure 41: Ascorbic acid deficiency does not alter detected luminescent signal from luminescent *S. aureus*

(**A**) The relative weights shown as a fraction of the pre-infection weights are shown for female *Gulo*$^{-/-}$ mice receiving either high (sufficient) or low (insufficient) ascorbic acid supplementation (n=4). The weights were compared by two-way analysis of variance (ANOVA) and found to not significantly differ (p=0.1750). (**B**) For the mice shown in (**A**), the corresponding infected and contralateral femurs were imaged on IVIS Spectrum for luminescent signal following dissection on post-infection Day 14. The infected and contralateral femurs are shown with the regions of interest used to quantify luminescent intensity (average radiance: p/s/cm^2/sr). At right, quantifications for only the infected femurs displayed are graphed and found to not significantly differ (ns) by unpaired, two-tailed Student's t-test (p=0.2573). (**C**) The weights shown as a fraction of the pre-infection weights are shown for male *Gulo*$^{-/-}$ mice receiving either high (sufficient) or low (insufficient) ascorbic acid supplementation (n=5). The weights were compared by two-way analysis of variance (ANOVA) and found to not significantly differ (p=0.9140). (**D**) For the mice shown in (**C**), the corresponding infected femurs were imaged on IVIS Spectrum for luminescent signal following dissection on post-infection Day 14. The infected femurs are shown with the regions of interest used to quantify luminescent intensity (average radiance: p/s/cm^2/sr). At right, quantifications for only the infected femurs displayed are graphed and found to not significantly differ (ns) by unpaired, two-tailed Student's t-test (p=0.3341). Error bars represent mean ± *SEM*.

To measure changes in pathologic bone remodeling, the infected femurs were imaged using microCT after IVIS imaging. Neither the cortical bone loss or the trabecular bone loss differed between the high and low ascorbic acid groups (**Figure 42**). Furthermore, when assessing differences in cortical bone loss between the high and low ascorbic acid supplementation groups of *Gulo*$^{-/-}$ mice, the male and female mice displayed opposite trends (**Figure 42A,C**). This could reflect a sex-specific difference or that no difference exists between the groups. The trabecular bone analysis showed that infection causes a significant decline in trabecular bone volume-per-total volume (BV/TV) as has been observed in wildtype mice previously [121]. In female mice, no difference was observed between the high and low ascorbic acid supplementation groups of *Gulo*$^{-/-}$ mice (**Figure 42B**). However, in the male mice, the low ascorbic acid group exhibited a significantly higher BV/TV (p=0.0140) by two-way analysis of variance (ANOVA) (**Figure 42D**). These data indicate that ascorbic acid deficiency may significantly impact pathologic bone loss during *S. aureus* osteomyelitis in male mice. Observing the trend in the male mice for decreased cortical bone destruction and the significant increase in BV/TV of low ascorbic acid mice may indicate a difference in bone remodeling in mice with low ascorbic acid during *S. aureus* osteomyelitis.

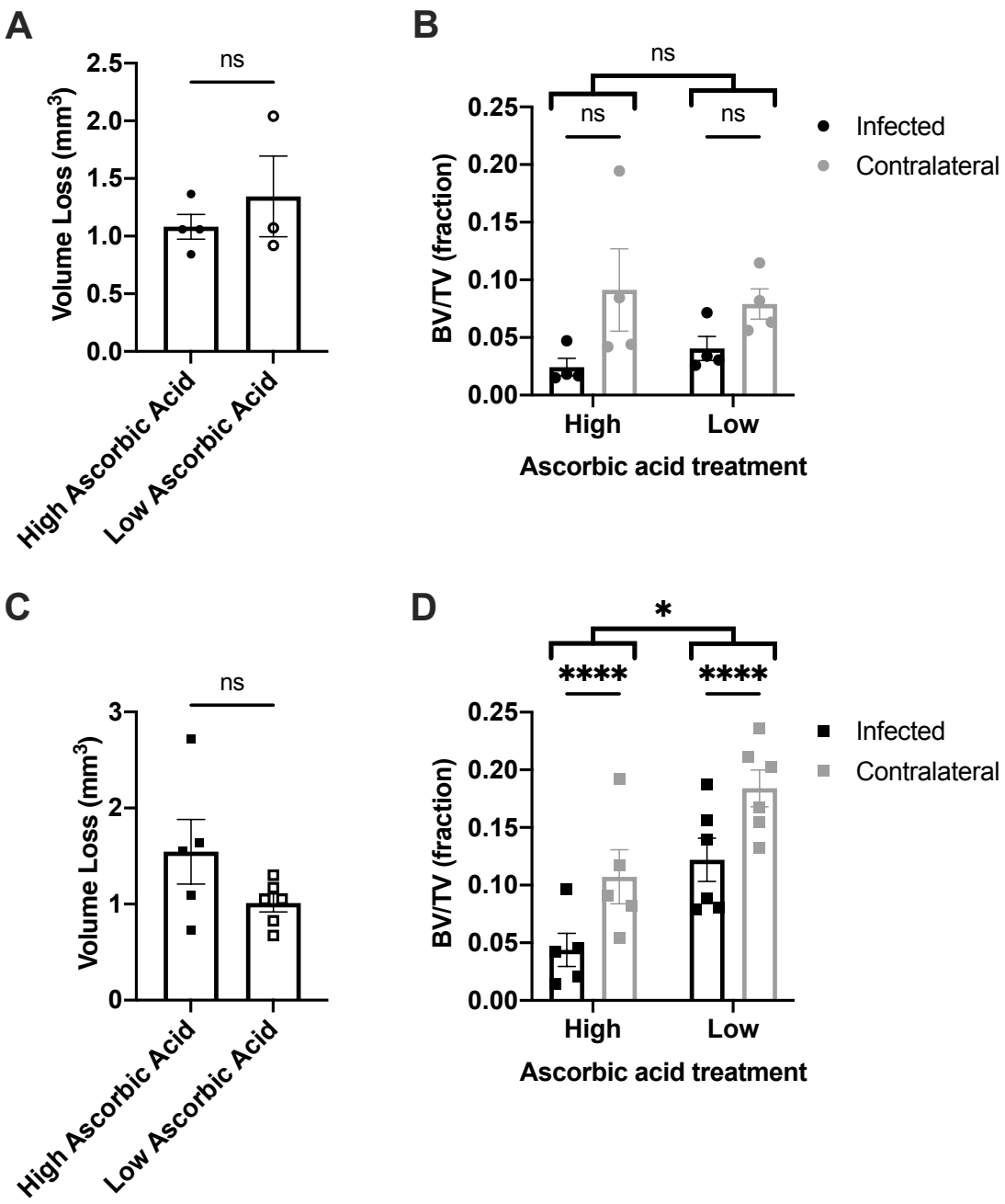

Figure 42: Male *Gulo*$^{-/-}$ mice with ascorbic acid deficiency have higher trabecular bone volume-per-total volume than male *Gulo*$^{-/-}$ with ascorbic acid supplementation following *S. aureus* osteomyelitis

(**A**) Cortical bone loss at post-infection Day 14 was measured via microcomputed tomography (microCT) in female *Gulo*$^{-/-}$ mice receiving either high (sufficient) or low (insufficient) ascorbic

acid supplementation (n=4). ns denotes not significant as determined by unpaired, two-tailed t-test (p=0.4483). (**B**) For the same bones analyzed in (**A**), trabecular bone volume-per-total volume (BV/TV) at post-infection Day 14 was measured via microCT (n=4). ns denotes not significant as determined by two-way analysis of variance (ANOVA) with multiple comparisons. Despite no difference when assessing multiple comparisons, the analysis found that infection caused a significant decrease in BV/TV (p=0.0329). (**C**) Cortical bone loss at post-infection Day 14 was measured via microCT in male *Gulo*$^{-/-}$ mice receiving either high (sufficient) or low (insufficient) ascorbic acid supplementation (n=5-6). ns denotes not significant as determined by unpaired, two-tailed t-test (p=0.1297). (**D**) For the same bones analyzed in (**C**), trabecular bone volume-per-total volume (BV/TV) at post-infection Day 14 was measured via microCT (n=5-6). *p<0.05 indicates that the treatment groups significantly differed; ****p<0.0001 indicates that infected and contralateral limbs significantly differed as determined by two-way ANOVA with multiple comparisons. Error bars represent mean ± *SEM*.

Discussion

Ascorbic acid has been studied in several different infection and inflammatory settings with mixed results [309–315]. In this study, the impact of ascorbic acid was tested in a murine model of *S. aureus* osteomyelitis. Using high doses of ascorbic acid administered daily, experiments tested the hypotheses that ascorbic acid supplementation impacts antibacterial responses and pathologic changes to bone architecture during *S. aureus* osteomyelitis. Furthermore, a genetic model of ascorbic acid deficiency was used to test the hypothesis that physiologically normal levels of ascorbic acid are necessary for antibacterial responses and bone remodeling during osteomyelitis.

Overall, these data show that excess administration of ascorbic acid is not beneficial to antibacterial responses and preventing pathologic bone loss. Additionally, while ascorbic acid is required for homeostasis in immune responses and bone remodeling, mild deficiency of ascorbic acid does not significantly alter bacterial clearance. It is possible that greater ascorbic acid deficiency through further reduction of ascorbic acid supplementation in the low ascorbic acid water group would elucidate the necessity of ascorbic acid during osteomyelitis. Alternatively, a prolonged period with low ascorbic acid greater than 4 weeks could achieve a similar result. Prior studies have found that, while low ascorbic acid treatment (~0.03 g/L ascorbic acid in water) causes significant declines in ascorbic acid in *Gulo*$^{-/-}$ mice, further withdrawal causes more profound phenotypes to emerge within one week [316].

Overall, these data do not support the supplementation of ascorbic acid as a therapeutic in nutritionally replete subjects suffering from *S. aureus* osteomyelitis though it is important to recognize the limitations of extrapolating data from animal experiments to clinical settings [317]. Ascorbic acid is critical for healthy immune responses and minimizing damage to the host during

oxidative attack of pathogens [301]. Ascorbic acid supplementation has been tested and recommended in the care of patients suffering from several infectious diseases [318]. Despite this, the data supporting ascorbic acid supplementation during management of patients with well-studied infectious sequalae, like sepsis, are mixed [314,315]. Each individual pathogen and infectious niche must be uniquely tested to determine the impact of ascorbic acid in such contexts.

Interestingly, while luminescence as a surrogate for bacterial burdens did not suggest a difference between *Gulo*$^{-/-}$ mice receiving either high (sufficient) or low (insufficient) ascorbic acid supplementation, the analysis of trabecular BV/TV indicated there may be a sex-dependent difference. Infected males with low ascorbic acid demonstrated higher trabecular BV/TV compared to male *Gulo*$^{-/-}$ mice that were maintained on a nutritionally replete regimen of ascorbic acid. It will be important to test if differences in ascorbic acid deficiency occurred in a sex-dependent manner and to confirm this finding with additional studies.

Limitations to these experiments include the use of only one bacterial strain and infection model. Furthermore, only post-mortem endpoints were tested for bacterial burdens and changes in bone architecture. Such studies lack longitudinal data and may miss transient differences. Furthermore, it is possible that ascorbic acid deficiency is more influential during chronic osteomyelitis rather than acute infection like that studied in this model. In future investigations, it will be important to confirm that changes in ascorbic acid in the drinking water of mice caused sufficient changes in ascorbic acid levels in the mice *in vivo* at time of infection. Despite this, these data suggest that ascorbic acid supplementation does not improve infection outcomes during *S. aureus* osteomyelitis and that mild deficiencies in ascorbic acid do not impact bacterial burdens during osteomyelitis.

It is also possible that ascorbic acid deficiency might have subtle impacts on bacterial clearance that are only elucidated when mice are subjected to standard-of-care treatments such as vancomycin, a bactericidal antibiotic. Furthermore, antibiotic administration has been shown to influence ascorbic acid levels [319]. To determine if ascorbic acid deficiency impacts bacterial clearance in the setting of standard-of-care therapy, mice could be subjected to a sub-therapeutic dose of vancomycin to prevent complete eradication. In this experiment, vancomycin would be administered every 12 hours for 7 days, and normal saline, the diluent, would be delivered as the vehicle control as done previously [201]. The vancomycin and normal saline groups would be tested in combination with both the high and low ascorbic acid groups. Infected femurs at post-infection Day 7 would be dissected using sterile technique, homogenized, and serially diluted to measure bacterial burdens as done previously [242]. By quantifying the bacterial burdens in vancomycin-treated mice with and without ascorbic acid deficiency, we would test the hypothesis that ascorbic acid is necessary for bacterial clearance of *S. aureus* during osteomyelitis.

B: Post-operative systemic infection with *S. aureus*

The Gram-positive bacterium *Staphylococcus aureus* is the most common etiologic agent of infectious osteomyelitis [2,3]. Trauma is a frequent cause of osteomyelitis due to direct bacterial seeding through breaks in the protective epithelial barrier of the skin [3]. Beyond direct seeding, trauma is theorized to precede episodes of hematogenous osteomyelitis that occur without clear preexisting conditions, primarily in pediatric populations [320]. To better understand if prior trauma predisposes to bacterial infection of bone, a set of experiments was conducted in which animals were injured using sterile technique using a sham model of our murine osteomyelitis model [122,237]. Following injury, mice were systemically infected via retroorbital injection (first set of experiments) or tail vein injection (second set of experiments) with 10^7 colony forming units (CFU) of a USA300-lineage strain of methicillin-resistant *S. aureus* (MRSA), AH1263 [122,235]. Nonoperative control mice were also injected in both experiments, which served as controls. Bacterial burdens from intravenous infection of *S. aureus* were measured in the injured (left) and contralateral (right) limbs of injured animals and in the left and right limbs of uninjured animals.

In the first experiment, retroorbital injection of 10^7 CFU of *S. aureus* was performed under Avertin sedation 48 h following sterile surgery with pinhole injury to the left femur. Following 4 days of infection, mice were euthanized to enumerate bacterial burdens in the kidney and femurs. For both the kidneys and femurs, bacterial burdens did not significantly differ between the groups with 1 or 2 animals exhibiting bacterial seeding in excess of 10^4 CFU/mL recovered from the femurs (**Figure 43**). In the kidneys, the bacterial burdens did not differ, and a large spread was observed in the uninjured group (**Figure 43A**).

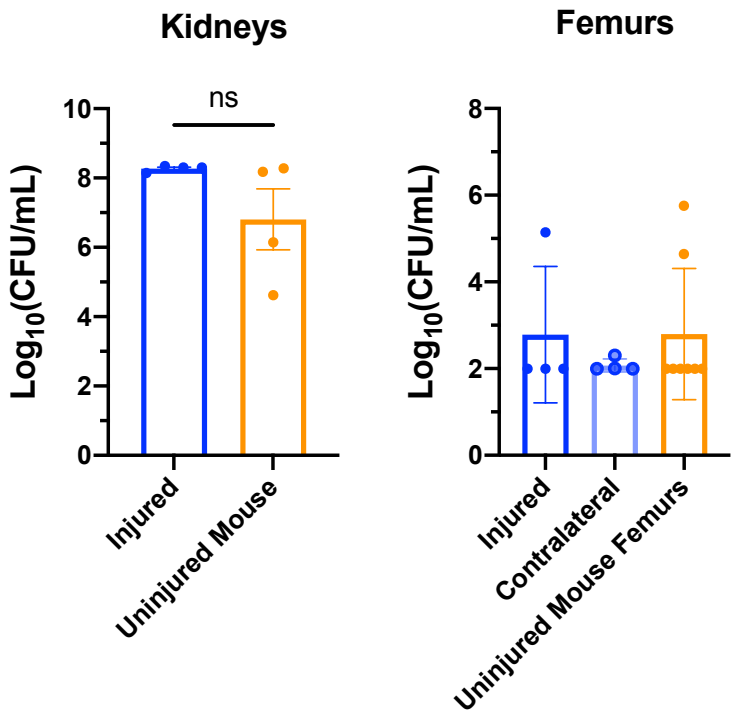

Figure 43: Prior injury does not alter bacterial burdens following retroorbital injection of *S. aureus*

48 h post-injury, mice were intravenously injected with 10^7 colony forming units of *S. aureus* along with uninjured control mice (n=4). On Day 4 post-infection, bacterial burdens were determined for kidneys and femurs as shown. Organs were homogenized in 500 µL PBS, serially diluted in PBS, and plated on tryptic soy agar to count bacterial colony forming units (CFU). Injured (left) and contralateral (right) femurs are shown separately for injured mice. For uninjured mice, the left and right femurs are aggregated as shown for a total of 8 femurs from 4 mice. When bacterial burdens were not detected, the limit of detection (10^2 CFU/mL) was arbitrarily set as the numerical value for graphing purposes (graphed at 2 on $\log_{10}$ scale). Bacterial burdens for kidneys are not significantly (ns) different as compared by unpaired, two-tailed Student's *t*-test. Bacterial burdens for femurs were not compared statistically as the data

are not normally distributed and appear to be stochastic with few femurs showing CFU above the limit of detection. Error bars represent mean ± *SEM*.

A second model of systemic infection following injury was used in which *S. aureus* was injected via the tail vein rather than via the retroorbital vein. Both injection sites have been used in prior studies in which an implant was inserted into bone prior to systemic infection [321,322]. It is possible that one injection model may demonstrate greater seeding to bone. As with the retroorbital-based method described previously, injury was induced via our osteomyelitis model. 48 h post-injury, 10^7 CFU *S. aureus* was injected via the lateral tail vein without sedation. The animals were monitored daily for 4 days prior to euthanizing the animals to assess bacterial burdens. The bacterial burdens were assessed by sterile dissection of the respective organ, homogenization in 500 μL PBS, serially dilution in PBS, and plating on tryptic soy agar to count CFU. The bacterial burdens in the kidneys and livers of the injured and uninjured mice were compared by two-way analysis of variance (ANOVA) and found to significantly differ (**Figure 44A**). With multiple comparisons, the CFU burdens in the liver were found to be higher in the uninjured mice (**Figure 44A**). These data suggest that prior trauma limited bacterial burdens in organs frequently seeded during systemic *S. aureus* infection. The bacterial burdens in the femurs were also compared between the groups. Though not reaching significance when analyzed by the Kruskall-Wallis test (p=0.3365), the average bacterial burdens in the femurs of uninjured animals were higher than those of the other groups, which is similar to the results seen in the livers and kidneys (**Figure 44B**). The data were analyzed by a non-parametric test because the data for the uninjured femurs appears bimodal and non-Gaussian. These results suggest that prior injury may be protective from systemic infection by an unclear mechanism.

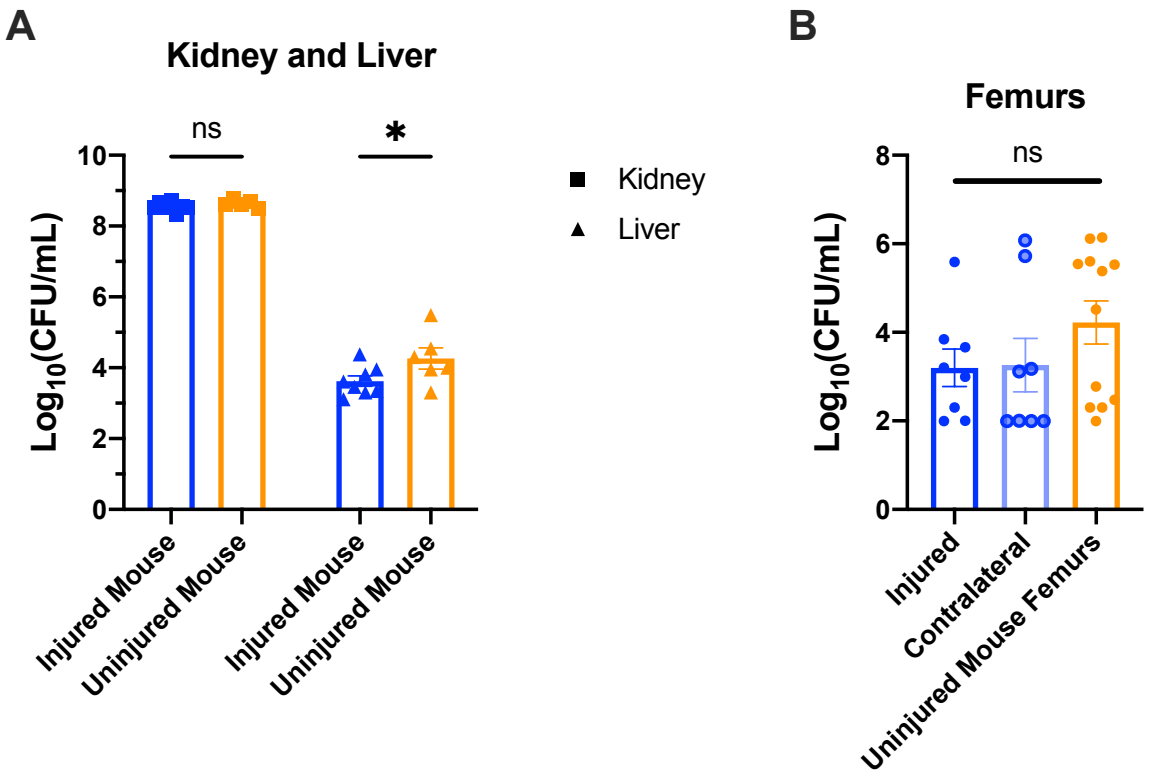

Figure 44: Prior injury decreases bacterial burdens in the liver following tail vein injection of *S. aureus*

(**A**) Bacterial burdens at post-infection Day 4 are displayed for both the kidneys and livers of mice following systemic infection via tail vein injection of 10^7 colony forming units (CFU) *S. aureus*. The groups compared are uninjured control mice and mice that were injured in a sterile mock infection of post-traumatic osteomyelitis. The bacterial burdens were compared by a mixed effects model and found to significantly differ between experimental groups (p=0.0180).*p<0.05 and ns denotes not significant as determined by multiple effects model with multiple comparisons. (**B**) Injured (left) and contralateral (right) femur bacterial burdens from injured mice are graphed in blue alongside burdens from right and left femurs from uninjured animals at post-infection Day 4. Femurs with no detectable bacterial burdens are arbitrarily graphed at the

limit of detection, 2. ns denotes not significant as determined by Kruskall-Wallis test (p=0.3365). N=8 (2 mice succumbed in the uninjured group and are not displayed; one kidney in the uninjured mouse group was contaminated during harvest and excluded). Error bars represent mean ± *SEM*.

Intriguingly, two mice in the uninfected group also succumbed to infection during the 4-day experiment while no mice in the injured group succumbed (**Figure 45A**). This finding is underpowered to draw clear conclusions but with the data showing significantly lower bacterial burdens in the livers may suggest that prior injury has a protective impact on antibacterial immunity. Over the course of the infection, the weights significantly differed between the groups. Because of the nature of the experimental design, the weights of the injured mice were perturbed by the surgical injury prior to the infection itself. Therefore, the data are graphed in two ways. In the first method, weights are normalized to the animal weights immediately prior to intravenous injection of *S. aureus* to initiate systemic infection in both groups (**Figure 45B**). In the second method, weights are normalized to the measured animal weights prior to initial perturbation. That is, weights in the injured group are normalized to the pre-surgical weight recorded two days prior to infection, and in the uninjured group, the weights are normalized to the pre-infection weight. (**Figure 45C**). When normalized to the weights just prior to infection via lateral tail vein injection, the uninjured animals demonstrated significantly greater percent weight loss relative to the injured group (**Figure 45B**). When normalized to weights prior to injury or infection depending on the group, the weights initially deviate as the injury itself caused weight loss not experienced by the uninjured mice; however, the weights equilibrated as weight loss was greater in the uninjured group following infection onset (**Figure 45C**). These data indicate that prior injury may limit the ability of *S. aureus* to infect the host. It is possible that prior injury causes an inflammatory response that trains the immune system or induces a hyper-inflammatory state that is more capable of limiting bacterial survival at early time points. However, given the lack of such findings in the model in which retroorbital injection was used, this may be coincidental. Future studies should determine whether such a protective phenotype

exists. Follow-up studies could then be conducted to understand what mechanism may be causing the observed differences between these groups.

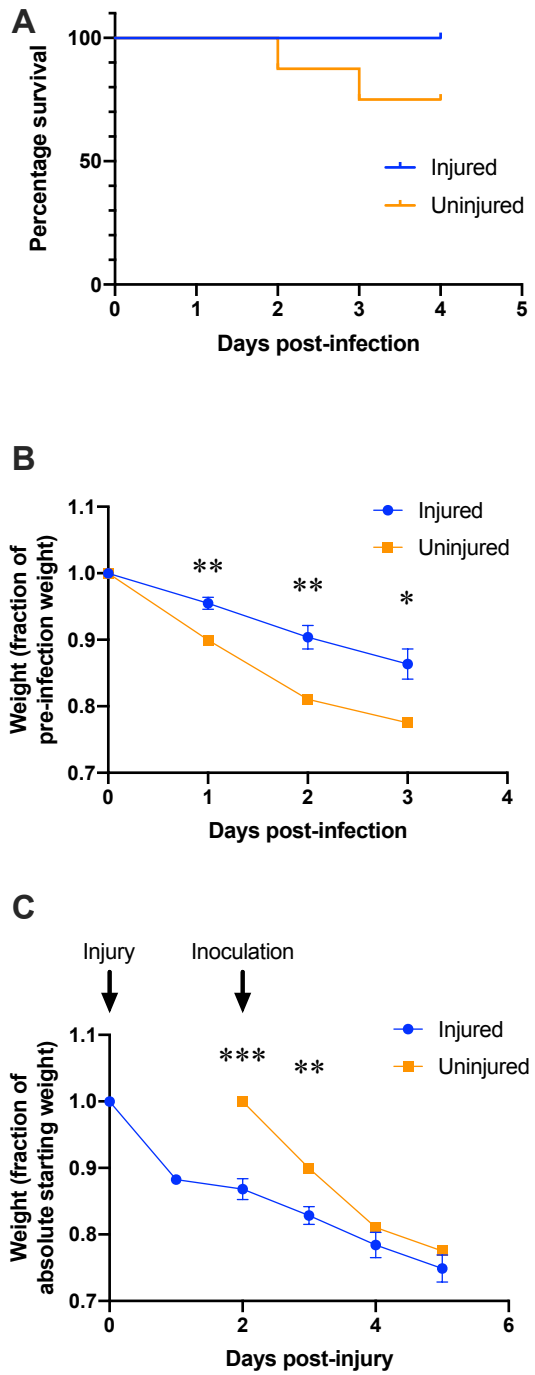

Figure 45: Prior injury alters systemic responses to *S. aureus* infection via tail vein injection

(**A**) The mortality curves are shown for injured (blue) and uninjured (orange) mice following systemic infection of *S. aureus* via lateral tail vein injection of 10^7 CFU. For the mice described

in the survival curve of (**A**), fraction of pre-infection weight (**B**) and fraction of absolute starting weight (**C**) are displayed for the duration of the experiment. *p<0.05, **p<0.01, and ***p<0.001 as determined by mixed effects analysis with multiple comparisons. N=8 (2 mice in the uninjured group succumbed as displayed in [**A**]). Error bars represent mean ± *SEM*.

C: Development of a fluorescent-luminescent double reporter strain of *S. aureus*

Fluorescent and luminescent reporter strains have been used in multiple animal infection models including bone infection models [323–325]. Fluorescent strains permit evaluation of bacterial localization in post-mortem samples and intravital imaging. Luminescent strains have been used as a surrogate for bacterial burdens in longitudinal evaluation [323]. Luminescent strains require active metabolism unlike many fluorophores which often maintain fluorescent capability in flash-frozen samples. Thus, double labeled strains allow longitudinal tracking through the luminescent reporter and post-mortem detection through identification of the fluorophore.

To generate dual fluorescent-luminescent strains of *S. aureus*, I used the phi-85 bacteriophage to transduce a previously published *luxBADCE* operon (chloramphenicol resistance) into erythromycin-sensitized LAC USA300 strains containing superfolder-green fluorescent protein (sfGFP, Cd resistance) or mCherry (tetracycline resistance) [127,324]. That is, the construct P*gapA*-*luxBADCE*, integrated into the chromosome within pseudogene USA300HOU_1102 [324], was transduced with phi-85 into LAC *attC*::P*sarA*-sfGFP [127] and into LAC *attC*::P*sarA*-*sodRBS*-mCherry. Prior to transducing the luminescent allele, LAC *attC*::P*sarA*-*sodRBS*-mCherry was generated as follows. The allele *attC*::P*sarA*-*sodRBS*-mCherry was integrated into LAC USA300 by the lab Victor Torres (New York University). The *attC*::P*sarA*-*sodRBS*-mCherry allele was PCR amplified from the genomic DNA of this strain by Valeria M. Reyes Ruiz (Laboratory of Eric Skaar, Vanderbilt University Medical Center) and cloned into PJC1306 using Gibson assembly. PJC1306 containing this allele was electroporated into RN9011 and integrated into the genome with tetracycline selection for successful integration. The *attC*::P*sarA*-*sodRBS*-mCherry allele was transduced with phi 85 into

an erythromycin-sensitized USA300-lineage *S. aureus*, AH1263 [235], by Brittney Gimza (Laboratory of Jim Cassat, Vanderbilt University Medical Center). The resulting LAC *attC*::P*sarA-sodRBS*-mCherry was the mutant into which the construct P*gapA-luxBADCE* was transduced. The resulting dual fluorescent-luminescent strains were confirmed by imaging on IVIS Spectrum to detect given fluorescent and luminescent markers (**Figure 46A,B**). sfGFP-Lux denotes the strain that contains sfGFP and the *luxBADCE* operon. mCherry-Lux denotes the strain that contains mCherry and the *luxBADCE* operon. To confirm that the gross virulence of *S. aureus* was maintained, the new strains were grown on sheep blood agar plates to observe hemolysis relative to the wildtype parental strain, an erythromycin-sensitized USA300-lineage *S. aureus*, AH1263 [235]. The hemolysis on the sheep blood agar plates (Remel: #01200) was similar between the samples tested (**Figure 46C,D**). These data suggest that two dual fluorescent-luminescent strains were generated that have similar hemolysis to the wildtype parental strain, AH1263.

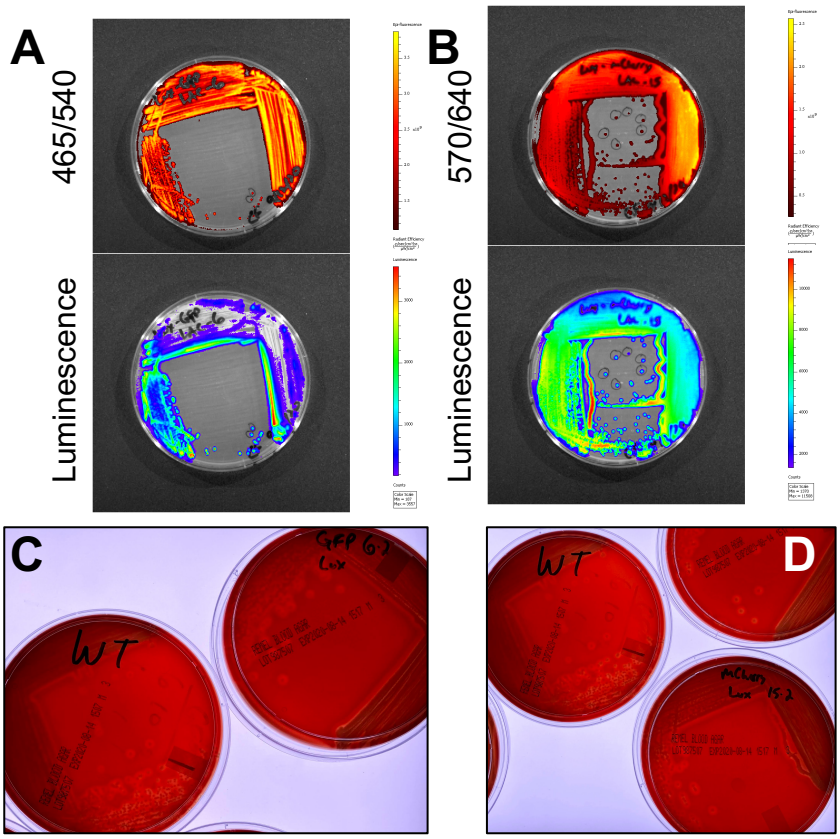

Figure 46: Confirmation of sfGFP-*lux* and mCherry-*lux* strains

(**A**) A transduction clone of sfGFP-Lux streaked out on tryptic soy agar containing $CdCl_2$ was imaged by IVIS for GFP fluorescence (Em: 465 nm/Ex: 540 nm, 5s exposure, small binning, high intensity f/stop of 2) and luminescence (5 second exposure). (**B**) A transduction clone of mCherry-Lux streaked out on tryptic soy agar containing tetracycline was imaged by IVIS for mCherry fluorescence (Ex: 570 nm/Em: 640 nm, 5s exposure, small binning, high intensity f/stop of 2) and luminescence (5 second exposure). (**C**) Sheep blood agar plates plated with wildtype (WT, image left) or sfGFP-Lux (image right) are shown after overnight growth displaying similar levels of hemolysis. (**D**) Sheep blood agar plates plated with WT (image left) or mCherry-Lux (image bottom right) are shown after overnight growth displaying similar levels of hemolysis.

Next, to understand if luminescence may be able to act as a surrogate for bacterial burden, the luminescence of sfGFP-Lux and mCherry-Lux strains was measured and compared to the concentration of *S. aureus* colony forming units (CFU) per mL. An overnight culture of sfGFP-*lux* and mCherry-*lux* strains was diluted in fresh tryptic soy broth (1:100). The subcultures were grown for 3 h prior to serial dilution in warm (37°C) tryptic soy broth in a sterile 96-well plate. The plate was imaged via IVIS imaging for luminescence. The bacterial concentrations of the wells were then evaluated by serial dilution and enumeration of CFU. Both strains demonstrated a strong relationship between CFU/mL and luminescence (**Figure 47**). The calculated R^2 for $\log_{10}$(photon counts) graphed against $\log_{10}$(CFU/mL) was 0.9895 and 0.9825 for sfGFP-Lux and mCherry-Lux, respectively.

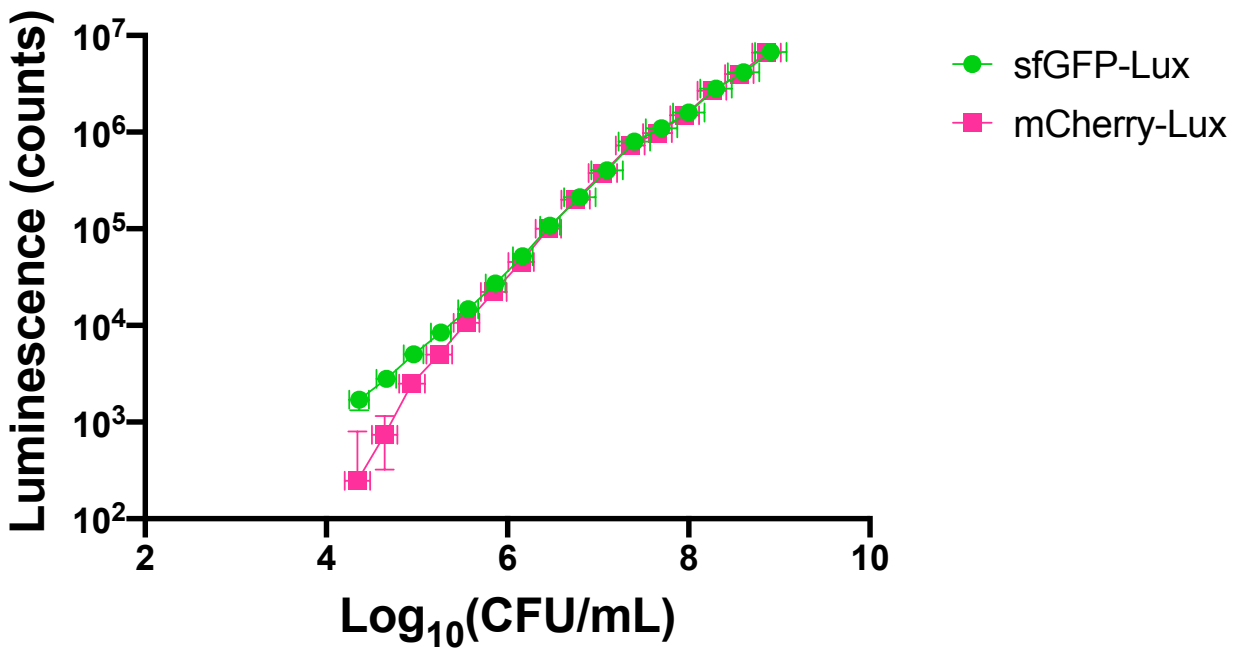

Figure 47: Luminescence as a function of *S. aureus* abundance

The measured luminescence (counts) from sfGFP-Lux and mCherry-Lux is graphed on a logarithmic scale as a function of $\log_{10}$(CFU/mL). *N*=3 independent replicates each with 3 technical replicates. Error bars represent mean ± *SEM*. R^2 for $\log_{10}$(CFU/mL) by $\log_{10}$(photon counts) was 0.9895 and 0.9825 for sfGFP-Lux and mCherry-Lux, respectively. CFU=colony forming units.

After confirming that sfGFP-Lux and mCherry-Lux generate light in proportion to bacterial concentration, I next investigated whether the double-labeled *S. aureus* could be used *in vivo* to detect the presence of active infection. Mice were infected with sfGFP-Lux using our previously characterized murine model of post-traumatic osteomyelitis [122]. On post-infection Day 5, mice were anesthetized with 1-5% isoflurane and imaged via IVIS Spectrum for luminescence and GFP signal. Using the Diffuse Luminescence Imaging Tomography (DLIT) and Fluorescence Imaging Tomography (FLIT), the IVIS Spectrum with Living Image Software can generate three-dimensional renderings of the bioluminescent or fluorescent source, respectively [326]. DLIT and FLIT images showed roughly overlapping signals originating about the left femur, indicative of the sfGFP-Lux *S. aureus* (**Figure 48**). These results are representative of several mice in the study and suggest that sfGFP-Lux (and likely mCherry-Lux) will be useful for *in vivo* tracking of infection during *S. aureus* osteomyelitis. An important next step will be to correlate the signal intensity with CFU burdens *in vivo*. The best first step would be to test an antimicrobial therapy and monitor bacterial clearance over the course of infection as described previously for a soft tissue infection model of *S. aureus* [323]. These studies demonstrate that bioluminescent and fluorescent markers may be a tractable method for monitoring bacterial burdens in our model of *S. aureus* osteomyelitis.

luxBADCE **Luminescence**

sfGFP 500/540nm

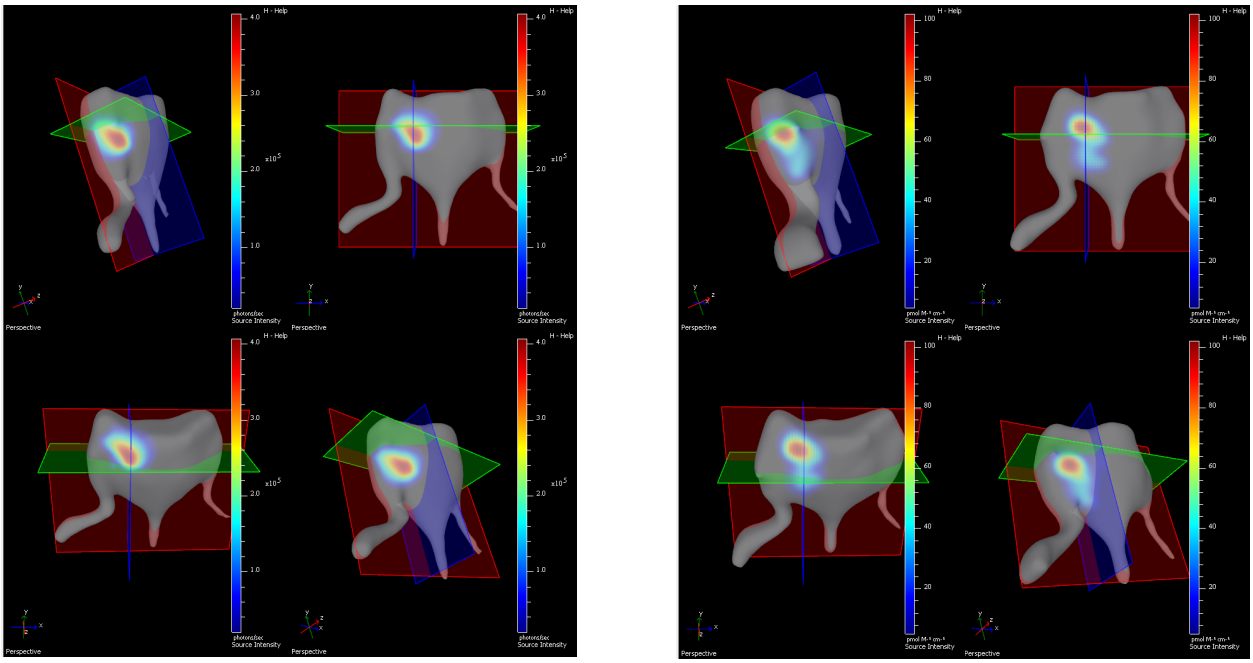

Figure 48: Diffuse Luminescence Imaging Tomography and Fluorescent Imaging Tomography of the infectious focus in mice infected with sfGFP-Lux

On post-infection Day 5, mice (*n*=5) infected with sfGFP-Lux in our osteomyelitis model were imaged via IVIS Spectrum using Diffuse Luminescence Imaging Tomography (DLIT) and Fluorescent Imaging Tomography (FLIT). A rendering of the surface of the caudal half of a representative mouse is shown with the three-dimensional rendering of the calculated luminescent/fluorescent source using Living Image Software. DLIT images are shown at left. FLIT (excitation: 500nm, emission: 540nm) images are shown at right in corresponding planes. The grey outline represents the surface of the caudal half of the mouse including the left and right hindlimbs and the tail. The red plane represents a frontal plane. The blue plane represents a

sagittal plane. The green plane represents a transverse plane. The planes have been positioned to intersect at the luminescent/fluorescent focus.

D: Interference of staphylococcal protein A in a multiplexed cytokine analysis technique

In prior studies in the lab, Luminex cytokine analysis has been used to quantify cytokine production during osteomyelitis [121]. When testing cytokine production *in vitro*, *Staphylococcus aureus*-stimulated cells appeared to display exceptionally high signal intensity for several cytokines (data not shown). These samples contained small amounts of concentrated bacterial supernatant from LAC Δ*psmα1-4*::*erm* (USA300-lineage, from parent strain: AH1263) grown in RPMI with casamino acids [122,235]. I hypothesized that staphylococcal protein A (SpA) interfered with this assay because Luminex is an antibody-based assay. SpA is known to bind the Fc domain of several IgG antibodies to subvert immune responses [20]. I generated a double-knockout strain (Δ*psm*/Δ*spa*) to compare to the standard Δ*psm* mutant used for prior experiments.

The parent strain of the mutants tested in the subsequent assays is an erythromycin-sensitized strain of USA300 LAC *S. aureus* (AH1263) [235]. The toxin-deficient strain LAC Δ*psmα1-4*::*erm* (Δ*psm*) is a mutant of AH1263 and has been characterized previously [121,122]. To generate a double knockout of *psmα1–4* and *spa* and a single mutant of *spa* in the AH1263 background, Δ*spa*::Tc^r was transduced into Δ*psm* [122] and AH1263 [235], respectively, from Newman Δ*spa*::Tc^r (DU5873) [236] with the bacteriophage phi-85 as previously described [117]. The knockouts, herein referred to as Δ*spa* and Δ*psm*/Δ*spa* for the single and double knockout, respectively, were confirmed by PCR. By PCR, Δ*spa* and Δ*psm*/Δ*spa* possessed the arginine catabolic mobile element (ACME), which is characteristic of USA300 but not Newman (parent of Δ*spa*::Tc^r) strains of *S. aureus* (**Figure 49A**). Furthermore, primers (**Table 4**) flanking the *spa* gene revealed that the knockout of *spa* caused a shift in the band length from the predicted ~2300 bp to a larger size that matched that of the parent strain of the *spa* mutant (**Figure 49B**).

Additionally, Δ*spa* and Δ*psm*/Δ*spa* demonstrated growth on appropriate antibiotic plates (data now shown). Concentrated supernatants from Δ*psm* and Δ*psm*/Δ*spa* were prepared as done previously [117]. The concentrated Δ*psm* and Δ*psm*/Δ*spa* supernatants were diluted to 5% (v/v) in α-minimal essential media (α-MEM) with 10% fetal bovine serum (FBS) and 1x penicillin/streptomycin. Theoretically, no cytokines should be present as no murine cells have conditioned the media. Cytokine abundance was measured in the media containing concentrated supernatants using Luminex, specifically the 32-plex Mouse Cytokine/Chemokine Magnetic Bead Panel (MCYTMAG-70K-PX32) on a FLEXMAP 3D, instrument as done previously [121]. The data demonstrated that several cytokines were at levels 1,000- to 10,000-fold higher than the minimal detection concentration for the kit when *spa* has not been knocked out (**Figure 50**). Several cytokines still showed signal greater than 10-fold higher than background in Δ*psm*/Δ*spa*, suggesting that additional mechanisms contribute to false positives (**Figure 50**). It is possible that Staphylococcal binding immunoglobulin protein (Sbi) may also contribute to crosslinking antibodies to produce a false-positive signal. The data strongly suggest that, when present at sufficiently high levels, SpA is capable of crosslinking antibodies in the 32-plex Mouse Cytokine/Chemokine Magnetic Bead Panel to produce falsely elevated cytokine abundance signals.

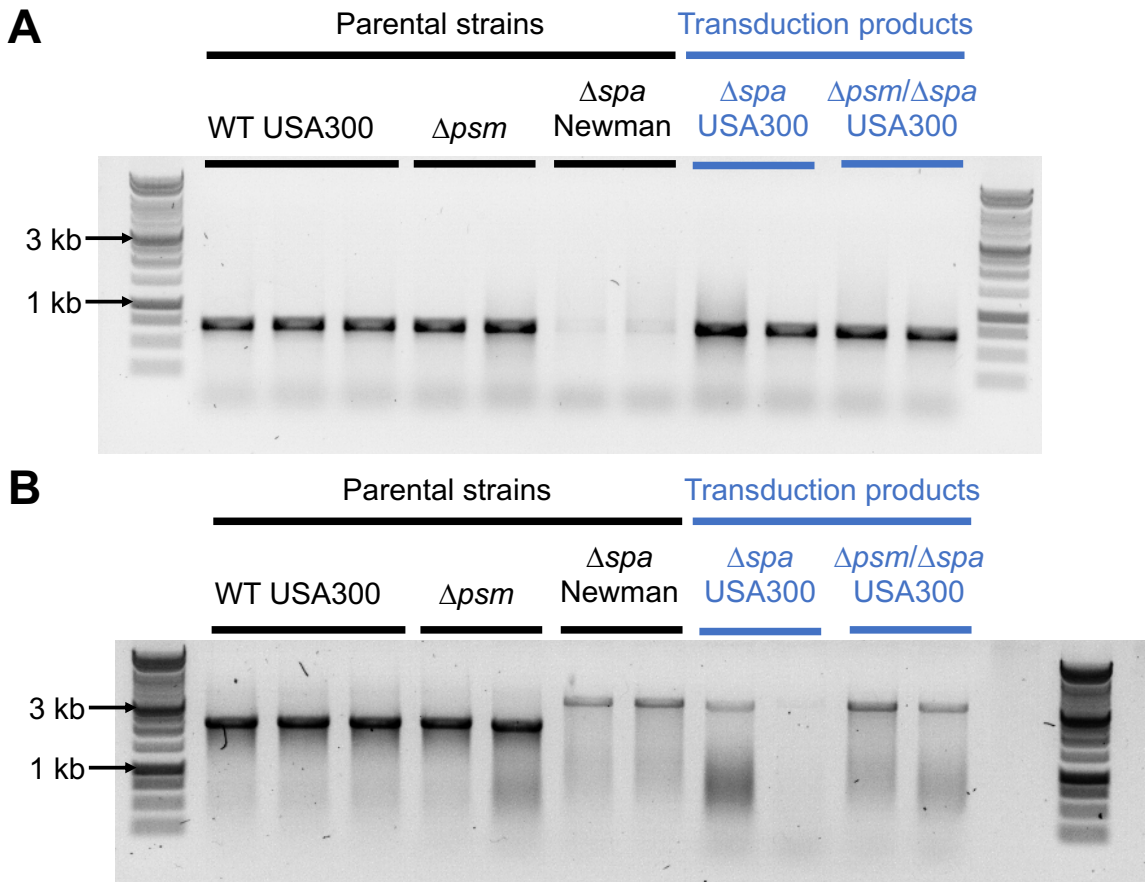

Figure 49: PCR demonstrates maintenance of ACME and acquisition of *spa* knockout

Ethidium bromide-containing 0.8% agarose gels are shown for equivalent samples using primers to identify the arginine catabolic mobile element (ACME, **A**) and the product size for primers flanking the *spa* gene (**B**). Both gels show equivalent samples with 1 kb ladder (Promega) as shown. The parental strains are shown at left in black. Δ*spa* Newman was used to harvest phi-85 phage and transduce the Δ*spa* genetic material into wildtype (WT) USA300 (erythromycin-sensitized AH1263) and Δ*psm*. The resulting transduced strains are shown at right in blue. The parental Newman strain lacks ACME unlike the transduced strains which mirror the USA300-lineage parental strains. PCR was conducted with Go-Taq DNA polymerase (Promega) for 30 cycles with a melting temperature of 47°C for ACME or 32 cycles with a melting temperature of 53°C for *spa*.

Table 4: Primers used for ACME and *spa* PCR

The forward and reverse primer sequences for ACME and *spa* PCR are shown.

Primer Name	Sequence	Source
ACME, #1	5'-CACGTAACTTGCTAGAACGAG-3'	(Montgomery et al., 2009)
ACME, #2	5'-GAGCCAGAAGTACGCGAG-3'	
spa, #1	5'-CCATTGCGACTGCAGCTGTT-3'	Developed with Primer-BLAST tool from the National Center for Biotechnology Information (NCBI)
spa, #2	5'- CCTCAGCACATTCAAAGCCC-3'	

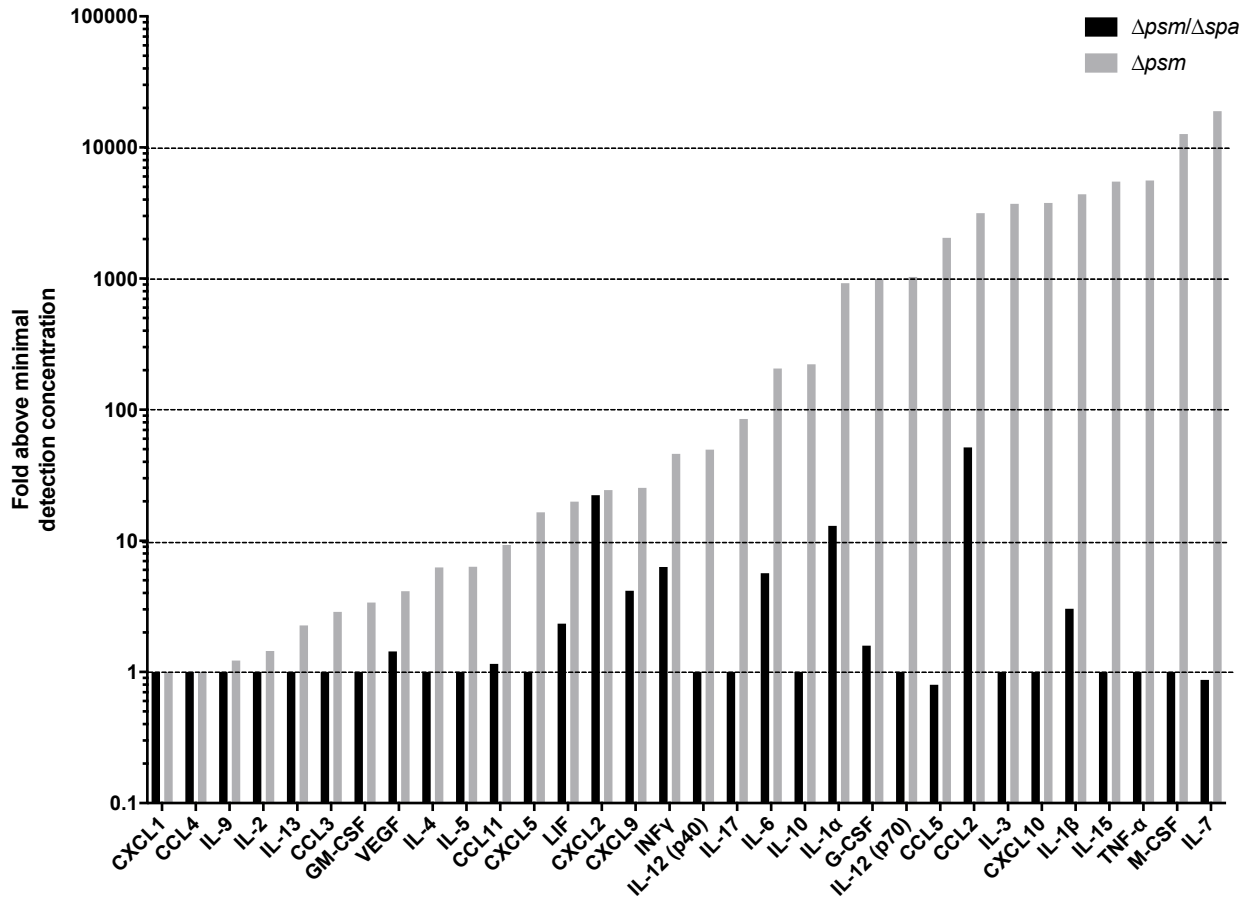

Figure 50: The interference of staphylococcal protein A in an antibody-based cytokine assay

The quantified pg/mL of each cytokine is displayed normalized by the stated minimal detection concentration for the assay. The data has been sorted in increasing intensity from left to right for the Δ*psm* supernatant containing media. The corresponding values for the Δ*psm*/Δ*spa* condition are shown to the left for each cytokine in the assay. The data represent the mean from technical duplicate from one replicate of the experiment.

REFERENCES

1. Cortés-Penfield NW, Kulkarni PA. The History of Antibiotic Treatment of Osteomyelitis. Open Forum Infect Dis [Internet]. 2019 May;6(5). Available from: https://academic.oup.com/ofid/article/doi/10.1093/ofid/ofz181/5432301

2. Lew DP, Waldvogel FA. Osteomyelitis. Lancet. 2004 Jul 24;364(9431):369–79.

3. Kremers HM, Nwojo ME, Ransom JE, Wood-Wentz CM, Melton LJ, Huddleston PM, III. Trends in the epidemiology of osteomyelitis: a population-based study, 1969 to 2009. J Bone Joint Surg Am. 2015 May;97(10):837–45.

4. Peltola H, Pääkkönen M. Acute Osteomyelitis in Children. N Engl J Med. 2014 Jan;370(4):352–60.

5. Jagodzinski NA, Kanwar R, Graham K, Bache CE. Prospective evaluation of a shortened regimen of treatment for acute osteomyelitis and septic arthritis in children. J Pediatr Orthop. 2009 Aug;29(5):518–25.

6. Peltola H, Pääkkönen M, Kallio P, Kallio MJT, Osteomyelitis-Septic Arthritis Study Group. Short- versus long-term antimicrobial treatment for acute hematogenous osteomyelitis of childhood: prospective, randomized trial on 131 culture-positive cases. Pediatr Infect Dis J. 2010 Dec;29(12):1123–8.

7. Campoccia D, Montanaro L, Arciola CR. The significance of infection related to orthopedic devices and issues of antibiotic resistance. Biomaterials. 2006;27:2331–9.

8. Hackett DJ, Rothenberg AC, Chen AF, Gutowski C, Jaekel D, Tomek IM, Parsley BS, Ducheyne P, Manner PA. The economic significance of orthopaedic infections. J Am Acad Orthop Surg. 2015 Apr;23 Suppl:S1-7.

9. Noskin GA, Rubin RJ, Schentag JJ, Kluytmans J, Hedblom EC, Smulders M, Lapetina E, Gemmen E. The burden of *Staphylococcus aureus* infections on hospitals in the United States: an analysis of the 2000 and 2001 Nationwide Inpatient Sample Database. Arch Intern Med. 2005 Aug 8;165(15):1756–61.

10. Centers for Disease Control and Prevention (U.S.). Antibiotic resistance threats in the United States, 2013 [Internet]. Current. Centers for Disease Control and Prevention (U.S.); 2013 [cited 2021 Mar 4] p. 114. Available from: https://stacks.cdc.gov/view/cdc/20705

11. Centers for Disease Control and Prevention (U.S.). Antibiotic resistance threats in the United States, 2019 [Internet]. Centers for Disease Control and Prevention (U.S.); 2019 Nov [cited 2021 Mar 4] p. 150. Available from: https://stacks.cdc.gov/view/cdc/82532

12. Darouiche RO. Treatment of infections associated with surgical implants. N Engl J Med. 2004 Apr 1;350(14):1422–9.

13. Parsons B, Strauss E. Surgical management of chronic osteomyelitis. Am J Surg. 2004 Jul;188(1A Suppl):57–66.

14. Lipsky BA, Berendt AR, Cornia PB, Pile JC, Peters EJG, Armstrong DG, Deery HG, Embil JM, Joseph WS, Karchmer AW, Pinzur MS, Senneville E, Infectious Diseases Society of America. 2012 Infectious Diseases Society of America clinical practice guideline for the diagnosis and treatment of diabetic foot infections. Clin Infect Dis. 2012 Jun;54(12):e132-173.

15. Zimmerli W, Moser C. Pathogenesis and treatment concepts of orthopaedic biofilm infections. FEMS Immunol Med Microbiol. 2012 Jul;65(2):158–68.

16. Stevens DL, Bisno AL, Chambers HF, Dellinger EP, Goldstein EJC, Gorbach SL, Hirschmann JV, Kaplan SL, Montoya JG, Wade JC. Practice Guidelines for the Diagnosis and Management of Skin and Soft Tissue Infections: 2014 Update by the Infectious Diseases Society of America. Clinical Infectious Diseases. 2014;59(2):e10-52.

17. Berbari EF, Kanj SS, Kowalski TJ, Darouiche RO, Widmer AF, Schmitt SK, Hendershot EF, Holtom PD, Huddleston PM, Petermann GW, Osmon DR, Infectious Diseases Society of America null. 2015 Infectious Diseases Society of America (IDSA) Clinical Practice Guidelines for the Diagnosis and Treatment of Native Vertebral Osteomyelitis in Adults. Clin Infect Dis. 2015 Sep 15;61(6):e26-46.

18. Gimza BD, Cassat JE. Mechanisms of Antibiotic Failure During *Staphylococcus aureus* Osteomyelitis. Front Immunol. 2021;12:638085.

19. Huemer M, Mairpady Shambat S, Bergada-Pijuan J, Söderholm S, Boumasmoud M, Vulin C, Gómez-Mejia A, Antelo Varela M, Tripathi V, Götschi S, Marques Maggio E, Hasse B, Brugger SD, Bumann D, Schuepbach RA, Zinkernagel AS. Molecular reprogramming and phenotype switching in *Staphylococcus aureus* lead to high antibiotic persistence and affect therapy success. Proc Natl Acad Sci U S A. 2021 Feb 16;118(7).

20. Muthukrishnan G, Masters EA, Daiss JL, Schwarz EM. Mechanisms of Immune Evasion and Bone Tissue Colonization That Make *Staphylococcus aureus* the Primary Pathogen in Osteomyelitis. Curr Osteoporos Rep. 2019 Dec;17(6):395–404.

21. Ketonis C, Barr S, Adams CS, Hickok NJ, Parvizi J. Bacterial Colonization of Bone Allografts: Establishment and Effects of Antibiotics. Clin Orthop Relat Res. 2010 Aug;468(8):2113–21.

22. Costerton W, Veeh R, Shirtliff M, Pasmore M, Post C, Ehrlich G. The application of biofilm science to the study and control of chronic bacterial infections. J Clin Invest. 2003 Nov;112(10):1466–77.

23. Otto M. Staphylococcal biofilms. Curr Top Microbiol Immunol. 2008;322:207–28.

24. Proctor RA, von Eiff C, Kahl BC, Becker K, McNamara P, Herrmann M, Peters G. Small colony variants: a pathogenic form of bacteria that facilitates persistent and recurrent infections. Nat Rev Microbiol. 2006 Apr;4(4):295–305.

25. Conlon BP, Nakayasu ES, Fleck LE, LaFleur MD, Isabella VM, Coleman K, Leonard SN, Smith RD, Adkins JN, Lewis K. Activated ClpP kills persisters and eradicates a chronic biofilm infection. Nature. 2013;503:365–70.

26. Garcia LG, Lemaire S, Kahl BC, Becker K, Proctor RA, Denis O, Tulkens PM, Van Bambeke F. Antibiotic activity against small-colony variants of *Staphylococcus aureus*: review of *in vitro*, animal and clinical data. J Antimicrob Chemother. 2013 Jul;68(7):1455–64.

27. Hammer ND, Cassat JE, Noto MJ, Lojek LJ, Chadha AD, Schmitz JE, Creech CB, Skaar EP. Inter- and intraspecies metabolite exchange promotes virulence of antibiotic-resistant *Staphylococcus aureus*. Cell Host Microbe. 2014 Oct 8;16(4):531–7.

28. Long F, Ornitz DM. Development of the Endochondral Skeleton. Cold Spring Harb Perspect Biol. 2013 Jan 1;5(1):a008334.

29. Parfitt AM. A structural approach to renal bone disease. J Bone Miner Res. 1998 Aug;13(8):1213–20.

30. Confavreux CB. Bone: from a reservoir of minerals to a regulator of energy metabolism. Kidney Int. 2011 Apr 1;79121:S14–9.

31. Ferron M, Wei J, Yoshizawa T, Del Fattore A, DePinho RA, Teti A, Ducy P, Karsenty G. Insulin signaling in osteoblasts integrates bone remodeling and energy metabolism. Cell. 2010 Jul 23;142(2):296–308.

32. Kapp FG, Perlin JR, Hagedorn EJ, Gansner JM, Schwarz DE, O'Connell LA, Johnson NS, Amemiya C, Fisher DE, Wölfle U, Trompouki E, Niemeyer CM, Driever W, Zon LI. Protection from UV light is an evolutionarily conserved feature of the haematopoietic niche. Nature. 2018 Jun;558(7710):445–8.

33. Shen Y, Nilsson SK. Bone, microenvironment and hematopoiesis. Curr Opin Hematol. 2012 Jul;19(4):250–5.

34. Araldi E, Schipani E. Hypoxia, HIFs and bone development. Bone. 2010 Aug;47(2):190–6.

35. Nilsson O, Marino R, De Luca F, Phillip M, Baron J. Endocrine regulation of the growth plate. Horm Res. 2005;64(4):157–65.

36. Hilton MJ, Tu X, Cook J, Hu H, Long F. Ihh controls cartilage development by antagonizing Gli3, but requires additional effectors to regulate osteoblast and vascular development. Development. 2005 Oct;132(19):4339–51.

37. Nakashima K, Zhou X, Kunkel G, Zhang Z, Deng JM, Behringer RR, de Crombrugghe B. The novel zinc finger-containing transcription factor osterix is required for osteoblast differentiation and bone formation. Cell. 2002 Jan 11;108(1):17–29.

38. Yang L, Tsang KY, Tang HC, Chan D, Cheah KSE. Hypertrophic chondrocytes can become osteoblasts and osteocytes in endochondral bone formation. Proc Natl Acad Sci U S A. 2014 Aug 19;111(33):12097–102.

39. Zhou X, von der Mark K, Henry S, Norton W, Adams H, de Crombrugghe B. Chondrocytes Transdifferentiate into Osteoblasts in Endochondral Bone during Development, Postnatal Growth and Fracture Healing in Mice. PLoS Genet [Internet]. 2014 Dec 4 [cited 2021 Jan 25];10(12). Available from: https://www.ncbi.nlm.nih.gov/pmc/articles/PMC4256265/

40. Engsig MT, Chen Q-J, Vu TH, Pedersen A-C, Therkidsen B, Lund LR, Henriksen K, Lenhard T, Foged NT, Werb Z, Delaissé J-M. Matrix Metalloproteinase 9 and Vascular Endothelial Growth Factor Are Essential for Osteoclast Recruitment into Developing Long Bones. J Cell Biol. 2000 Nov 13;151(4):879–90.

41. Teitelbaum SL. Bone Resorption by Osteoclasts. Science. 2000 Sep 1;289(5484):1504–8.

42. Rutkovskiy A, Stensløkken K-O, Vaage IJ. Osteoblast Differentiation at a Glance. Med Sci Monit Basic Res. 2016 Sep 26;22:95–106.

43. Bonewald LF. Osteocytes as Dynamic Multifunctional Cells. Ann N Y Acad Sci. 2007;1116(1):281–90.

44. Sims NA, Martin TJ. Coupling the activities of bone formation and resorption: a multitude of signals within the basic multicellular unit. Bonekey Rep. 2014 Jan 8;3:481.

45. Yoshida H, Hayashi S, Kunisada T, Ogawa M, Nishikawa S, Okamura H, Sudo T, Shultz LD, Nishikawa S. The murine mutation osteopetrosis is in the coding region of the macrophage colony stimulating factor gene. Nature. 1990 May 31;345(6274):442–4.

46. Fuller K, Owens JM, Jagger CJ, Wilson A, Moss R, Chambers TJ. Macrophage colony-stimulating factor stimulates survival and chemotactic behavior in isolated osteoclasts. J Exp Med. 1993 Nov 1;178(5):1733–44.

47. Kong YY, Yoshida H, Sarosi I, Tan HL, Timms E, Capparelli C, Morony S, Oliveira-dos-Santos AJ, Van G, Itie A, Khoo W, Wakeham A, Dunstan CR, Lacey DL, Mak TW, Boyle WJ, Penninger JM. OPGL is a key regulator of osteoclastogenesis, lymphocyte development and lymph-node organogenesis. Nature. 1999 Jan 28;397(6717):315–23.

48. Simonet WS, Lacey DL, Dunstan CR, Kelley M, Chang MS, Lüthy R, Nguyen HQ, Wooden S, Bennett L, Boone T, Shimamoto G, DeRose M, Elliott R, Colombero A, Tan HL, Trail G, Sullivan J, Davy E, Bucay N, Renshaw-Gegg L, Hughes TM, Hill D, Pattison W, Campbell P, Sander S, Van G, Tarpley J, Derby P, Lee R, Boyle WJ. Osteoprotegerin:

a novel secreted protein involved in the regulation of bone density. Cell. 1997 Apr 18;89(2):309–19.

49. Hofbauer LC, Gori F, Riggs BL, Lacey DL, Dunstan CR, Spelsberg TC, Khosla S. Stimulation of osteoprotegerin ligand and inhibition of osteoprotegerin production by glucocorticoids in human osteoblastic lineage cells: potential paracrine mechanisms of glucocorticoid-induced osteoporosis. Endocrinology. 1999 Oct;140(10):4382–9.

50. Lacey DL, Timms E, Tan HL, Kelley MJ, Dunstan CR, Burgess T, Elliott R, Colombero A, Elliott G, Scully S, Hsu H, Sullivan J, Hawkins N, Davy E, Capparelli C, Eli A, Qian YX, Kaufman S, Sarosi I, Shalhoub V, Senaldi G, Guo J, Delaney J, Boyle WJ. Osteoprotegerin ligand is a cytokine that regulates osteoclast differentiation and activation. Cell. 1998 Apr 17;93(2):165–76.

51. Sims NA, Vrahnas C. Regulation of cortical and trabecular bone mass by communication between osteoblasts, osteocytes and osteoclasts. Arch Biochem Biophys. 2014 Nov 1;561:22–8.

52. Tang Y, Wu X, Lei W, Pang L, Wan C, Shi Z, Zhao L, Nagy TR, Peng X, Hu J, Feng X, Van Hul W, Wan M, Cao X. TGF-β1–induced migration of bone mesenchymal stem cells couples bone resorption with formation. Nat Med. 2009 Jul;15(7):757–65.

53. Xian L, Wu X, Pang L, Lou M, Rosen C, Qiu T, Crane J, Frassica F, Zhang L, Rodriguez JP, Jia X, Yakar S, Xuan S, Efstratiadis A, Wan M, Cao X. Matrix IGF-1 regulates bone mass by activation of mTOR in mesenchymal stem cells. Nat Med. 2012 Jul;18(7):1095–101.

54. Ikebuchi Y, Aoki S, Honma M, Hayashi M, Sugamori Y, Khan M, Kariya Y, Kato G, Tabata Y, Penninger JM, Udagawa N, Aoki K, Suzuki H. Coupling of bone resorption and formation by RANKL reverse signalling. Nature. 2018 Sep;561(7722):195–200.

55. Ducy P, Zhang R, Geoffroy V, Ridall AL, Karsenty G. Osf2/Cbfa1: a transcriptional activator of osteoblast differentiation. Cell. 1997 May 30;89(5):747–54.

56. Nakashima K, de Crombrugghe B. Transcriptional mechanisms in osteoblast differentiation and bone formation. Trends Genet. 2003 Aug 1;19(8):458–66.

57. Chen J, Shi Y, Regan J, Karuppaiah K, Ornitz DM, Long F. *Osx-Cre* targets multiple cell types besides osteoblast lineage in postnatal mice. PLoS One. 2014;9(1):e85161.

58. Elefteriou F, Yang X. Genetic mouse models for bone studies—Strengths and limitations. Bone. 2011 Dec;49(6):1242–54.

59. Wang Y, Wan C, Deng L, Liu X, Cao X, Gilbert SR, Bouxsein ML, Faugere M-C, Guldberg RE, Gerstenfeld LC, Haase VH, Johnson RS, Schipani E, Clemens TL. The hypoxia-inducible factor α pathway couples angiogenesis to osteogenesis during skeletal development. J Clin Invest. 2007 Jun 1;117(6):1616–26.

60. Nizet V, Johnson RS. Interdependence of hypoxic and innate immune responses. Nat Rev Immunol. 2009 Sep;9(9):609–17.

61. Wan C, Shao J, Gilbert SR, Riddle RC, Long F, Johnson RS, Schipani E, Clemens TL. Role of HIF-1α in skeletal development. Ann N Y Acad Sci. 2010 Mar;1192:322–6.

62. Semenza GL. Oxygen sensing, hypoxia-inducible factors, and disease pathophysiology. Annu Rev Pathol. 2014;9:47–71.

63. Semenza GL, Nejfelt MK, Chi SM, Antonarakis SE. Hypoxia-inducible nuclear factors bind to an enhancer element located 3' to the human erythropoietin gene. Proc Natl Acad Sci U S A. 1991 Jul 1;88(13):5680–4.

64. Wang GL, Jiang BH, Rue EA, Semenza GL. Hypoxia-inducible factor 1 is a basic-helix-loop-helix-PAS heterodimer regulated by cellular O2 tension. Proc Natl Acad Sci U S A. 1995 Jun 6;92(12):5510–4.

65. Arany Z, Huang LE, Eckner R, Bhattacharya S, Jiang C, Goldberg MA, Bunn HF, Livingston DM. An essential role for p300/CBP in the cellular response to hypoxia. Proc Natl Acad Sci U S A. 1996 Nov 12;93(23):12969–73.

66. Ema M, Hirota K, Mimura J, Abe H, Yodoi J, Sogawa K, Poellinger L, Fujii-Kuriyama Y. Molecular mechanisms of transcription activation by HLF and HIF1α in response to hypoxia: their stabilization and redox signal-induced interaction with CBP/p300. EMBO J. 1999 Apr 1;18(7):1905–14.

67. Semenza GL, Roth PH, Fang HM, Wang GL. Transcriptional regulation of genes encoding glycolytic enzymes by hypoxia-inducible factor 1. J Biol Chem. 1994 Sep 23;269(38):23757–63.

68. Beck I, Weinmann R, Caro J. Characterization of hypoxia-responsive enhancer in the human erythropoietin gene shows presence of hypoxia-inducible 120-Kd nuclear DNA-binding protein in erythropoietin-producing and nonproducing cells. Blood. 1993 Aug 1;82(3):704–11.

69. Ema M, Taya S, Yokotani N, Sogawa K, Matsuda Y, Fujii-Kuriyama Y. A novel bHLH-PAS factor with close sequence similarity to hypoxia-inducible factor 1alpha regulates the VEGF expression and is potentially involved in lung and vascular development. Proc Natl Acad Sci U S A. 1997 Apr 29;94(9):4273–8.

70. Holmquist-Mengelbier L, Fredlund E, Löfstedt T, Noguera R, Navarro S, Nilsson H, Pietras A, Vallon-Christersson J, Borg A, Gradin K, Poellinger L, Påhlman S. Recruitment of HIF-1α and HIF-2α to common target genes is differentially regulated in neuroblastoma: HIF-2α promotes an aggressive phenotype. Cancer Cell. 2006 Nov;10(5):413–23.

71. Kaelin WG, Ratcliffe PJ. Oxygen sensing by metazoans: the central role of the HIF hydroxylase pathway. Mol Cell. 2008 May 23;30(4):393–402.

72. Makino Y, Kanopka A, Wilson WJ, Tanaka H, Poellinger L. Inhibitory PAS Domain Protein (IPAS) Is a Hypoxia-inducible Splicing Variant of the Hypoxia-inducible Factor-3α Locus. J Biol Chem. 2002 Sep 6;277(36):32405–8.

73. van Uden P, Kenneth NS, Rocha S. Regulation of hypoxia-inducible factor-1α by NF-κB. Biochem J. 2008 Jun 15;412(Pt 3):477–84.

74. Karar J, Maity A. PI3K/AKT/mTOR Pathway in Angiogenesis. Front Mol Neurosci [Internet]. 2011 [cited 2021 Jan 25];4. Available from: https://www.frontiersin.org/articles/10.3389/fnmol.2011.00051/full#B7

75. Huang LE, Gu J, Schau M, Bunn HF. Regulation of hypoxia-inducible factor 1α is mediated by an O_2-dependent degradation domain via the ubiquitin-proteasome pathway. Proc Natl Acad Sci U S A. 1998 Jul 7;95(14):7987–92.

76. Ivan M, Kondo K, Yang H, Kim W, Valiando J, Ohh M, Salic A, Asara JM, Lane WS, Kaelin WG. HIFα targeted for VHL-mediated destruction by proline hydroxylation: implications for O_2 sensing. Science. 2001 Apr 20;292(5516):464–8.

77. Jaakkola P, Mole DR, Tian Y-M, Wilson MI, Gielbert J, Gaskell SJ, Kriegsheim A von, Hebestreit HF, Mukherji M, Schofield CJ, Maxwell PH, Pugh ‡ Christopher W., Ratcliffe ‡ Peter J. Targeting of HIF-α to the von Hippel-Lindau Ubiquitylation Complex by O_2-Regulated Prolyl Hydroxylation. Science. 2001 Apr 20;292(5516):468–72.

78. Berra E, Benizri E, Ginouvès A, Volmat V, Roux D, Pouysségur J. HIF prolyl-hydroxylase 2 is the key oxygen sensor setting low steady-state levels of HIF-1α in normoxia. EMBO J. 2003 Aug 15;22(16):4082–90.

79. Maxwell PH, Wiesener MS, Chang GW, Clifford SC, Vaux EC, Cockman ME, Wykoff CC, Pugh CW, Maher ER, Ratcliffe PJ. The tumour suppressor protein VHL targets hypoxia-inducible factors for oxygen-dependent proteolysis. Nature. 1999 May 20;399(6733):271–5.

80. Ohh M, Park CW, Ivan M, Hoffman MA, Kim TY, Huang LE, Pavletich N, Chau V, Kaelin WG. Ubiquitination of hypoxia-inducible factor requires direct binding to the beta-domain of the von Hippel-Lindau protein. Nat Cell Biol. 2000 Jul;2(7):423–7.

81. Salceda S, Caro J. Hypoxia-inducible factor 1α (HIF-1α) protein is rapidly degraded by the ubiquitin-proteasome system under normoxic conditions. Its stabilization by hypoxia depends on redox-induced changes. J Biol Chem. 1997 Sep 5;272(36):22642–7.

82. Jiang BH, Semenza GL, Bauer C, Marti HH. Hypoxia-inducible factor 1 levels vary exponentially over a physiologically relevant range of O_2 tension. Am J Physiol. 1996 Oct;271(4 Pt 1):C1172-1180.

83. Yu AY, Frid MG, Shimoda LA, Wiener CM, Stenmark K, Semenza GL. Temporal, spatial, and oxygen-regulated expression of hypoxia-inducible factor-1 in the lung. Am J Physiol. 1998 Oct;275(4):L818-826.

84. Epstein ACR, Gleadle JM, McNeill LA, Hewitson KS, O'Rourke J, Mole DR, Mukherji M, Metzen E, Wilson MI, Dhanda A, Tian Y-M, Masson N, Hamilton DL, Jaakkola P, Barstead R, Hodgkin J, Maxwell PH, Pugh CW, Schofield CJ, Ratcliffe PJ. *C. elegans* EGL-9 and Mammalian Homologs Define a Family of Dioxygenases that Regulate HIF by Prolyl Hydroxylation. Cell. 2001 Oct 5;107(1):43–54.

85. Mahon PC, Hirota K, Semenza GL. FIH-1: a novel protein that interacts with HIF-1α and VHL to mediate repression of HIF-1 transcriptional activity. Genes Dev. 2001 Oct 15;15(20):2675–86.

86. Dhillon S. Roxadustat: First Global Approval. Drugs. 2019 Apr 1;79(5):563–72.

87. Chen N, Hao C, Liu B-C, Lin H, Wang C, Xing C, Liang X, Jiang G, Liu Z, Li X, Zuo L, Luo L, Wang J, Zhao M-H, Liu Z, Cai G-Y, Hao L, Leong R, Wang C, Liu C, Neff T, Szczech L, Yu K-HP. Roxadustat Treatment for Anemia in Patients Undergoing Long-Term Dialysis. N Engl J Med. 2019 Sep 12;381(11):1011–22.

88. Wan C, Gilbert SR, Wang Y, Cao X, Shen X, Ramaswamy G, Jacobsen KA, Alaql ZS, Eberhardt AW, Gerstenfeld LC, Einhorn TA, Deng L, Clemens TL. Activation of the hypoxia-inducible factor-1α pathway accelerates bone regeneration. Proc Natl Acad Sci U S A. 2008 Jan 15;105(2):686–91.

89. Hu K, Olsen BR. Osteoblast-derived VEGF regulates osteoblast differentiation and bone formation during bone repair. J Clin Invest. 2016;126(2):509–26.

90. Liu Y, Berendsen AD, Jia S, Lotinun S, Baron R, Ferrara N, Olsen BR. Intracellular VEGF regulates the balance between osteoblast and adipocyte differentiation. J Clin Invest. 2012 Sep;122(9):3101–13.

91. Shomento SH, Wan C, Cao X, Faugere M-C, Bouxsein ML, Clemens TL, Riddle RC. Hypoxia-inducible factors 1α and 2α exert both distinct and overlapping functions in long bone development. J Cell Biochem. 2010 Jan 1;109(1):196–204.

92. Miyauchi Y, Sato Y, Kobayashi T, Yoshida S, Mori T, Kanagawa H, Katsuyama E, Fujie A, Hao W, Miyamoto K, Tando T, Morioka H, Matsumoto M, Chambon P, Johnson RS, Kato S, Toyama Y, Miyamoto T. HIF1α is required for osteoclast activation by estrogen deficiency in postmenopausal osteoporosis. Proc Natl Acad Sci U S A. 2013 Oct 8;110(41):16568–73.

93. Tando T, Sato Y, Miyamoto K, Morita M, Kobayashi T, Funayama A, Kanaji A, Hao W, Watanabe R, Oike T, Nakamura M, Matsumoto M, Toyama Y, Miyamoto T. Hif1α is required for osteoclast activation and bone loss in male osteoporosis. Biochem Biophys Res Commun. 2016 Feb 5;470(2):391–6.

94. Peng J, Lai ZG, Fang ZL, Xing S, Hui K, Hao C, Jin Q, Qi Z, Shen WJ, Dong QN, Bing ZH, Fu DL. Dimethyloxalylglycine Prevents Bone Loss in Ovariectomized C57BL/6J Mice through Enhanced Angiogenesis and Osteogenesis. PLoS One [Internet]. 2014 Nov

13 [cited 2021 Jan 19];9(11). Available from: https://www.ncbi.nlm.nih.gov/pmc/articles/PMC4231053/

95. Regan JN, Lim J, Shi Y, Sang Joeng K, Arbeit JM, Shohet RV, Long F. Up-regulation of glycolytic metabolism is required for HIF1α-driven bone formation. Proc Natl Acad Sci U S A. 2014;111(23):8673–8.

96. Wu C, Rankin EB, Castellini L, Alcudia JF, Fernandez-Alcudia J, LaGory EL, Andersen R, Rhodes SD, Wilson TLS, Mohammad KS, Castillo AB, Guise TA, Schipani E, Giaccia AJ. Oxygen-sensing PHDs regulate bone homeostasis through the modulation of osteoprotegerin. Genes Dev. 2015 Apr 15;29(8):817–31.

97. Buettmann EG, McKenzie JA, Migotsky N, Sykes DA, Hu P, Yoneda S, Silva MJ. VEGFA From Early Osteoblast Lineage Cells (Osterix+) Is Required in Mice for Fracture Healing. J Bone Miner Res. 2019 Sep;34(9):1690–706.

98. Lee SY, Park KH, Yu H-G, Kook E, Song W-H, Lee G, Koh J-T, Shin H-I, Choi J-Y, Huh YH, Ryu J-H. Controlling hypoxia-inducible factor-2α is critical for maintaining bone homeostasis in mice. Bone Res [Internet]. 2019 May 13 [cited 2021 Jan 21];7. Available from: https://www.ncbi.nlm.nih.gov/pmc/articles/PMC6513851/

99. Deng Z, Lin B, Jiang Z, Huang W, Li J, Zeng X, Wang H, Wang D, Zhang Y. Hypoxia-Mimicking Cobalt-Doped Borosilicate Bioactive Glass Scaffolds with Enhanced Angiogenic and Osteogenic Capacity for Bone Regeneration. Int J Biol Sci. 2019 Apr 22;15(6):1113–24.

100. Liu X, Tu Y, Zhang L, Qi J, Ma T, Deng L. Prolyl hydroxylase inhibitors protect from the bone loss in ovariectomy rats by increasing bone vascularity. Cell Biochem Biophys. 2014 May;69(1):141–9.

101. Shen X, Wan C, Ramaswamy G, Mavalli M, Wang Y, Duvall CL, Deng LF, Guldberg RE, Eberhart A, Clemens TL, Gilbert SR. Prolyl hydroxylase inhibitors increase neoangiogenesis and callus formation following femur fracture in mice. J Orthop Res. 2009;27(10):1298–305.

102. Woo KM, Jung H-M, Oh J-H, Rahman S ur, Kim SM, Baek J-H, Ryoo H-M. Synergistic effects of dimethyloxalylglycine and butyrate incorporated into α-calcium sulfate on bone regeneration. Biomaterials. 2015 Jan 1;39:1–14.

103. Hulley PA, Papadimitriou-Olivgeri I, Knowles HJ. Osteoblast–Osteoclast Coculture Amplifies Inhibitory Effects of FG-4592 on Human Osteoclastogenesis and Reduces Bone Resorption. JBMR Plus [Internet]. 2020 May 14 [cited 2021 Feb 26];4(7). Available from: https://www.ncbi.nlm.nih.gov/pmc/articles/PMC7340438/

104. Yellowley CE, Genetos DC. Hypoxia signaling in the skeleton: implications for bone health. Curr Osteoporos Rep. 2019 Feb;17(1):26–35.

105. Wang W, Yeung KWK. Bone grafts and biomaterials substitutes for bone defect repair: A review. Bioact Mater. 2017 Jun 7;2(4):224–47.

106. Wu C, Zhou Y, Xu M, Han P, Chen L, Chang J, Xiao Y. Copper-containing mesoporous bioactive glass scaffolds with multifunctional properties of angiogenesis capacity, osteostimulation and antibacterial activity. Biomaterials. 2013 Jan;34(2):422–33.

107. Zhang W, Chang Q, Xu L, Li G, Yang G, Ding X, Wang X, Cui D, Jiang X. Graphene Oxide-Copper Nanocomposite-Coated Porous CaP Scaffold for Vascularized Bone Regeneration via Activation of Hif-1α. Adv Healthc Mater. 2019 Mar;8(5):e1900067.

108. Liu R, Tang Y, Liu H, Zeng L, Ma Z, Li J, Zhao Y, Ren L, Yang K. Effects of combined chemical design (Cu addition) and topographical modification (SLA) of Ti-Cu/SLA for promoting osteogenic, angiogenic and antibacterial activities. J Mater Sci Technol. 2020 Jun 15;47:202–15.

109. Yan F, Lv M, Zhang T, Zhang Q, Chen Y, Liu Z, Wei R, Cai L. Copper-Loaded Biodegradable Bone Wax with Antibacterial and Angiogenic Properties in Early Bone Repair. ACS Biomater Sci Eng [Internet]. 2021 Jan 27 [cited 2021 Feb 1]; Available from: https://doi.org/10.1021/acsbiomaterials.0c01471

110. Chatterjee AK, Sarkar RK, Chattopadhyay AP, Aich P, Chakraborty R, Basu T. A simple robust method for synthesis of metallic copper nanoparticles of high antibacterial potency against *E. coli*. Nanotechnology. 2012 Feb 1;23(8):085103.

111. Josse J, Velard F, Gangloff SC. *Staphylococcus aureus* vs. Osteoblast: Relationship and Consequences in Osteomyelitis. Front Cell Infect Microbiol. 2015;5(85):1–17.

112. Fischer B, Vaudaux P, Magnin M, el Mestikawy Y, Proctor RA, Lew DP, Vasey H. Novel animal model for studying the molecular mechanisms of bacterial adhesion to bone-implanted metallic devices: role of fibronectin in *Staphylococcus aureus* adhesion. J Orthop Res. 1996 Nov;14(6):914–20.

113. Tung H s, Guss B, Hellman U, Persson L, Rubin K, Rydén C. A bone sialoprotein-binding protein from *Staphylococcus aureus*: a member of the staphylococcal Sdr family. Biochem J. 2000 Feb 1;345(Pt 3):611–9.

114. Johansson A, Flock JI, Svensson O. Collagen and fibronectin binding in experimental staphylococcal osteomyelitis. Clin Orthop Relat Res. 2001 Jan;(382):241–6.

115. Elasri MO, Thomas JR, Skinner RA, Blevins JS, Beenken KE, Nelson CL, Smeltzer MS. *Staphylococcus aureus* collagen adhesin contributes to the pathogenesis of osteomyelitis. Bone. 2002 Jan;30(1):275–80.

116. Potter AD, Butrico CE, Ford CA, Curry JM, Trenary IA, Tummarakota SS, Hendrix AS, Young JD, Cassat JE. Host nutrient milieu drives an essential role for aspartate biosynthesis during invasive *Staphylococcus aureus* infection. Proc Natl Acad Sci U S A. 2020 Jun 2;117(22):12394–401.

117. Wilde AD, Snyder DJ, Putnam NE, Valentino MD, Hammer ND, Lonergan ZR, Hinger SA, Aysanoa EE, Blanchard C, Dunman PM, Wasserman GA, Chen J, Shopsin B, Gilmore MS, Skaar EP, Cassat JE. Bacterial Hypoxic Responses Revealed as Critical Determinants of the Host-Pathogen Outcome by TnSeq Analysis of *Staphylococcus aureus* Invasive Infection. Otto M, editor. PLoS Pathog. 2015 Dec;11(12):e1005341.

118. Otto M. Phenol-soluble modulins. Int J Med Microbiol. 2014 Mar;304(2):164–9.

119. Spaan AN, van Strijp JAG, Torres VJ. Leukocidins: staphylococcal bi-component pore-forming toxins find their receptors. Nat Rev Microbiol. 2017 Jul;15(7):435–47.

120. Mbalaviele G, Novack DV, Schett G, Teitelbaum SL. Inflammatory osteolysis: a conspiracy against bone. J Clin Rheumatol. 2017 Jun;127(6):2030–9.

121. Putnam NE, Fulbright LE, Curry JM, Ford CA, Petronglo JR, Hendrix AS, Cassat JE. MyD88 and IL-1R signaling drive antibacterial immunity and osteoclast-driven bone loss during *Staphylococcus aureus* osteomyelitis. Miller LS, editor. PLoS Pathog. 2019 Apr;15(4):e1007744.

122. Cassat JE, Hammer ND, Campbell JP, Benson MA, Perrien DS, Mrak LN, Smeltzer MS, Torres VJ, Skaar EP. A Secreted Bacterial Protease Tailors the *Staphylococcus aureus* Virulence Repertoire to Modulate Bone Remodeling during Osteomyelitis. Cell Host and Microbe. 2013;13:759–72.

123. Hendrix AS, Spoonmore TJ, Wilde AD, Putnam NE, Hammer ND, Snyder DJ, Guelcher SA, Skaar EP, Cassat JE. Repurposing the Nonsteroidal Anti-inflammatory Drug Diflunisal as an Osteoprotective, Antivirulence Therapy for *Staphylococcus aureus* Osteomyelitis. Antimicrob Agents Chemother. 2016 Sep;60(9):5322–30.

124. Clauditz A, Resch A, Wieland K-P, Peschel A, Götz F. Staphyloxanthin plays a role in the fitness of *Staphylococcus aureus* and its ability to cope with oxidative stress. Infect Immun. 2006 Aug;74(8):4950–3.

125. Clements MO, Foster SJ. Stress resistance in *Staphylococcus aureus*. Trends Microbiol. 1999 Nov;7(11):458–62.

126. Mandell GL. Catalase, superoxide dismutase, and virulence of *Staphylococcus aureus*. *In vitro* and *in vivo* studies with emphasis on staphylococcal--leukocyte interaction. J Clin Invest. 1975 Mar;55(3):561–6.

127. Krauss JL, Roper PM, Ballard A, Shih C-C, Fitzpatrick JAJ, Cassat JE, Ng PY, Pavlos NJ, Veis DJ. *Staphylococcus aureus* Infects Osteoclasts and Replicates Intracellularly. mBio [Internet]. 2019 Oct [cited 2021 Feb 16];10(5). Available from: https://www.ncbi.nlm.nih.gov/pmc/articles/PMC6794488/

128. García-Gil A, Lopez-Bailon LU, Ortiz-Navarrete V. Beyond the antibody: B cells as a target for bacterial infection. J Leukoc Biol. 2019 May;105(5):905–13.

129. Zhang L, Jacobsson K, Vasi J, Lindberg M, Frykberg L. A second IgG-binding protein in *Staphylococcus aureus*. Microbiology (Reading). 1998 Apr;144 (Pt 4):985–91.

130. Zhang L, Jacobsson K, Ström K, Lindberg M, Frykberg L. *Staphylococcus aureus* expresses a cell surface protein that binds both IgG and β_2-glycoprotein I. Microbiology (Reading). 1999 Jan;145 (Pt 1):177–83.

131. Kronvall G, Williams RC. Differences in anti-protein A activity among IgG subgroups. J Immunol. 1969 Oct;103(4):828–33.

132. Sjodahl J. Repetitive sequences in protein A from *Staphylococcus aureus*. Arrangement of five regions within the protein, four being highly homologous and Fc-binding. Eur J Biochem. 1977 Mar 1;73(2):343–51.

133. Moks T, Abrahmsén L, Nilsson B, Hellman U, Sjöquist J, Uhlén M. Staphylococcal protein A consists of five IgG-binding domains. Eur J Biochem. 1986 May 2;156(3):637–43.

134. Forsgren A, Quie PG. Effects of staphylococcal protein A on heat labile opsonins. J Immunol. 1974 Mar;112(3):1177–80.

135. Forsgren A, Nordström K. Protein A from *Staphylococcus aureus*: the biological significance of its reaction with IgG. Ann N Y Acad Sci. 1974 Jul 31;236(1):252–66.

136. Roben PW, Salem AN, Silverman GJ. VH3 family antibodies bind domain D of staphylococcal protein A. J Immunol. 1995;154(12):6437–45.

137. Graille M, Stura EA, Corper AL, Sutton BJ, Taussig MJ, Charbonnier JB, Silverman GJ. Crystal structure of a *Staphylococcus aureus* protein a domain complexed with the Fab fragment of a human IgM antibody: Structural basis for recognition of B-cell receptors and superantigen activity. Proc Natl Acad Sci U S A. 2000 May;97(10):5399–404.

138. Thammavongsa V, Kim HK, Missiakas D, Schneewind O. Staphylococcal manipulation of host immune responses. Nat Rev Microbiol. 2015 Sep;13(9):529–43.

139. Pauli NT, Kim HK, Falugi F, Huang M, Dulac J, Henry Dunand C, Zheng N-Y, Kaur K, Andrews SF, Huang Y, DeDent A, Frank KM, Charnot-Katsikas A, Schneewind O, Wilson PC. *Staphylococcus aureus* infection induces protein A-mediated immune evasion in humans. J Exp Med. 2014 Nov 17;211(12):2331–9.

140. Sun Y, Emolo C, Holtfreter S, Wiles S, Kreiswirth B, Missiakas D, Schneewind O. Staphylococcal Protein A Contributes to Persistent Colonization of Mice with *Staphylococcus aureus*. J Bacteriol. 2018 May 1;200(9).

141. Cramer T, Yamanishi Y, Clausen BE, Förster I, Pawlinski R, Mackman N, Haase VH, Jaenisch R, Corr M, Nizet V, Firestein GS, Gerber H-P, Ferrara N, Johnson RS. HIF-1α Is Essential for Myeloid Cell-Mediated Inflammation. Cell. 2003 Mar 7;112(5):645–57.

142. Stothers C, Luan L, Fensterheim B, Bohannon J. Hypoxia-inducible factor-1α regulation of myeloid cells. J Mol Med (Berl). 2018 Dec;96(12):1293–306.

143. Devraj G, Beerlage C, Brüne B, Kempf VAJ. Hypoxia and HIF-1 activation in bacterial infections. Microbes Infect. 2017 Mar;19(3):144–56.

144. Werth N, Beerlage C, Rosenberger C, Yazdi AS, Edelmann M, Amr A, Bernhardt W, Von Eiff C, Becker K, Schäfer A, Peschel A, Kempf VAJ. Activation of Hypoxia Inducible Factor 1 Is a General Phenomenon in Infections with Human Pathogens. PLoS One. 2010;5(7):e11576.

145. Rius J, Guma M, Schachtrup C, Akassoglou K, Zinkernagel AS, Nizet V, Johnson RS, Haddad GG, Karin M. NF-κB links innate immunity to the hypoxic response through transcriptional regulation of HIF-1α. Nature. 2008 Jun 5;453(7196):807–11.

146. Gerald D, Berra E, Frapart YM, Chan DA, Giaccia AJ, Mansuy D, Pouysségur J, Yaniv M, Mechta-Grigoriou F. JunD Reduces Tumor Angiogenesis by Protecting Cells from Oxidative Stress. Cell. 2004 Sep 17;118(6):781–94.

147. Hellwig-Bürgel T, Rutkowski K, Metzen E, Fandrey J, Jelkmann W. Interleukin-1β and Tumor Necrosis Factor-α Stimulate DNA Binding of Hypoxia-Inducible Factor-1. Blood. 1999 Sep 1;94(5):1561–7.

148. Haddad JJ, Land SC. A non-hypoxic, ROS-sensitive pathway mediates TNF-α-dependent regulation of HIF-1α. FEBS Lett. 2001 Sep 14;505(2):269–74.

149. Jung Y-J, Isaacs JS, Lee S, Trepel J, Neckers L. IL-1β-mediated up-regulation of HIF-1α via an NFκB/COX-2 pathway identifies HIF-1 as a critical link between inflammation and oncogenesis. FASEB J. 2003;17(14):2115–7.

150. Haddad JJ, Harb HL. Cytokines and the regulation of hypoxia-inducible factor (HIF)-1α. Int Immunopharmacol. 2005 Mar;5(3):461–83.

151. Walmsley SR, Print C, Farahi N, Peyssonnaux C, Johnson RS, Cramer T, Sobolewski A, Condliffe AM, Cowburn AS, Johnson N, Chilvers ER. Hypoxia-induced neutrophil survival is mediated by HIF-1α–dependent NF-κB activity. J Exp Med. 2005 Jan 3;201(1):105–15.

152. Walmsley SR, Cowburn AS, Clatworthy MR, Morrell NW, Roper EC, Singleton V, Maxwell P, Whyte MKB, Chilvers ER. Neutrophils from patients with heterozygous germline mutations in the von Hippel Lindau protein (pVHL) display delayed apoptosis and enhanced bacterial phagocytosis. Blood. 2006 Nov;108(9):3176–8.

153. Peyssonnaux C, Datta V, Cramer T, Doedens A, Theodorakis EA, Gallo RL, Hurtado-Ziola N, Nizet V, Johnson RS. HIF-1α expression regulates the bactericidal capacity of phagocytes. J Clin Invest. 2005 Jul 1;115(7):1806–15.

154. Cheng S-C, Quintin J, Cramer RA, Shepardson KM, Saeed S, Kumar V, Giamarellos-Bourboulis EJ, Martens JHA, Rao NA, Aghajanirefah A, Manjeri GR, Li Y, Ifrim DC, Arts RJW, van der Meer BMJW, Deen PMT, Logie C, O'Neill LA, Willems P, van de Veerdonk FL, van der Meer JWM, Ng A, Joosten LAB, Wijmenga C, Stunnenberg HG, Xavier RJ, Netea MG. mTOR/HIF1α-mediated aerobic glycolysis as metabolic basis for trained immunity. Science. 2014 Sep 26;345(6204):1250684.

155. Wickersham M, Wachtel S, Fok TW, Richardson A, Parker D, Correspondence AP, Wong T, Lung F, Soong G, Jacquet R, Prince A. Metabolic Stress Drives Keratinocyte Defenses against *Staphylococcus aureus* Infection. Cell Rep. 2017;18(11):2742–51.

156. Peyssonnaux C, Boutin AT, Zinkernagel AS, Datta V, Nizet V, Johnson RS. Critical role of HIF-1α in keratinocyte defense against bacterial infection. J Invest Dermatol. 2008 Aug;128(8):1964–8.

157. Peyssonnaux C, Cejudo-Martin P, Doedens A, Zinkernagel AS, Johnson RS, Nizet V. Cutting Edge: Essential Role of Hypoxia Inducible Factor-1α in Development of Lipopolysaccharide-Induced Sepsis. J Immunol. 2007 Jun 15;178(12):7516–9.

158. Mahabeleshwar GH, Qureshi MA, Takami Y, Sharma N, Lingrel JB, Jain MK. A Myeloid Hypoxia-inducible Factor 1α-Krüppel-like Factor 2 Pathway Regulates Gram-positive Endotoxin-mediated Sepsis. J Biol Chem. 2012 Jan 6;287(2):1448–57.

159. Taylor CT. Interdependent roles for hypoxia inducible factor and nuclear factor-κB in hypoxic inflammation. J Physiol. 2008 Sep 1;586(17):4055–9.

160. Bhandari T, Nizet V. Hypoxia-Inducible Factor (HIF) as a Pharmacological Target for Prevention and Treatment of Infectious Diseases. Infect Dis Ther. 2014 Dec;3(2):159–74.

161. Buchman J. The Rationale of the Treatment of Chronic Osteomyelitis with Special Reference to Maggot Therapy. Ann Surg. 1934 Feb;99(2):251–9.

162. Hatzenbuehler J, Pulling TJ. Diagnosis and management of osteomyelitis. Am Fam Physician. 2011 Nov 1;84(9):1027–33.

163. Ventola CL. The Antibiotic Resistance Crisis. P T. 2015 Apr;40(4):277–83.

164. Dickey SW, Cheung GYC, Otto M. Different drugs for bad bugs: antivirulence strategies in the age of antibiotic resistance. Nat Rev Drug Discov. 2017 Jul;16(7):457–71.

165. Sievert DM, Ricks P, Edwards JR, Schneider A, Patel J, Srinivasan A, Kallen A, Limbago B, Fridkin S, National Healthcare Safety Network (NHSN) Team and Participating NHSN Facilities. Antimicrobial-resistant pathogens associated with healthcare-associated infections: summary of data reported to the National Healthcare Safety Network at the Centers for Disease Control and Prevention, 2009-2010. Infect Control Hosp Epidemiol. 2013 Jan;34(1):1–14.

166. Maura D, Ballok AE, Rahme LG. Considerations and caveats in anti-virulence drug development. Curr Opin Microbiol. 2016 Oct;33:41–6.

167. Le KY, Otto M. Quorum-sensing regulation in staphylococci-an overview. Front Microbiol. 2015;6:1174.

168. Cheung GYC, Joo H-S, Chatterjee SS, Otto M. Phenol-soluble modulins--critical determinants of staphylococcal virulence. FEMS Microbiol Rev. 2014 Jul;38(4):698–719.

169. Queck SY, Jameson-Lee M, Villaruz AE, Bach T-HL, Khan BA, Sturdevant DE, Ricklefs SM, Li M, Otto M. RNAIII-independent target gene control by the *agr* quorum-sensing system: insight into the evolution of virulence regulation in *Staphylococcus aureus*. Mol Cell. 2008 Oct 10;32(1):150–8.

170. Khan BA, Yeh AJ, Cheung GYC, Otto M. Investigational therapies targeting quorum-sensing for the treatment of *Staphylococcus aureus* infections. Expert Opin Investig Drugs. 2015 May;24(5):689–704.

171. Piewngam P, Chiou J, Chatterjee P, Otto M. Alternative approaches to treat bacterial infections: targeting quorum-sensing. Expert Rev Anti Infect Ther. 2020 Jun;18(6):499–510.

172. Thoendel M, Kavanaugh JS, Flack CE, Horswill AR. Peptide signaling in the Staphylococci. Chem Rev. 2011 Jan 12;111(1):117–51.

173. Mansson M, Nielsen A, Kjærulff L, Gotfredsen CH, Wietz M, Ingmer H, Gram L, Larsen TO. Inhibition of virulence gene expression in *Staphylococcus aureus* by novel depsipeptides from a marine photobacterium. Mar Drugs. 2011 Dec;9(12):2537–52.

174. Nakayama J, Uemura Y, Nishiguchi K, Yoshimura N, Igarashi Y, Sonomoto K. Ambuic Acid Inhibits the Biosynthesis of Cyclic Peptide Quormones in Gram-Positive Bacteria. Antimicrob Agents Chemother. 2009 Feb;53(2):580–6.

175. Sully EK, Malachowa N, Elmore BO, Alexander SM, Femling JK, Gray BM, DeLeo FR, Otto M, Cheung AL, Edwards BS, Sklar LA, Horswill AR, Hall PR, Gresham HD. Selective Chemical Inhibition of *agr* Quorum Sensing in *Staphylococcus aureus* Promotes Host Defense with Minimal Impact on Resistance. PLoS Pathog [Internet]. 2014 Jun 12 [cited 2021 Mar 2];10(6). Available from: https://www.ncbi.nlm.nih.gov/pmc/articles/PMC4055767/

176. Jarraud S, Lyon GJ, Figueiredo AMS, Gérard L, Vandenesch F, Etienne J, Muir TW, Novick RP. Exfoliatin-Producing Strains Define a Fourth *agr* Specificity Group in *Staphylococcus aureus*. J Bacteriol. 2000 Nov;182(22):6517–22.

177. Ji G, Beavis R, Novick RP. Bacterial interference caused by autoinducing peptide variants. Science. 1997 Jun 27;276(5321):2027–30.

178. Canovas J, Baldry M, Bojer MS, Andersen PS, Grzeskowiak PK, Stegger M, Damborg P, Olsen CA, Ingmer H. Corrigendum: Cross-Talk between *Staphylococcus aureus* and Other Staphylococcal Species via the *agr* Quorum Sensing System. Front Microbiol [Internet]. 2017 Jun 8 [cited 2021 Feb 27];8. Available from: https://www.ncbi.nlm.nih.gov/pmc/articles/PMC5463500/

179. Canovas J, Baldry M, Bojer MS, Andersen PS, Grzeskowiak PK, Stegger M, Damborg P, Olsen CA, Ingmer H. Cross-Talk between *Staphylococcus aureus* and Other Staphylococcal Species via the *agr* Quorum Sensing System. Front Microbiol. 2016;7:1733.

180. Otto M, Echner H, Voelter W, Götz F. Pheromone Cross-Inhibition between *Staphylococcus aureus* and *Staphylococcus epidermidis*. Infect Immun. 2001 Mar;69(3):1957–60.

181. Williams MR, Costa SK, Zaramela LS, Khalil S, Todd DA, Winter HL, Sanford JA, O'Neill AM, Liggins MC, Nakatsuji T, Cech NB, Cheung AL, Zengler K, Horswill AR, Gallo RL. Quorum sensing between bacterial species on the skin protects against epidermal injury in atopic dermatitis. Sci Transl Med [Internet]. 2019 May 1 [cited 2021 Jan 22];11(490). Available from: https://www.ncbi.nlm.nih.gov/pmc/articles/PMC7106486/

182. Horswill AR, Gordon CP. Structure-Activity Relationship Studies of Small Molecule Modulators of the Staphylococcal Accessory Gene Regulator. J Med Chem. 2020 Mar 26;63(6):2705–30.

183. Lyon GJ, Wright JS, Christopoulos A, Novick RP, Muir TW. Reversible and specific extracellular antagonism of receptor-histidine kinase signaling. J Biol Chem. 2002 Feb 22;277(8):6247–53.

184. Mayville P, Ji G, Beavis R, Yang H, Goger M, Novick RP, Muir TW. Structure-activity analysis of synthetic autoinducing thiolactone peptides from *Staphylococcus aureus* responsible for virulence. Proc Natl Acad Sci U S A. 1999 Feb;96(4):1218–23.

185. Tal-Gan Y, Ivancic M, Cornilescu G, Yang T, Blackwell HE. Highly Stable, Amide-Bridged Autoinducing Peptide Analogues that Strongly Inhibit the AgrC Quorum Sensing Receptor in *Staphylococcus aureus*. Angew Chem Int Ed Engl. 2016 Jul 25;55(31):8913–7.

186. Baldry M, Nakamura Y, Nakagawa S, Frees D, Matsue H, Núñez G, Ingmer H. Application of an *agr*-Specific antivirulence compound as therapy for *Staphylococcus aureus*-Induced inflammatory skin disease. J Infect Dis. 2018 Aug 14;218(6):1009–13.

187. Baldry M, Kitir B, Frøkiær H, Christensen SB, Taverne N, Meijerink M, Franzyk H, Olsen CA, Wells JM, Ingmer H. The *agr* Inhibitors Solonamide B and Analogues Alter Immune Responses to *Staphylococccus aureus* but Do Not Exhibit Adverse Effects on Immune Cell Functions. Rohde H, editor. PLoS One. 2016 Jan;11(1):e0145618.

188. Nielsen A, Mańsson M, Bojer MS, Gram L, Larsen TO, Novick RP, Frees D, Frøkiær H, Ingmer H. Solonamide B inhibits quorum sensing and reduces *Staphylococcus aureus* mediated killing of human neutrophils. PLoS One [Internet]. 2014 Jan;9(1). Available from: https://pubmed.ncbi.nlm.nih.gov/24416329/

189. Piewngam P, Zheng Y, Nguyen TH, Dickey SW, Joo H-S, Villaruz AE, Glose KA, Fisher EL, Hunt RL, Li B, Chiou J, Pharkjaksu S, Khongthong S, Cheung GYC, Kiratisin P, Otto M. Pathogen elimination by probiotic *Bacillus* via signaling interference. Nature. 2018 Oct;562(7728):532–7.

190. Hannah J, Ruyle WV, Jones H, Matzuk AR, Kelly KW, Witzel BE, Holtz WJ, Houser RW, Shen TY, Sarett LH. Discovery of diflunisal. Br J Clin Pharmacol. 1977 Feb;4 Suppl 1:7S-13S.

191. Khodaverdian V, Pesho M, Truitt B, Bollinger L, Patel P, Nithianantham S, Yu G, Delaney E, Jankowsky E, Shoham M. Discovery of antivirulence agents against methicillin-resistant *Staphylococcus aureus*. Antimicrob Agents Chemother. 2013 Aug;57(8):3645–52.

192. Kupferwasser LI, Yeaman MR, Nast CC, Kupferwasser D, Xiong Y-Q, Palma M, Cheung AL, Bayer AS. Salicylic acid attenuates virulence in endovascular infections by targeting global regulatory pathways in *Staphylococcus aureus*. J Clin Invest. 2003 Jul 15;112(2):222–33.

193. Boles BR, Horswill AR. *agr*-Mediated Dispersal of *Staphylococcus aureus* Biofilms. Cossart P, editor. PLoS Pathog. 2008 Apr;4(4):e1000052.

194. Cheung GYC, Bae JS, Liu R, Hunt RL, Zheng Y, Otto M. Bacterial virulence plays a crucial role in MRSA sepsis. PLoS Pathog. 2021 Feb 25;17(2):e1009369.

195. Nishitani K, Sutipornpalangkul W, de Mesy Bentley KL, Varrone JJ, Bello-Irizarry SN, Ito H, Matsuda S, Kates SL, Daiss JL, Schwarz EM. Quantifying the natural history of biofilm formation *in vivo* during the establishment of chronic implant-associated *Staphylococcus aureus* osteomyelitis in mice to identify critical pathogen and host factors. J Orthop Res. 2015 Sep;33(9):1311–9.

196. Vuong C, Saenz HL, Götz F, Otto M. Impact of the *agr* Quorum-Sensing System on Adherence to Polystyrene in *Staphylococcus aureus*. J Infect Dis. 2000 Dec;182(6):1688–93.

197. Brady RA, Leid JG, Calhoun JH, Costerton JW, Shirtliff ME. Osteomyelitis and the role of biofilms in chronic infection. FEMS Immunol Med Microbiol. 2008 Jan;52(1):13–22.

198. He L, Le KY, Khan BA, Nguyen TH, Hunt RL, Bae JS, Kabat J, Zheng Y, Cheung GYC, Li M, Otto M. Resistance to leukocytes ties benefits of quorum-sensing dysfunctionality to biofilm infection. Nat Microbiol. 2019 Jul;4(7):1114–9.

199. Suligoy CM, Lattar SM, Noto Llana M, González CD, Alvarez LP, Robinson DA, Gómez MI, Buzzola FR, Sordelli DO. Mutation of *agr* Is Associated with the Adaptation of *Staphylococcus aureus* to the Host during Chronic Osteomyelitis. Front Cell Infect Microbiol [Internet]. 2018 Feb 2 [cited 2021 Jan 25];8. Available from: https://www.ncbi.nlm.nih.gov/pmc/articles/PMC5801681/

200. Traber KE, Lee E, Benson S, Corrigan R, Cantera M, Shopsin B, Novick RP. *agr* function in clinical *Staphylococcus aureus* isolates. Microbiology (Reading). 2008 Aug;154(8):2265–74.

201. Spoonmore TJ, Ford CA, Curry JM, Guelcher SA, Cassat JE. Concurrent local delivery of diflunisal limits bone destruction but fails to improve systemic vancomycin efficacy during *Staphylococcus aureus* osteomyelitis. Antimicrob Agents Chemother. 2020 Jun 23;64(7).

202. Wolfram J, Zhu M, Yang Y, Shen J, Gentile E, Paolino D, Fresta M, Nie G, Chen C, Shen H, Ferrari M, Zhao Y. Safety of nanoparticles in medicine. Curr Drug Targets. 2015;16(14):1671–81.

203. Boyd BJ. Past and future evolution in colloidal drug delivery systems. Expert Opin Drug Deliv. 2008 Jan;5(1):69–85.

204. Oliver SE, Gargano JW, Marin M, Wallace M, Curran KG, Chamberland M, McClung N, Campos-Outcalt D, Morgan RL, Mbaeyi S, Romero JR, Talbot HK, Lee GM, Bell BP, Dooling K. The Advisory Committee on Immunization Practices' Interim Recommendation for Use of Pfizer-BioNTech COVID-19 Vaccine - United States, December 2020. MMWR Morb Mortal Wkly Rep. 2020 Dec 18;69(50):1922–4.

205. Ferreira SMZMD, Domingos GP, Ferreira D dos S, Rocha TGR, Serakides R, de Faria Rezende CM, Cardoso VN, Fernandes SOA, Oliveira MC. Technetium-99m-labeled ceftizoxime loaded long-circulating and pH-sensitive liposomes used to identify osteomyelitis. Bioorg Med Chem Lett. 2012 Jul 15;22(14):4605–8.

206. Ferreira D dos S, Boratto FA, Cardoso VN, Serakides R, Fernandes SO, Ferreira LAM, Oliveira MC. Alendronate-coated long-circulating liposomes containing ^{99m}technetium-ceftizoxime used to identify osteomyelitis. Int J Nanomedicine. 2015;10:2441–50.

207. Qadri S, Haik Y, Mensah-Brown E, Bashir G, Fernandez-Cabezudo MJ, Al-Ramadi BK. Metallic nanoparticles to eradicate bacterial bone infection. Nanomedicine. 2017 Oct;13(7):2241–50.

208. Peng K-T, Chiang Y-C, Huang T-Y, Chen P-C, Chang P-J, Lee C-W. Curcumin nanoparticles are a promising anti-bacterial and anti-inflammatory agent for treating periprosthetic joint infections. Int J Nanomedicine. 2019;14:469–81.

209. Shi Z, Neoh KG, Kang ET, Wang W. Antibacterial and mechanical properties of bone cement impregnated with chitosan nanoparticles. Biomaterials. 2006 Apr;27(11):2440–9.

210. Hassani Besheli N, Mottaghitalab F, Eslami M, Gholami M, Kundu SC, Kaplan DL, Farokhi M. Sustainable Release of Vancomycin from Silk Fibroin Nanoparticles for Treating Severe Bone Infection in Rat Tibia Osteomyelitis Model. ACS Appl Mater Interfaces. 2017 Feb 15;9(6):5128–38.

211. Cobb LH, McCabe EM, Priddy LB. Therapeutics and delivery vehicles for local treatment of osteomyelitis. J Orthop Res. 2020 Oct;38(10):2091–103.

212. Cong Y, Quan C, Liu M, Liu J, Huang G, Tong G, Yin Y, Zhang C, Jiang Q. Alendronate-decorated biodegradable polymeric micelles for potential bone-targeted delivery of vancomycin. J Biomater Sci Polym Ed. 2015;26(11):629–43.

213. Rotman SG, Thompson K, Grijpma DW, Richards RG, Moriarty TF, Eglin D, Guillaume O. Development of bone seeker-functionalised microspheres as a targeted local antibiotic delivery system for bone infections. J Orthop Translat. 2020 Mar;21:136–45.

214. Sindhwani S, Syed AM, Ngai J, Kingston BR, Maiorino L, Rothschild J, MacMillan P, Zhang Y, Rajesh NU, Hoang T, Wu JLY, Wilhelm S, Zilman A, Gadde S, Sulaiman A, Ouyang B, Lin Z, Wang L, Egeblad M, Chan WCW. The entry of nanoparticles into solid tumours. Nat Mater. 2020 May;19(5):566–75.

215. Greish K. Enhanced permeability and retention (EPR) effect for anticancer nanomedicine drug targeting. Methods Mol Biol. 2010;624:25–37.

216. Maeda H. Vascular permeability in cancer and infection as related to macromolecular drug delivery, with emphasis on the EPR effect for tumor-selective drug targeting. Proc Jpn Acad Ser B Phys Biol Sci. 2012;88(3):53–71.

217. Maeda H, Wu J, Sawa T, Matsumura Y, Hori K. Tumor vascular permeability and the EPR effect in macromolecular therapeutics: a review. J Control Release. 2000 Mar 1;65(1–2):271–84.

218. Pober JS, Cotran RS. Cytokines and endothelial cell biology. Physiol Rev. 1990 Apr;70(2):427–51.

219. Quan L, Purdue PE, Liu X, Boska MD, Lele SM, Thiele GM, Mikuls TR, Dou H, Goldring SR, Wang D. Development of a macromolecular prodrug for the treatment of inflammatory arthritis: mechanisms involved in arthrotropism and sustained therapeutic efficacy. Arthritis Res Ther. 2010;12(5):R170.

220. Wang D, Goldring SR. The bone, the joints and the Balm of Gilead. Mol Pharm. 2011 Aug 1;8(4):991–3.

221. Napoli A, Valentini M, Tirelli N, Müller M, Hubbell JA. Oxidation-responsive polymeric vesicles. Nat Mater. 2004 Mar;3(3):183–9.

222. Gupta MK, Meyer TA, Nelson CE, Duvall CL. Poly(PS-b-DMA) micelles for reactive oxygen species triggered drug release. J Control Release. 2012 Sep 28;162(3):591–8.

223. Gupta MK, Martin JR, Werfel TA, Shen T, Page JM, Duvall CL. Cell protective, ABC triblock polymer-based thermoresponsive hydrogels with ROS-triggered degradation and drug release. J Am Chem Soc. 2014 Oct 22;136(42):14896–902.

224. Gupta MK, Martin JR, Dollinger BR, Hattaway ME, Duvall CL. Thermogelling, ABC Triblock Copolymer Platform for Resorbable Hydrogels with Tunable, Degradation-Mediated Drug Release. Adv Funct Mater. 2017 Dec 15;27(47).

225. Poole KM, Nelson CE, Joshi RV, Martin JR, Gupta MK, Haws SC, Kavanaugh TE, Skala MC, Duvall CL. ROS-responsive microspheres for on demand antioxidant therapy in a model of diabetic peripheral arterial disease. Biomaterials. 2015 Feb;41:166–75.

226. Vanderburgh JP, Kwakwa KA, Werfel TA, Merkel AR, Gupta MK, Johnson RW, Guelcher SA, Duvall CL, Rhoades JA. Systemic delivery of a Gli inhibitor via polymeric nanocarriers inhibits tumor-induced bone disease. J Control Release. 2019 Oct;311–312:257–72.

227. Vanderburgh J, Hill JL, Gupta MK, Kwakwa KA, Wang SK, Moyer K, Bedingfield SK, Merkel AR, d'Arcy R, Guelcher SA, Rhoades JA, Duvall CL. Tuning Ligand Density To Optimize Pharmacokinetics of Targeted Nanoparticles for Dual Protection against Tumor-Induced Bone Destruction. ACS Nano. 2020 Jan 28;14(1):311–27.

228. Ford CA, Cassat JE. Advances in the local and targeted delivery of anti-infective agents for management of osteomyelitis. Expert Rev Anti Infect Ther. 2017 Sep;15(9):851–60.

229. Hadjidakis DJ, Androulakis II. Bone remodeling. Ann N Y Acad Sci. 2006 Dec;1092:385–96.

230. Ford CA, Hurford IM, Cassat JE. Antivirulence Strategies for the Treatment of *Staphylococcus aureus* Infections: A Mini Review. Front Microbiol. 2021 Jan 14;11:3568.

231. Wertheim HFL, Melles DC, Vos MC, van Leeuwen W, van Belkum A, Verbrugh HA, Nouwen JL. The role of nasal carriage in *Staphylococcus aureus* infections. Lancet Infect Dis. 2005 Dec;5(12):751–62.

232. Schaffer K, Taylor CT. The impact of hypoxia on bacterial infection. FEBS J. 2015 Jun;282(12):2260–6.

233. Semenza GL, Wang GL. A nuclear factor induced by hypoxia via *de novo* protein synthesis binds to the human erythropoietin gene enhancer at a site required for transcriptional activation. Mol Cell Biol. 1992 Dec;12(12):5447–54.

234. Semenza GL. Hypoxia-inducible factors in physiology and medicine. Cell. 2012 Feb 3;148(3):399–408.

235. Boles BR, Thoendel M, Roth AJ, Horswill AR. Identification of genes involved in polysaccharide-independent *Staphylococcus aureus* biofilm formation. PLoS One. 2010 Apr 14;5(4):e10146.

236. Hartleib J, Köhler N, Dickinson RB, Chhatwal GS, Sixma JJ, Hartford OM, Foster TJ, Peters G, Kehrel BE, Herrmann M. Protein A is the von Willebrand factor binding protein on *Staphylococcus aureus*. Blood. 2000 Sep 15;96(6):2149–56.

237. Klopfenstein N, Cassat JE, Monteith A, Miller A, Drury S, Skaar E, Serezani CH. Murine Models for Staphylococcal Infection. Curr Protoc. 2021 Mar;1(3):e52.

238. Rodda SJ, McMahon AP. Distinct roles for Hedgehog and canonical Wnt signaling in specification, differentiation and maintenance of osteoblast progenitors. Development. 2006 Aug 15;133(16):3231–44.

239. Haase VH, Glickman JN, Socolovsky M, Jaenisch R. Vascular tumors in livers with targeted inactivation of the von Hippel-Lindau tumor suppressor. Proc Natl Acad Sci U S A. 2001 Feb 13;98(4):1583–8.

240. Ryan HE, Poloni M, McNulty W, Elson D, Gassmann M, Arbeit JM, Johnson RS. Hypoxia-inducible factor-1α is a positive factor in solid tumor growth. Cancer Res. 2000 Aug 1;60(15):4010–5.

241. Clausen BE, Burkhardt C, Reith W, Renkawitz R, Förster I. Conditional gene targeting in macrophages and granulocytes using LysMcre mice. Transgenic Res. 1999 Aug;8(4):265–77.

242. Ford CA, Spoonmore TJ, Gupta MK, Duvall CL, Guelcher SA, Cassat JE. Diflunisal-loaded poly(propylene sulfide) nanoparticles decrease *S. aureus*-mediated bone destruction during osteomyelitis. J Orthop Res. 2021 Jan 29;39(2):426–37.

243. Dirckx N, Tower RJ, Mercken EM, Vangoitsenhoven R, Moreau-Triby C, Breugelmans T, Nefyodova E, Cardoen R, Mathieu C, Van der Schueren B, Confavreux CB, Clemens TL, Maes C. *Vhl* deletion in osteoblasts boosts cellular glycolysis and improves global glucose metabolism. J Clin Invest. 2018 Mar 1;128(3):1087–105.

244. Dempster DW, Compston JE, Drezner MK, Glorieux FH, Kanis JA, Malluche H, Meunier PJ, Ott SM, Recker RR, Parfitt AM. Standardized nomenclature, symbols, and units for bone histomorphometry: a 2012 update of the report of the ASBMR Histomorphometry Nomenclature Committee. J Bone Miner Res. 2013 Jan;28(1):2–17.

245. Johnson RW, White JD, Walker EC, Martin TJ, Sims NA. Myokines (muscle-derived cytokines and chemokines) including ciliary neurotrophic factor (CNTF) inhibit osteoblast differentiation. Bone. 2014 Jul;64:47–56.

246. Schmittgen TD, Livak KJ. Analyzing real-time PCR data by the comparative C_T method. Nat Protoc. 2008;3(6):1101–8.

247. Wang L, Deng L, Zhu Y, Wei L, Qi J. 低氧/低氧诱导因子-1α 通路对成骨细胞与破骨细胞耦联的调控作用 [Regulation of interaction of osteoblasts and osteoclasts by hypoxia/hypoxia inducible factor-1α pathway]. Journal of Shanghai Jiaotong University (Medical Science). 2012;32(03):274-278+292.

248. Kang H, Yang K, Xiao L, Guo L, Guo C, Yan Y, Qi J, Wang F, Ryffel B, Li C, Deng L. Osteoblast Hypoxia-Inducible Factor-1α Pathway Activation Restrains Osteoclastogenesis *via* the Interleukin-33-MicroRNA-34a-Notch1 Pathway. Front Immunol. 2017;8:1312.

249. Li M, Kim WY. Two sides to every story: the HIF-dependent and HIF-independent functions of pVHL. J Cell Mol Med. 2011 Feb;15(2):187–95.

250. Horiuchi K, Kimura T, Miyamoto T, Miyamoto K, Akiyama H, Takaishi H, Morioka H, Nakamura T, Okada Y, Blobel CP, Toyama Y. Conditional inactivation of TACE by a *Sox9* promoter leads to osteoporosis and increased granulopoiesis via dysregulation of IL-17 and G-CSF. J Immunol. 2009 Feb 15;182(4):2093–101.

251. Salem S, Gao C, Li A, Wang H, Nguyen-Yamamoto L, Goltzman D, Henderson JE, Gros P. A novel role for interferon regulatory factor 1 (IRF1) in regulation of bone metabolism. Journal of Cellular and Molecular Medicine. 2014;18(8):1588–98.

252. Sadvakassova G, Tiedemann K, Steer KJD, Mikolajewicz N, Stavnichuk M, In-Kyung Lee I, Sabirova Z, Schranzhofer M, Komarova SV. Active hematopoiesis triggers exosomal release of PRDX2 that promotes osteoclast formation. Physiol Rep. 2021 Feb;9(3):e14745.

253. Shim J-H, Stavre Z, Gravallese EM. Bone Loss in Rheumatoid Arthritis: Basic Mechanisms and Clinical Implications. Calcif Tissue Int. 2018 May;102(5):533–46.

254. Ke K, Chen TH-P, Arra M, Mbalaviele G, Swarnkar G, Abu-Amer Y. Attenuation of NF-κB in Intestinal Epithelial Cells Is Sufficient to Mitigate the Bone Loss Comorbidity of Experimental Mouse Colitis. J Bone Miner Res. 2019 Oct;34(10):1880–93.

255. Adami G, Fassio A, Rossini M, Caimmi C, Giollo A, Orsolini G, Viapiana O, Gatti D. Osteoporosis in Rheumatic Diseases. Int J Mol Sci. 2019 Nov 22;20(23).

256. Frost J, Galdeano C, Soares P, Gadd MS, Grzes KM, Ellis L, Epemolu O, Shimamura S, Bantscheff M, Grandi P, Read KD, Cantrell DA, Rocha S, Ciulli A. Potent and selective chemical probe of hypoxic signalling downstream of HIF-α hydroxylation via VHL inhibition. Nat Commun. 2016 Nov 4;7:13312.

257. Haase VH. HIF-prolyl hydroxylases as therapeutic targets in erythropoiesis and iron metabolism. Hemodial Int. 2017 Jun;21 Suppl 1:S110–24.

258. Schwarz EM, Parvizi J, Gehrke T, Aiyer A, Battenberg A, Brown SA, Callaghan JJ, Citak M, Egol K, Garrigues GE, Ghert M, Goswami K, Green A, Hammound S, Kates SL, McLaren AC, Mont MA, Namdari S, Obremskey WT, O'Toole R, Raikin S, Restrepo C, Ricciardi B, Saeed K, Sanchez-Sotelo J, Shohat N, Tan T, Thirukumaran CP, Winters B. 2018 International Consensus Meeting on Musculoskeletal Infection: Research Priorities from the General Assembly Questions. J Orthop Res. 2019 May;37(5):997–1006.

259. Ghosh C, Sarkar P, Issa R, Haldar J. Alternatives to Conventional Antibiotics in the Era of Antimicrobial Resistance. Trends Microbiol. 2019 Apr;27(4):323–38.

260. Kurtz SM, Lau E, Watson H, Schmier JK, Parvizi J. Economic burden of periprosthetic joint infection in the United States. J Arthroplasty. 2012 Sep;27(8 Suppl):61-65.e1.

261. Zimmerli W, Waldvogel FA, Vaudaux P, Nydegger UE. Pathogenesis of foreign body infection: description and characteristics of an animal model. J Infect Dis. 1982 Oct;146(4):487–97.

262. Masters EA, Trombetta RP, de Mesy Bentley KL, Boyce BF, Gill AL, Gill SR, Nishitani K, Ishikawa M, Morita Y, Ito H, Bello-Irizarry SN, Ninomiya M, Brodell JD, Lee CC, Hao SP, Oh I, Xie C, Awad HA, Daiss JL, Owen JR, Kates SL, Schwarz EM, Muthukrishnan G. Evolving concepts in bone infection: redefining "biofilm", "acute vs. chronic osteomyelitis", "the immune proteome" and "local antibiotic therapy." Bone Res [Internet]. 2019 Jul 15 [cited 2021 Jan 29];7. Available from: https://www.ncbi.nlm.nih.gov/pmc/articles/PMC6804538/

263. Oerlemans C, Bult W, Bos M, Storm G, Nijsen JFW, Hennink WE. Polymeric micelles in anticancer therapy: targeting, imaging and triggered release. Pharm Res. 2010 Dec;27(12):2569–89.

264. Danhier F, Ansorena E, Silva JM, Coco R, Le Breton A, Préat V. PLGA-based nanoparticles: an overview of biomedical applications. J Control Release. 2012 Jul 20;161(2):505–22.

265. Cheng H, Chawla A, Yang Y, Li Y, Zhang J, Jang HL, Khademhosseini A. Development of nanomaterials for bone-targeted drug delivery. Drug Discov Today. 2017 Sep;22(9):1336–50.

266. Diekema DJ, Richter SS, Heilmann KP, Dohrn CL, Riahi F, Tendolkar S, McDanel JS, Doern GV. Continued emergence of USA300 methicillin-resistant *Staphylococcus aureus* in the United States: results from a nationwide surveillance study. Infect Control Hosp Epidemiol. 2014 Mar;35(3):285–92.

267. Shi Y, van Steenbergen MJ, Teunissen EA, Novo L, Gradmann S, Baldus M, van Nostrum CF, Hennink WE. Π-π stacking increases the stability and loading capacity of thermosensitive polymeric micelles for chemotherapeutic drugs. Biomacromolecules. 2013 Jun 10;14(6):1826–37.

268. Elsana H, Olusanya TOB, Carr-Wilkinson J, Darby S, Faheem A, Elkordy AA. Evaluation of novel cationic gene based liposomes with cyclodextrin prepared by thin film hydration and microfluidic systems. Sci Rep. 2019 Oct 22;9(1):15120.

269. Inoue Y, Izawa K, Kiryu S, Tojo A, Ohtomo K. Diet and abdominal autofluorescence detected by *in vivo* fluorescence imaging of living mice. Mol Imaging. 2008 Feb;7(1):21–7.

270. Danson S, Ferry D, Alakhov V, Margison J, Kerr D, Jowle D, Brampton M, Halbert G, Ranson M. Phase I dose escalation and pharmacokinetic study of pluronic polymer-bound

doxorubicin (SP1049C) in patients with advanced cancer. Br J Cancer. 2004 Jun 1;90(11):2085–91.

271. Strickley RG. Solubilizing excipients in oral and injectable formulations. Pharm Res. 2004 Feb;21(2):201–30.

272. Dunnill C, Patton T, Brennan J, Barrett J, Dryden M, Cooke J, Leaper D, Georgopoulos NT. Reactive oxygen species (ROS) and wound healing: the functional role of ROS and emerging ROS-modulating technologies for augmentation of the healing process. Int Wound J. 2017 Feb;14(1):89–96.

273. Moslehi J, Rathmell WK. The 2019 Nobel Prize honors fundamental discoveries in hypoxia response. J Clin Invest. 2020 Jan 2;130(1):4–6.

274. Guerra FE, Borgogna TR, Patel DM, Sward EW, Voyich JM. Epic Immune Battles of History: Neutrophils vs. *Staphylococcus aureus*. Front Cell Infect Microbiol. 2017;7:286.

275. Gardner PJ, Liyanage SE, Cristante E, Sampson RD, Dick AD, Ali RR, Bainbridge JW. Hypoxia inducible factors are dispensable for myeloid cell migration into the inflamed mouse eye. Sci Rep [Internet]. 2017 Jan 23 [cited 2021 Mar 3];7. Available from: https://www.ncbi.nlm.nih.gov/pmc/articles/PMC5256030/

276. Suwanpradid J, Shih M, Pontius L, Yang B, Birukova A, Guttman-Yasky E, Corcoran DL, Que LG, Tighe RM, MacLeod AS. Arginase1 deficiency in monocytes/macrophages up-regulates iNOS to promote cutaneous contact hypersensitivity. J Immunol. 2017 Sep 1;199(5):1827–34.

277. Li B, Jiang B, Boyce BM, Lindsey BA. Multilayer polypeptide nanoscale coatings incorporating IL-12 for the prevention of biomedical device associated infections. Biomaterials. 2009 May;30(13):2552–8.

278. Fisher S, Burgess WL, Hines KD, Mason GL, Owiny JR. Interstrain Differences in CO_2-Induced Pulmonary Hemorrhage in Mice. J Am Assoc Lab Anim Sci. 2016 Nov;55(6):811–5.

279. Frazziano G, Moreno L, Moral-Sanz J, Menendez C, Escolano L, Gonzalez C, Villamor E, Alvarez-Sala JL, Cogolludo AL, Perez-Vizcaino F. Neutral sphingomyelinase, NADPH oxidase and reactive oxygen species. Role in acute hypoxic pulmonary vasoconstriction. J Cell Physiol. 2011 Oct;226(10):2633–40.

280. Zhang W, Li Q, Li D, Li J, Aki D, Liu Y-C. The E3 ligase VHL controls alveolar macrophage function via metabolic-epigenetic regulation. J Exp Med. 2018 Dec 3;215(12):3180–93.

281. Izquierdo HM, Brandi P, Gómez M-J, Conde-Garrosa R, Priego E, Enamorado M, Martínez-Cano S, Sánchez I, Conejero L, Jimenez-Carretero D, Martín-Puig S, Guilliams M, Sancho D. Von Hippel-Lindau Protein Is Required for Optimal Alveolar Macrophage

Terminal Differentiation, Self-Renewal, and Function. Cell Rep. 2018 Aug 14;24(7):1738–46.

282. Fawell JK, Thomson C, Cooke L. Respiratory artefact produced by carbon dioxide and pentobarbitone sodium euthanasia in rats. Lab Anim. 1972 Sep;6(3):321–6.

283. Boivin GP, Bottomley MA, Schiml PA, Goss L, Grobe N. Physiologic, Behavioral, and Histologic Responses to Various Euthanasia Methods in C57BL/6NTac Male Mice. J Am Assoc Lab Anim Sci. 2017 Jan;56(1):69–78.

284. Loots GG, Robling AG, Chang JC, Murugesh DK, Bajwa J, Carlisle C, Manilay JO, Wong A, Yellowley CE, Genetos DC. *Vhl* deficiency in osteocytes produces high bone mass and hematopoietic defects. Bone. 2018 Nov;116:307–14.

285. Oritani K, Kincade PW. Identification of stromal cell products that interact with pre-B cells. J Cell Biol. 1996 Aug;134(3):771–82.

286. Shen B, Tasdogan A, Ubellacker JM, Zhang J, Nosyreva ED, Du L, Murphy MM, Hu S, Yi Y, Kara N, Liu X, Guela S, Jia Y, Ramesh V, Embree C, Mitchell EC, Zhao YC, Ju LA, Hu Z, Crane GM, Zhao Z, Syeda R, Morrison SJ. A mechanosensitive peri-arteriolar niche for osteogenesis and lymphopoiesis. Nature. 2021 Feb 24;

287. Khare D, Or R, Resnick I, Barkatz C, Almogi-Hazan O, Avni B. Mesenchymal Stromal Cell-Derived Exosomes Affect mRNA Expression and Function of B-Lymphocytes. Front Immunol. 2018;9:3053.

288. Aurrand-Lions M, Mancini SJC. Murine Bone Marrow Niches from Hematopoietic Stem Cells to B Cells. Int J Mol Sci [Internet]. 2018 Aug 10 [cited 2021 Mar 2];19(8). Available from: https://www.ncbi.nlm.nih.gov/pmc/articles/PMC6121419/

289. Chicana B, Donham C, Millan AJ, Manilay JO. Wnt Antagonists in Hematopoietic and Immune Cell Fate: Implications for Osteoporosis Therapies. Curr Osteoporos Rep. 2019 Apr;17(2):49–58.

290. Safran M, Kim WY, O'Connell F, Flippin L, Günzler V, Horner JW, Depinho RA, Kaelin WG. Mouse model for noninvasive imaging of HIF prolyl hydroxylase activity: assessment of an oral agent that stimulates erythropoietin production. Proc Natl Acad Sci U S A. 2006 Jan;103(1):105–10.

291. Nishikimi M, Fukuyama R, Minoshima S, Shimizu N, Yagi K. Cloning and chromosomal mapping of the human nonfunctional gene for L-gulono-gamma-lactone oxidase, the enzyme for L-ascorbic acid biosynthesis missing in man. J Biol Chem. 1994 May 6;269(18):13685–8.

292. Nishikimi M, Yagi K. Biochemistry and molecular biology of ascorbic acid biosynthesis. Subcell Biochem. 1996;25:17–39.

293. Lind J. A Treatise on the Scurvy: In Three Parts. Containing an inquiry Into the Nature, Causes, and Cure, of that Disease. Together with a Critical and Chronological View of what has been published on the subject. First Edition. Edinburgh: Sands, Murray and Cochran for A Kincaid and A Donaldson; 1753. 584 p.

294. Svirbely JL, Szent-Györgyi A. The chemical nature of vitamin C. Biochem J. 1932;26(3):865–70.

295. Figueroa-Méndez R, Rivas-Arancibia S. Vitamin C in Health and Disease: Its Role in the Metabolism of Cells and Redox State in the Brain. Front Physiol [Internet]. 2015 [cited 2021 Feb 15];6. Available from: https://www.frontiersin.org/articles/10.3389/fphys.2015.00397/full

296. Schwarz RI, Kleinman P, Owens N. Ascorbate can act as an inducer of the collagen pathway because most steps are tightly coupled. Ann N Y Acad Sci. 1987;498:172–85.

297. Barnes MJ. Function of ascorbic acid in collagen metabolism. Ann N Y Acad Sci. 1975 Sep 30;258:264–77.

298. Kivirikko KI, Myllylä R. Post-translational processing of procollagens. Ann N Y Acad Sci. 1985;460:187–201.

299. Nytko KJ, Maeda N, Schläfli P, Spielmann P, Wenger RH, Stiehl DP. Vitamin C is dispensable for oxygen sensing *in vivo*. Blood. 2011 May 19;117(20):5485–93.

300. Hemilä H. Vitamin C and Infections. Nutrients. 2017 Apr;9(4):339.

301. Carr AC, Maggini S. Vitamin C and Immune Function. Nutrients [Internet]. 2017 Nov 3 [cited 2021 Feb 15];9(11). Available from: https://www.ncbi.nlm.nih.gov/pmc/articles/PMC5707683/

302. Grbic R, Miric DJ, Kisic B, Popovic L, Nestorovic V, Vasic A. Sequential analysis of oxidative stress markers and vitamin C status in acute bacterial osteomyelitis. Mediators Inflamm. 2014;2014:975061.

303. Abbasy MA, Harris LslieJ, Hill NG. VITAMIN C AND INFECTION EXCRETION OF VITAMIN C IN OSTEOMYELITIS. Lancet. 1937 Jul 24;230(5943):177–80.

304. Cui J, Yuan X, Wang L, Jones G, Zhang S. Recent loss of vitamin C biosynthesis ability in bats. PLoS One. 2011;6(11):e27114.

305. Drouin G, Godin J-R, Pagé B. The genetics of vitamin C loss in vertebrates. Curr Genomics. 2011 Aug;12(5):371–8.

306. Jackel SS, Mosbach EH, Burns JJ, King CG. The synthesis of l-ascorbic acid by the albino rat. J Biol Chem. 1950 Oct;186(2):569–79.

307. Maeda N, Hagihara H, Nakata Y, Hiller S, Wilder J, Reddick R. Aortic wall damage in mice unable to synthesize ascorbic acid. Proc Natl Acad Sci U S A. 2000 Jan 18;97(2):841–6.

308. Consoli DC, Brady LJ, Bowman AB, Calipari ES, Harrison FE. Ascorbate deficiency decreases dopamine release in *Gulo*$^{-/-}$ and APP/PSEN1 mice. J Neurochem. 2020 Aug 14;

309. Li W, Maeda N, Beck MA. Vitamin C Deficiency Increases the Lung Pathology of Influenza Virus–Infected *Gulo*$^{-/-}$ Mice. J Nutr. 2006 Oct;136(10):2611–6.

310. Kim Y, Kim H, Bae S, Choi J, Lim SY, Lee N, Kong JM, Hwang Y-I, Kang JS, Lee WJ. Vitamin C Is an Essential Factor on the Anti-viral Immune Responses through the Production of Interferon-α/β at the Initial Stage of Influenza A Virus (H3N2) Infection. Immune Netw. 2013 Apr;13(2):70–4.

311. Marik PE, Khangoora V, Rivera R, Hooper MH, Catravas J. Hydrocortisone, Vitamin C, and Thiamine for the Treatment of Severe Sepsis and Septic Shock: A Retrospective Before-After Study. Chest. 2017 Jun;151(6):1229–38.

312. Ran L, Zhao W, Wang J, Wang H, Zhao Y, Tseng Y, Bu H. Extra Dose of Vitamin C Based on a Daily Supplementation Shortens the Common Cold: A Meta-Analysis of 9 Randomized Controlled Trials. Biomed Res Int. 2018;2018:1837634.

313. Hemilä H, Chalker E. Vitamin C Can Shorten the Length of Stay in the ICU: A Meta-Analysis. Nutrients. 2019 Mar 27;11(4).

314. Hemilä H, Chalker E. Reanalysis of the Effect of Vitamin C on Mortality in the CITRIS-ALI Trial: Important Findings Dismissed in the Trial Report. Front Med (Lausanne) [Internet]. 2020 Oct 7 [cited 2021 Feb 15];7. Available from: https://www.ncbi.nlm.nih.gov/pmc/articles/PMC7575729/

315. Fowler AA, Truwit JD, Hite RD, Morris PE, DeWilde C, Priday A, Fisher B, Thacker LR, Natarajan R, Brophy DF, Sculthorpe R, Nanchal R, Syed A, Sturgill J, Martin GS, Sevransky J, Kashiouris M, Hamman S, Egan KF, Hastings A, Spencer W, Tench S, Mehkri O, Bindas J, Duggal A, Graf J, Zellner S, Yanny L, McPolin C, Hollrith T, Kramer D, Ojielo C, Damm T, Cassity E, Wieliczko A, Halquist M. Effect of Vitamin C Infusion on Organ Failure and Biomarkers of Inflammation and Vascular Injury in Patients With Sepsis and Severe Acute Respiratory Failure: The CITRIS-ALI Randomized Clinical Trial. JAMA. 2019 Oct 1;322(13):1261–70.

316. Kim H, Bae S, Yu Y, Kim Y, Kim H-R, Hwang Y, Kang JS, Lee WJ. The Analysis of Vitamin C Concentration in Organs of *Gulo*$^{-/-}$ Mice Upon Vitamin C Withdrawal. Immune Netw. 2012 Feb;12(1):18–26.

317. Michels AJ, Frei B. Myths, Artifacts, and Fatal Flaws: Identifying Limitations and Opportunities in Vitamin C Research. Nutrients. 2013 Dec 16;5(12):5161–92.

318. Vitamin C and contribution to the normal function of the immune system: evaluation of a health claim pursuant to Article 14 of Regulation (EC) No 1924/2006. EFSA Journal. 2015;13(11):4298.

319. Alabi ZO, Thomas KD, Ogunbona O, Elegbe IA. The effect of antibacterial agents on plasma vitamin C levels. Afr J Med Med Sci. 1994 Jun;23(2):143–6.

320. Labbé J-L, Peres O, Leclair O, Goulon R, Scemama P, Jourdel F, Menager C, Duparc B, Lacassin F. Acute osteomyelitis in children: the pathogenesis revisited? Orthop Traumatol Surg Res. 2010 May;96(3):268–75.

321. Mills RJ, Boyling A, Cheng TL, Peacock L, Savage PB, Tägil M, Little DG, Schindeler A. CSA-90 reduces periprosthetic joint infection in a novel rat model challenged with local and systemic *Staphylococcus aureus*. J Orthop Res. 2020 Sep;38(9):2065–73.

322. Wang Y, Cheng LI, Helfer DR, Ashbaugh AG, Miller RJ, Tzomides AJ, Thompson JM, Ortines RV, Tsai AS, Liu H, Dillen CA, Archer NK, Cohen TS, Tkaczyk C, Stover CK, Sellman BR, Miller LS. Mouse model of hematogenous implant-related *Staphylococcus aureus* biofilm infection reveals therapeutic targets. Proc Natl Acad Sci U S A. 2017 Jun 27;114(26):E5094–102.

323. Francis KP, Joh D, Bellinger-Kawahara C, Hawkinson MJ, Purchio TF, Contag PR. Monitoring bioluminescent *Staphylococcus aureus* infections in living mice using a novel *luxABCDE* construct. Infect Immun. 2000 Jun;68(6):3594–600.

324. Plaut RD, Mocca CP, Prabhakara R, Merkel TJ, Stibitz S. Stably Luminescent *Staphylococcus aureus* Clinical Strains for Use in Bioluminescent Imaging. PLoS One [Internet]. 2013 Mar 12 [cited 2021 Mar 2];8(3). Available from: https://www.ncbi.nlm.nih.gov/pmc/articles/PMC3595258/

325. Archer NK, Wang Y, Ortines RV, Liu H, Nolan SJ, Liu Q, Alphonse MP, Dikeman DA, Mazhar M, Miller RJ, Anderson LS, Francis KP, Simon SI, Miller LS. Preclinical Models and Methodologies for Monitoring *Staphylococcus aureus* Infections Using Noninvasive Optical Imaging. Methods Mol Biol. 2020;2069:197–228.

326. Tseng J-C, Vasquez K, Peterson JD. Optical Imaging on the IVIS SpectrumCT System: General and Technical Considerations for 2D and 3D Imaging. Waltham, MA, USA: PerkinElmer, Inc.; 2015 p. 18.